Design and Synthesis of Rhenium and Ruthenium Complexes and Their Catalytic Applications Towards Sustainable Transformation

Thesis Submitted for the Degree of

Doctor of Philosophy (Science)

By

Uday Shee

Index no. 45/20/chem./27

Department of Chemistry

Jadavpur University

Kolkata - 700032

August, 2025

Prof. Kajal Krishna Rajak,
Professor,
Department of Chemistry

JADAVPUR UNIVERSITY
KOLKATA - 700002, INDIA
E-mail: kajalrajak@gmail.com
Mobile: +91-9830905167

CERTIFICATE FROM THE SUPERVISORS

This is to certify that the thesis entitled " **Design and Synthesis of Rhenium and Ruthenium Complexes and Their Catalytic Applications Towards Sustainable Transformation**" submitted by **Mr. Uday Shee** who got his name registered on **October 16, 2020** for the award of Ph.D. (Science) degree of Jadavpur University, is absolutely based on his own work under my supervision and that neither this thesis nor any part of it has been submitted for either any degree/diploma or any other academic award anywhere before.

Date: 26th August 2025

Kajal Krishna Rajak

(Prof. Kajal Krishna Rajak)
Signature of the Supervisor & date with seal
Department of Chemistry
Jadavpur University
Kolkata-700032

DEDICATION

In loving memory of my mother,
my first teacher and eternal inspiration.

And to my father,
for his unwavering support, trust, and love.

PREFACE

The thesis entitled ***"Design and Synthesis of Rhenium and Ruthenium Complexes and Their Catalytic Applications Towards Sustainable Transformation"*** offers an overview of recent research focused on advancing sustainable chemical processes. It reflects a continued effort to develop and understand rhenium and ruthenium based complexes as catalysts for green synthetic methodologies, with particular emphasis on applications in artificial photosynthesis and environmentally benign transformations.

The thesis comprises of five chapters.

Chapter 1

This chapter encompasses a comprehensive summary of the research work presented, along with a brief description of the physical techniques and instrumental methods employed throughout the study.

Chapter 2

This chapter presents two dinuclear rhenium(V) oxo complexes that function as homogeneous electrocatalysts for water oxidation in acetonitrile–water mixtures. Oxygen evolution was verified using GC-TCD analysis. Controlled potential electrolysis (CPE) performed at 1.30 V (vs Ag/AgCl, pH ~7) generated their monocationic species through a redox-induced electron transfer (RIET) process, which were subsequently oxidized in situ to high-valent Re(VI)=O intermediates. In addition, this chapter includes experimental investigations of the photophysical properties of these complexes, complemented by comprehensive DFT and TDDFT calculations.

Chapter 3

This chapter presents six isomeric rhenium(I) tricarbonyl complexes with asymmetric diimine ligands, synthesized and fully characterized by spectroscopy and X-ray crystallography. These complexes catalyze both electrochemical and visible-light-driven CO_2 reduction. In the presence of trifluoroethanol (TFE), electrochemical reduction yielded CH_4 and CO, while photochemical reduction in acetonitrile with triethanolamine (TEOA) selectively produced CO. The complex with the 2-(pyridin-2-yl)naphtho[1,2-d]oxazole ligand showed the highest

activity, with a turnover number (TON) of 660 for CO in 5 hours. Mechanistic insights from NMR, UV-Vis, and TD-DFT studies underscore the role of ligand design in optimizing photocatalytic performance for solar-to-fuel applications.

Chapter 4

This chapter explores novel ruthenium complexes incorporating bis(2-picolyl)amine, bipyridine, and BF_2-chelated dipyrromethane (BODIPY) ligands, modified with electron-donating groups to enhance light absorption and catalytic performance. Designed as self-photosensitizing systems, these complexes were evaluated for visible-light-driven CO_2 reduction to CO. The study investigates solvent effects, product evolution, and reaction selectivity, alongside spectroscopic and electrochemical analyses to identify intermediates and understand redox behaviour. The findings offer valuable insights into designing efficient, integrated photocatalysts for CO_2 reduction.

Chapter 5

This work demonstrates the use of well-defined Ru(III) polypyridyl complexes as organocatalysts for dehydrogenative annulation reactions, enabling the synthesis of substituted quinolines from 2-aminobenzyl alcohols with secondary alcohols or ketones. The study highlights the cooperative role of the redox-active polypyridyl ligands with the Ru(III) center in facilitating hydrogen removal and bond formation, underscoring the efficiency and versatility of these systems in oxidative couplings and their potential in atom-economical synthesis.

ACKNOWLEDGEMENT

I am delighted to acknowledge the contributions of those who have supported me during this research.

I extend my heartfelt thanks and deep respect to my supervisor, **Prof. Kajal Krishna Rajak**, for offering me this research opportunity. His exceptional mentorship, insightful guidance, and continuous encouragement have been a constant source of inspiration. His remarkable foresight and practical wisdom have been instrumental in navigating the complexities of this work and bringing this thesis to its conclusion.

I sincerely thank **Prof. Partha Roy**, Section-in-Charge, Inorganic Chemistry Section, along with **Prof. Kaushikisankar Pramanik**, **Prof. Samaresh Bhattacharya** and **Prof. Sujoy Baitalik** for their valuable suggestions and support throughout this work. I am also deeply grateful to **Dr. Prasanta Ghosh** (RKM Residential College, Narendrapur) and **Prof. Chhanda Mukhopadhyay** (University of Calcutta), whose consistent encouragement, insightful advice, and thoughtful guidance have significantly contributed to the progress and completion of this research. Their support has been a constant source of motivation throughout my academic journey.

I would like to express my deepest gratitude to my beloved parents for their unwavering love, constant support, and endless sacrifices throughout every stage of my life. Their encouragement, both emotional and moral, has been the foundation of all my achievements. Their patience and faith in me gave me strength during the most challenging moments of this academic journey.

I would like to express my heartfelt gratitude to my confidante and closest supporter, **Ms. Barbie Chaudhury**, for her constant encouragement, understanding, and unwavering belief in me. Her emotional strength and reassuring presence have been instrumental throughout this journey. In times of doubt and difficulty, her support uplifted me and gave me the courage to persevere. I am truly thankful for the positivity, patience, and inspiration she has brought into my life during the course of this work.

I am truly grateful for **Dr. Sandip Mondal's** mentorship and his sincere involvement at every stage of my research. I also extend my heartfelt thanks to both my former and current labmates **Dr. Debopom Sinha**, **Dr. Tapashi Das**, **Dr. Mitali Majumdar**, **Supriya Debnath**,

Dr. Roumi Patra, **Sneha Ray**, and **Biswajit Khutia** - for their constant cooperation and for fostering a friendly and supportive environment that greatly contributed to the successful preparation of my thesis.

Special thanks are due to **Anupam Jana (Mof)**, **Dr. Debasis Jana (Boss)**, **Gopal Karnar (Gopu Da)**, **Arijit Maity**, **Sampad Malik**, **Dr. Rakesh Debnath**, **Supriyo Halder**, **Srijita Naskar**, **Sourav Sarkar** and **Soumitra Rana** (University of Calcutta) for their generous help and support in various ways throughout the course of my research. Their assistance, both academic and personal, has been truly appreciated.

I would also like to extend my sincere thanks to my friends **Dr. Soumen Nayak**, **Malay Jana**, **Dr. Sayak Gupta** and **Someswar Banerjee** for their constant support, encouragement, and friendship, which have always been a source of strength and positivity throughout my journey.

I thank **CSIR**, New Delhi for my fellowship and contingency grants.

I gratefully acknowledge Jadavpur University for providing me the infrastructural facilities for my research.

I also acknowledge all my friends, teachers, relatives and well-wishers for their support, whom I could not mention by name.

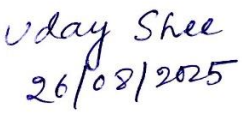

Uday Shee

CONTENTS

Chapter I

A Concise Literature Review of Rhenium and Ruthenium chemistry and their catalytic activities

I.1 General Introduction

Rhenium (Re)[1-4] and Ruthenium (Ru)[5-9], occupying neighbouring groups 7 and 8 in the periodic table, stand out as fascinating transition metals with rich and diverse chemistries that have garnered significant attention in catalysis and energy conversion research. Discovered in 1925, Rhenium is characterized by its exceptionally high melting point and density, coupled with a wide array of accessible oxidation states ranging from -1 to +7. Ruthenium, a precious metal discovered earlier in 1844, is renowned for its corrosion resistance and versatile catalytic capabilities, exhibiting oxidation states from 0 to +8. Both elements readily form coordination complexes with various ligands, including halides, oxygen donors, phosphines, carbonyls, and notably, nitrogen-containing heterocyclic ligands such as pyridines, bipyridines, and phenanthrolines, enabling their use as catalysts where a central metal atom, fine-tuned by appropriate ligands, serves to lower activation energies and facilitate electron transfer processes, demonstrating remarkable activity in numerous chemical transformations spanning organic synthesis to industrial processes, including hydrogenation[10-14], oxidation[15-17], and carbon-carbon bond formation[18-21].

In recent years, the quest to uncover the unique chemical properties of rhenium has spurred extensive research across a wide range of scientific disciplines. Beyond its well-established role in catalysis[22,23], rhenium has gained prominence in areas such as nuclear medicine[24-29], biological applications[30-33], photophysics[34-40], chemosensing and molecular recognition[41-45], materials science, and coordination chemistry.

Rhenium's +5 oxidation state displays distinct chemical behaviour, forming valuable complexes often with coordination numbers of 4, 5, or 6, particularly the oxo complexes (containing Re=O) such as LL'Re(O)Cl_3 or $L_2Cl_3Re{=}O$, which are effective catalysts for oxidation reactions, like the conversion of thiols to disulfides by activating sulfoxides for oxygen transfer[46]. Rhenium(I) complexes also exhibit notable catalytic versatility, exhibiting diverse properties prominently featured in photocatalytic CO_2 reduction[47-50], especially with polypyridyl ligands that facilitate light absorption and electron transfer; they also function as homogeneous catalysts in hydrogenation and transfer hydrogenation of unsaturated compounds, olefin metathesis in specific instances, selective epoxidation of olefins, and are being explored for C-H activation and various other organic transformations including cycloadditions and rearrangements, highlighting their potential in both energy conversion and organic synthesis.

Outside catalysis, rhenium compounds have demonstrated remarkable utility in nuclear medicine, particularly through the use of rhenium-188 (^{188}Re)-a high-energy β^--emitting

radioisotope with a 16.9-hour half-life. Its beta radiation (average energy: 784 keV; max: 2.12 MeV) is potent enough to selectively destroy abnormal tissues, while its low-abundance γ-emission (155 keV, 15%) supports effective imaging and dosimetry. As a result, ^{188}Re-labeled compounds have been successfully used in the clinical management of primary tumours, bone metastases, rheumatoid arthritis, and endovascular treatments[51-53].

Additionally, rhenium complexes continue to draw interest in biological and medicinal chemistry due to their cytotoxicity profiles and ability to interact with biomolecules, making them candidates for anticancer and antibacterial applications. In photophysical research, rhenium(I) tricarbonyl diimine complexes are widely studied for their strong metal-to-ligand charge transfer (MLCT) emissions and long excited-state lifetimes, making them valuable in photoactive materials, light-harvesting systems, and luminescent sensors. Their redox-active nature and tunable photophysical properties have also been leveraged in the development of electrochemical sensors, molecular switches, and solar energy conversion systems.

Similarly, Ruthenium exhibits a wide range of catalytic properties, making it indispensable in both industrial and academic settings, acting as an effective catalyst in hydrogenation, dehydrogenation, and isomerization reactions due to its high activity and resistance to poisoning. Ruthenium-based catalysts are critical in large-scale industrial processes like the Fischer-Tropsch process for syngas conversion to hydrocarbons[54] and in ammonia synthesis under mild conditions[55-56]. In organic synthesis, ruthenium complexes are powerful catalysts for olefin metathesis (e.g., Grubbs' catalysts), C–H activation, and oxidation reactions, such as the oxidation of alcohols to aldehydes or ketones. Their applications extend into photocatalysis and electrocatalysis, where ruthenium complexes are employed for water splitting, CO_2 reduction, and dye-sensitized solar cells due to their favourable redox properties and strong absorption of visible light. Overall, ruthenium's versatility stems from its multiple oxidation states, robust coordination chemistry, and ability to stabilize reactive intermediates.

Given the distinct yet complementary catalytic attributes of rhenium and ruthenium, their integrated application has garnered significant attention in the domain of photocatalysis, particularly for the challenging and urgent task of carbon dioxide (CO_2) reduction. Ruthenium(II) polypyridyl complexes, exemplified by $[Ru(bpy)_3]^{2+}$ and its derivatives[57], are widely recognized as highly efficient photosensitizers owing to their strong absorption in the visible spectrum, long-lived excited states, and favorable photophysical and redox properties. In numerous photocatalytic systems designed for the reduction of CO_2, such photosensitizers are commonly paired with rhenium(I) carbonyl complexes, such as $[Re(bpy)(CO)_3Cl]$[58-59],

which serve as effective catalytic centers for the multi-electron reduction of CO_2 to value-added products, including carbon monoxide, formic acid, and in certain systems, methane.

This synergy has found relevance in the broader context of artificial photosynthesis, a rapidly evolving field driven by the global need for clean and sustainable energy solutions. A critical component of artificial photosynthesis is water splitting, wherein the water oxidation half-reaction responsible for O_2 evolution presents a major kinetic and thermodynamic challenge due to the complex four-electron, four-proton transfer process it entails. Efficient and stable catalysts are essential for this transformation to proceed under benign conditions. Simultaneously, the dramatic rise in atmospheric CO_2 concentrations continues to pose serious environmental and energy-related challenges, necessitating the development of efficient carbon capture and utilization (CCU) strategies. Catalytic CO_2 reduction into fuels and chemical feedstocks provides a promising pathway to close the anthropogenic carbon loop and reduce dependence on fossil resources. However, the thermodynamic stability and kinetic inertness of CO_2 make its selective transformation into reduced products highly demanding. Effective catalysis for CO_2 conversion requires the orchestration of multi-electron, multi-proton transfer steps under low overpotentials, with high selectivity and durability. Transition metal complexes, particularly those incorporating ruthenium and rhenium, have demonstrated significant potential in this context. Their modular coordination environments, redox versatility, and ability to mediate key catalytic steps have made them leading candidates in homogeneous CO_2 reduction systems, often in conjunction with sacrificial electron donors such as 1,3-dimethyl-2-phenyl-2,3-dihydro-1H-benzo[d]imidazole (BIH), under visible-light irradiation.

While metal-based catalysis particularly involving rhenium and ruthenium continues to underpin a vast array of chemical transformations, significant advances have also been made in organic synthesis mediated by ruthenium catalysts. Ruthenium complexes, especially those bearing polypyridyl or pincer-type ligands, have proven highly versatile in promoting a variety of oxidative and dehydrogenative transformations, including annulation, olefination, and cross-coupling reactions. Their redox flexibility, structural tunability, and ability to access multiple oxidation states enable ruthenium catalysts to participate in both single-electron and multi-electron processes under mild conditions. These systems often facilitate atom-economical pathways, offering enhanced selectivity and functional group tolerance.

I.2 Summary of the present work:

This thesis investigates the synergistic coordination chemistry and diverse catalytic roles of rhenium and ruthenium, two pivotal elements in contemporary chemical research. Specifically, it explores their applications in water oxidation, carbon dioxide reduction, and organic transformation. By examining the interplay between these transition metals, this work seeks to advance the field of sustainable energy and enhance our understanding of their complex chemical behaviour.

I.2.1 Chapter II

This chapter delves into the characteristics and catalytic performance of two dinuclear rhenium(V)-oxo complexes: $[Re^{V}(O)(Cl)_3(DBQ^{2-})Re^{V}(O)(Cl)_3]^{2-}$ (1) and $[Re^{V}(O)(Cl)_3(CA^{2-})Re^{V}(O)(Cl)_3]^{2-}$ (2). These complexes, featuring dianionic 2,5-dihydroxy-1,4-benzoquinone (DBQ^{2-}) and chloranilic acid (CA^{2-}) ligands respectively, exhibit rapid and efficient electrocatalytic activity for the water oxidation reaction (WOR) in homogeneous solutions. The employment of redox non-innocent 1,4-benzoquinone-based ligands is crucial for the formation of stable bimetallic complexes with terminal oxo groups (M=O). These ligands actively participate in the electron transfer processes essential for the water oxidation catalytic cycle.

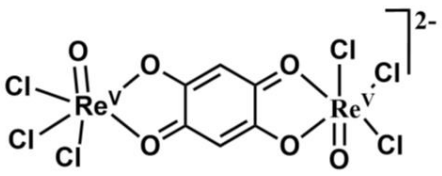

1

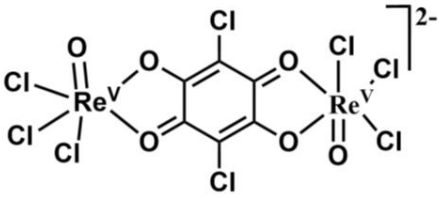

2

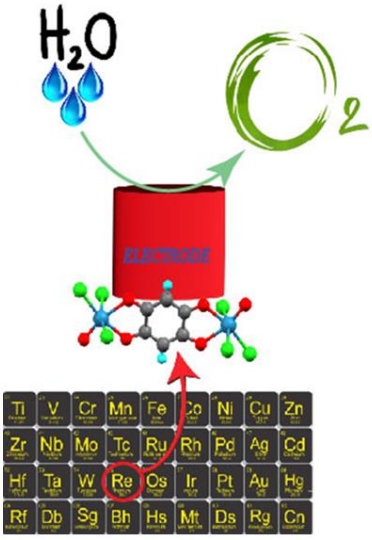

I.2.2 Chapter III

This chapter introduces a promising new series of rhenium(I) complexes incorporating pyridine, quinoline, and isoquinoline-substituted benzo[d]oxazole ligands and their derivatives as potential high-performance photocatalysts and electrocatalysts for CO_2 reduction.

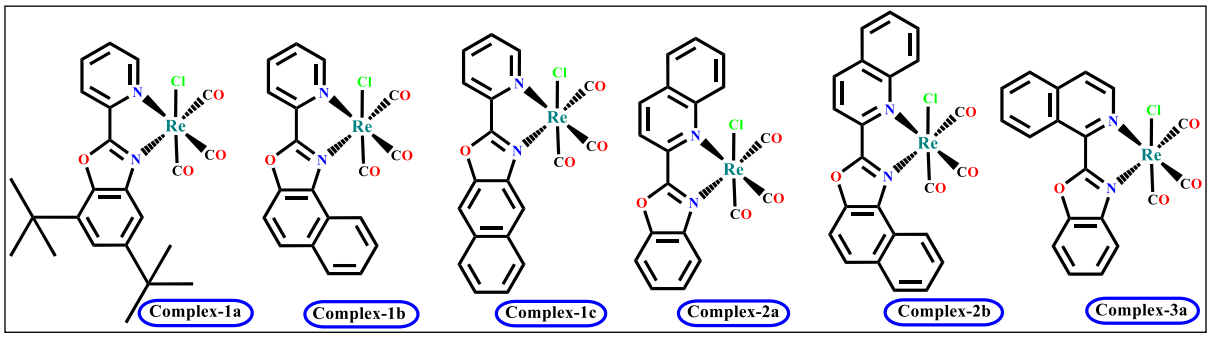

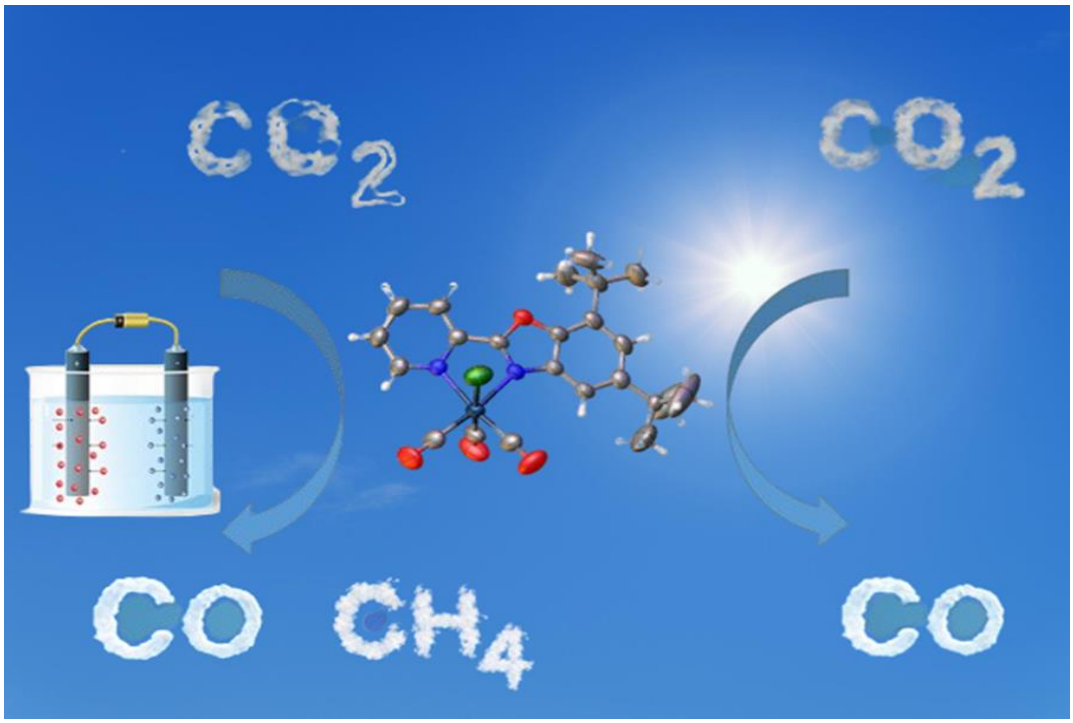

I.2.3 Chapter IV

This chapter delves into the explore of three variants of hexadentate ruthenium complexes, each featuring a substituted bis(2-picolyl)amine moiety on one side and a bipyridine unit with either methyl or N,N-dimethyl substituents on the other. Additionally, we introduce BF_2-chelated dipyrromethene into the catalyst's structural framework, enabling the catalyst to function as a self-photosensitizing system. This dual functionality aims to enhance the

efficiency of light harvesting and catalytic activity, providing a promising approach for photocatalytic applications. To know the rate variation by substitution of Cl by CH_3CN we also synthesize the acetonitrile substituted complex.

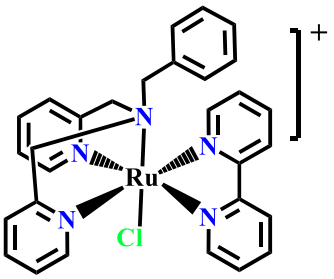

Complex-1

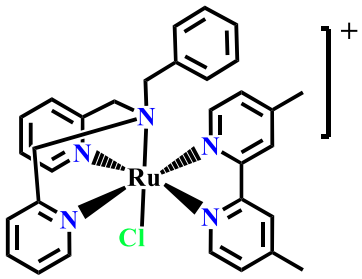

Complex-2

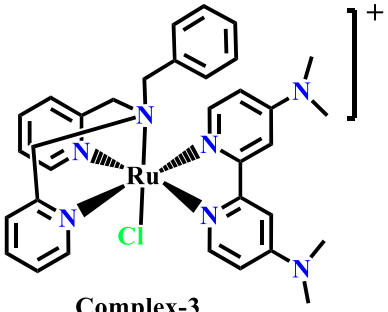

Complex-3

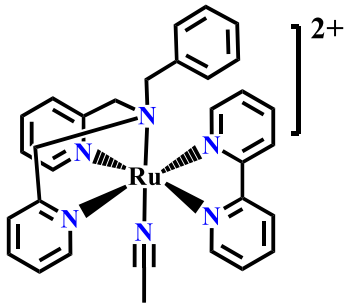

Complex-4

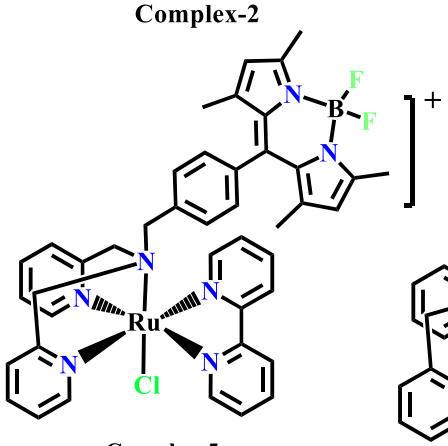

Complex-5

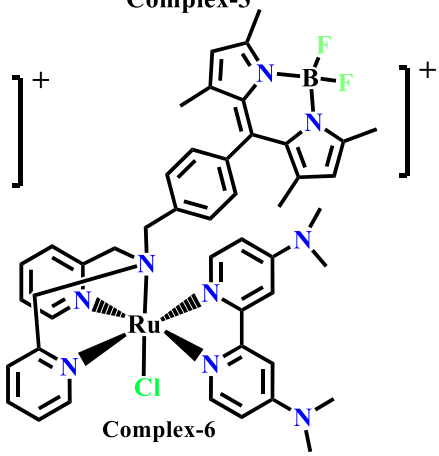

Complex-6

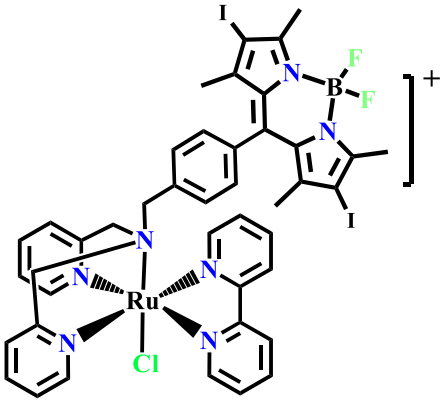

Complex-7

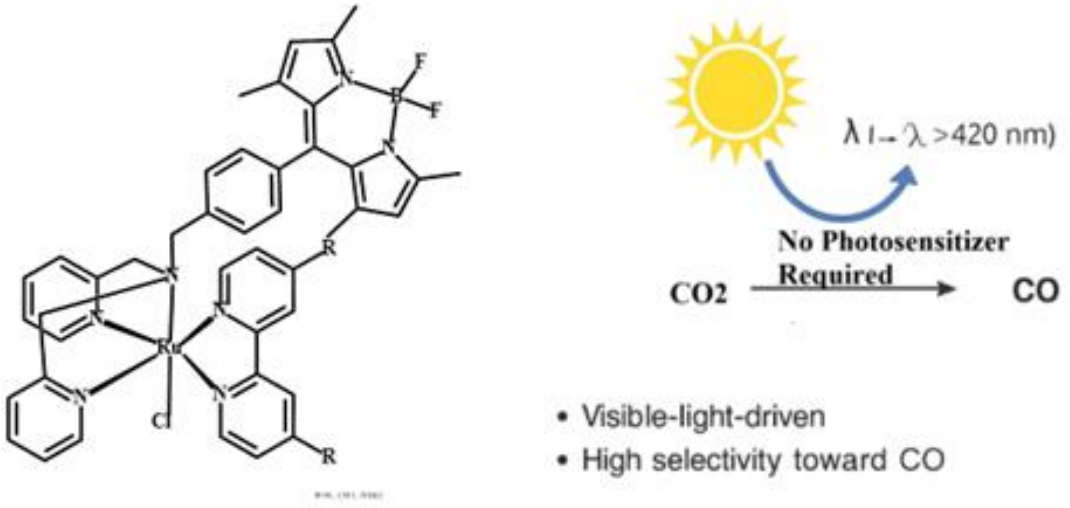

I.2.4 Chapter V

In this study, we report organocatalytic dehydrogenative transformations catalyzed by structurally well-defined Ru(III) polypyridyl complexes. The reaction involves the synthesis of substituted quinolines *via* dehydrogenative annulation of 2-aminobenzyl alcohols with secondary alcohols and ketones. This reactivity showcases the efficiency and versatility of Ru(III)-polypyridyl systems in mediating challenging oxidative couplings. The redox-active nature of the polypyridyl ligand framework is proposed to play a cooperative role with the metal center, promoting efficient hydrogen removal and facilitating key bond-forming steps. These findings highlight the underexplored potential of Ru(III) polypyridyl catalysts in dehydrogenative transformations and contribute to the advancement of atom-economical synthetic methodologies.

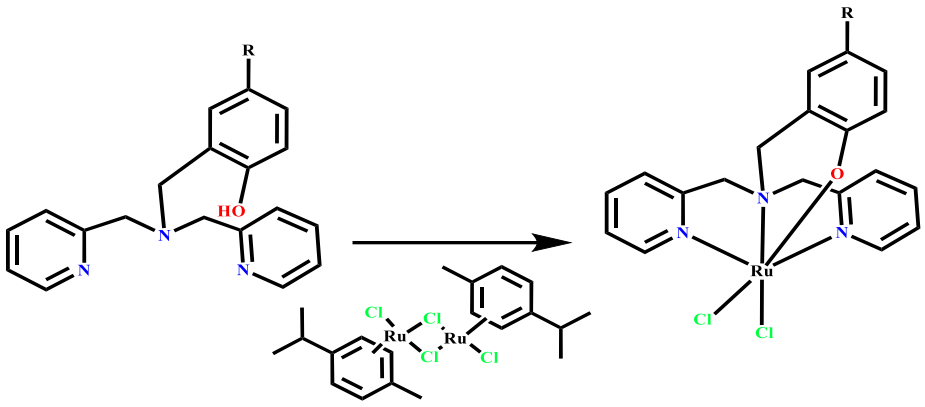

R= H, CH_3, OCH_3, Br

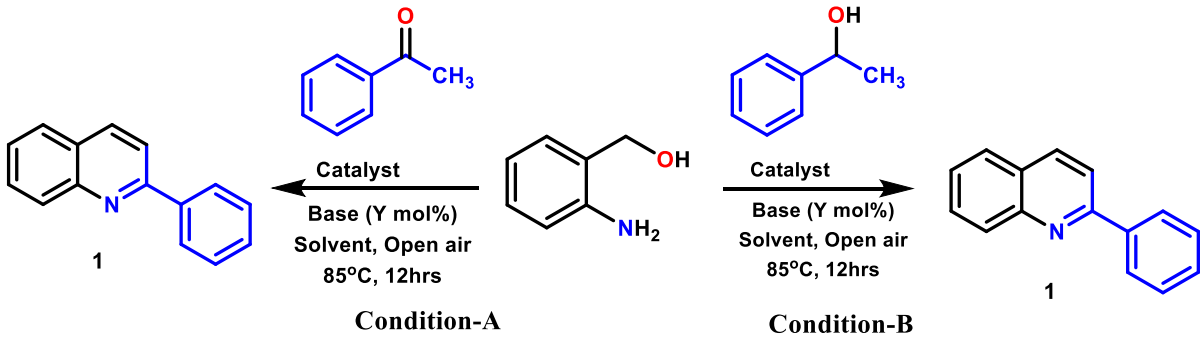

Condition-A Condition-B

I.3 Experimental Details

1.3.1 Physical Measurements

A range of physicochemical techniques was employed to characterize and investigate the structural and electronic properties of the synthesized compounds. A detailed description of these methods is provided in the subsequent chapters, with a concise overview presented below.

NMR Spectroscopy.

Proton (^{1}H), carbon (^{13}C), and fluorine (^{19}F) NMR spectra were recorded at room temperature using Bruker 300 and 400 MHz FT-NMR spectrometers. Deuterated solvents such as DMSO-d_6 and $CDCl_3$ were employed, with tetramethylsilane (TMS) serving as the internal standard. The assignment of signals to individual nuclei was based on chemical shift values, spin-spin coupling patterns, and the influence of substituents.

Electronic Spectra.

Electronic spectra were recorded on Perkin-Elmer LAMBDA EZ-301 and a LAMBDA 25 UV-VIS spectrometer (200-1200 nm). A matched pair of quartz cells of path length 1 cm was used.

Fluorescence Spectra.

The emission data were collected on Horiba Fluoromax-4 fluorescence spectrometer. For all luminescence measurements excitation and emission slit width of 5 nm were used. Cells are same as that of the electronic spectra.

Quantum yields Measurements

Quantum yield of the complexes was determined in freeze-pump-thaw-degassed solutions of the complexes using quinine sulphate and fluorescein in the same solvent as the standard [Φ_{std}=0.54 at 298 K in 0.1 M H_2SO_4 at λ_{ex}=350 nm] by usual method. The quantum yields were calculated by using Eq. S1.

$$\Phi_r = \Phi_{std} \frac{A_{std}}{A_r} \frac{I_r}{I_{std}} \frac{\eta_r^2}{\eta_{std}^2}$$

where Φ_r and Φ_{std} are the quantum yields of unknown and standard samples, A_r and A_{std} refer to the solution absorbances at the excitation wavelength (λ_{ex}), I_r and I_{std} are the integrated emission intensities, η_r and η_{std} are the refractive indices of the solvent. Time-correlated-single-photon-counting (TCSPC) measurements were performed for the luminescence decay of the

complexes in acetonitrile and dichloromethane. The fluorescence decay data were collected on a Hamamatsu MCP photomultiplier (R3809) and were analysed by using IBH DAS6 software.

Electrochemical Measurements.

Electrochemical studies were conducted using a CHI 620A electrochemical analyzer. All measurements were carried out under an inert argon atmosphere at 298 K. The recorded potentials are referenced against the Ag/AgCl electrode, without applying junction potential correction.

Mass Spectrometry.

Electrospray ionization mass spectra (ESI-MS) (70 eV) were recorded on a Qtof Micro YA263 spectrometer.

Elemental Analysis.

The carbon, hydrogen, and nitrogen content of the samples was determined using a Perkin-Elmer 2400 Series II elemental analyzer, which operates based on thermal conductivity detection of combustion gases (CO_2, H_2O, and N_2). Samples were introduced into the combustion chamber at temperatures typically ranging from 900 to 980 °C. Pure oxygen was employed to facilitate complete combustion, while high-purity helium served as the carrier gas.

Infrared Spectra.

IR spectra were recorded with the help of a Perkin-Elmer L-0100 spectrometer.

EPR Spectroscopy.

EPR spectrum was recorded on a JEOL JES-FA200 spectrometer at X band.

X-ray Structure Determination

X-ray diffraction data were collected on a Bruker D8 QUEST diffractometer using Mo-Kα radiation at 298 K. The structures of all compounds were solved by direct methods using APPEX 3.0 and OLEX 2.0. Molecular structure plots were drawn using ORTEP. *R1*, *wR2* and goodness-of-fit (GOF) are given by the following equations 1, 2 and 3 respectively.

$R1 = S½½Fo½- ½Fc½½/ S½ Fo½$ (1)

$wR2 = [S[w(Fo2 - Fc2)2] / S[w(Fo2)2]]^{1/2}$ (2)

$GOF = S = [\Sigma[w(Fo2 - Fc2)2] / (n_o – n_p)]^{1/2}$ (3)

n_o = number of reflections

n_p = total number of parameters refined

Gas Detection by Gas Chromatography (GC):

The gas evolved during BE was detected by using GC instrument of model no. 8860 (G2790A), serial no. CN2211C039 fitted with TCD. 500 µl gases was syringed out by a gas tight syringe from the head space of the working chamber of the H cell and was injected into the inlet of the GC.

Photocatalytic testing: Photocatalytic reactions were performed using a 300 W Xe lamp equipped with a $\lambda \geq 400$ nm cut-off filter as the light source. Prior to photocatalytic testing, the reaction solution was degassed with N_2 gas for 20 minutes, followed by bubbling with CO_2 (99.999%, Airgas) in the dark for 30 minutes. The reaction mixture was then irradiated at room temperature under continuous stirring to facilitate photocatalytic CO_2 reduction. Gas samples from the headspace above the reaction solution were collected at designated time intervals using a gastight syringe and analyzed with an Agilent 8860 gas chromatograph equipped with a thermal conductivity detector (TCD) and a flame ionization detector (FID), along with a 60/80 Carboxen-1000 packed column (Supelco). The gaseous products were identified and quantified using standard gas references.

I.3.2 Computational Studies

The geometrical structures of the singlet ground state and triplet excited state of the synthesized Re complexes were optimized by the DFT method[60] using B3LYP exchange correlation functional[61] approach. The geometry of the Re complexes was fully optimized in solution phase (namely dichloromethane and acetonitrile) without any symmetry constraints. There was a good agreement between the theoretically modelled and experimental structures. Based on the optimized ground state geometry, both the absorption and emission properties in acetonitrile and dichloromethane solvent was calculated by time-dependent density functional theory (TDDFT)[62] approaches related with the conductor-like polarizable continuum model (CPCM)[63]. We computed the lowest 50 singlet-singlet transition and the results obtained from the TD calculations were qualitatively very similar. The TDDFT approach had been established to be reliable for calculating spectral properties of many transition metal complexes[64]. Due to the presence of electronic correlation in the TDDFT (B3LYP) method it can yield more accurate electronic excitation energies. Hence TDDFT had been shown to provide a reasonable spectral

feature for the complexes of our examination. In the calculation, the quasi-relativistic pseudo potentials of Re atoms were predicted by using Hay and Wadt[65] with 14 valence electrons [outer-core ($5s^2 5p^6$) electrons and the ($5d^6$) valence electrons] were employed, and a "double-ξ" quality basis set LANL2DZ was adopted as the basis set for Re atoms. For H 6-31(g) basis set was used and the 6-31+ G (d, p) basis set was used for C, N, O and Cl atoms for the optimization of the ground state and excited state geometries. Gauss View 5.1 software was utilized to originate the figures showing MOs and the difference density plots. All the calculations were performed with the Gaussian 09W software package[66].

I.3.3 Chemicals And Solvents:

All chemicals and solvents employed in this study were of analytical grade and used as received without additional purification, unless otherwise specified. Solvents used in ligand synthesis were dried following standard procedures. Details of purification steps, when applicable, are provided in the relevant chapters. Reagents and starting materials for ligand synthesis were procured from MERCK (India) and Sigma-Aldrich Chemicals Ltd.

I.4 References:

1. F. A. Cotton, Wilkinson, G. *Advanced Inorganic Chemistry*, 5th Ed.; John Wiley & Sons, 1988, p 850.
2. K. A. Conner, R. A. Walton, *In Comprehensive Coordinated Chemistry, The Synthesis, Reactions, Properties and Application of Coordination Compounds*. G. Wilkinson, R. D. Gillard, J. A. McCleverty, Eds.; Permagon Press, Oxford, 1987, vol. 4, p125.
3. N. V. Sidgewick, *The chemical Elements and Their Compounds*, Oxford, 1952, vol. II, p 1292.
4. J. D. Lee, *Concise Inorganic Chemistry*, 5th Ed.; ELBS, 1996, p 734.
5. B.R. James, *Inorg. Chim. Acta* Rev., 4, 73 (1970).
6. P. Legzdins, R.W. Mitchell, G. Rempel, J.D. Ruddick and G. Wilkinson, *J. Chem.Soc*., 1970, **3322.**
7. M.M.Taquikhan and A.E. Martell, *Homogeneous Catalysis by Metal Complexes*, vol.l, Academic press, New York (1974).
8. S.Cenini, A. Fusi and G. Gapparella, J. *Inorg. Nucl. Chem*., 1971,**33**,3576.
9. D.E. Ewing, B. Hudson, D.E. Webster and P.B. Wells, *J. Chem. Soc., Dalton Trans*., 1972,**1287**.
10. W. Baratta, P. Da Ros, A. Del Zotto, A. Sechi, E. Zangrando, P. Rigo. *Angew. Chem. Int. Ed*. 2004, **43**, 3584 –3588.
11. W. Baratta, K. Siega and P. Rigo, *Chem. Eur. J.*, 2007, **13**, 7479–7486.
12. A. Landwehr, B. Dudle, T. Fox, O. Blacque and H. Berke, *Chem. Eur. J.*, 2012, **18**, 5701–5714.
13. M. L. Gothe, K. L. C. Caetano, A. L. Figueredo, J. L. Fiorio, J. Rozendo, B. Manduca, V. Simizu, R. S. Freire, M. A. S. Garcia and P. Vidinha, *European Journal of Inorganic Chemistry*, 2021, **39**, 4043–4065.
14. J. Luo and C. Liang, *ACS Catal.*, 2024, **14**, 7032–7049.
15. Y. Kuninobu and K. Takai, *Chem. Rev.*, 2011, **111**, 1938–1953.
16. J. J. Concepcion, M.-K. Tsai, J. T. Muckerman and T. J. Meyer, *J. Am. Chem. Soc.*, 2010, **132**, 1545–1557.
17. W.-M. Cheung, H.-Y. Ng, I. D. Williams and W.-H. Leung, *Inorg. Chem.*, 2008, **47**, 4383–4391.
18. Y. Kuninobu and K. Takai, *Chem. Rev.*, 2011, **111**, 1938–1953.

19. J. G. Stack, J. J. Doney, R. G. Bergman, C. H. Heathcock, *Organometallics*, 1990, **9**, 453–466.
20. S. Ueno, N. Chatani and F. Kakiuchi, *J. Am. Chem. Soc.*, 2007, **129**, 6098–6099.
21. S. I. Murahashi, T. Naota, H. Taki, M. Mizuno, H. Takaya, S. Komiya, Y. Mizuho, N. Oyasato, M. Hiraoka, *J. Am. Chem. Soc.*, 1995, **117**, 12436–12451.
22. H. S. Broadbent, G. C. Campbell, W. J. Bartley and J. H. Johnson, *J. Org. Chem*. 1959, **24**, 12, 1847–1854
23. H. Chen, J. F. Hartwig, *Angew. Chem. Int. Ed.,* 1999, **13** (12), 3391-3393
24. N. Lepareur, F. Lacoeuille, C. Bouvry, F. Hindré, E. Garcion, M. Chérel, N. Noiret, E. Garin and F. F. Russ Knapp Jr., *Frontiers in medicine*, 2019, **6**, 132.
25. A. Guertin, C. Duchemin, F. Haddad, N. Michel, V. Métivier, *Nucl Med Biol.* 2014, **41** 16–8.
26. M. E. Moustapha, G. J. Ehrhardt, C. J. Smith, L. P. Szajek, Eckelman WC, S. S. Jurisson, *Nucl Med Biol.* 2006, **33**, 81–9. doi: 10.1016/j.nucmedbio.2005.09.006
27. J. R. Dilworth, S. J. Parrott, *Chem Soc Rev.* 1998 **27**, 43–55.
28. F. Mévellec, N. Lepareur, A. Roucoux, N. Noiret, H. Patin, G. Bandoli, *Inorg Chem.* 2002, **41**, 1591–7.
29. J. H. Wang, R. Eychenne, M. Wolff, S. Mallet-Ladeira, N. Lepareur, E. Benoist, *Eur J Inorg Chem.* 2017, **18**, 3908.
30. J. L. Wedding, H. H. Harris, C. A. Bader, S. E. Plush, R. Mak, M. Massi, D. A. Brooks, B. Lai, S. Vogt, M. V. Werrett, P. V. Simpson, B. W. Skelton, S. Stagni, Metallomics, 2017, **9**, 382.
31. V. Sathish, E. Babu, A. Ramdass, Z-Z. Lu, M. Velayudham, P. Thanasekaran, K-L. Lu, S. Rajagopal, Talanta, 2014, **130**, 274.
32. J. Shelly, P. M. Kevin, W. B. John, F. V. John, D. Laurie, Z. Jon, *Bioconjugate chemistry*, 2006, **17**, 590.
33. H. Y. V. Ching, X. Wang, M. He, N. P. Holland, R. Guillot, C. Slim, S. Griveau, H. C. Bertrand, C. Policar, F. Bedioui, M. Fontecave, *Inorg. Chem*., 2017, **56**, 2966.
34. J. Rohacova, O. Ishitani *Dalton Trans*., 2017, **46**, 8899-8919.
35. R. Sun, T. Wang, S. Zhang, X. Chu, B. Zhu, *RSC Adv*., 2017, **7**, 17063.
36. M. Felber, M. Bauwens, S. Imstepf, T. Fox.; F. M. Mottaghy, R. Alberto, Eur. J. *Inorg. Chem.*, 2017, **1772**.
37. A. Frei, D. Sidler, P.Mokolokolo, H. Braband, T. Fox, B. Spingler, A. Roodt, R. Alberto, *Inorg. Chem.,* 2016, **55**, 9352.

38. C. Y. Chan, P. A. Pellegrini, I.Greguric, P. J. Barnard, *Inorg. Chem*., 2014, **53**, 10862.
39. T. Mukuta, P. V. Simpson, J. G. Vaughan, B. W. Skelton, S. Stagni, M. Massi, K. Koike, O. Ishitani, K. Onda, *Inorg. Chem*., 2017, **56**, 3404.
40. S. Satoa, O. Ishitani; *Coordination Chemistry Reviews*, 2015, **282**, 50–59.
41. N. J. Lundin, P. J. Walsh, S. L. Howell, A. G. Blackman and K. C. Gordon*, Chem.–Eur. J.* 2008, **14**, 11573
42. S. T. Lam, N. Zhu, V. W. W. Yam*, Inorg. Chem*. 2009, **48**, 9664
43. X. Li, D. Zhang, G. Lu, G. Xiao, H. Chi, Y. Dong, Z. Zhang and Z. Hu, J. *Photochem. Photobiol*. 2012, **241**, 1
44. W. K. Chu, C. C. Ko, K. C. Chan, S. M. Yiu, F. L. Wong, C. S. Lee and V. A. L. Roy, *Chem. Mater*. 2014, **26**, 2544
45. G. W. Zhao, Y. X. Hu, H. J. Chi, Y. Dong, G. Y. Xiao, X. Li and D. Y. Zhang, *Opt. Mater.* 2015, **47**, 173
46. J. B. Arterburn, M. C. Perry, S. L. Nelson, B. R. Dible and M. S. Holguin, *J. Am. Chem. Soc.*, 1997, ***119***, 9309–9310.
47. J. Hawecker, J. M. Lehn, R. Ziessel, *J. Chem. Soc., Chem. Commun*, 1983, **536-538**.
48. J. Hawecker, J.-M. Lehn, R. Ziessel, *Helv. Chim. Acta*, 1986, **69**, 1990−2012.
49. J. K. Nganga, L. M. Wolf, K. Mullick, E. Reinheimer, C. Saucedo, M. E. Wilson, K. A. Grice, M. Z. Ertem and A. M. Angeles-Boza, *Inorg Chem,* 2021, **60**, 3572-3584.
50. J. K. Nganga, C. R. Samanamu, J. M. Tanski, C. Pacheco, C. Saucedo, V. S. Batista, K. A. Grice, M. Z. Ertem and A. M. Angeles-Boza, *Inorg Chem*, 2017, **56**, 3214-3226.
51. W. A. Volkert, T. J. Hoffman *Chem Rev.* 1999, **99**, 2269–92
52. J. F. Chatal, C. A. Hoefnagel, *Lancet.* 1999**,** ***354***, 931–5.
53. S. Srivastava, E. Dadachova *Recent Nucl Med.* 2001**, 31**, 330–41.
54. Q. Zhang, K. Cheng, J. Kang, W. Deng and Y. Wang, *ChemSusChem*, 2014, **7**, 1251–1264.
55. H. Fang, D. Liu, Y. Luo, Y. Zhou, S. Liang, X. Wang, B. Lin and L. Jiang, *ACS Catal.*, 2022, **12**, 3938–3954.
56. T. Cholewa, B. Steinbach, C. Heim, F. Nestler, T. Nanba, R. Güttel and O. Salem, *Sustainable Energy Fuels*, 2024, **8**, 2245–2255.
57. S. P. Pitre, C. D. McTiernan, W. Vine, R. DiPucchio, D. E. Graff and J. C. Scaiano, *Sci. Rep.*, 2015, **5**, 16397.
58. J. Hawecker, J. M. Lehn, R. Ziessel, J. Chem. Soc., *Chem. Commun*, 1983, 536-538.
59. J. Hawecker, J.-M. Lehn, R. Ziessel, Helv. *Chim. Acta*, 1986, **69**, 1990−2012.

60. E. Runge and E. K. U. Gross, *Phys. Rev. Lett.*, 1984, **52**, 997 1000.
61. (a) A. D. Becke, *J. Chem. Phys.*, 1993, **98**, 5648–5652; (b) C. Lee, W. Yang and R. G. Parr, *Phys. Rev. B: Condens. Matter*, 1988, **37**, 785–789.
62. (a) M. E. Casida, C. Jamoroski, K. C. Casida and D. R. Salahub, *J. Chem. Phys.*, 1998, **108**, 4439–4449; (b) R. E. Stratmann, G. E. Scuseria and M. J. Frisch, *J. Chem. Phys.*, 1998, **109**, 8218–8224; (c) R. Bauernschmitt and R. Ahlrichs, *Chem. Phys. Lett.*, 1996, **256**, 454–464.
63. (a) V. Barone and M. Cossi, *J. Phys. Chem. A*, 1998, **102**, 1995–2001; (b) M. Cossi and V. Barone, *J. Chem. Phys.*, 2001, **115**, 4708–4717; (c) M. Cossi, N. Rega, G. Scalmani and V. Barone, *J. Comput. Chem.*, 2003, **24**, 669–681.
64. (a) T. Liu, H.-X. Zhang and B.-H. Xia, *J. Phys. Chem. A*, 2007, **111**, 8724–8730; (b) X. Zhou, H.-X. Zhang, Q.-J. Pan, B.-H. Xia and A.-C. Tang, *J. Phys. Chem. A*, 2005, **109**, 8809 8818; (c) X. Zhou, A.-M. Ren and J.-K. Feng, *J. Organomet. Chem.*, 2005, **690**, 338–347; (d) A. Albertino, C. Garino, S. Ghiani, R. Gobetto, C. Nervi, L. Salassa, E. Rosenverg, A. Sharmin, G. Viscardi, R. Buscaino, G. Cross and M. Milanesio, *J. Organomet. Chem.*, 2007, **692**, 1377–1391.
65. (a) P. J. Hay and W. R. Wadt, *J. Chem. Phys.*, 1985, **82**, 270-283; (b) P. J. Hay and W. R. Wadt, *J. Chem. Phys.*, 1985, **82**, 299–310.
66. M. J. Frisch, G. W. Trucks, H. B. Schlegel, G. E. Scuseria, M. A. Robb, J. R. Cheeseman, G. Scalmani, V. Barone, B. Mennucci, G. A. Petersson, H. Nakatsuji, M. Caricato, X. Li, H. P. Hratchian, A. F. Izmaylov, J. Bloino, G. Zheng, J. L. Sonnenberg, M. Hada, M. Ehara, K. Toyota, R. Fukuda, J. Hasegawa, M. Ishida, T. Nakajima, Y. Honda, O. Kitao, H. Nakai, T. Vreven, J. A. Montgomery Jr., J. E. Peralta, F. Ogliaro, M. Bearpark, J. J. Heyd, E. Brothers, K. N. Kudin, V. N. Staroverov, R. Kobayashi, J. Normand, K. Raghavachari, A. Rendell, J. C. Burant, S. S. Iyengar, J. Tomasi, M. Cossi, N. Rega, J. M. Millam, M. Klene, J. E. Knox, J. B. Cross, V. Bakken, C. Adamo, J. Jaramillo, R. Gomperts, R. E. Stratmann, O. Yazyev, A. J. Austin, R. Cammi, C. Pomelli, J. W. Ochterski, R. L. Martin, K. Morokuma, V. G. Zakrzewski, G. A. Voth, P. Salvador, J. J. Dannenberg, S. Dapprich, A. D. Daniels, Ö. Farkas, J. B. Foresman, J. V. Ortiz, J. Cioslowski and D. J. Fox, *GAUS-SIAN 09 (Revision A.1)*, Gaussian, Inc., Wallingford, CT, 2009.

Chapter II

Electrochemical Water Oxidation Reaction by Dinuclear Re (V) Oxo Complexes with 1, 4-Benzoquinone Core via Redox Induced Electron Transfer (RIET) Process

II.1 Introduction:

Humanity is currently grappling with significant energy shortages and the escalating crisis of global warming. Addressing the world's growing energy needs necessitates the development of innovative technologies and efficient energy storage solutions. A crucial shift from reliance on fossil fuels to sustainable renewable energy sources is urgently required to conserve finite resources and mitigate the carbon dioxide emissions that contribute to global warming[1].

Artificial photosynthesis has emerged as a highly promising approach for building sustainable energy systems within our society[2,3]. Mimicking the natural process where sunlight fuels the conversion of carbon dioxide and water into chemical energy in the form of carbohydrates, artificial photosynthesis offers a route to generate valuable chemical fuels from environmentally benign resources. This process largely involves two interconnected reactions: oxidation and reduction, with the water oxidation process being a key component. Traditionally, this oxidation occurs via either a two-electron process yielding hydrogen peroxide[4-6] ($2H_2O \rightarrow H_2O_2 + 2H^+ + 2e^-$, E^0 = 1.76 V vs NHE) or a more efficient four-electron process producing oxygen[7,8] ($2H_2O \rightarrow O_2 + 4H^+ + 4e^-$, E^0 = 1.23 V vs NHE). While the former process producing hydrogen peroxide initially garnered less attention, current research in water oxidation heavily focuses on the latter.

These catalysts can be broadly categorized as either heterogeneous, primarily consisting of metal oxides, or homogeneous, which typically involve metal complexes. Homogeneous catalysts are particularly attractive due to the ability to fine-tune their redox properties and employ well-established spectroscopic techniques to investigate reaction mechanisms at the molecular level. The first reported example of a water oxidation catalyst was the blue dimer, *cis*-$[(H_2O)Ru^{III}(bpy)_2(\mu\text{-}O)Ru^{III}(bpy)_2(OH_2)]^{4+}$ an active molecular catalyst discovered by Meyer and colleagues in 1982[9]. The past four decades have witnessed substantial advancements in the field of water oxidation catalysis. Numerous transition metal complexes, including mononuclear, binuclear, and multinuclear forms of manganese[10-14], ruthenium[15-20], iridium[21-29], iron[30-33], cobalt[34-37], nickel[38-42], copper[43-46], and vanadium[47-48], have been explored for their activity in water oxidation reactions (WOR).

Under controlled potential electrolysis oxidation, the high-valent metal-oxo (M=O) unit may undergo a water nucleophilic attack (WNA) pathway, leading to the formation of a metal peroxo (O-O) species[49,50]. Numerous studies have demonstrated that stable complexes can be formed by coordinating these high-valent metal oxo species with strong chelating ligands like

tri- or tetra-valent entities. These stable complexes can then participate in WOR through either the WNA mechanism or via the interaction of two M-O units (I2M) through a radical coupling mechanism[49,51]. Recent investigations have highlighted the potential of unique macrocyclic ligands such corrole[52,53], cyclam[54,55], porphyrins[56] like structures to form stable catalytic complexes for WOR. In these systems, the primary role of the ligands is to stabilize the catalytic complexes through their strong chelation, rather than directly participating in electron transfer to the metal center.

Chart II.1. Isolated Re(V) oxo complexes of **1** and **2**

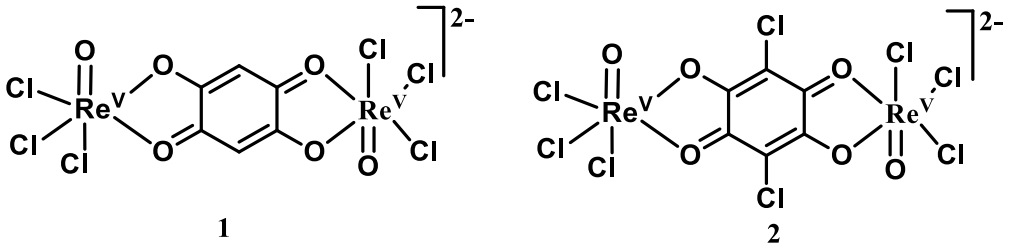

Here, we introduce for the first time the use of high-valent rhenium oxo complexes as active catalysts for WOR. we prepared the dinuclear-rhenium(V)-oxo complexes of $[Re^{V}(O)(Cl)_3(DBQ^{2-})Re^{V}(O)(Cl)_3]^{2-}$ (**1**) and $[Re^{V}(O)(Cl)_3(CA^{2-})Re^{V}(O)(Cl)_3]^{2-}$ (**2**) where DBQ^{2-} and CA^{2-} are the dianionic 2, 5-dihydroxy 1,4-benzoquinone and di-anionic chloranilic acid ligands respectively (as illustrated in **Chart II.1)** which are efficient, rapid electro-catalyst for WOR in homogeneous process. Herein, redox non-innocent 1,4-bezoquinone based ligands form the stable bimetallic M=O complexes where the ligands are playing an electron transfer to metal in water oxidation catalysis which was documented so far[57]. In controlled potential electrolysis (CPE) study, at anode **1** and **2** were oxidized in dry acetonitrile solvent at 1.30 V *vs* Ag/AgCl electrode to generate $\mathbf{1}^{+}$, $[Re^{VI}(O)(Cl)_3(DBQ^{\bullet 3-})Re^{VI}(O)(Cl)_3]^{-}$ and $\mathbf{2}^{+}$, $[Re^{VI}(O)(Cl)_3(CA^{\bullet 3-})Re^{VI}(O)(Cl)_3]^{-}$ respectively. In electrochemically isolated $\mathbf{1}^{+}$ and $\mathbf{2}^{+}$ ions the 1,4-benzoquinone-based ligand is reduced whereas both the rhenium metals are oxidized via redox induced electron transfer (RIET) process[58,59,60]. Thus, both the metal goes to higher oxidation state ($Re^{V}=O \rightarrow Re^{VI}O$) while 1,4-benzoquinone core of ligand reduced to semiquinone state ($DBQ^{\bullet 3-}$ and $CA^{\bullet 3-}$). $\mathbf{1}^{+}$ and $\mathbf{2}^{+}$ ions gives different types of strong EPR signals in fluid solution and frozen glass condition due to $[Re^{VI}(O)(Cl)_3(L^{\bullet 3-})Re^{VI}(O)(Cl)_3]^{-} \leftrightarrow$

$[Re^{VI}(O)(Cl)_3(L^{2-})Re^{V}(O)(Cl)_3]^-$ (where L = DBQ and CA) equilibrium. In complexes of **1** and **2,** the dianionic ligands of DBQ^{2-} and CA^{2-}ions were redox non-innocent in nature which can exists in different redox states described in **Scheme II.1.**

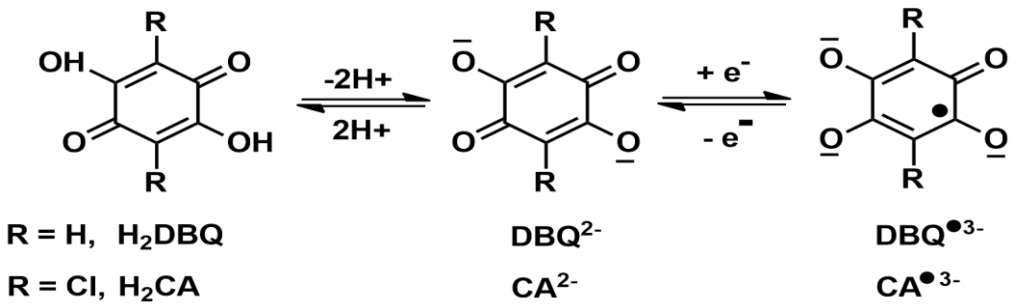

Scheme II.1. Electronic state of dianionic ligands

However, **1** and **2** were performed as active WOC while continuing the CPE study (1.30 V vs Ag/AgCl) in presence of acetonitrile-water mixture. In situ generated oxidised species of $\mathbf{1}^+$ and $\mathbf{2}^+$ further oxidized to higher valent Re^{VI}=O via RIET process. Now, the Re^{VI}=O species bound to water through water nucleophilic attack (WNA) to produce peroxide species of $[Re^{V}(OOH)(Cl)_3(DBQ^{2-})Re^{V}(OOH)(Cl)_3]$ (**A^1**) and $[Re^{V}(OOH)(Cl)_3(CA^{2-})Re^{V}(OOH)(Cl)_3]$ (**A^2**) intermediates of **1** and **2** catalysts respectively. It is noteworthy that the peroxide species (**A^1** and **A^2**), the active precursors of the water oxidation process, were detected and analyse by mass spectrometry and IR spectroscopy. Thus, authentication of the intermediates of plausible reaction mechanism is a challenging task in WOR. In literature study, most of the mechanism proposed that O-O bond formation prior to the rate-determining step[61] of the WOR. Similarly, in our work, the electrochemically oxidized species of high valent Re^{VI}=O centred bound with molecular water to form the metal peroxide intermediates (**A^1** and **A^2**) which further proceeds through several redox process like proton electron transfer process to produce the molecular dioxygen. Moreover, maximum turnover frequency (TOF) of electrocatalyst **1** was 2.1 sec^{-1} at low over potential of 0.27 V which is very significant in WOR. Furthermore, the molecular geometry, electronic and redox properties of **1** and **2** were elucidated through combined experimental and theoretical DFT study.

II.2 Experimental Section

II.2.1. Materials:

All chemicals used in the synthesis were of reagent grade and used without further purification. 2, 5 dihydroxy 1, 4 benzoquinone (H_2DBQ) and Chloranilic acid (H_2CA) were purchased from Sigma-Aldrich. Solvents were distilled from the appropriate drying agents under nitrogen before use. All syntheses were performed in a dry oxygen-free box.

II.2.2. Synthesis of ligands and complexes:

$[Cl_3ORe(v)(DBQ^{2-})Re(v)Cl_3O](NBu_4)_2$(1):

To a 10 ml acetone solution of $[ReOCl_4]^+[NBu_4]^-$ (60 mg, 0.1 mmol) was added to a acetone solution (10 mL) of H_2DBQ (7 mg, 0.05mmol) in a wet box. Then, the solution became dark blue. After stirring about 2 hours at room temperature, the precipitation came out. This precipitation was layered in CH_2Cl_2 and n-hexane. Single crystals of 1 were obtained by slow diffusion of n-hexane to a CH_2Cl_2 solution of crude product of 1 at RT. [Yield: 40 mg (59.7% with respect to rhenium)]. ^{1}H NMR (400 MHz, Acetone) δ 5.78 (s, 2H), 3.48 (s, 16H), 1.84 (d, *J* = 8.2 Hz, 16H), 1.47 – 1.42 (m, 16H), 1.01 (d, *J* = 7.3 Hz, 24H). ^{13}C NMR (CD_3CN, 101MHz): δ 179.48, 174.85, 174.61, 172.82, 103.39, 59.37, 24.32, 20.33(d, j=2.5 Hz), 13.81.

$[Cl_3ORe(V)(CA^{2-})Re(V)Cl_3O](NBu_4)_2$ (2):

To a 10 ml acetone solution of $[ReOCl_4][NBu_4]$ (60 mg, 0.1 mmol) was added a acetone solution (10 ml) of CA (10 mg, 0.05mmol) in a wet box, and the solution became dark blue. After stirring about 2 hours at room temperature, the precipitation comes out. This precipitation was layered in $CH_2Cl_2$and n-hexane mixture. Single crystals of 2 were obtained by slow diffusion of n-hexane to a CH_2Cl_2 solution of crude product of 2 at RT. [Yield: 45 mg (64%with respect to rhenium]. ^{13}C NMR (CD3CN, 101 MHz): δ 172.07, 167.93, 167.59, 166.32, 107.34, 58.50-58.34(m), 23.37, 19.39 (d,j=2.3Hz), 12.86.

II.2.3. NMR spectra

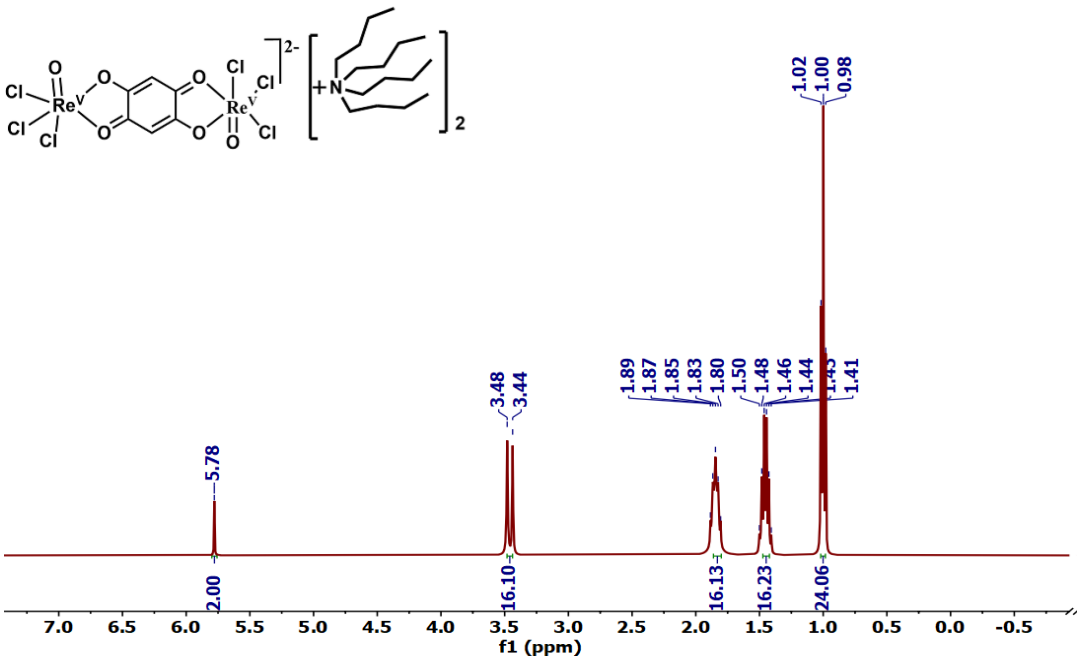

Figure II.1. ^{1}H NMR spectra of the **complex 1** in CD_3CN

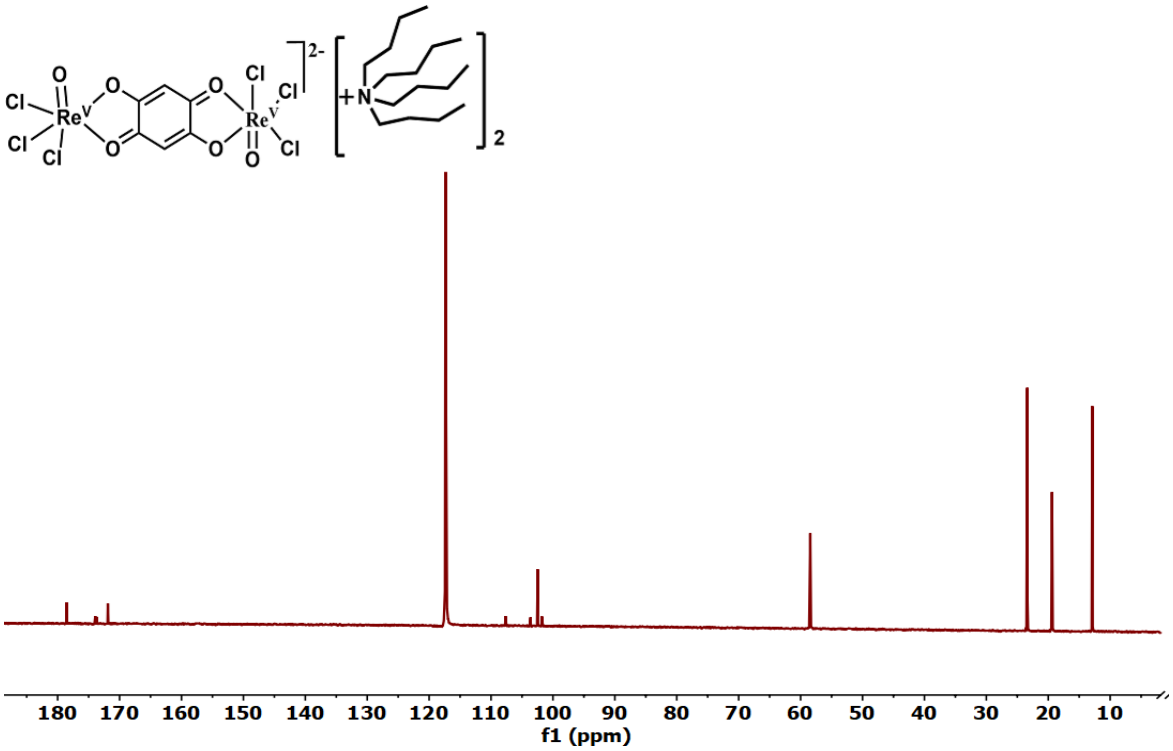

Figure II.2. ^{13}C NMR spectra of the **complex 1** in CD_3CN

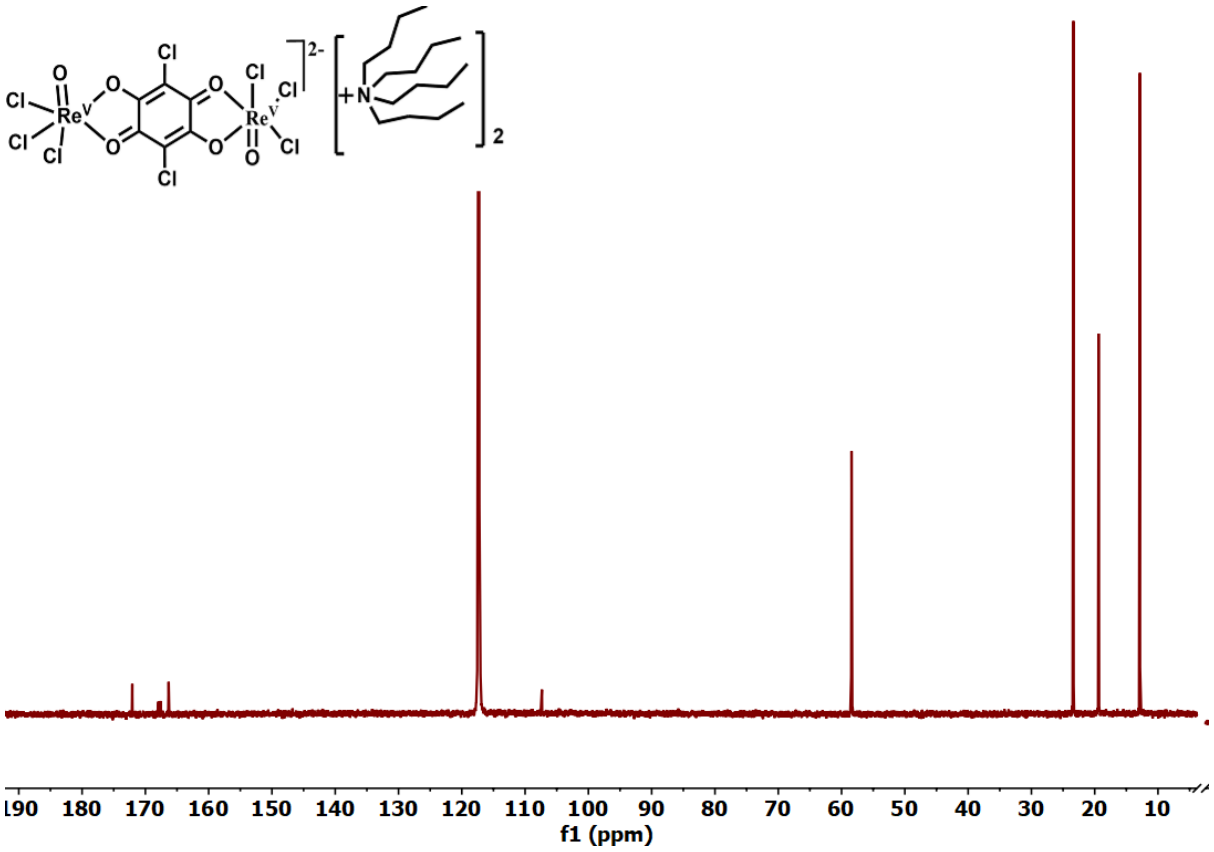

Figure II.3. ^{13}C NMR spectra of the **complex 2** in CD_3CN

II.2.4. IR spectra

The infrared spectra revealed distinct sharp vibrations for both **complex 1** and **complex 2**. **Complex 1** exhibited these vibrations at approximately 2970, 1526, and 990 cm^{-1}, while **complex 2** showed similar vibrations around 2970, 1515, and 990 cm^{-1}. The observed ν_{co} values in complexes 1526, 1515 cm^{-1} along with a vibration at 990 cm^{-1}, is attributed to the stretching frequency for Re=O.

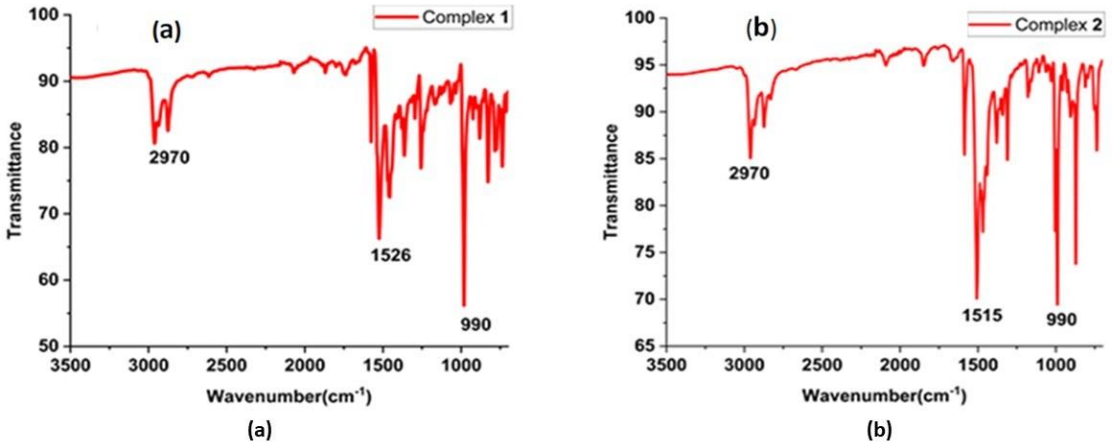

Figure II.4. Infra-red spectra of **(a) Complex 1** and **(b) Complex 2**

II.2.5. X-ray Crystallography

The crystal structures of the di-anionic rhenium-oxo complexes 1 and 2 were determined at 295 K using single-crystal X-ray diffraction. The positive charges were balanced by two tertiary butyl ammonium cations. **Complex 1** crystallizes in the P21/n space group (CCDC 2181451). As illustrated in **Figure II.5** with its atom labelling scheme, the molecular structure of **complex 1** was analysed, and key bond lengths and the X ray crystallographic data are detailed in **Table II.1** and **Table II.2** respectively. Within crystal 1, the bond lengths for C(1)-O(2) and C(2)-O(2) were measured as 1.273 (7) Å and 1.281(8) Å, respectively. The axial Re(1)-Cl(1) and Re(1)-Cl(3) bond lengths, at 2.3659(15) Å and 2.3425 (15) Å, were slightly longer than the equatorial Re(1)-Cl(2) bond, which measured 2.2989 (15) Å. The bond lengths within the p-benzoquinone fragment were notably elongated, while the phenolato bonds were shorter. These observations suggest a strong conjugation between the phenolato ion and the p-benzoquinone fragment in the coordinated structure of complex 1, as depicted in Chart 2. The Re(1)-O(1) bond length was found to be 1.684(4) Å, consistent with typical rhenium-oxo

complexes. Analysis of the quinone core bond lengths in crystal 1 indicates the presence of two five-centered 6π-electron delocalization units. These units consist of O(2)–C(2)–C(3)–C(4)–O(4) and O(1)–C(1)–C(6)–C(5)–O(3) atoms, which align with the symmetrical Qp-OO state[67].

Chart II.2

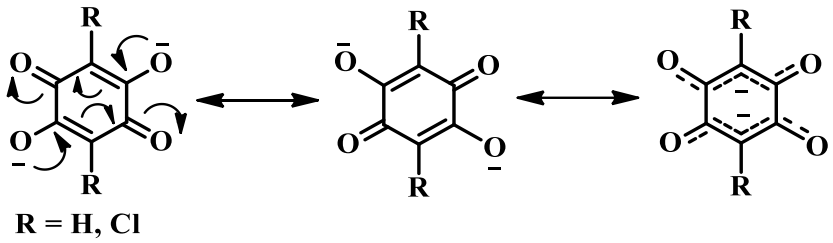

Similar to **complex 1**, **complex 2** also crystallizes in the P21/n space group. Although a stable single crystal of **complex 2** could not be obtained for X-ray diffraction measurements, even at 115 K, its molecular structure analysis revealed a coordination environment and ligand binding sites that closely resemble those of **complex 1**. This similarity suggests that the instability did not significantly affect the redox properties or its potential as a water oxidation reaction (WOR) catalyst. Consistent with **complex 1**, the calculated bond parameters for the quinone core of **complex 2** indicate the presence of two five-centered 6π-electron delocalization units, as shown in **Chart II.2**.

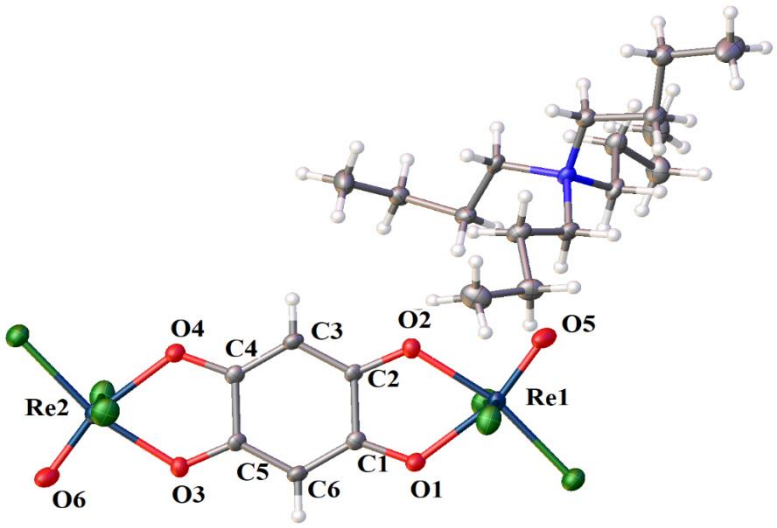

Figure II.5. Molecular geometries of **Complex-1** in the crystal state (40% thermal ellipsoids).

Table II.1: Experimental and theoretical bond lengths of **complex 1** and theoretical bond lengths of $\mathbf{1}^{+}$ and $\mathbf{1}^{-}$**.**

Experimental		**Calculated bond lengths(Å)**		
Bond Lengths (Å)		**1**	$\mathbf{1}^{+}$	$\mathbf{1}^{-}$
C1-C2	1.490(8)	1.508	1.494	1.451
C2-C3	1.381(8)	1.401	1.393	1.409
C3-C4	1.395(7)	1.387	1.390	1.391
C4-C5	1.490(8)	1.508	1.494	1.451
C5-C6	1.381(8)	1.401	1.393	1.409
C6-C1	1.395(7)	1.387	1.390	1.391
C1-O1	1.281(7)	1.275	1.276	1.348
C2-O2	1.273(7)	1.267	1.280	1.328
C5-O3	1.273(7)	1.267	1.280	1.328
C4-O4	1.281(7)	1.275	1.276	1.348
Re1-O5	1.682(4)	1.676	1.676	1.716
Re2-O6	1.682(4)	1.676	1.676	1.716
Re1-Cl1	2.3659(15)	2.431	2.388	2.524
Re1-Cl2	2.2989(15)	2.370	2.327	2.465
Re1-Cl3	2.3425(15)	2.431	2.388	2.524
Re2-Cl4	2.3425(15)	2.431	2.388	2.524
Re2-Cl5	2.3659(15)	2.431	2.388	2.524
Re2-Cl6	2.2989(15)	2.370	2.327	2.465

Table II.2. X-ray crystallographic data of **complex 1.**

	Complex 1
Formula	$C_{38}H_{74}N_2O_6Cl_6Re_2$
Molecular weight	1240.11
Crystal system	monoclinic
Space group	P 21/n
a/ Å	10.488(3)
b/ Å	13.127(13)
c/ Å	17.843(6)
α/°	90
β/°	91.283(18)
γ/°	90
V/ $Å^3$	2456(3)
Z	2
D_{calcd} /g cm^{-3}	1.677
μ/mm^{-1}	5.292
2θ/°	3.86 to 54.32
T/K	296
R^1, wR^2 [I>2σ(I)]	R_1 = 0.0335, wR_2 = 0.0767
GOF on F^2	1.078

II.2.6. Absorption Spectra

The UV-vis-NIR absorption spectra of the **complex 1** and **complex 2** were recorded in CH_2Cl_2 at 298 K, as shown in **Figure II.6(a)** and **6b**, by employing concentrations in the range ~20 µM. In all complexes, multiple absorption bands are attributed primarily to the charge-transfer transitions within the quinone core with varying contribution of metal d orbitals. The most pertinent transitions, energies, characteristics and oscillator strengths of **complex 1** have been provided in the **Table II.3**. Transition at 980 nm is calculated to be near 950.30 nm assigned as mainly $d_{xz}(Re)\rightarrow\pi^*(lig)$ MLCT character. The transition at 640 nm is computed at near 617.72nm can be described as primarily $d_{xz}(Re)\rightarrow\pi^*(lig)$ MLCT and dxz(Re) → dxy(Re) d-d transition. The near-UV band at 360 nm is calculated at near 372.97 nm which again may be ascribed as $d_{yz\rightarrow\pi^*(lig)}$ MLCT type.

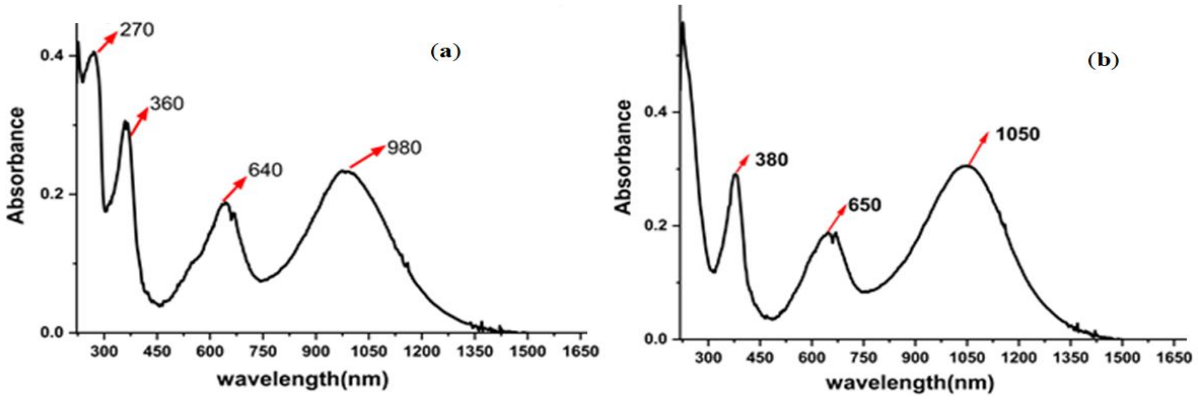

Figure II.6. UV−vis−NIR absorption spectra of **(a) 1** and **(b) 2** in CH_2Cl_2 at 295 K

Table II.3. Main calculated optical transition for the **complex 1** with composition in terms of molecular orbital contribution of the transition, vertical excitation energies (λ/nm), and oscillator strength in acetonitrile.

Complex	Transition	Experimental λ_{max}(nm)	Calculated λ_{max}(nm) (osc. strength)	Major contributions	Assigned major Transitions
1	$S_0 \rightarrow S_1$	980	950.30 (0.053)	HOMO->LUMO (47%) H-1->L+1(29%) HOMO->L+4 (22%)	d_{xz}(Re)→π*(lig) dxz(Re) → dyz(Re) dxz(Re) →dxy(Re)
	$S_0 \rightarrow S_6$	640	617.72 (0.3509)	HOMO>LUMO (49%), HOMO->L+4 (34%)	d_{xz}(Re)→ π*(lig) dxz(Re)→dxy(Re)
	$S_0 \rightarrow S_{20}$	360	372.97 (0.1885)	H-5->LUMO (76%)	dyz→ π*(lig)

II.3. RESULTS AND DISCUSSION

II.3.1. Redox induced electron transfer (RIET) process:

All the isolated complexes were electro paramagnetic resonance (EPR) silent in the solid state as well as in solution at room temperature and 110 K. The 1,4-benzoquinone based ligands types of 2,5-Dihydroxy-1,4-benzoquinone (H_2DBQ) and chloranilic acid (H_2CA) are react with rhenium (V) precursor to produce binuclear complexes of $[Re^{V}(O)(Cl)_3$**(**DBQ^{2-})$Re^{V}(O)(Cl)_3]^{2-}$ (**1)** and $[Re^{V}(O)(Cl)_3$**(**CA^{2-})$Re^{V}(O)(Cl)_3]^{2-}$ (**2**). In complexes of **1** and **2**, both the metal centre was Re^{V}=O species and ligands were in the di-anionic state (DBQ^{2-} and CA^{2-}). However, **1** and **2** were electrochemically oxidized at 1.30V *vs* Ag/AgCl (glassy carbon electrode (GCE) as working electrode) in dry acetonitrile solvent by applying controlled potential electrolysis (CPE) to generate $\mathbf{1}^{+}$ $[Re^{VI}(O)(Cl)_3$**(**$DBQ^{\bullet 3-}$)$Re^{VI}(O)(Cl)_3]^{-}$ and $\mathbf{2}^{+}$ $[Re^{VI}(O)(Cl)_3$**(**$CA^{\bullet 3-}$)$Re^{VI}(O)(Cl)_3]^{-}$ ions respectively. The colour has been changed from blue to green. The noteworthy point is that the $\mathbf{1}^{+}$ and $\mathbf{2}^{+}$ ions were paramagnetic and gave strong EPR signals. In case of both the **1** and **2**, one of the Re(V) centre was first oxidized to Re^{VI}=O by CPE condition and then fascinatingly another Re^{V}=O got converted to Re^{VI}=O and simultaneously quinone

core was reduced to semiquinone forms (i.e. $DBQ^{2-} \rightarrow DBQ^{\bullet 3-}$ and $CA^{2-} \rightarrow CA^{\bullet 3-}$) (Eqn 1 and 2) via redox induced electron transfer (RIET) process as shown in **Scheme II.2**.

$$Re^{V}(O)Cl_3(DBQ^{2-})Re^{V}(O)Cl_3 \rightarrow Re^{VI}(O)Cl_3(DBQ^{\bullet 3-})Re^{VI}(O)Cl_3 + e^{-} \quad \text{Eqn 1}$$

$$Re^{V}(O)Cl_3(CA^{2-})Re^{V}(O)Cl_3 \rightarrow Re^{VI}(O)Cl_3(CA^{\bullet 3-})Re^{VI}(O)Cl_3 + e^{-} \quad \text{Eqn 2}$$

Scheme II.2. Electrochemically oxidized species of $\mathbf{1}^{+}$ and $\mathbf{2}^{+}$ ions participate in RIET process.

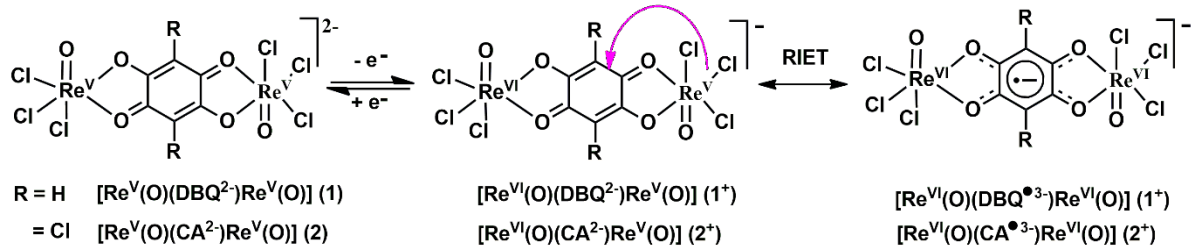

Furthermore, the EPR spectroscopy study (*vide infra*) reveals the generation of $DBQ^{\bullet 3-}$ and $CA^{\bullet 3-}$ ions via RIET process in electrolytic oxidation at room temperature contrary to the mixed valance state of $\mathbf{1}^{+}$ and $\mathbf{2}^{+}$. Consequently, $\mathbf{1}^{+}$ and $\mathbf{2}^{+}$ ions gave strong X-band EPR signals in fluid solution due to presence of semiquinone radical of ligand whereas at frozen glass condition gave rise to detectable signals of Re(VI). The temperature dependent EPR spectra inferred the $[Re^{VI}(O)Cl_3(L^{\bullet 3-})Re^{VI}(O)Cl_3]^{-} \leftrightarrow [Re^{VI}(O)Cl_3(L^{2-})Re^{V}(O)Cl_3]^{-}$ (where $L^{2-} = DBQ^{2-}$ and CA^{2-}) equilibrium (see, **Scheme II.2**) which are further elaborated in EPR section.

II.3.2. Electrochemical Characterization 1 and 2:

By using cyclic voltammetry (CV) at a glassy carbon electrode in dry CH_3CN with 0.2 M $[N(n\text{-}Bu)_4]PF_6$ as the supporting electrolyte and an inert dinitrogen atmosphere, the electrochemical characteristics of the complexes of **1** and **2** were studied as depicted in **Figures II.7a** and **7b** respectively and all the data are summarized in **Table II.4**. Cyclic voltammogram of complex **1** in acetonitrile solution showed two reversible anodic waves at 1.0 V and 1.58 V *vs* Ag/AgCl and one cathodic wave at -0.34 V. The first oxidation wave of **1** arise due to $Re^{V}Re^{V}/Re^{VI}Re^{V}$ redox couple[63] and consecutively another one rhenium centre got oxidized and subsequently quinone centre was reduced to $DBQ^{\bullet 3-}$ state via RIET process to form $[Re^{VI}(O)(DBQ^{\bullet 3-})Re^{VI}(O)]^{-}$. Interestingly, the second anodic wave of **1** appeared at high potential predicting the ligand centred oxidation of $Re^{VI}(O)(DBQ^{\bullet 3-})Re^{VI}(O)/Re^{VI}(O)(DBQ^{2-})Re^{VI}(O)$ redox couple as

depicted in **Scheme II.3**. The reversible cathodic wave of **1** at -0.34 V is assigned to a DBQ^{2-} /$DBQ^{\bullet 3-}$ redox couple where both the metals are Re^{V} centred[64] (see, **Scheme II.3**). Similar to **1**, the complex **2** also gave the same pattern of cyclic voltammograms data. The first anodic wave at 1.10 V was due to $Re^{V}Re^{V}/Re^{VI}Re^{V}$ redox couple whereas the second anodic waves at 1.40 V was for $Re^{VI}(O)(CA^{\bullet 3-})Re^{VI}(O)/Re^{VI}(O)(CA^{2-})Re^{VI}(O)$ redox couple (see, **Scheme II.3**) and the current generation compare to the **1** was quite small due to electron withdrawing chlorine groups are present in redox non-innocent quinone system.

Scheme II.3.

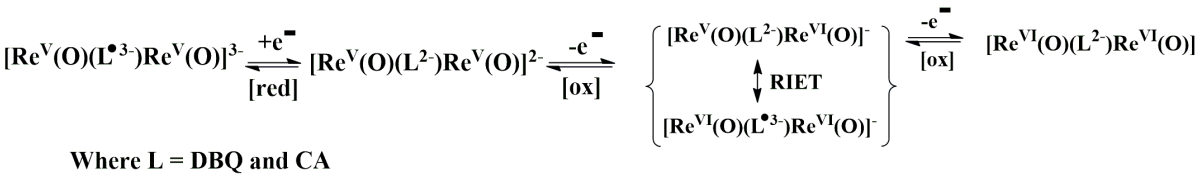

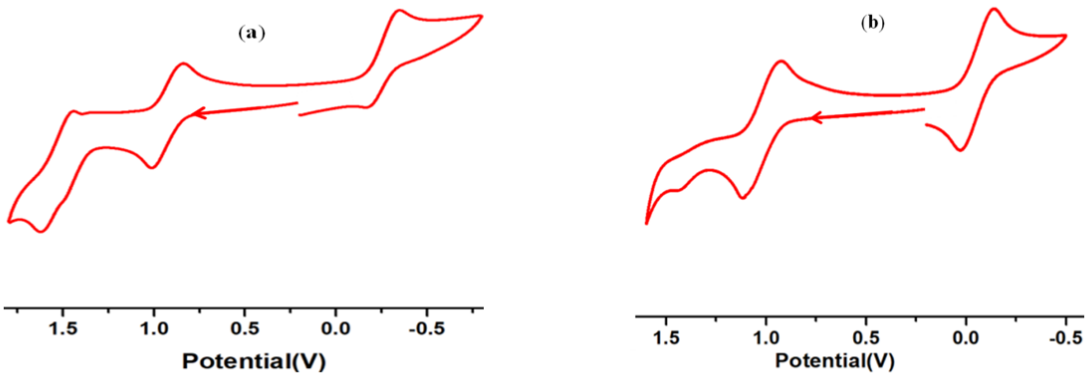

Figure II.7. Cyclic voltammograms of the **(a) 1**and **(b) 2** Complexes in CH_3CN at 298 K. Conditions: 0.2 M $[N(n\text{-}Bu)_4]PF_6$ supporting electrolyte; scan rate, 100 mV s^{-1}; glassy carbon working electrode**.**

Table II.4. Electrochemical Characterization of the **1 and 2** Complexes in CH_3CN (0.2 M $N(n\text{-}Bu)_4]PF_6$) *vs* Ag/AgCl.

complex	1st oxidation potential	2nd oxidation potential	Reduction potential
1	1.0 V	1.58 V	-0.34 V
2	1.1 V	1.4 V	-0.20 V

II.3.3. EPR Spectroscopy and DFT calculation:

The redox states of complexes **1** and **2** were investigated using X-band EPR spectroscopy following constant potential electrolysis at 1.3 V versus Ag/AgCl. The EPR spectrum of the $\mathbf{1}^+$ ion in acetonitrile solution at room temperature (298 K) showed a strong signal at g = 2.002, characteristic of a quinone-centered organic radical (**Figure II.8a**). In frozen-glass conditions, $\mathbf{1}^+$ displayed an anisotropic rhombic spectrum (**Figure II.8b**), consistent with a rhenium(VI) oxidation state. These EPR results suggest that $\mathbf{1}^+$ is best described as a rhenium(VI) complex coordinated to a semiquinonate radical anion ($DBQ^{\cdot 3-}$), as outlined in **Scheme II.2**. Similar EPR patterns were observed for the $\mathbf{2}^+$ ion.

Conversely, electrolysis at -0.5 V (vs Ag/AgCl) generated the $\mathbf{1}^-$ and $\mathbf{2}^-$ ions, which exhibited single-line EPR signals in acetonitrile at 295 K, also attributed to a quinone-centered radical ($DBQ^{\cdot 3-}$). Notably, the electrochemically generated $\mathbf{1}^+$ species in a water-acetonitrile mixture under constant potential electrolysis during the water oxidation reaction was EPR silent. This observation indicates that the water oxidation proceeds via the formation of a diamagnetic metal-peroxide (M-OOH) intermediate. Complex $\mathbf{2}^+$ follows a similar mechanistic pathway to $\mathbf{1}^+$.

Gas-phase geometry optimization of complex **1** was performed using DFT at the B3LYP level, considering a singlet spin state for **1** and a doublet spin state for $\mathbf{1}^+$. The calculated bond parameters (Table 2) for the optimized structure of **1** are in good agreement with the experimental values. Similar agreement was found for the bond parameters of complex 2.

Analysis of the frontier molecular orbitals for 1 and 2 (**Tables II.5** and **II.6**) reveals that the highest occupied molecular orbital (HOMO) is predominantly located on the rhenium center, while the lowest unoccupied molecular orbital (LUMO) involves both the rhenium center and the π orbitals of the quinone core. For $\mathbf{1}^+$ and $\mathbf{2}^+$, the HOMO and LUMO are predicted to be primarily localized on the quinone ring in conjunction with the metal center. The corresponding excited states, however, are predominantly metal-centered. Mulliken spin population analysis of $\mathbf{1}^+$ and $\mathbf{2}^+$ shows the spin density distributed across the benzoquinone ring and the metal

center (**Tables II.5** and **II.6**). The atoms bearing the maximum spin density are C(3) (6%), C(2) (6%), and rhenium (50%) for $\mathbf{1}^{+}$, and C(3) (9%), C(2) (5%), and rhenium (51%) for $\mathbf{2}^{+}$. This DFT study corroborates the EPR findings, indicating that the $\mathbf{1}^{+}$ and $\mathbf{2}^{+}$ ions are rhenium(VI) complexes of the semiquinonate radical anion ($DBQ^{\cdot 3-}$).

Furthermore, the EPR spectra and spin density calculations strongly suggest that the electronic structures of $\mathbf{1}^{+}$ and $\mathbf{2}^{+}$ can be represented as delocalized states: $[Re^{VI}(O)(DBQ^{\cdot 3-})Re^{VI}(O)] \leftrightarrow [Re^{V}(O)(DBQ^{2-})Re^{VI}(O)]$ and $[Re^{VI}(O)(CA^{\cdot 3-})Re^{VI}(O)] \leftrightarrow [Re^{V}(O)(CA^{2-})Re^{VI}(O)]$, respectively (Scheme 2).

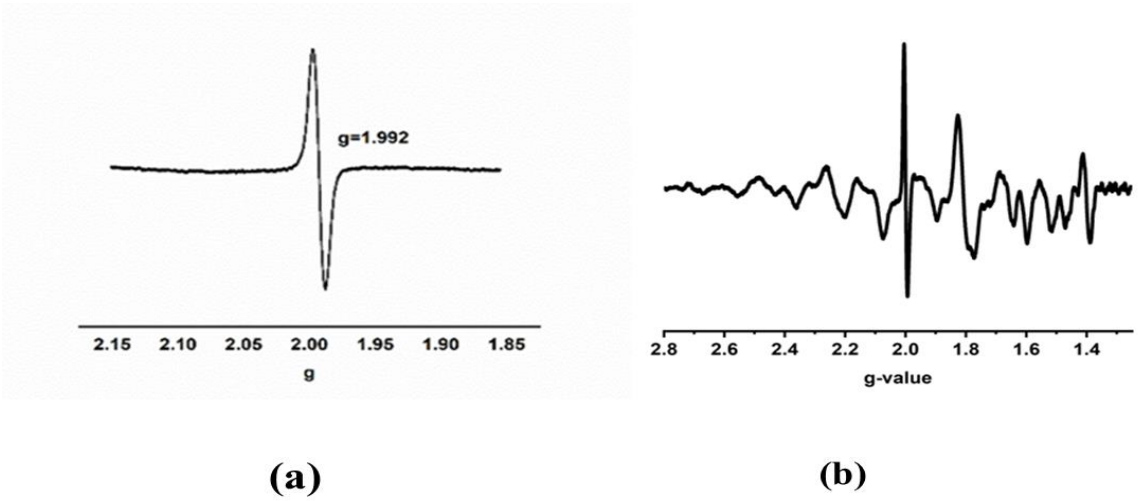

Figure II.8. X-band EPR spectra of **(a)** $\mathbf{1}^{+}$ at 298 K and **(b)** $\mathbf{1}^{+}$ at 115 K.

Table II.5. Isodensity plot of the selected orbital and Spin density plot of the excited states for Complex **1**

Complex 1	HOMO	LUMO
Optimised Ground state	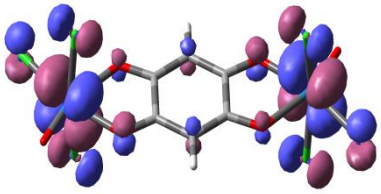	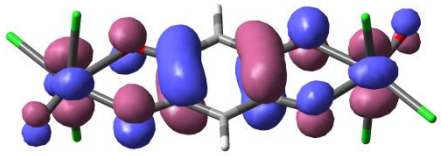
Optimised Excited state (Oxidised)	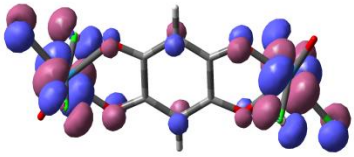	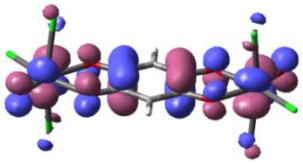
Optimised Excited state (Reduced)	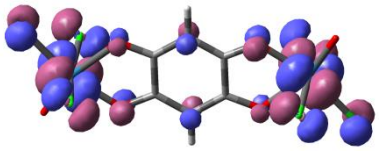	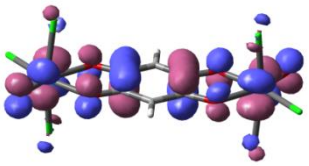
Spin density (Oxidised)	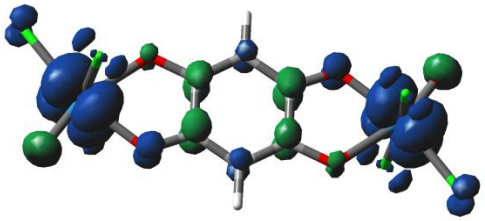	
Spin density (Reduced)	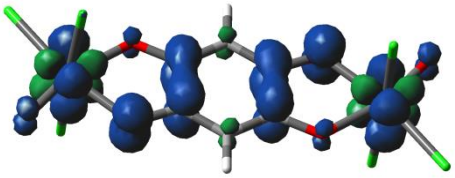	

Table II.6. Isodensity plot of the selected orbital and Spin density plot of the excited states for Complex **2**

Complex 2	HOMO	LUMO
Optimised Ground state	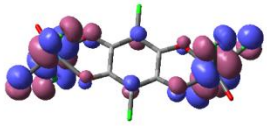	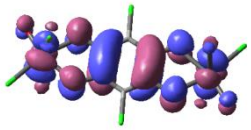
Optimised Excited state (Oxidised)	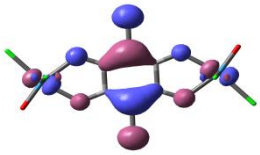	
Optimised Excited state (Reduced)	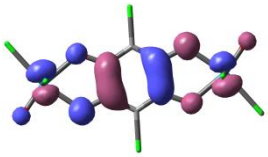	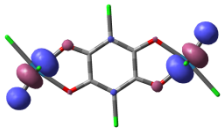
Spin density (Oxidised)	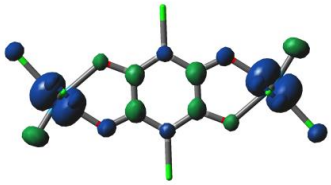	
Spin density (Reduced)	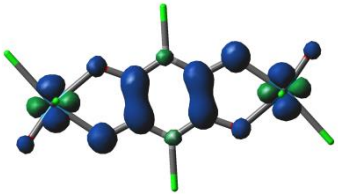	

II.3.4. Catalytic properties of complex 1 and 2:

The CV studies of **1** and **2** in CH_3CN-Water mixture observed a first irreversible anodic peak at $E_{p.a}$= 1.1 V and 1.3 V for **1** and **2** respectively whereas a second anodic peak at 1.62 V for both complexes as shown in **Figures II.9a and II.9b**. The voltammograms of complexes **1** and **2** had an enhanced current above background suggesting the catalytic process to be associated with the oxidation of water molecules. The catalytic onset potential also shifted to a lower value with increasing concentration of water in acetonitrile medium, spanning from 1mM to 5mM (**Figures II.10** and **II.11**), suggesting the oxidation occurred by deprotonation step as may be expected for a proton-coupled electron transfer (PCET) process. The linear increase of the square of the water oxidation current (i_p) with water concentration as well as catalyst concentration indicated that the catalytic process was first order with respect to water concentration (**Figures II.10** and **II.11**) and also with the catalyst concentration (**Figures II.12** and **II.13**). Complexes **1** and **2** showed linear relation with respect to current generation with different scan rate at a fixed potential. The Scan rate vs current generation plot suggested that the catalytic reaction follow first order kinetics as shown in **Figures II.14** and **II.15** for complexes **1** and **2** respectively. The evolved O_2 was detected in situ by reverse cathodic scan an inert dinitrogen atmosphere (**Figure II.16**). A controlled potential electrolysis (CPE) experiment of **1** was performed at 1.3 V with 0.15 mM catalyst in acetonitrile with 5mM neutral water (**Figure II.17**). The Faradaic yield (FY) thus calculated for water oxidation to oxygen is determined to be 67% by measuring the volume of oxygen produced (1.2 mL) through displacement of water at 1 atm pressure. Moreover, the maximum turnover frequency calculation of Complex **1** from current *vs* potential plot at different scan rate as shown in found to be 2.1 s^{-1}. The extent of current generation under similar condition also suggested that the complex **1** is superior catalytic role to Complex **2** for water oxidation reaction. It is noteworthy that the water oxidation processes can lead to formation of only O_2 as a sole product (no H_2O_2 is produced, further examined by xylenol orange assay test).

Calculation of diffusion constants from cyclic voltammogram:

The peak current is given by the Randles-Sevcik equation (1).

$$\boldsymbol{i_P = 0.4463(F/RT)^{1/2} n_P^{3/2} F A D^{1/2} [C] v^{1/2}} \qquad (\mathbf{1})$$

In equation (1), i_p is peak current, F is Faraday's constant (F = 96500 C mol^{-1}), R is the universal gas constant (R = 8.31 J K^{-1} mol^{-1}), T is temperature (T = 300 K), n_p is the number of electrons

transferred (n_p = 1 for $Re^{VI/V}$ redox couple), A is the active surface area of the electrode (A = 0.02 cm^2), D is the diffusion coefficient for the complex, [C] is the concentration of the catalyst, and ν is the scan rate. The diffusion coefficients (D) were calculated from the slopes of i_p– $\nu^{1/2}$ plots. Therefore, For Complex **1**, D = $\mathbf{5.82 \times 10^{-5}}$ cm^2 s^{-1} and for Complex **2**, D = $\mathbf{9.85 \times 10^{-5}}$ cm^2 s^{-1} .

Faradaic Yield Calculation of Complex 1:

FY is determined by the equation FY (%) = 100 X 4 X amount of O_2 produced (mol)/ (Amount of charge consumed during BE/F)

During the constant potential electrolysis (working electrode Glassy carbon electrode) at 1.3 V, total charged consumed 51.1 C, gas produced= 1.97 ml. So, FY is 67 %

TOF_{max} calculations of Complex 1 from cyclic voltammetry experiments:

The turnover frequency (TOF) is an inherent characteristic of catalysts, which represents the rate of conversion reactants into products per mole of active catalyst per unit time. The TOF value for **1** was derived using the following equation below from the catalytic cyclic voltammograms recorded CH_3CN solutions in presence of 5 mM water.

$$i_{cat}/i_P = 4.484 \times (RT/F)^{1/2}(TOF_{\max})^{1/2}\upsilon^{-1/2}$$

Where, i_p is peak current, i_{cat} is the catalytic current, F is Faraday's constant (F = 96500 C), R is the universal gas constant (R = 8.314 J K^{-1} mol^{-1}), T is temperature (T = 300 K) and ν is the scan rate. The TOF_{max} was calculated from the slope of i_{cat}/i_p *vs* $\nu^{-1/2}$ plot. From the i_{cat}/i_p vs 1/sqrt (scan rate), we get the slope (m) = 1.04.

Therefore, $1.04 = 4.484 \times (RT/F)^{1/2}(TOF_{\max})^{1/2}$

$TOF_{\max} = (1.04)^2 \times 96500/(4.484^2 \times 8.314 \times 298)$ = 2.1 s^{-1}

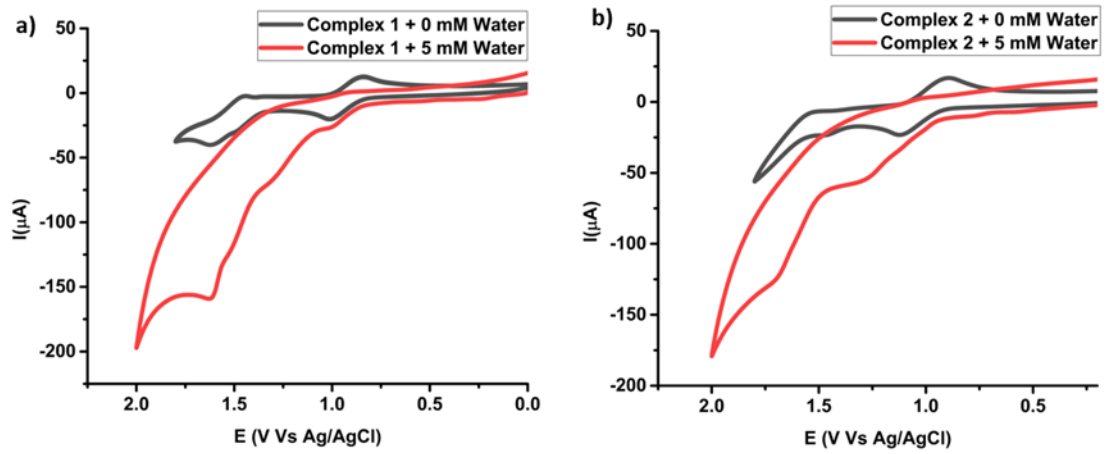

Figure II.9. Homogeneous electro catalytic water oxidation with complexes **(a) 1** and **(b) 2**. Cyclic voltammograms (Scan rate = 100 mV/s) of 0.15 mM **1** and **2** in acetonitrile in the absence (black) and presence of 5 mM water (red) using GCE as the working electrode, Ag/AgCl as the reference electrode and Pt as the counter electrode.

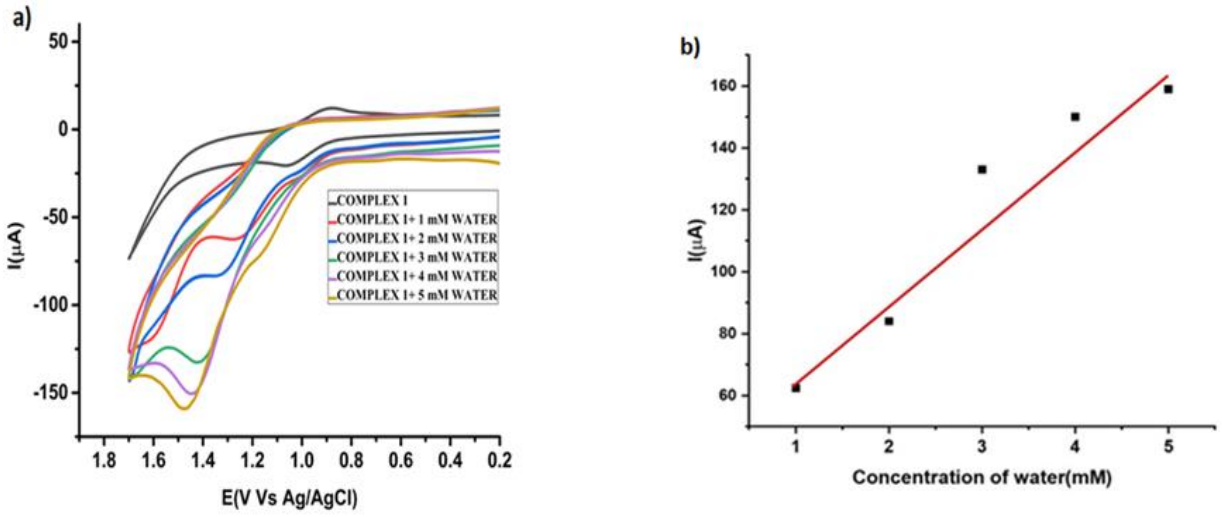

Figure II.10. H_2O concentration dependence of catalysis of Complex **1 (**a) Current *vs.* potential plot with gradual addition of 1μM of water and (b) Current vs. Concentration of water plot.

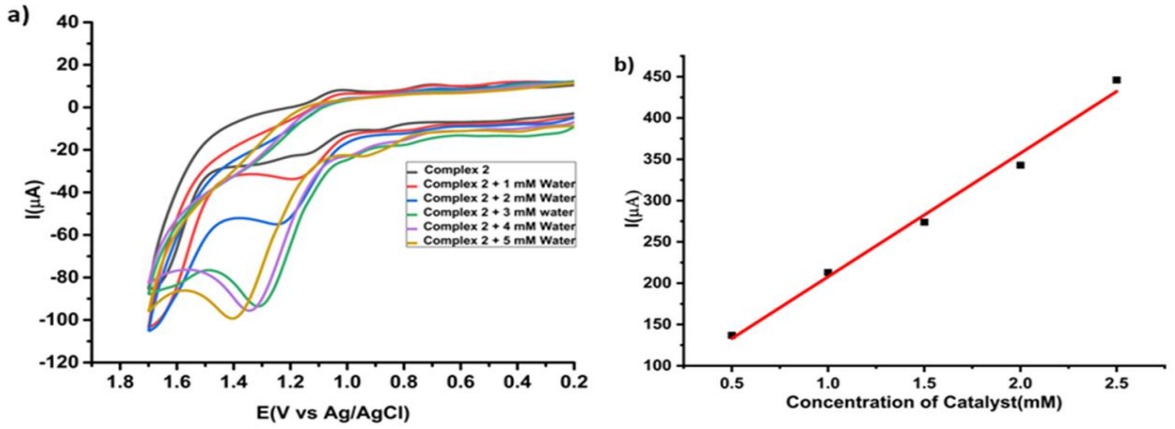

Figure II.11. H_2O concentration dependence of catalysis of Complex **2** (a) Current *vs.* potential plot with gradual addition of 1μM of water and (b) Current vs. Concentration of water plot

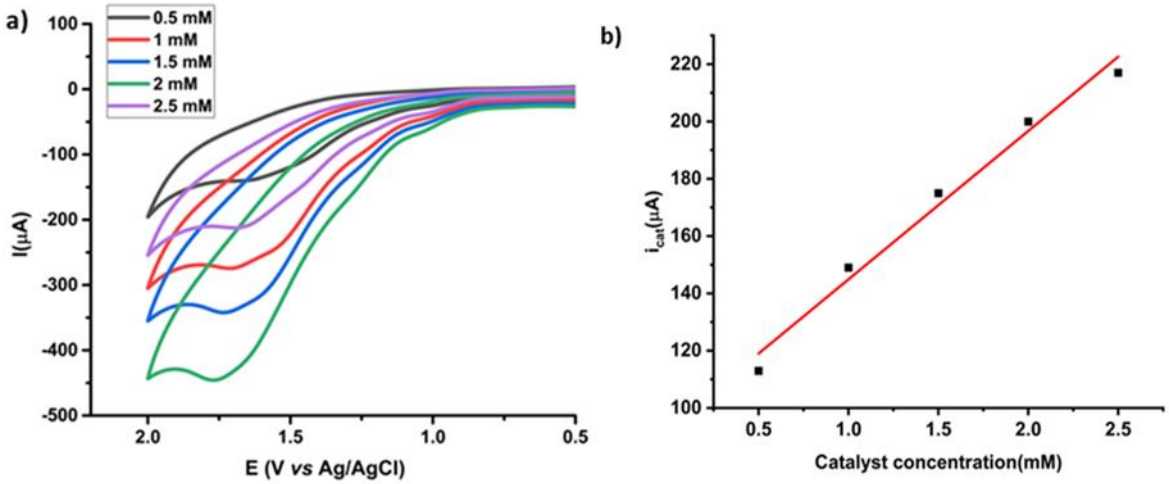

Figure II.12. Catalyst concentration dependence of catalysis of Complex **1 a)** Current *vs.* potential plot with gradual addition of 0.5 μM of catalyst and **b)** Current vs. Concentration of Catalyst plot

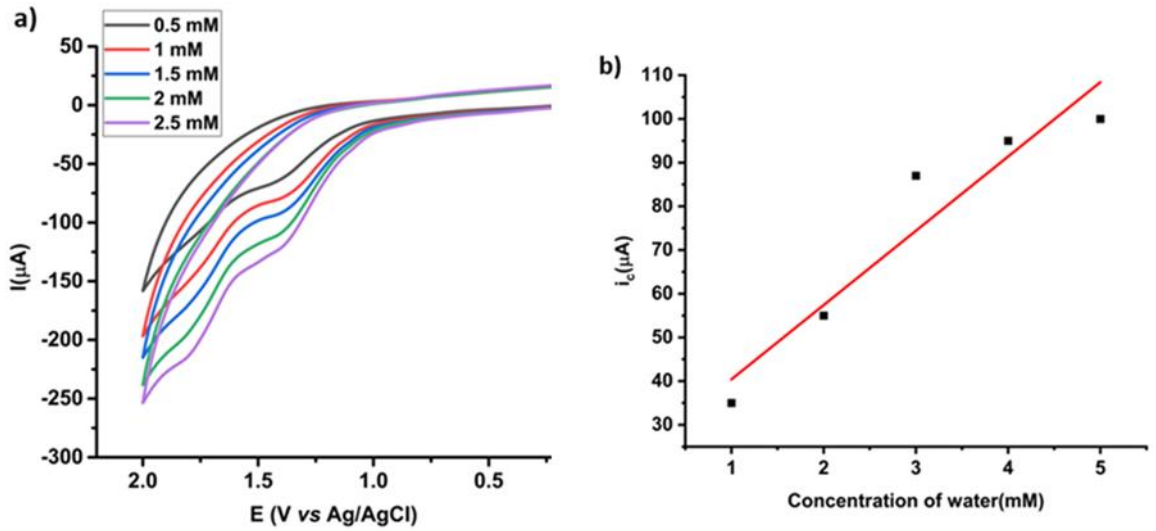

Figure II.13. Catalyst concentration dependence of catalysis of Complex **2 (a)** Current *vs.* potential plot with gradual addition of 0.5 µM of catalyst and **(b)** Current vs. Concentration of Catalyst plot.

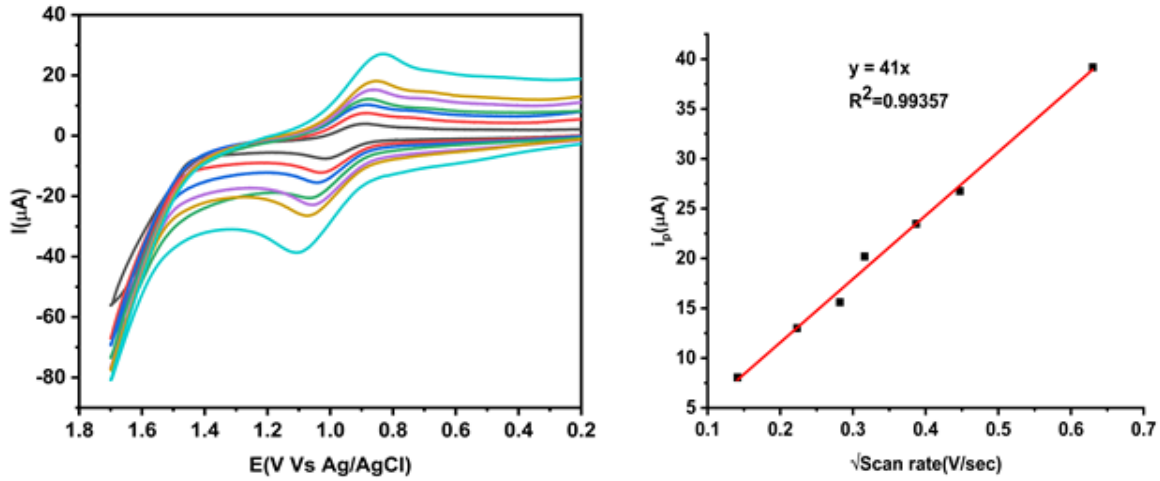

Figure II.14. a) Current *vs.* potential plot in different scan rate and **b)** Ip vs. $\nu^{1/2}$ plot **Complex-1**

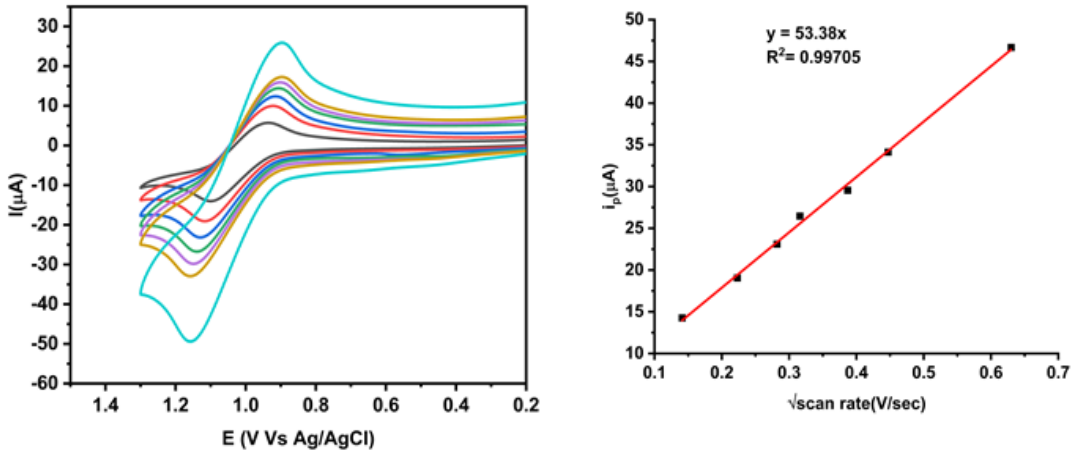

Figure II.15. a) Current *vs.* potential plot in different scan rate and **b)** Ip vs. $\nu^{1/2}$ plot **Complex-2**

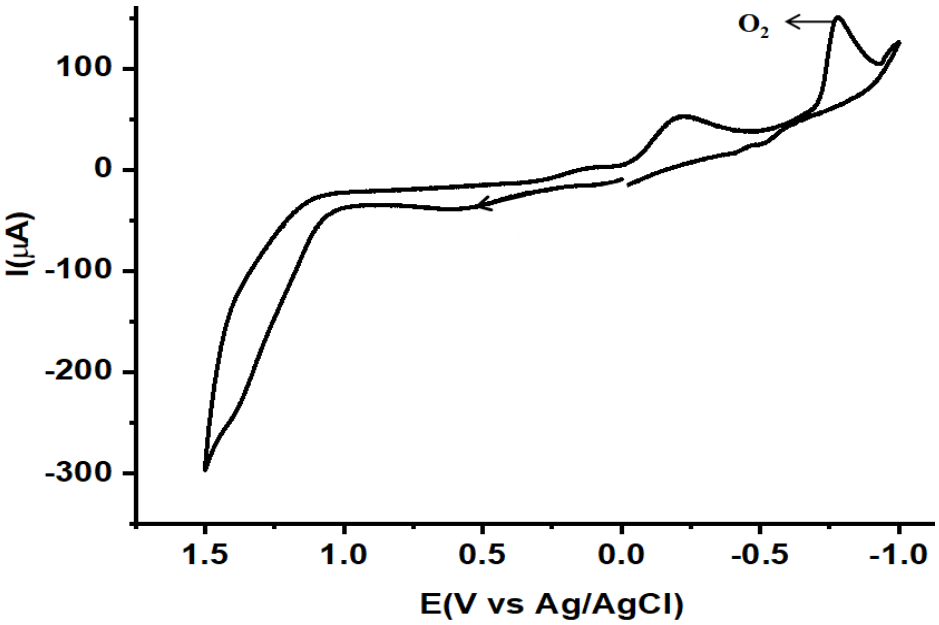

Figure II.16. O_2 produced during OER (Oxygen Evolution Reaction) reduced in-situ by the working electrode at the reverse cathodic scan at argon atmosphere.

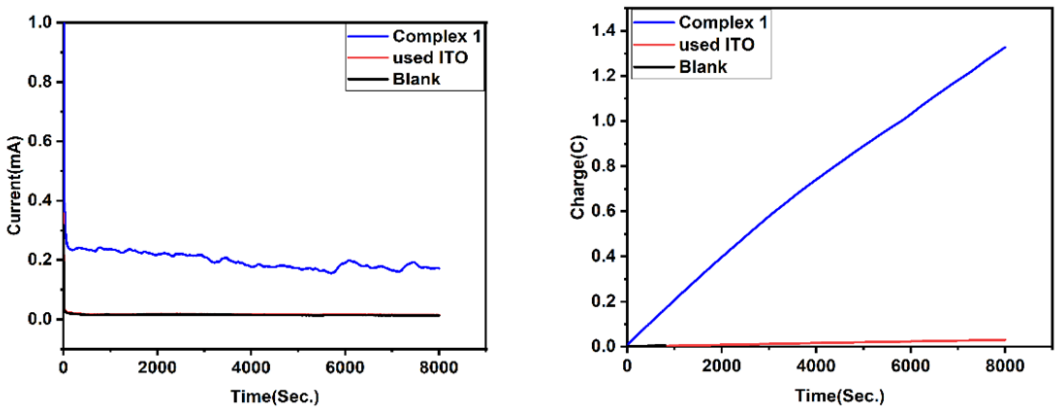

Figure II.17. (a) charge build up during CPE **(b)** I–t curves of the solution using ITO as the working electrode at 1.3 V. Black line for the 5ml solution containing CH_3CN and H_2O (10:1, v/v) and the complex 1(0.1mM). Red line for the used ITO electrode and blue line for the blank solution.

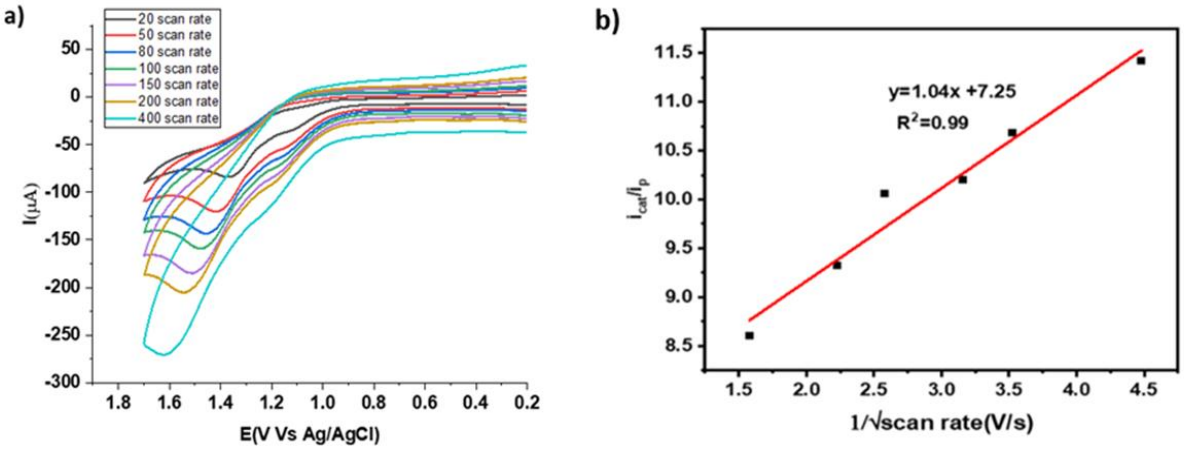

Figure II.18. Calculation of TOF_{max} for Complex **1: a)** current vs potential plot at different scan rate **b)** i_{cat}/i_p *vs* $\nu^{-1/2}$ plot

II.4. Mechanistic Investigation:

Now, on electrochemical oxidation of **1** and **2** by CPE study (1.30 V *vs* Ag/AgCl) in dry CH_3CN solvent no dioxygen gas was detected at anode and the reaction ended up furnishing EPR active $\mathbf{1}^+$ and $\mathbf{2}^+$ ions whereas, **1** and **2** carried out water oxidation in presence of CH_3CN-water mixture solution under the same CPE study (**Scheme II.4**).

Scheme II.4. Probable fate of electrochemically oxidised species of $[Re^{VI}(O)Cl_3(L^{\bullet 3-})Re^{VI}(O)Cl_3]^-$ in dry CH_3CN solvent and in CH_3CN-Water mixture solution under CPE study.

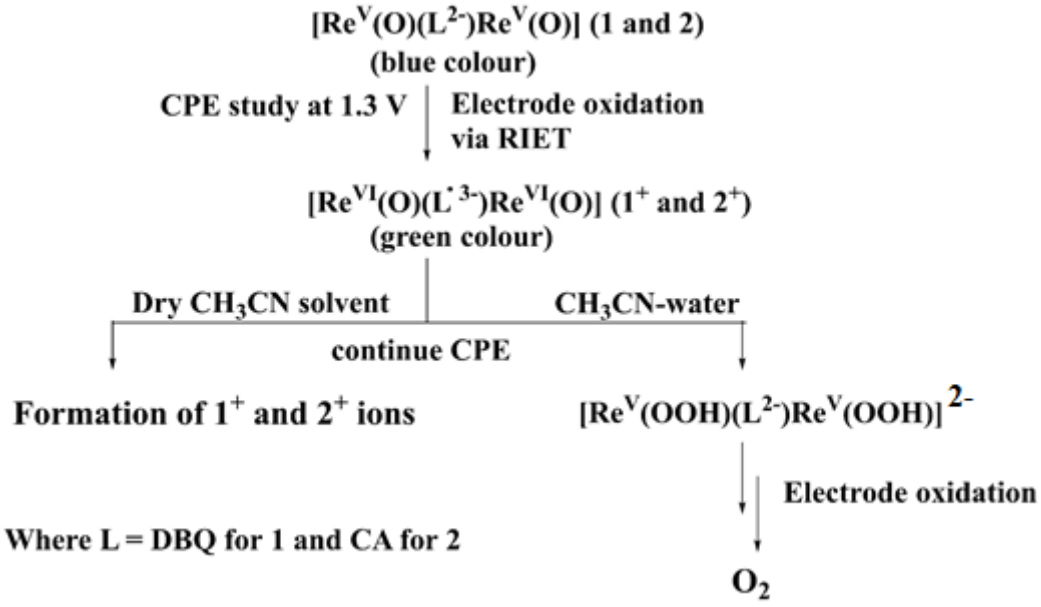

1 and **2** were active water oxidation catalyst in electrolysis process under CPE study and generate rapid molecular oxygen gas at anode in presence of CH_3CN-water mixture solution. **1** and **2** performed as homogeneous catalyst under CPE analyses at +1.30 V potential and neutral pH on glassy carbon electrode (GCE) as working electrode in acetonitrile-water mixture.

To understand the active species during electrocatalytic water oxidation, infrared (IR), electron paramagnetic resonance (EPR), and mass spectra were recorded over the course of the reaction. Now, the CPE study (1.30 V *vs.* Ag/AgCl) of complex **1** in acetonitrile-water mixture, *in situ* generated oxidised species of $\mathbf{1}^+$ $[Re^{VI}(O)Cl_3(\ DBQ^{\bullet 3-})Re^{VI}(O)Cl_3]^-$ further oxidized to higher valent $[Re^{VI}(O)Cl_3(DBQ^{2-})Re^{VI}(O)Cl_3]$ species which bound to molecular water by water nucleophilic attack (WNA) to produce peroxide intermediate species of $[Re^{V}(OOH)Cl_3(DBQ^{2-})Re^{V}(OOH)Cl_3]^{2-}$ ($\mathbf{A}^1$) as depicted in **Scheme II.4**. The Intermediate $\mathbf{A}^1$ underwent oxidation

through PCET, water addition to liberate molecular dioxygen gas at anode which detected by GC-TCD analysis. The peroxide intermediate of $\mathbf{A}^1$ is the key step towards water oxidation reaction (WOR). Recently, many research group proposed that the high valent metal O-O as the active water oxidation precursor [62]. The intermediate $\mathbf{A^1}$ was detected by ESI mass spectrometry (see, **Figure II.20**) of the reaction mixture after 40 min during the CPE measurement and the mass peak was observed at m/z = 789.3261 for **1** (calculated exact mass 787.72). Interestingly, the intermediate $\mathbf{A^1}$ was also detected by IR spectroscopy (see, **Figure II.19**) of the reaction mixture after 40 minutes during the CPE measurement in acetonitrile-water medium. The IR spectra of **1** and **2** are shown in acetonitrile medium. The $\nu_{\mathrm{Re-O\ (oxo)}}$ [63] for complex **1** was reported at 990 cm^{-1} whereas in CPE study of water oxidation process the IR band shifted to lower wave number at 922 cm^{-1} assigned the $\nu_{\mathrm{Re=O(oxo)}} \rightarrow \nu_{\mathrm{Re-O(single\ bond)}}$ conversion and additionally a new vibrational band appeared at 850 cm^{-1} due to formation of peroxo bond ($\nu_{\mathrm{O-O}}$) reported for stretching vibration of peroxide species[66]. Thus, the IR and mass spectrometry results were authenticated to identify the intermediate $\mathbf{A^1}$ in the mechanistic study of WOR which is very significant in water oxidation field as described in **Scheme II.4**. Similarly, the complex **2** also performed the WOR under CPE condition (1.30 V *vs* Ag/AgCl, GC electrode) in presence of water meditated acetonitrile solvent. The overall mechanism remaining essentially the same for the water oxidation process as described in **Scheme II.4**.

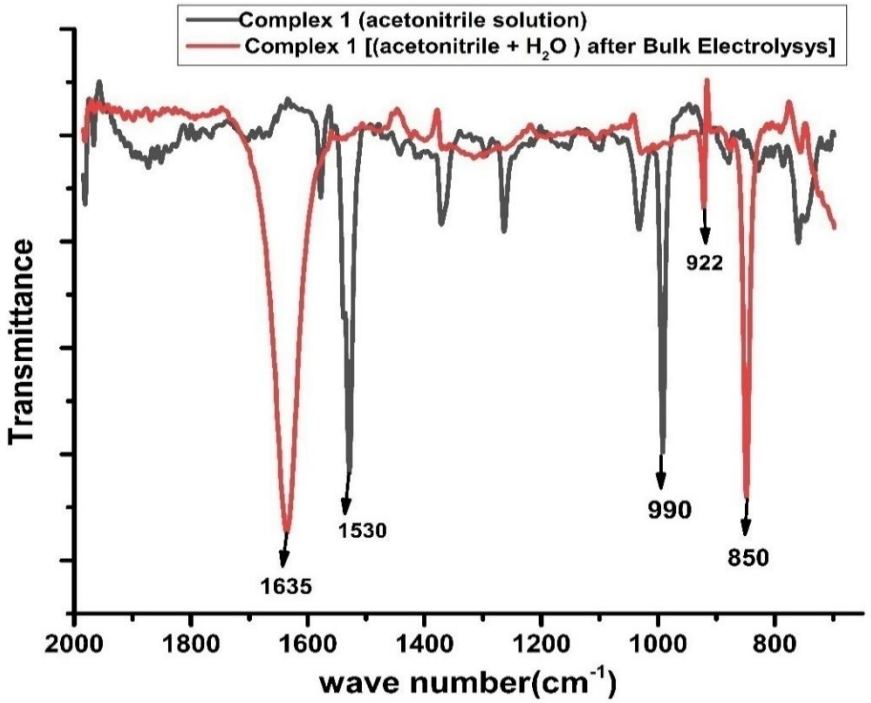

Figure II.19. FT-IR spectrum of Complex **1** before and after bulk electrolysis in CH_3CN/Water mixture at 1.3 V.

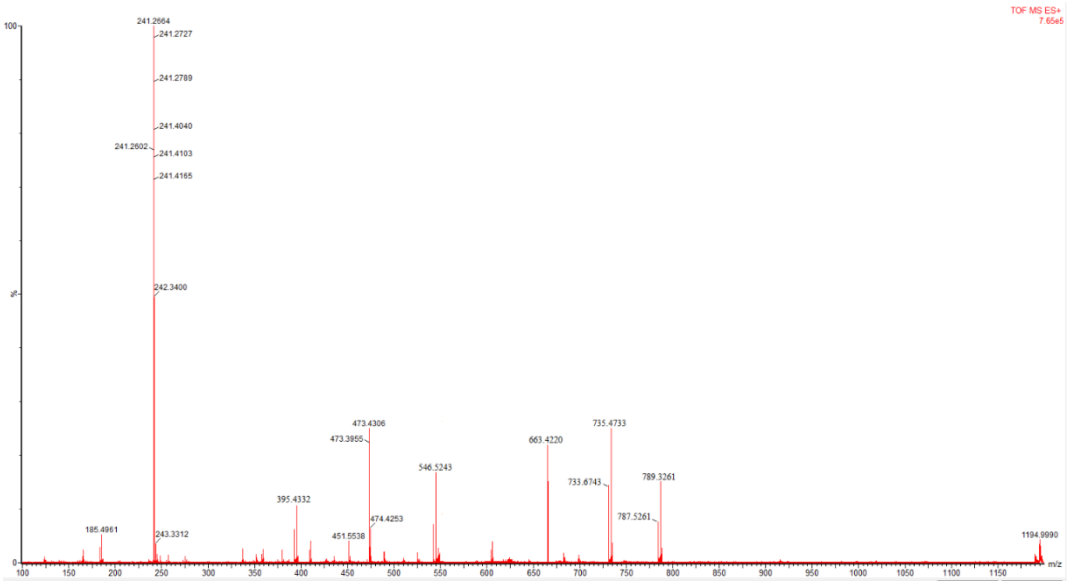

Figure II.20. ESI-MS Spectra of the Intermediate $\mathbf{A^1}$ for catalysis of **complex 1.**

Scheme II.4. Proposed mechanistic pathway of WOR under CPE condition.

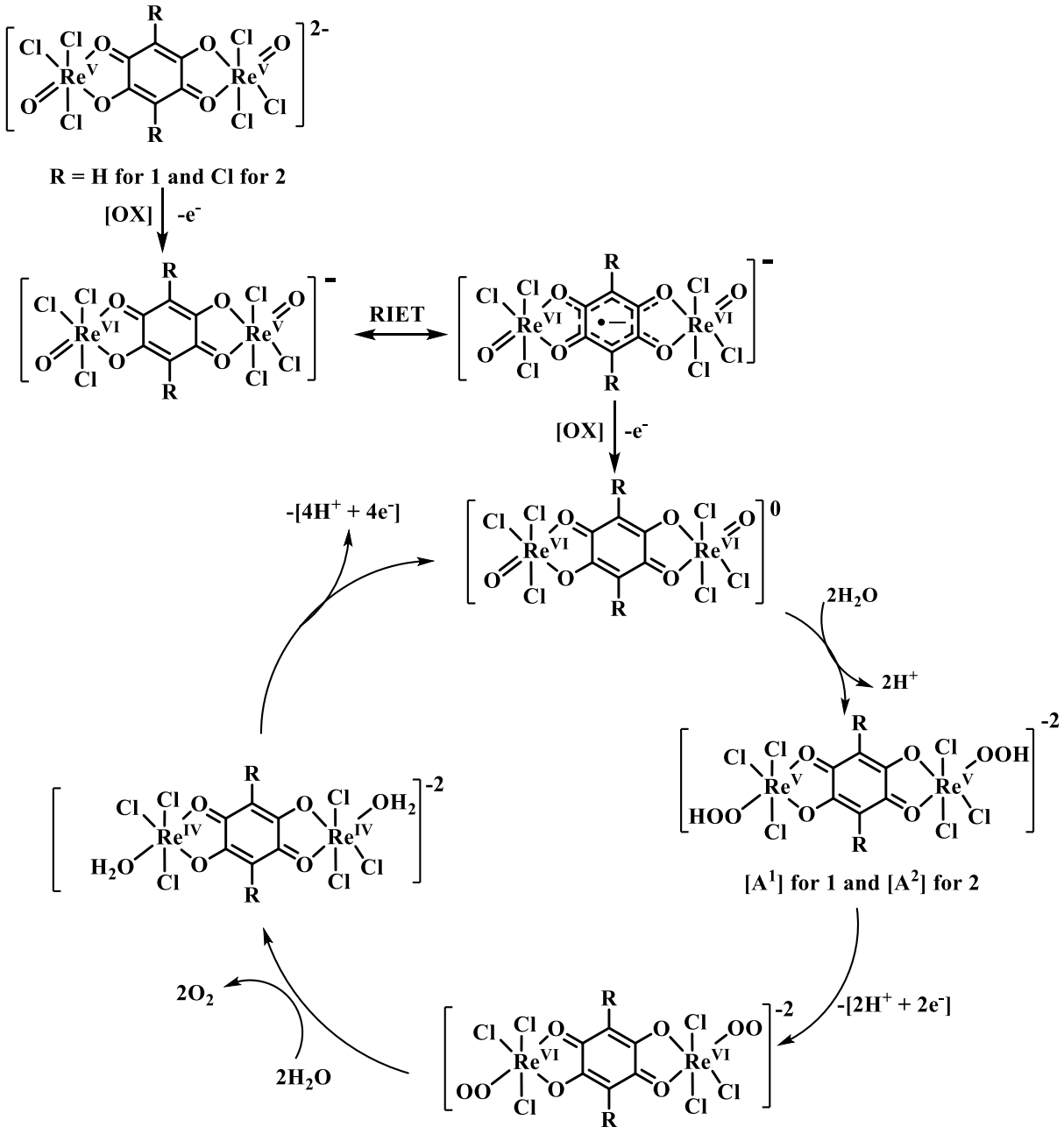

II.5. Conclusion

The CV studies of **1** and **2** in CH_3CN-Water mixture observed a first irreversible anodic peak at $E_{p.a}$= 1.1 V and 1.3 V for **1** and **2** respectively whereas a second anodic peak at 1.62 V for both complexes. The voltammograms of complexes **1** and **2** had an enhanced current above background suggesting the catalytic process to be associated with the oxidation of water molecules. The catalytic onset potential also shifted to a lower value with increasing concentration of water in acetonitrile medium, spanning from 1mM to 5Mm, suggesting the oxidation occurred by deprotonation step as may be expected for a proton-coupled electron transfer (PCET) process. The linear increase of the square of the water oxidation current (i_p) with water concentration as well as catalyst concentration indicated that the catalytic process was first order with respect to water concentration and also with the catalyst concentration. Complexes **1** and **2** showed linear relation with respect to current generation with different scan rate at a fixed potential. The Scan rate vs current generation plot suggested that the catalytic reaction follow first order kinetics for complexes **1** and **2**. The evolved O_2 was detected in situ by reverse cathodic scan an inert dinitrogen atmosphere. A controlled potential electrolysis (CPE) experiment of **1** was performed at 1.3 V with 0.15 mM catalyst in acetonitrile with 5mM neutral water. The Faradaic yield (FY) thus calculated for water oxidation to oxygen is determined to be 67% by measuring the volume of oxygen produced (1.2 mL) through displacement of water at 1 atm pressure. Moreover, the maximum turnover frequency calculation of Complex **1** from current *vs* potential plot at different scan rate found to be 2.1 s^{-1}. The extent of current generation under similar condition also suggested that the complex **1** is superior catalytic role to Complex **2** for water oxidation reaction. It is noteworthy that the water oxidation processes can lead to formation of only O_2 as a sole product (no H_2O_2 is produced, further examined by xylenol orange assay test).

II.6. Reference:

1. S. Solomon, G.K. Plattner, R Knutti, P Friedlingstein, *Proc. Nat. Acad. Sci.*, 2009, **106(6)**, 1704-1709.
2. N.S. Lewis, D.G. Nocera, *Proc. Nat. Acad. Sci.*, 2006, **103(43)**, 15729-15735.
3. B. Zhang, L. Sun, *Chem. Soc. Rev*., 2019, **48**, 2216-2264.
4. C. Zhang, Z. Liu, L. Zhang, A. Zhu, F. Liao, J. Wan, J. Zhou, Y. Tian, *Angew. Chem., Int. Ed.*, 2020, **59**, 20538−20544.
5. C. Xia, S. Back, S. Ringe, K. Jiang, F. Chen, X. Sun, S. Siahrostami, K. Chan, H. Wang, *Nat. Catal*., 2020, **3 (2)**, 125−134.
6. C. P. D. Leon, *Nat*. *Catal*., 2020, **3 (2)**, 96−97.
7. C. Yuan, K. Hui, H. Yin, S. Zhu, J. Zhang, X. Wu, X. Hong, W. Zhou, X. Fan, F. Bin, F. Chen, K. Hui, *ACS Mater. Lett.*, 2021, **3 (6)**, 752-780.
8. A. Llobet, *Nat. Catal*., 2022, **5(2)**, 79-82.
9. T. J. Meyer, *Acc. Chem. Res.*, 1989, **22 (5)**, 163-170.
10. W. A. A. Arafa, M. D. Kärkäs, B. L. Lee, T. Åkermark, R. Z. Liao, H. M. Berends, J. Messinger, P. M. Siegbahna, B. Åkermark, *Phys. Chem. Chem. Phys*., 2014, **16**, 11950-11964.
11. E. A. Karlsson, B. L. Lee, T. kermark, E. V. Johnston, M. D. Kärkäs, J. Sun, Ö. Hansson, J. Bäckvall, B. kermar, *Angew. Chem. Int. Ed*., 2011, **50**, 11715 –11718.
12. J. K. Young, J. B. Brennan, R. Tagore, W. G. Brudvig, *Acc. Chem. Res*., 2015, **48**, 567−574.
13. R, Brimblecombe, A, Koo, C. G. Dismukes, F. G. Swiegers, L. Spiccia, *J. Am. Chem. Soc*., 2010, **132**, 2892–2894
14. M. Wiechen, M. H. Berends, P. Kurz, *Dalton Trans*., 2012, **41**, 21–31.
15. L. F. Huber, M. A. Wernbacher, D. Perleth, D. Nauroozi, L. González, *Inorg Chem.*, 2021, **60(17)**, 13299-13308.

16. W. Rabten, M. D. Kärkäs, T. Åkermark, H. Chen, R-Z. Liao, F. Tinnis, J. Sun, P. E. M. Siegbahn, P. G. Andersson, B. Åkermark, *Inorg Chem.*, 2015, **54 (10)**, 4611-4620.

17. Y. Xu, L. Duan, L. Tong, B. Åkermark, L. Sun, *Chem. Commun.*, 2010, **46**, 6506-6508.

18. M. A. Hoque, M. Gil-Sepulcre, A. de Aguirre et al, *Nat. Chem*., 2020, **12**, 1060–1066.

19. M. Hirahara, H. Goto, M. Yagi, Y. Umemura, *Chem.Commun*., 2020, **56**, 12825-12828

20. A. Kundu, S. Dey, S. Dey, A. Anoop, S. Mandal, *Inorg. Chem*., 2020, **59**, 2, 1461–1470.

21. S. Sheehan, J. Thomsen, U. Hintermair et al., *Nat Commun.*, 2015, **6**, 6469.

22. J. M. Thomsen, S. W. Sheehan, S. M. Hashmi, J. Campos, U. Hintermair, R. H. Crabtree, G. W. Brudvig, *J. Am. Chem. Soc*., 2014, **136**, 39, 13826–13834.

23. G. Gatto, A. D. Palo, A. C. Carrasco, A. M. Pizarro, S. Zacchini, G. Pampaloni, F. Marchetti, A. Macchioni, *Catal. Sci. Technol*., 2021, **11**, 2885-2895

24. X. Liu, Y. Maegawa, Y. Goto, K. Hara, S. Inagaki, *Angew. Chem. Int. Ed*., 2016, **55**, 7943–7947.

25. J. F. Hull, D. Balcells, J. D. Blakemore, C. D. Incarvito, O. Eisenstein, G. W. Brudvig, R. H. Crabtree, *J. Am. Chem. Soc.*, 2009, **131**, 25, 8730–8731.

26. J. M Thomsen, D. L Huang, R. H Crabtree, G. W Brudvig, *Dalton Trans*., 2015, **44**, 12452-12472**.**

27. A. Volpe, C. Tubaro, M. Natali, A. Sartorel, G. W. Brudvig, M. Bonchio, *Inorg. Chem.*, 2019, **58**, 16537−16545.

28. K. S. Joya, N. K. Subbaiyan, F. D'Souza, H. J. M. de Groot, *Angew. Chem. Int. Ed*., 2012, **51,** 9601–9605.

29. B.V. Dijk, G. M. Rodriguez, L. Wu, J. P. Hofmann, A. Macchioni, D. G. H. Hetterscheid, *ACS Catal*., 2020, **10 (7)**, 4398-4410**.**

30. J. L. Fillol, Z. Codolà, I. Garcia-Bosch, L. Gómez, J. J. Pla, M. Costas, *Nat. Chem.*, 2011, **3**, 807–813.

31. W. C. Ellis, N. D. McDaniel, S. Bernhard, T. J. Collins, *J. Am. Chem. Soc.*, 2010, **132 (32)**, 10990-10991.

32. L. D. Wickramasinghe, R. Zhou, R. Zong, P. Vo, K. J. Gagnon, R. P. Thummel, *J. Am. Chem. Soc*., 2015, **137 (41)**, 13260-13263.

33. D. Hong, S. Mandal, Y. Yamada, Y.M. Lee, W. Nam, A. Llobet, S. Fukuzumi, *Inorg Chem.*, 2013, **52 (16)**, 9522-9531.

34. Z. Shaghaghi, M. Aligholivand, R. Mohammad-Rezaei, *Int. J. Hydrog. Energy*., 2021, **46(1)**, 389-402.

35. S. Biswas, S. Bose, J. Debgupta, P. Das, A. N. Biswas, *Dalton Trans*., 2020, **49,** 7155-7165.

36. D. Hong, J. Jung, J. Park, Y. Yamada, T. Suenobu, Y.M. Lee, W. Nam, S. Fukuzumi, *Energy Environ. Sci.*, 2012, **5**, 7606-7616.

37. M. L. Rigsby, S. Mandal, W. Nam, L. C. Spencer, A. Llobet, S. S. Stahl, *Chem. Sci*., 2012, **3**, 3058-3062.

38. L. Zhang, F. Yu, Y. Shi, F. Li, H. Li, *Chem. Commun*., 2019, **55**, 6122-6125**.**

39. M. Aligholivand, Z. Shaghaghi, R. Bikas, A. Kozakiewicz, *RSC Adv*., 2019, **9**, 40424-40436.

40. Y. Han, Y. Wu, W. Lai, R. Cao, *Inorg Chem.*, 2015, **54 (11)**, 5604-5613.

41. L. Francàs, S. Corby, S. Selim, D. Lee, C. A. Mesa, R. Godin, E. Pastor, I. E. Stephens, K. Choi, J. R. Durrant, *Nat. Commun.*, 2019, **10(1)**, 1-10.

42. D. Wang, C. O. Bruner, *Inorg Chem.*, 2017, **56 (22)**, *13638-13641*

43. J. Shen, M. Wang, P. Zhang, J. Jiang, L. Sun, *Chem. Commun*., 2017, **53**, 4374-4377.

44. A. M. Geer, C. Musgrave III, C. Webber, R. J. Nielsen, B. A. McKeown, C. Liu, P. P. M. Schleker, P. Jakes, X. Jia, D. A. Dickie, J. Granwehr, S. Zhang, C. W. Machan, W. A. Goddard III, T. B. Gunnoe, *ACS Catal*., 2021, **11**, 12, 7223–7240.

45. X. J. Su, M. Gao, L. Jiao, R. Z. Liao, P. E. M. Siegbahn, J. P. Cheng, M. T. Zhang, *Angew. Chem., Int. Ed*., 2015, **54(16),** 4909-4914.

46. T. Zhang, C. Wang, S. Liu, J. L. Wang, W. Lin, *J. Am. Chem. Soc*., 2014, **136**, 273−281.

47. M. P. Santoni, G. L. Ganga, V. M. Nardo, M. Natali, F. Puntoriero, F. Scandola, S. Campagna, *J. Am. Chem. Soc*., 2014, **136**, 23, 8189–8192.

48. Z. Zand, P. Salimi, M. R. Mohammadi, R. Bagheri, P. Chernev, Z. Song, H. Dau, M. Görlin, M. M. Najafpour , *ACS Sustain. Chem. Eng.*, 2019, **7 (20),** 17252-17262.

49. Y. Pushkar, Y. Pineda-Galvan, A. K. Ravari, T. Otroshchenko, D. A. Hartzler, *J. Am. Chem. Soc*., 2018, **140 (42),** 13538-13541.

50. X. Zhang, Q. F. Chen, J. Deng, X. Xu, J. Zhan, H. Y. Du, Z. Yu, M. Li, M. T. Zhang, Y. Shao, *J. Am. Chem. Soc*., 2022, **144 (39)**, 17748-17752.

51. Y. Xie, D. W. Shaffer, J. J. Concepcion, *Inorg Chem.*, 2018, **57 (17)**, 10533-10542.

52. X. Li, X. P. Zhang, M. Guo, B. Lv, K. Guo, X. Jin, W. Zhang, Y. M. Lee, S. Fukuzumi, W. Nam, R. Cao, *J. Am. Chem. Soc.*, 2021, **143 (36)**, 14613-14621.

53. W. Sinha, A. Mahammed, N. Fridman, Z. Gross, *ACS Catalysis.*, 2020**, 10 (6),** 3764-3772.

54. P. Tan, H. Kwong, T. Lau, *Chem. Commun.*, 2015, **51**, 12189-12192.

55. J. L. Fillol, Z. Codolà, I. Garcia-Bosch, L. Gómez, J. J. Pla, M. Costas, *Nat. Chem*., 2011, **3(10)**, 807-813.

56. Y. Han, Y. Wu, W. Lai, R. Cao, *Inorg Chem.*, 2015, **54 (11)**, 5604-5613

57. J. T. Muckerman, D. E. Polyansky, T. Wada, K. Tanaka, E. Fujita, *Inorg Chem.*, 2008, **47 (6)**, 1787-1802

58. J. S. Miller, K. S. Min, *Angew. Chem., Int. Ed*., 2009, **48(2)**, 262-272.

59. K. S. Min, A. G. DiPasquale, A. L. Rheingold, H. S. White, J. S. Miller, *J. Am. Chem. Soc.*, 2009, **131 (17),** 6229-6236.

60. L. Lohmeyer, F. Schçn, E. Kaifer, H. J. Himmel, *Angew. Chem., Int. Ed*, 2021, **60(18)**, 10415-10422.

61. Y. Zhang, H. Zhang, A. Liu, C. Chen, W. Song, J. Zhao, *J. Am. Chem. Soc.*, 2018, **140 (9)**, 3264-3269.

62. J. D. Blakemore, R. H. Crabtree, G. W. Brudvig, *Chem. Rev.*, 2015**, 115 (23),** 12974-13005.

63. A. Mondal, S. Sarkar, D. Chopra, T. N. Guru Row, K. K. Rajak, *Dalton Trans*., 2004, 3244-3250.

64. M. D. Ward, *Inorg Chem.*, 1996, **35 (6),** 1712-1714.

65. R. Sarkar, A. Hens, K. K. Rajak, *RSC Adv*., 2015, **5**, 15084-15095.

66. W. Lin, H. Frei, *J. Am. Chem. Soc.*, 2002, **124**, 31, 9292–9298.

67. P. Saha. A. S. Roy, T. Weyhermüller, P. Ghosh, *Chem. Commun.*, 2014, **50**, 86, 13073-13076

Chapter III

Highly Efficient Photocatalytic Reduction of CO_2 to CO under Visible Light Using Rhenium Benzo[d]Oxazole Complexes.

III.1. Introduction:

The escalating global climate crisis, largely driven by anthropogenic greenhouse gas emissions particularly carbon dioxide (CO_2) demands innovative mitigation strategies. The combustion of fossil fuels significantly contributes to rising atmospheric CO_2 levels, which have exceeded 400 parts per million (ppm), intensifying the impacts of climate change[1]. Consequently, the conversion of CO_2 into valuable liquid fuels using renewable energy has emerged as a critical area of research[2,3]. Among various renewable sources, solar energy holds particular promise for driving the photocatalytic reduction of CO_2 into products such as CO, CH_4, and HCOOH etc[4-8].

To this end, both homogeneous and heterogeneous photocatalytic systems have been explored. However, homogeneous catalysis offers greater flexibility in catalyst design and optimization, with enhanced potential for improved catalytic efficiency, sustainability, and atom economy[9]. A wide variety of metal complexes—including those based on Ir[10-13], Ru[14-18], Re[19-23], Co[24-27], Fe[28-33], and Ni[34-38]—have been investigated for their ability to catalyze CO_2 reduction.

The general mechanism of photocatalytic CO_2 reduction involves three main components: a photosensitizer (PS) that captures light energy, a sacrificial electron donor (SED) that supplies electrons, and a catalyst that utilizes these electrons to reduce CO_2. Most molecular systems designed for photocatalytic CO_2 reduction consist of two discrete functional components: a catalyst and a photosensitizer. Recently, the development of self-photosensitizing mononuclear complexes capable of functioning both as a photosensitizer and as a CO_2 reduction catalyst has marked a significant advancement in the field[39-49].

Seminal work by Lehn and co-workers laid the foundation for this area by demonstrating the photo- and electrocatalytic reduction of CO_2 to CO using $Re(bpy)(CO)_3X$ complexes (where bpy = 2,2'-bipyridine and X is a monodentate apical ligand)[50-51]. The photophysical behavior of these rhenium bipyridyl tricarbonyl complexes is governed by a combination of metal-centered ligand field excited states, π-π* transitions localized on the bipyridine ligand, and metal-to-ligand charge transfer (MLCT) states. Early studies revealed CO production under visible light, with turnover numbers (TON) up to 48 and quantum yields (Φ) reaching 0.38, although these complexes typically absorb

poorly in the visible range. Importantly, the emissive ^{3}MLCT state can be modulated via chemical modifications to the bpy ligand[52-54].

Building upon these insights, numerous structurally diverse photo- and electrocatalysts based on the Re(bpy)(CO)$_3$X motif have been developed, offering fundamental understanding of CO_2 activation mechanisms. Despite the progress achieved with Re(I) diimine complexes, there remains a need for catalysts that efficiently facilitate multi-electron CO_2 reduction beyond the two-electron product CO.

A notable advancement has been reported by Angeles-Boza et al., who introduced a new class of rhenium complexes featuring pyridine-oxazoline ligands as electrochemical CO_2 reduction catalysts. Expanding upon this approach, our research presents a novel series of Re(I) complexes incorporating pyridine-, quinoline-, and isoquinoline-substituted benzo[d]oxazole ligands and their derivatives, as promising candidates for both photocatalytic and electrocatalytic CO_2 reduction[55-56].

The benzo[d]oxazole ligand framework is particularly advantageous due to its stability under reductive conditions and its synthetic accessibility, which allows for fine-tuning of steric and electronic properties. The electron-rich nitrogen center in benzo[d]oxazoline facilitates key catalytic steps such as oxidative addition. Moreover, the oxazole moiety, beyond serving as a diimine donor, is likely involved in hydride storage and transfer, potentially contributing to methane formation during catalysis[55].

Given the established effectiveness of bipyridine- and phenanthroline-based metal complexes in CO_2 reduction, this study aims to expand the ligand design space by exploring pyridine-, quinoline-, and isoquinoline-benzo[d]oxazole derivatives. These ligands may offer improved efficiency and selectivity in catalysis.

This research introduces a promising new series of rhenium(I) complexes incorporating pyridine, quinoline, and isoquinoline-substituted benzo[d]oxazole ligands and their derivatives as potential high-performance photocatalysts and electrocatalysts for CO_2 reduction. (**Figure III.1**). All synthesized complexes exhibited fluorescence emission arising from both ligand-centered π-π^* transitions and ^{3}MLCT transitions, observed at distinct wavelengths. The inclusion of additional aromatic units in the ligand scaffold led to a bathochromic shift of the MLCT band, enhancing absorption in the visible region. This

suggests that the complexes possess intrinsic photosensitizing properties, eliminating the need for an external photosensitizer.

The study comprehensively evaluates the influence of various parameters on catalytic performance, including solvent effects, product evolution over time, and selectivity under different conditions. Additionally, the electrocatalytic activity of the complexes toward CO_2 reduction is investigated, providing further insight into their potential for practical application.

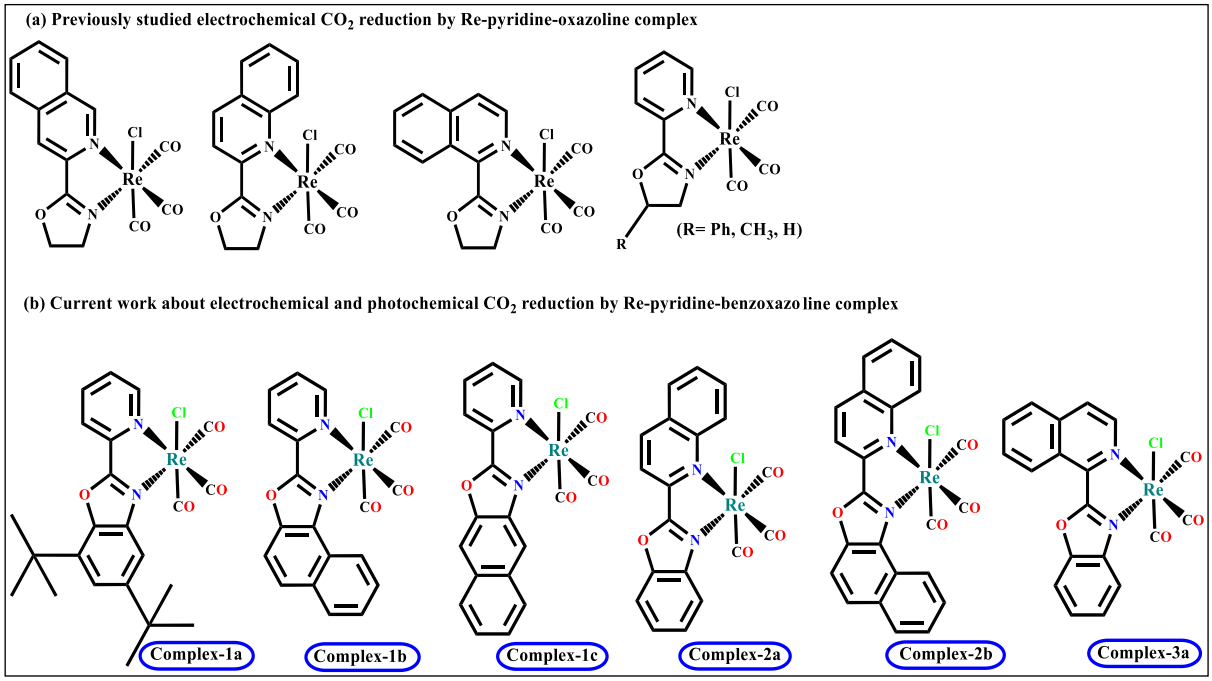

Figure III.1 Structure of the catalysts.

III.2. Result and Discussion

III.2.1 Materials:

Toluene, hexane, ethyl acetate, methanol, dichloromethane, N,*N*-dimethylformamide, and triethylamine were acquired from Mark and subjected to drying prior to use. 2-Picolylamine, 3,5-di-tert-butylcatechol, 2-picolinic acid, quinoline-2-carboxylic acid hydrochloride, 1-amino-2-naphthol hydrochloride, 3-amino-2-naphthol, Isoquinoline-1-carboxylic acid, 2,2,2-trifluoroethanol, 2,3-dihydro-1,3-dimethyl-2-phenylbenzimidazole(BIH), and pentacarbonylchlororhenium(I) were purchased from Sigma-Aldrich. Electrochemical-grade tetrabutylammonium hexafluorophosphate ($[^{n}Bu_4N]PF_6$) with a minimum purity of 99.0% was also obtained from Sigma-Aldrich.

III.2.2 Synthesis:

Synthesis of 5,7-di-tert-butyl-2-(pyridin-2-yl)benzo[d]oxazole (1)

A solution of 2-picolylamine (1.00 mmol, 108 mg) and 3,5-di-tert-butylcatechol (1.00 mmol, 222 mg) in dichloromethane (30 mL) was stirred for 72 hours, resulting in the formation of a yellow solution. The mixture was then purified by column chromatography on neutral alumina using a hexane:ethyl acetate (20:1) eluent, affording the desired compound as a yellow oily product.

^{1}H NMR (300 MHz, $CDCl_3$) δ 8.83 (d, *J* = 4.5 Hz, 1H), 8.29 (d, *J* = 7.8 Hz, 1H), 7.91 – 7.85 (m, 1H), 7.69 (d, *J* = 1.8 Hz, 1H), 7.45 – 7.40 (m, 1H), 7.36 (d, *J* = 1.8 Hz, 1H), 1.57 (s, 9H), 1.40 (s, 9H). ^{13}C NMR (75 MHz, $CDCl_3$) δ 163.4, 150.6, 148.2, 147.5, 146.6, 142.3, 137.0, 134.3, 125.3, 123.3, 122.8, 122.3, 120.6, 114.9, 35.2, 34.7, 32.0, 30.3 ppm.

Synthesis of 2-(pyridin-2-yl)naphtho[1,2-d]oxazole (2) :

The ligand was synthesized following a previously published method[57]. A mixture of pyridine-2-carboxylic acid and 1-amino-2-naphthol hydrochloride was heated in polyphosphoric acid at around 170 °C for 6 hours. The resulting mixture was dissolved in water, neutralized, and extracted into dichloromethane. The crude product was then purified using column chromatography. The structure of the ligand was verified by spectroscopic analysis. ^{1}H NMR (400 MHz, $CDCl_3$) δ 8.85 (d, *J* = 4.8 Hz, 1H), 8.65 (d, *J* = 8.4 Hz, 1H), 8.44 (d, *J* = 8.0 Hz, 1H), 7.98 (d, *J* = 8.0 Hz, 1H), 7.94 – 7.89 (m, 1H), 7.86 (d, *J* = 9.2 Hz, 1H), 7.80 (d, *J* = 8.8 Hz, 2H), 7.69 (t, *J* = 7.6 Hz, 1H), 7.57 (t, *J* = 7.6 Hz, 1H), 7.47 – 7.43 (m, 1H). ^{13}C NMR (101

MHz, $CDCl_3$) δ 160.8, 150.5, 148.7, 146.4, 137.3, 131.5, 131.1, 128.8, 127.4, 127.3, 126.9, 125.8, 125.3, 123.3, 122.5, 111.3 ppm.

Synthesis 2-(pyridin-2-yl)naphtho[2,3-d]oxazole (3) :

This ligand was synthesized according to the aforementioned process. ^{1}H NMR (300 MHz, $CDCl_3$) δ 8.86 (d, *J* = 4.2 Hz, 1H), 8.44 (d, *J* = 7.8 Hz, 1H), 8.27 (s, 1H), 8.03 (s, 1H), 8.03 – 7.86 (m, 3H), 7.51 – 7.46 (m, 3H). ^{13}C NMR (75 MHz, $CDCl_3$) δ 163.3, 150.4, 145.9, 141.6, 139.3, 137.3, 132.3, 131.7, 128.7, 128.1, 126.1, 125.9, 124.9, 124.2, 118.3, 114.1, 107.1 ppm.

Synthesis 2-(quinolin-2-yl)benzo[d]oxazole(4):

This ligand was synthesized according to the aforementioned process (*vide supra*). ^{1}H NMR (400 MHz, $CDCl_3$) δ 8.49 (d, *J* = 8.4 Hz, 1H), 8.37 (d, *J* = 8.4 Hz, 2H), 7.90 (t, *J* = 8.0 Hz, 2H), 7.82 (t, *J* = 7.6 Hz, 1H), 7.75 (d, *J* = 7.6 Hz, 1H), 7.65 (t, *J* = 7.6 Hz, 1H), 7.48 – 7.41 (m, 2H). ^{13}C NMR (75 MHz, $CDCl_3$) δ 137.5, 130.6, 130.4, 128.3, 127.8, 126.4, 125.2, 120.9, 120.4, 111.6 ppm.

Synthesis of 2-(quinolin-2-yl)naphtho[1,2-d]oxazole (5) :

The synthesis of this ligand followed the procedure employed for the preparation of l**igand 3**. ^{1}H NMR (400 MHz, $CDCl_3$) δ 8.71 (d, *J* = 8.2 Hz, 1H), 8.62 (d, *J* = 8.5 Hz, 1H), 8.47 – 8.39 (m, 2H), 8.03 (d, *J* = 8.3 Hz, 1H), 7.98 – 7.88 (m, 3H), 7.84 (d, *J* = 6.9 Hz, 1H), 7.74 (d, *J* = 7.0 Hz, 1H), 7.65 (dt, *J* = 21.9, 7.4 Hz, 2H). ^{13}C NMR (101 MHz, $CDCl_3$) δ 167.9, 152.2, 149.0, 139.4, 137.7, 136.0, 131.5, 128.8, 128.1, 127.8, 127.7, 127.4, 126.9, 125.9, 124.9, 122.5, 120.4, 114.2, 111.5 ppm.

Synthesis of 2-(isoquinolin-1-yl)benzo[d]oxazole (6):

The synthesis of this ligand followed the procedure employed for the preparation of ligand 3. ^{1}H NMR (300 MHz, $CDCl_3$) δ 9.74 – 9.71 (m, 1H), 8.79 (d, *J* = 5.5 Hz, 1H), 7.96 – 7.93 (m, 2H), 7.86 (d, *J* = 5.4 Hz, 1H), 7.82 – 7.75 (m, 3H), 7.48 – 7.44 (m, 2H). ^{13}C NMR (75 MHz, $CDCl_3$) δ 142.3, 137.2, 130.8, 129.2, 127.5, 127.4, 127.3, 126.5, 125.0, 123.7, 121.0, 111.5 ppm.

Synthesis of Complex-1a:

A mixture of 30.8 mg of the **ligand-1** and 20.0 mg of pentacarbonylchlororhenium(I) in toluene (30 mL) was subjected to reflux conditions for 4 hours. The resulting reaction mixture was purified by column chromatography on neutral alumina using a hexane:ethyl acetate (10:1) gradient. The second red eluate was collected and characterized as the desired complex. ^{1}H NMR (400 MHz, $CDCl_3$) δ 9.11 (d, *J* = 5.2 Hz, 1H), 8.30 (d, *J* = 7.6 Hz, 1H), 8.20 – 8.16 (m, 1H), 7.85 (d, *J* = 2.0 Hz, 1H), 7.70 – 7.66 (m, 1H), 7.57 (d, *J* = 1.6 Hz, 1H), 1.55 (s, 9H), 1.44 (s, 9H). ^{13}C NMR (101 MHz, $CDCl_3$) δ 196.1, 187.6, 164.7, 154.5, 151.7, 147.5, 144.5, 139.5, 138.9, 135.6, 128.7, 124.4, 124.1, 113.9, 77.4, 77.1, 76.8, 35.6, 34.8, 31.6, 30.2 ppm. Elem. Anal. Calcd. for $ReC_{23}H_{24}ClN_2O_4$: C, 44.98; H, 3.94 and N, 4.56. Found: C, 44.82; H, 3.96; and N, 4.73. ESI-MS (CH_3CN): m/z 620.1533 $[M\text{-}Cl^- + CH_3CN]^+$.

Synthesis of complex-1b:

Complex-1b was prepared using a synthetic methodology analogous to that employed for **complex 1a**, substituting **ligand 1** with **ligand 2**. ^{1}H NMR (300 MHz, $CDCl_3$) δ 9.74 – 9.71 (m, 1H), 8.79 (d, *J* = 5.5 Hz, 1H), 7.96 – 7.93 (m, 2H), 7.86 (d, *J* = 5.4 Hz, 1H), 7.82 – 7.75 (m, 3H), 7.48 – 7.44 (m, 2H). ^{13}C NMR (75 MHz, $CDCl_3$) δ 142.2, 137.2, 130.8, 129.2, 127.5, 127.4, 127.3, 126.5, 125.0, 123.7, 121.0, 111.5, 77.5, 77.1, 76.7 ppm. Elem. Anal. Calcd. for $ReC_{19}H_{10}ClN_2O_4$: C, 41.35; H, 1.83 and N, 5.08. Found: C, 41.25; H, 1.76; and N, 5.33. ESI-MS (CH_3CN): m/z 558.0342 $[M\text{-}Cl^- + CH_3CN]^+$.

Synthesis of Complex-1c:

Complex-1c was synthesized using a method similar to that of **complex-1a**, employing **ligand 3** instead of **ligand 1**. ^{1}H NMR (300 MHz, DMSO) δ 9.01 (d, *J* = 5.2 Hz, 1H), 8.51 – 8.48 (m, 2H), 8.33 – 8.27 (m, 1H), 8.18 – 8.14 (m, 2H), 7.82 – 7.77 (m, 1H), 7.54 – 7.50 (m, 2H), 7.09 – 7.07 (m, 2H). ^{13}C NMR (75 MHz, DMSO) δ 198.7, 188.7, 173.0, 154.7, 148.3, 143.1, 141.1, 137.2, 136.8, 132.5, 131.6, 128.9, 128.4, 128.2, 127.4, 126.6, 126.4, 125.3, 116.2, 109.3, 40.3, 40.0, 39.8, 39.5, 39.2, 38.9, 38.6 ppm. Elem. Anal. Calcd. for $ReC_{19}H_{10}ClN_2O_4$: C, 41.35; H, 1.83 and N, 5.08. Found: C, 41.17; H, 1.78; and N, 5.31. ESI-MS (CH_3CN): m/z 558.0433 $[M\text{-}Cl^- + CH_3CN]^+$.

Synthesis of complex-2a:

Complex-2a was synthesized using a method similar to that of **complex 1a**, employing **ligand 4** instead of **ligand 1**. ^{1}H NMR (400 MHz, DMSO) δ 9.13 (d, *J* = 8.4 Hz, 1H), 8.74 (d, *J* = 8.8 Hz, 1H), 8.66 (d, *J* = 8.4 Hz, 1H), 8.40 (d, *J* = 8.0 Hz, 1H), 8.28 (t, *J* = 8.0 Hz, 1H), 8.04 – 8.00 (m, 2H), 7.85 – 7.83 (m, 2H), 7.57 – 7.48 (m, 1H). ^{13}C NMR (101 MHz, DMSO) δ 195.1, 182.6, 161.1, 146.5, 145.8, 142.6, 138.3, 134.0, 130.5, 130.4, 130.0, 129.3, 128.3, 125.3, 120.7, 118.6, 113.1, 40.1, 39.9, 39.7, 39.5, 39.3, 39.1, 38.9 ppm. Elem. Anal. Calcd. for $ReC_{19}H_{10}ClN_2O_4$: C, 41.35; H, 1.83 and N, 5.08. Found: C, 41.31; H, 1.69; and N, 5.07. ESI-MS (CH_3CN): m/z 558.0464 [M-Cl^- + CH_3CN]$^+$.

Synthesis of complex-2b:

Complex-2b was synthesized using a method similar to that of **complex-1a**, employing **ligand 5** instead of **ligand 1**. ^{1}H NMR (300 MHz, $CDCl_3$) δ 9.24 (d, *J* = 8.4 Hz, 1H), 8.98 (d, *J* = 9.0 Hz, 1H), 8.64 (d, *J* = 8.7 Hz, 1H), 8.40 (d, *J* = 8.7 Hz, 1H), 8.12 – 8.08 (m, 2H), 8.03 – 8.02 (m, 1H), 7.84 – 7.84 (m, 1H), 7.73 – 7.69 (m, 2H), 7.53 (dd, *J* = 5.7, 3.3 Hz, 2H). ^{13}C NMR (101 MHz, $CDCl_3$) δ 195.0, 190.2, 171.3, 158.8, 150.1, 146.1, 144.1, 137.2, 135.2, 133.8, 128.2, 126.6, 125.4, 125.3, 124.7, 123.7, 122.7, 120.3, 118.2, 113.9, 112.0, 109.3, 40.1, 39.9, 39.7, 39.5, 39.3, 39.1, 38.8 ppm. Elem. Anal. Calcd. for $ReC_{23}H_{12}ClN_2O_4$: C, 45.80; H, 1.88 and N, 4.68. Found: C, 45.89; H, 2.01; and N, 4.65. ESI-MS (CH_3CN): m/z 607.6189 [M-Cl^- + CH_3CN]$^+$.

Synthesis of complex-3a:

Complex-3a was synthesized using a method similar to that of **complex 1**, employing **ligand 6** instead of **ligand 1**. ^{1}H NMR (400 MHz, DMSO) δ 9.33 (d, *J* = 8.0 Hz, 1H), 9.04 (d, *J* = 6.0 Hz, 1H), 8.43 (d, *J* = 6.4 Hz, 1H), 8.41 – 8.38 (m, 1H), 8.28 (d, *J* = 8.0 Hz, 1H), 8.19 – 8.13 (m, 2H), 7.98 – 7.96 (m, 1H), 7.89 – 7.83 (m, 2H). ^{13}C NMR (101 MHz, DMSO) δ 197.1, 187.2, 167.6, 150.4, 146.2, 143.2, 137.3, 137.0, 133.6, 131.8, 129.3, 128.3, 128.0, 128.0, 126.7, 124.8, 118.5, 113.3, 40.1, 39.9, 39.7, 39.5, 39.3, 39.1, 38.8. Elem. Anal. Calcd. For $ReC_{19}H_{10}ClN_2O_4$: C, 41.35; H, 1.83 and N, 5.08. Found: C, 41.27; H, 1.81; and N, 5.22. ESI-MS (CH_3CN): m/z 558.0424 [M-Cl^- + CH_3CN]$^+$.

III.2.3. NMR spectra

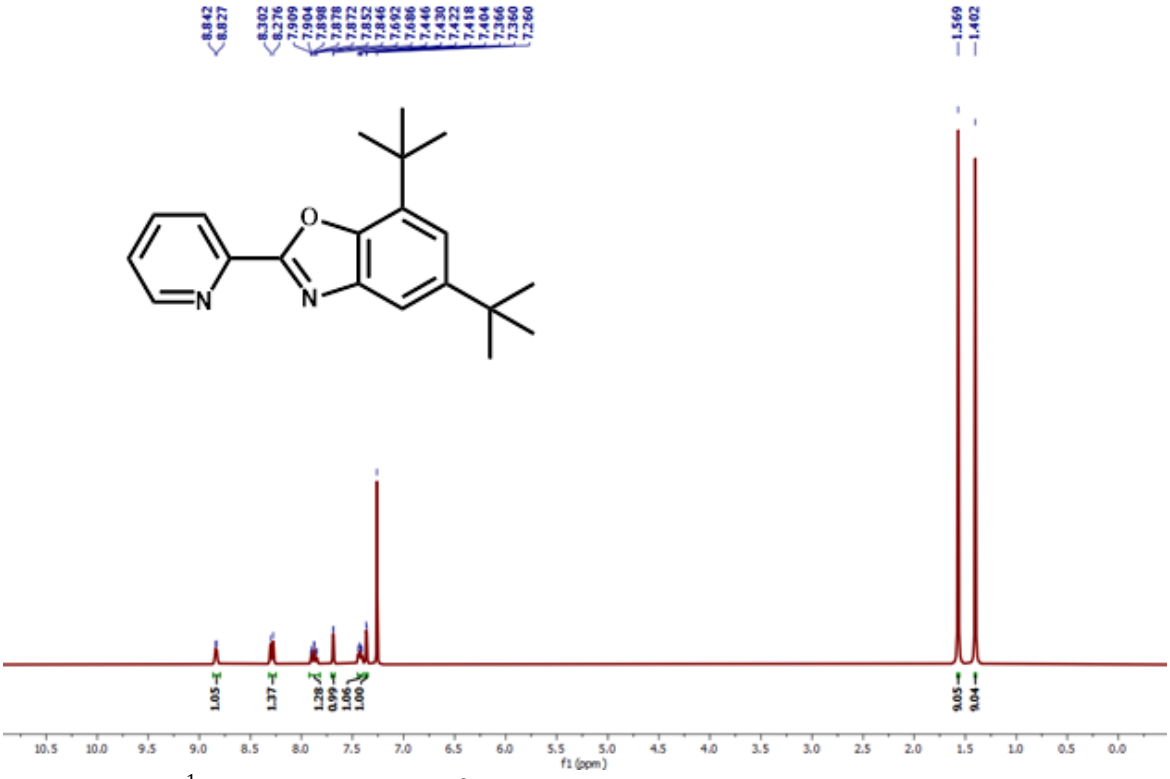

Figure III.2 ^{1}H NMR Spectrum of **Ligand-1a** in $CDCl_3$.

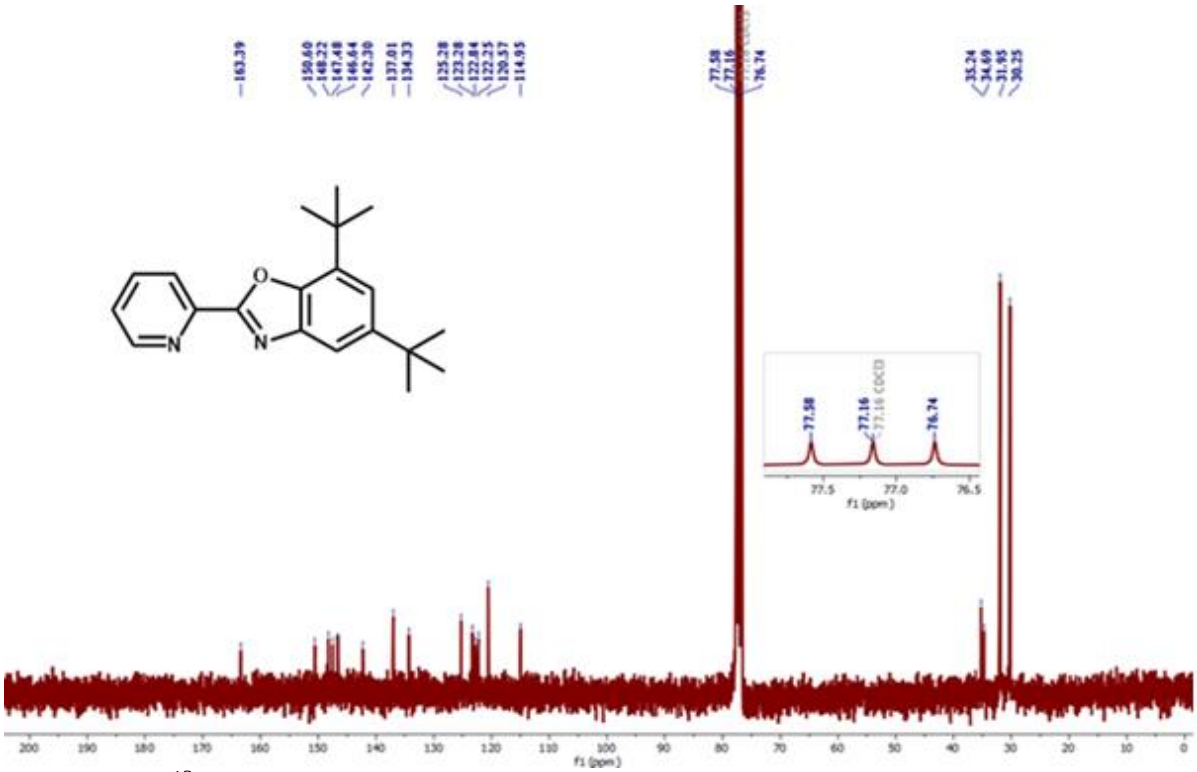

Figure III.3 ^{13}C NMR Spectrum of **Ligand-1a** in $CDCl_3$.

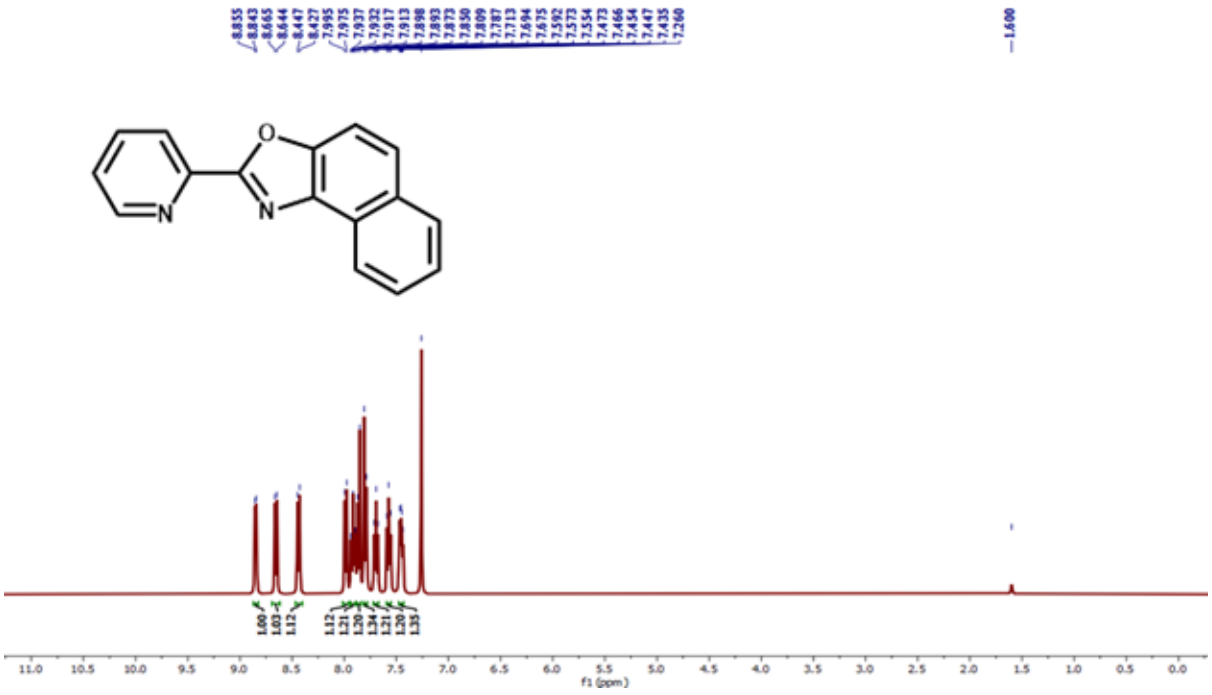

Figure III.4 ^{1}H NMR Spectrum of **Ligand-1b** in $CDCl_3$

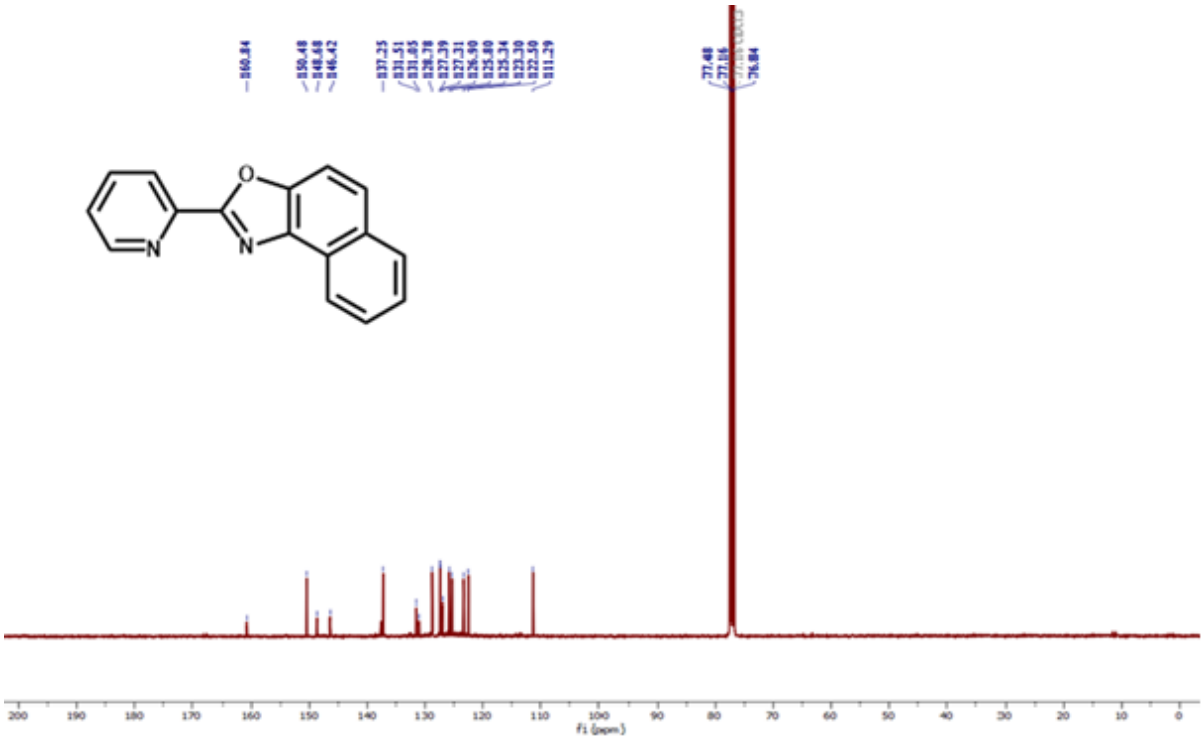

Figure III.5 ^{13}C NMR Spectrum of **Ligand-1b** in $CDCl_3$.

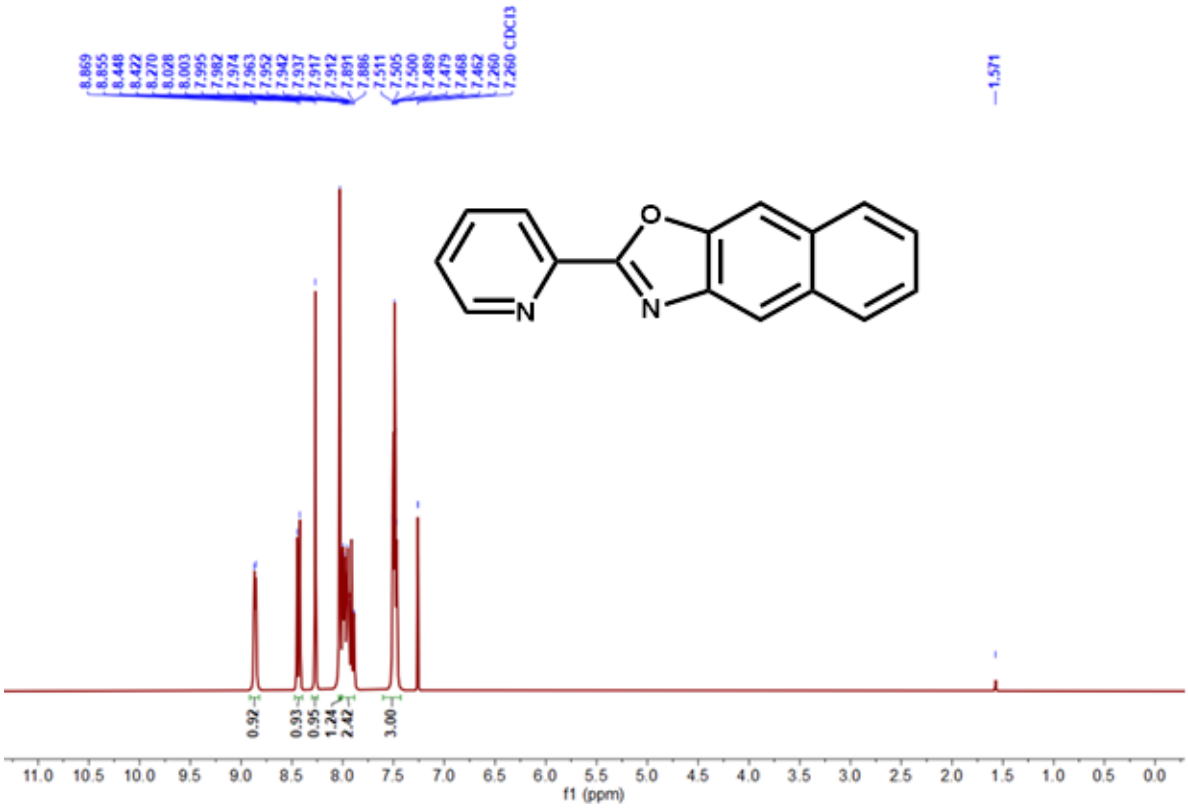

Figure III.6 ^{1}H NMR Spectrum of **Ligand-1c** in $CDCl_3$.

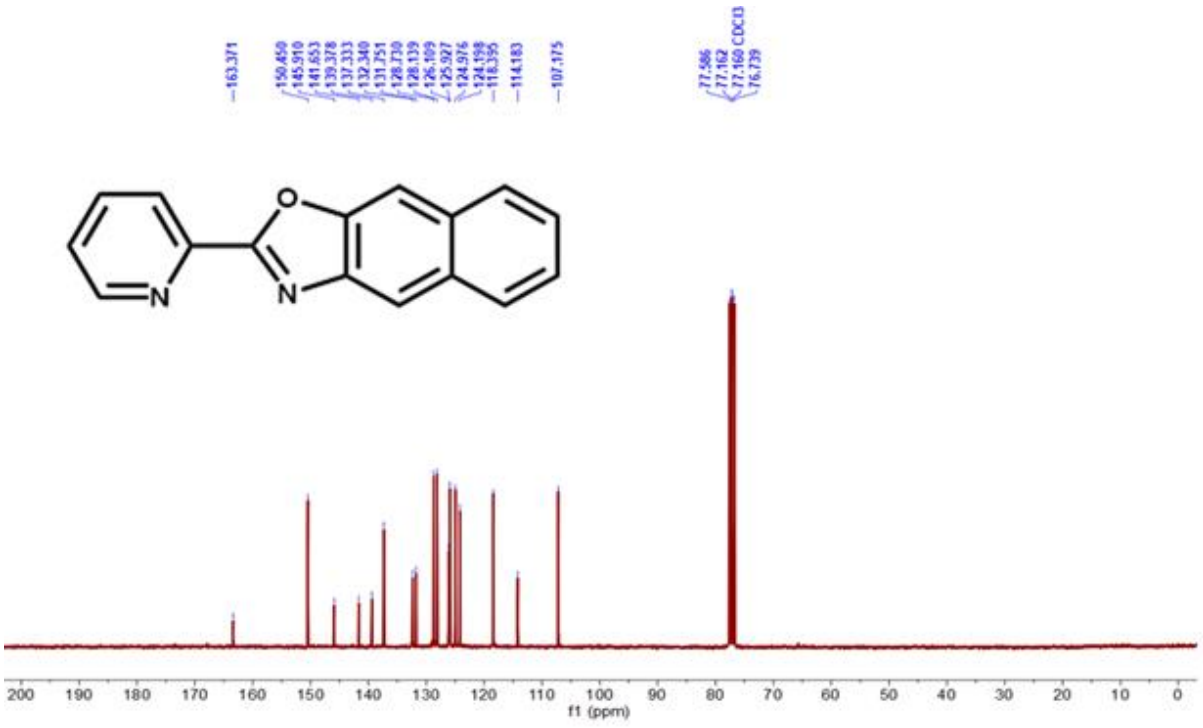

Figure III.7 ^{13}C NMR Spectrum of **Ligand-1c** in $CDCl_3$.

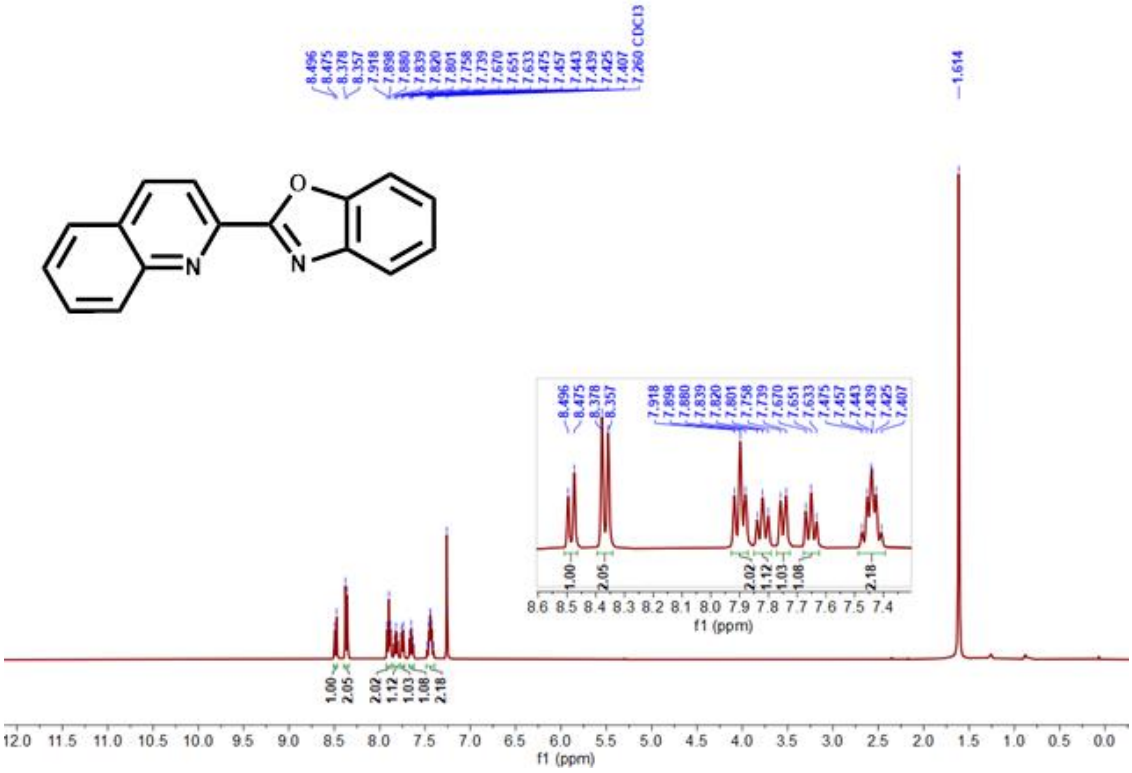

Figure III.8 ^{1}H NMR Spectrum of **Ligand-2a** in $CDCl_3$.

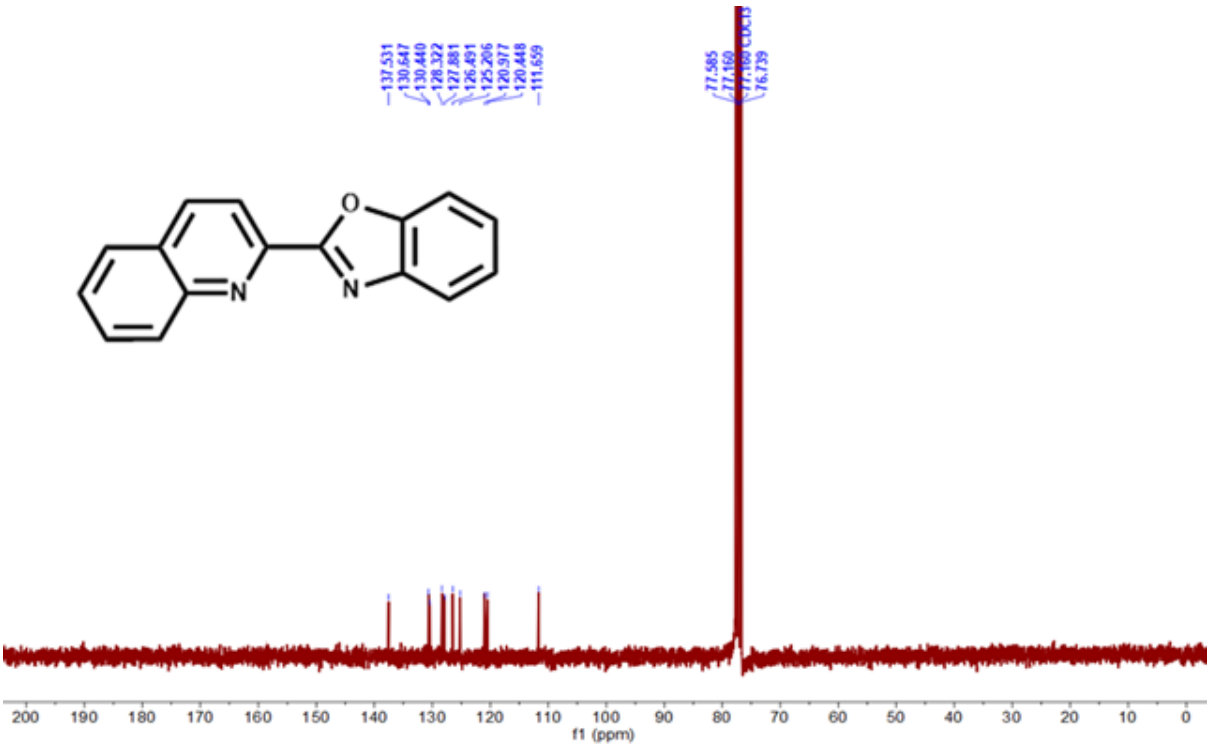

Figure III.9 ^{13}C NMR Spectrum of **Ligand-2a** in $CDCl_3$.

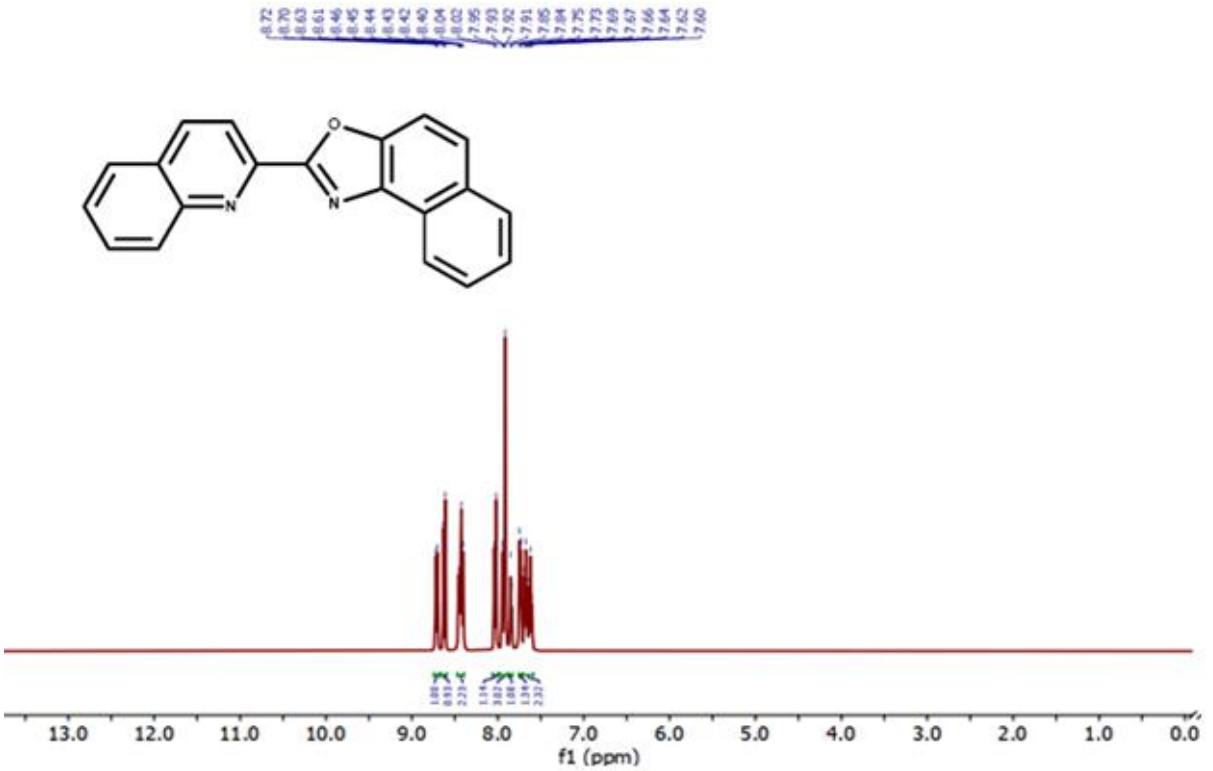

Figure III.10 ^{1}H NMR Spectrum of **Ligand-2b** in $CDCl_3$

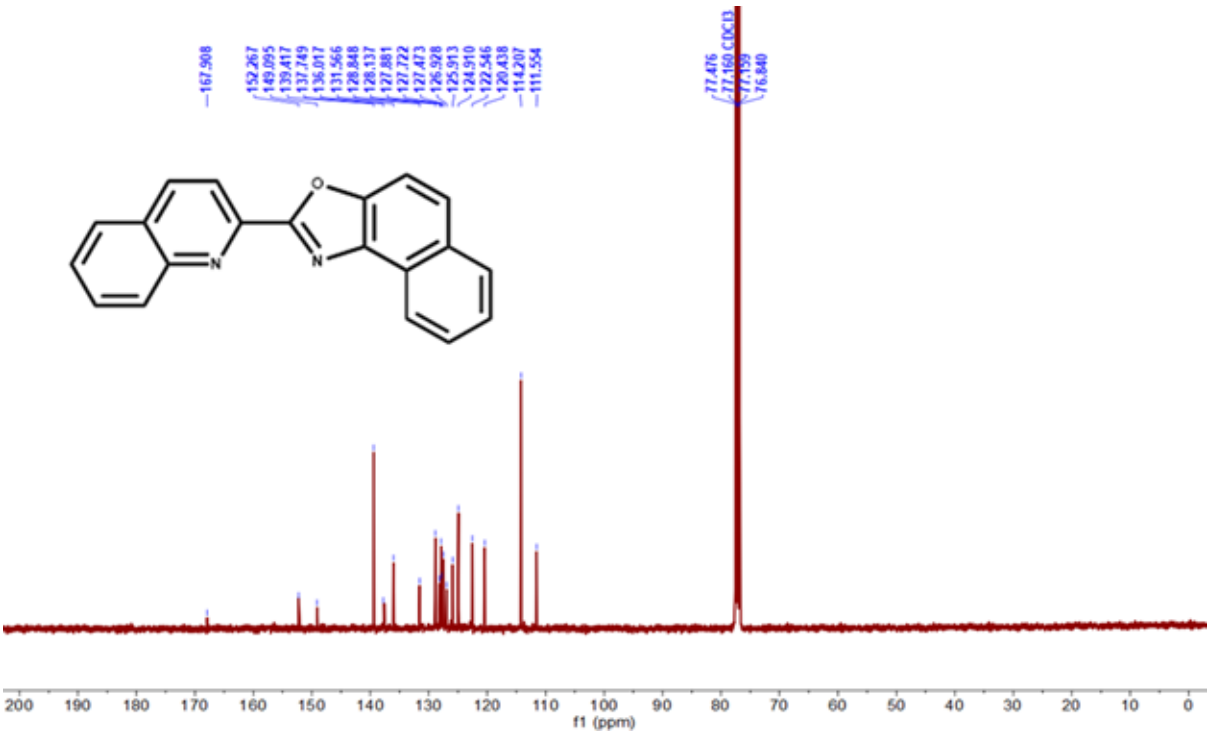

Figure III.11 ^{13}C NMR Spectrum of **Ligand-2b** in $CDCl_3$.

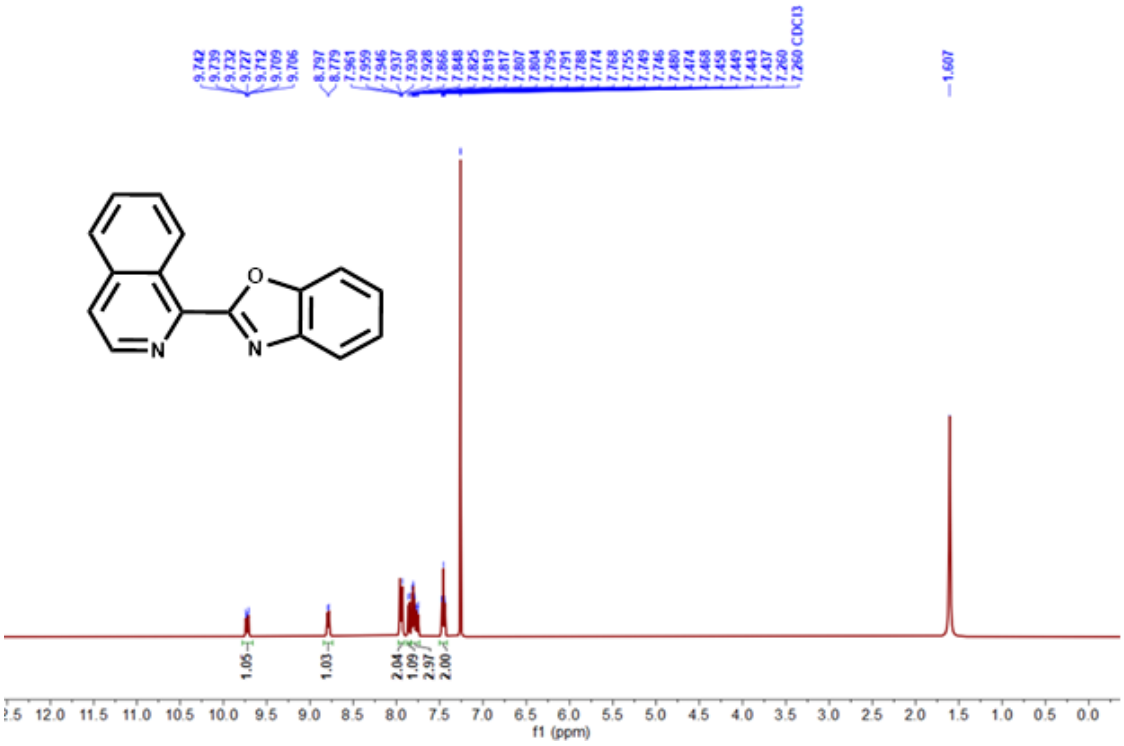

Figure III.12 ^{1}H NMR Spectrum of **Ligand-3a** in $CDCl_3$.

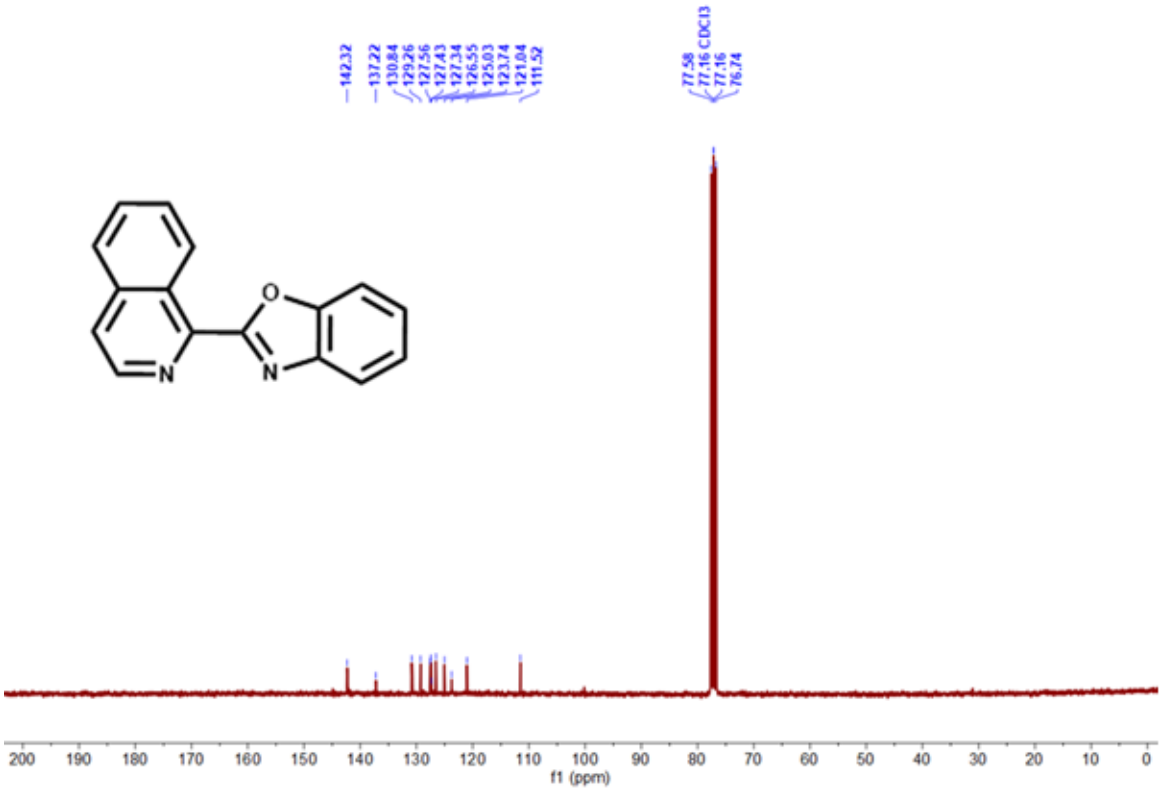

Figure III.13 ^{13}C NMR Spectrum of **Ligand-3a** in $CDCl_3$.

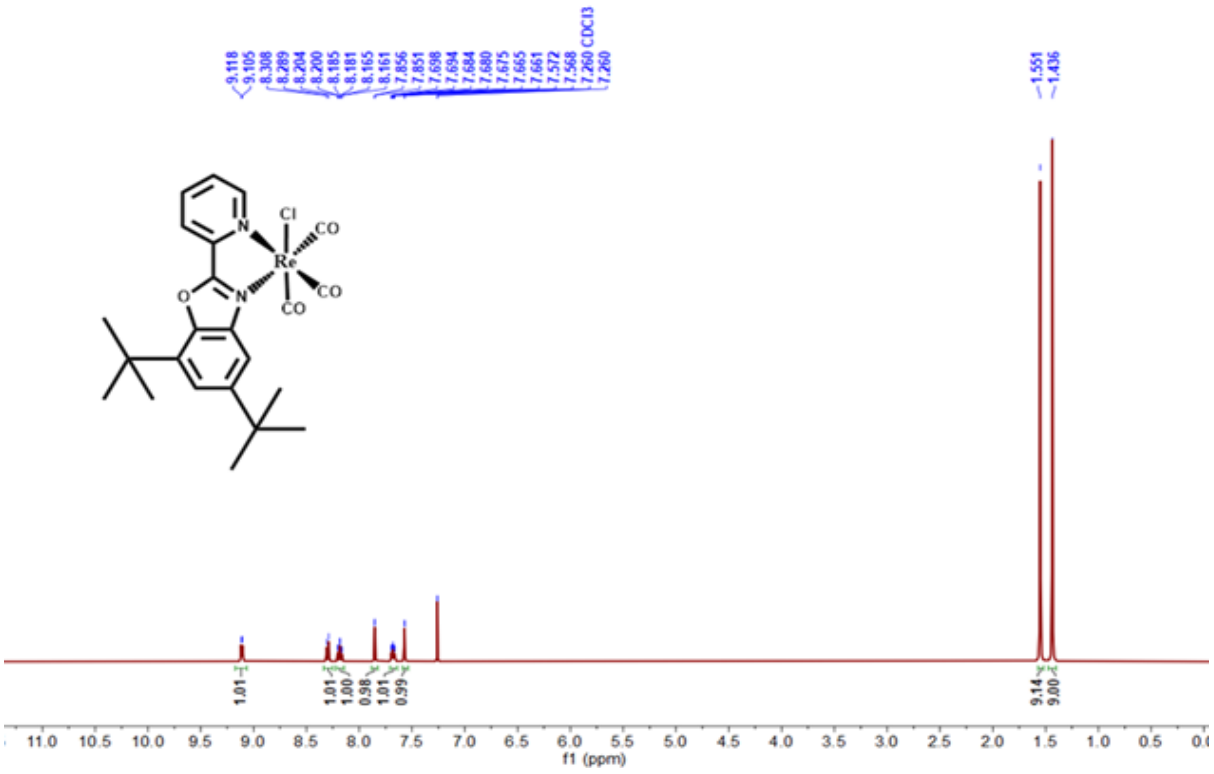

Figure III.14 ^{1}H NMR Spectrum of **Complex-1a** in $CDCl_3$.

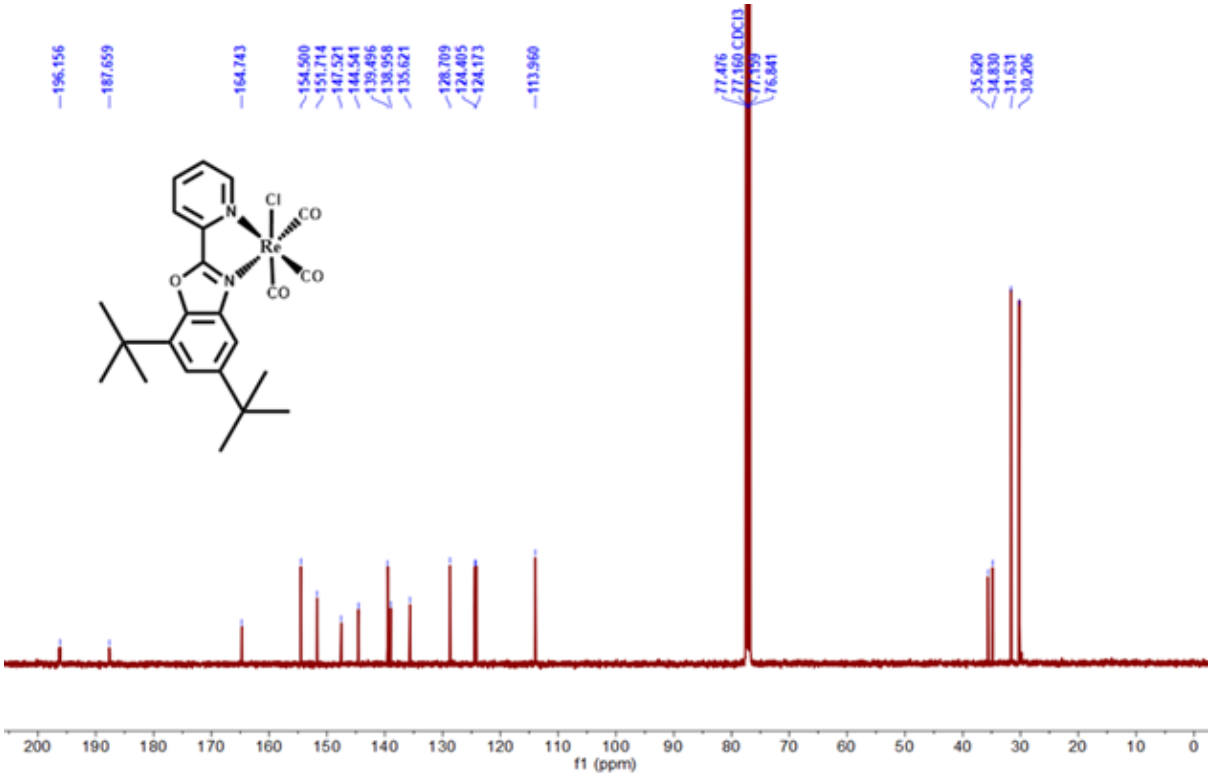

Figure III.15 ^{13}C NMR Spectrum of **Complex-1a** in $CDCl_3$.

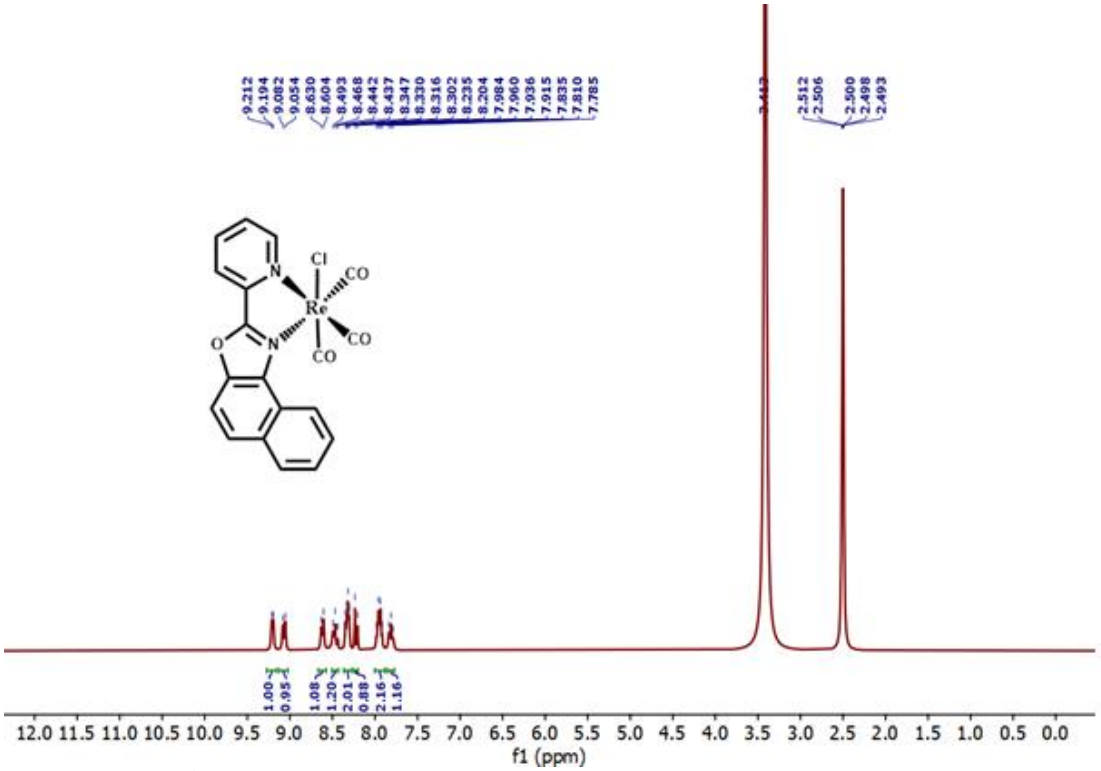

Figure III.16 ^{1}H NMR Spectrum of **Complex**-1b in DMSO-d_6.

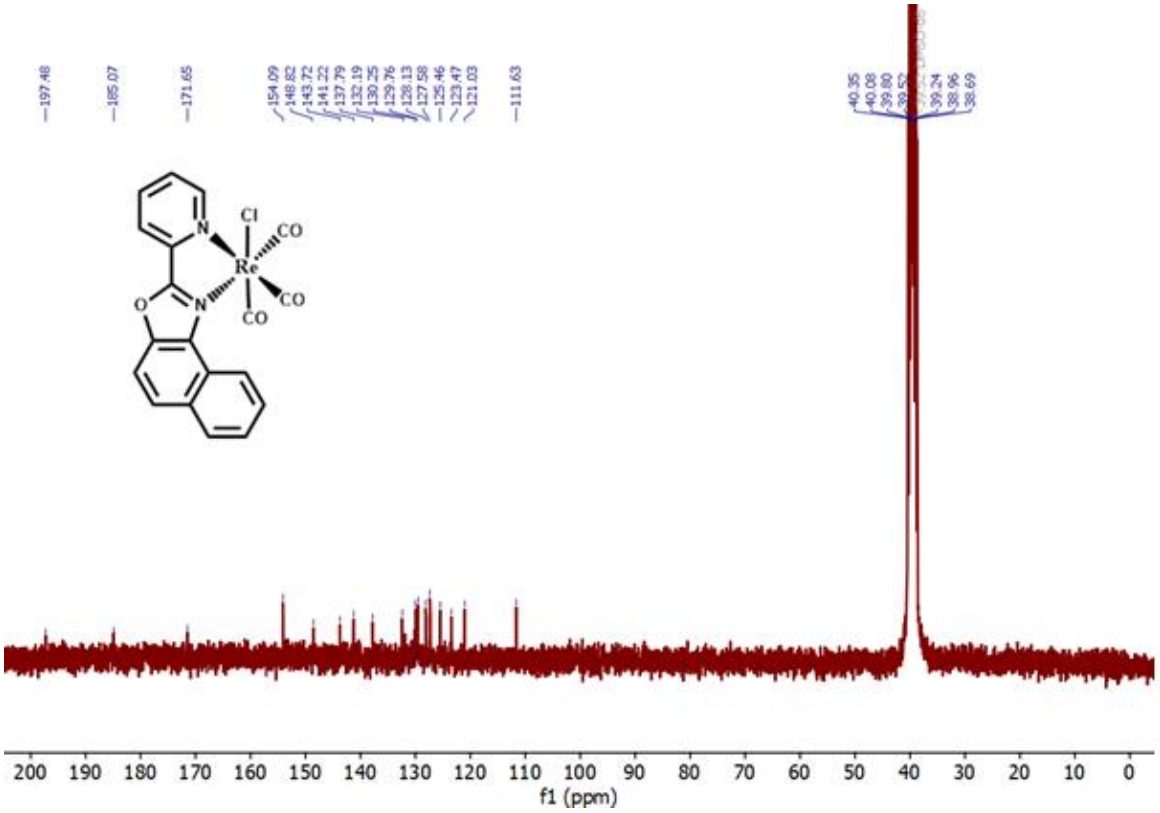

Figure III.17 ^{13}C NMR Spectrum of **Complex-1b** in DMSO-d_6.

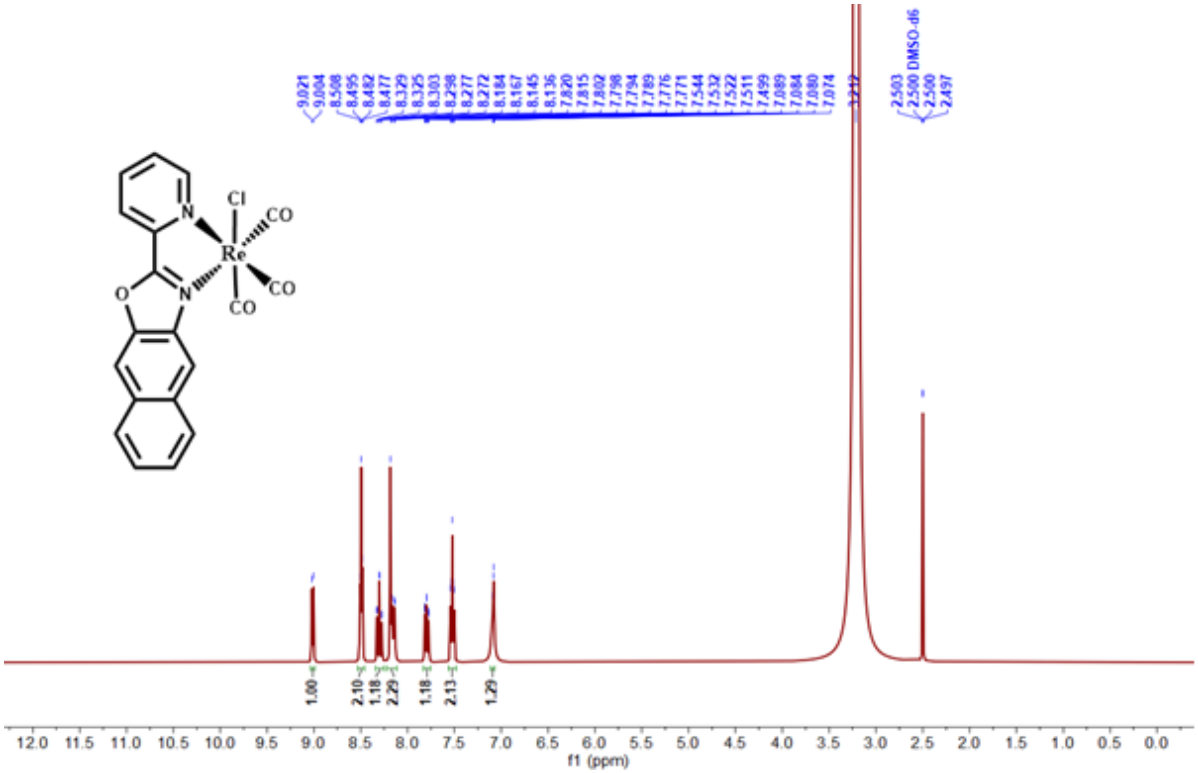

Figure III.18 1H NMR Spectrum of **Complex-1c** in DMSO-d6.

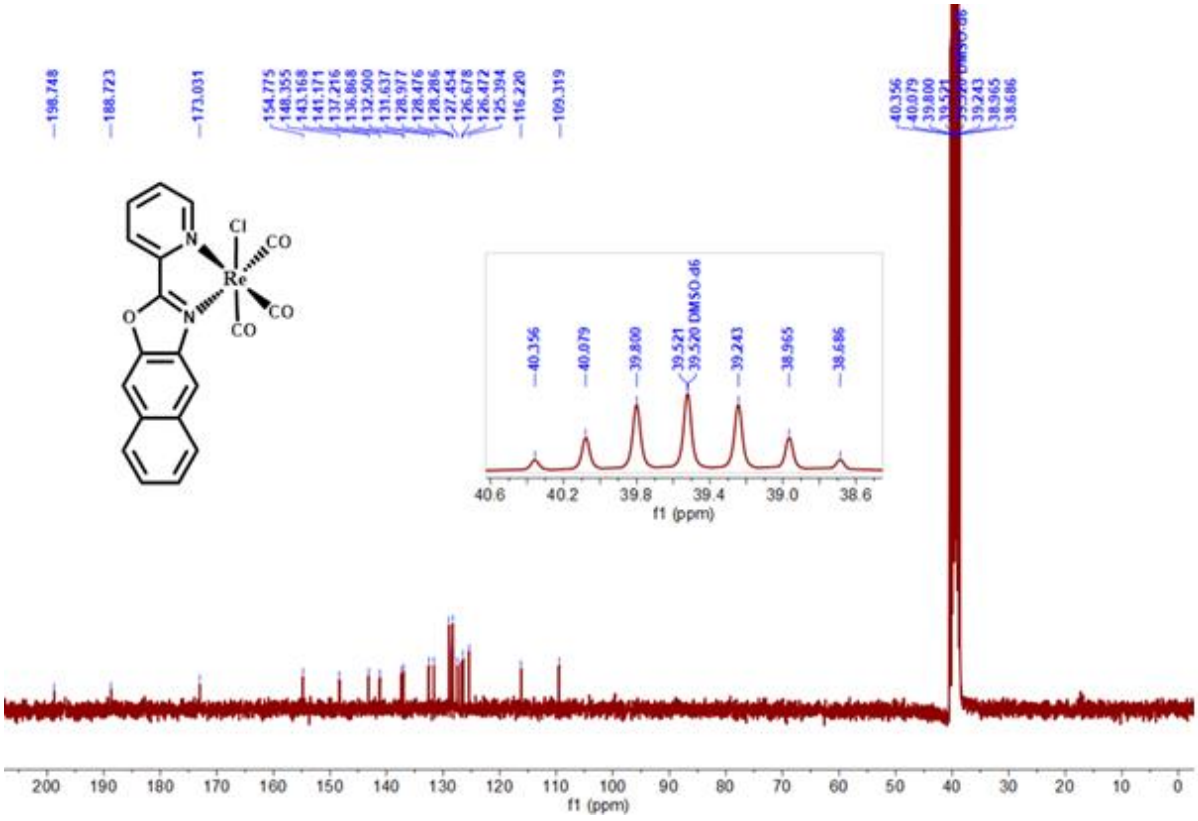

Figure III.19 ^{13}C NMR Spectrum of **Complex-1c** in DMSO-d_6.

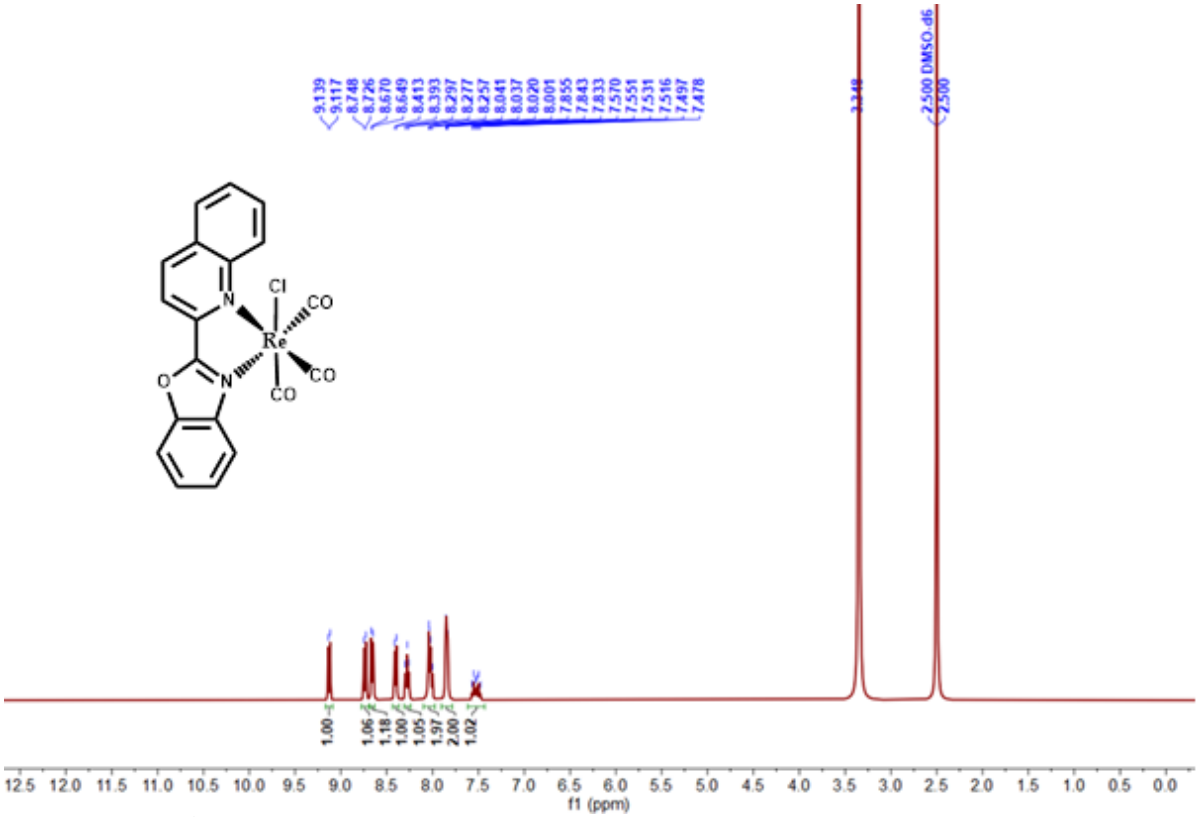

Figure III.20 ^{1}H NMR Spectrum of **Complex-2a** in DMSO-d_6

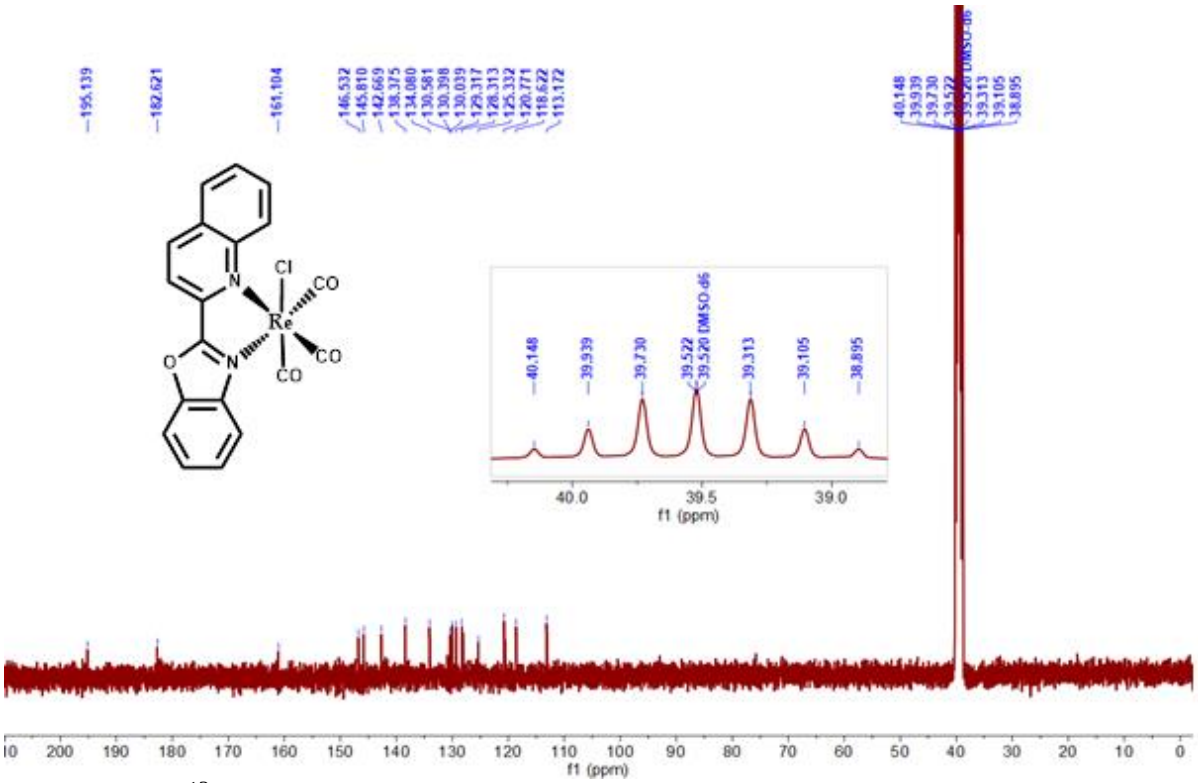

Figure III.21 ^{13}C NMR Spectrum of **Complex-2a** in DMSO-d_6.

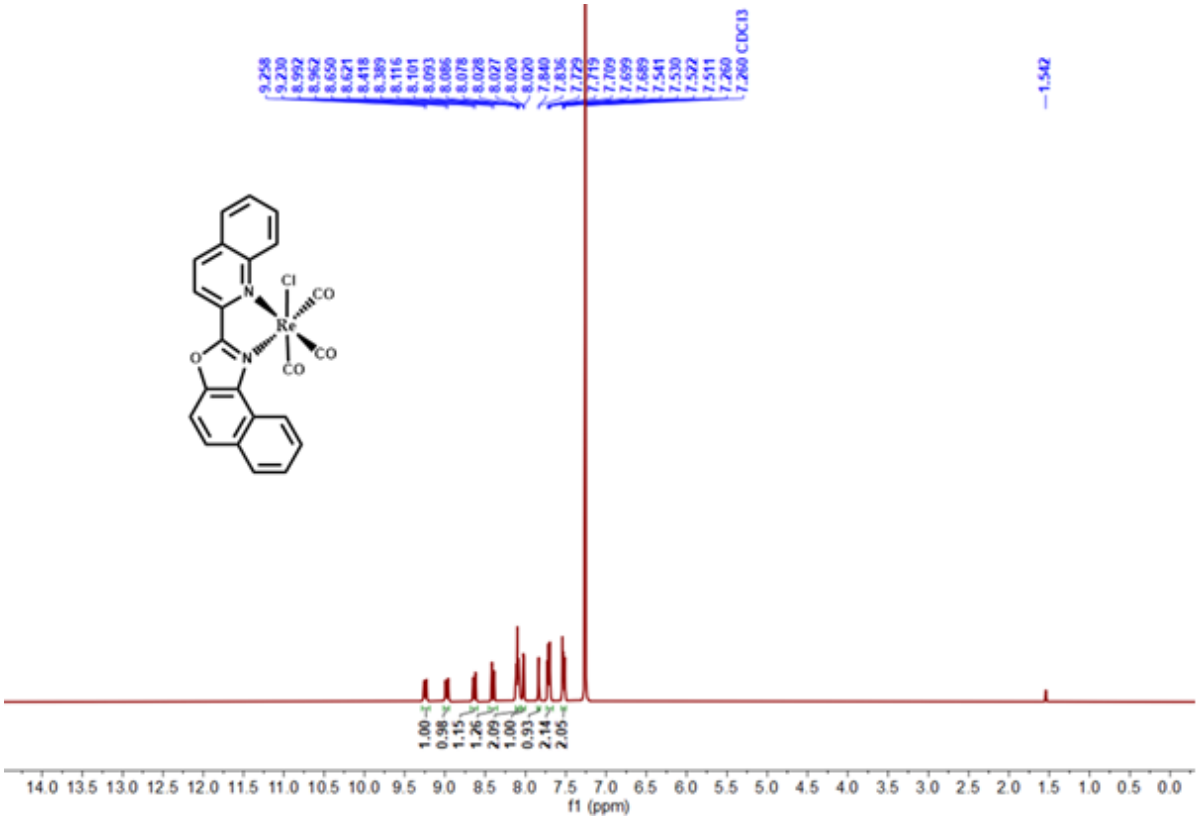

Figure III.22 ^{1}H NMR Spectrum of **Complex-2b** in DMSO-d_6

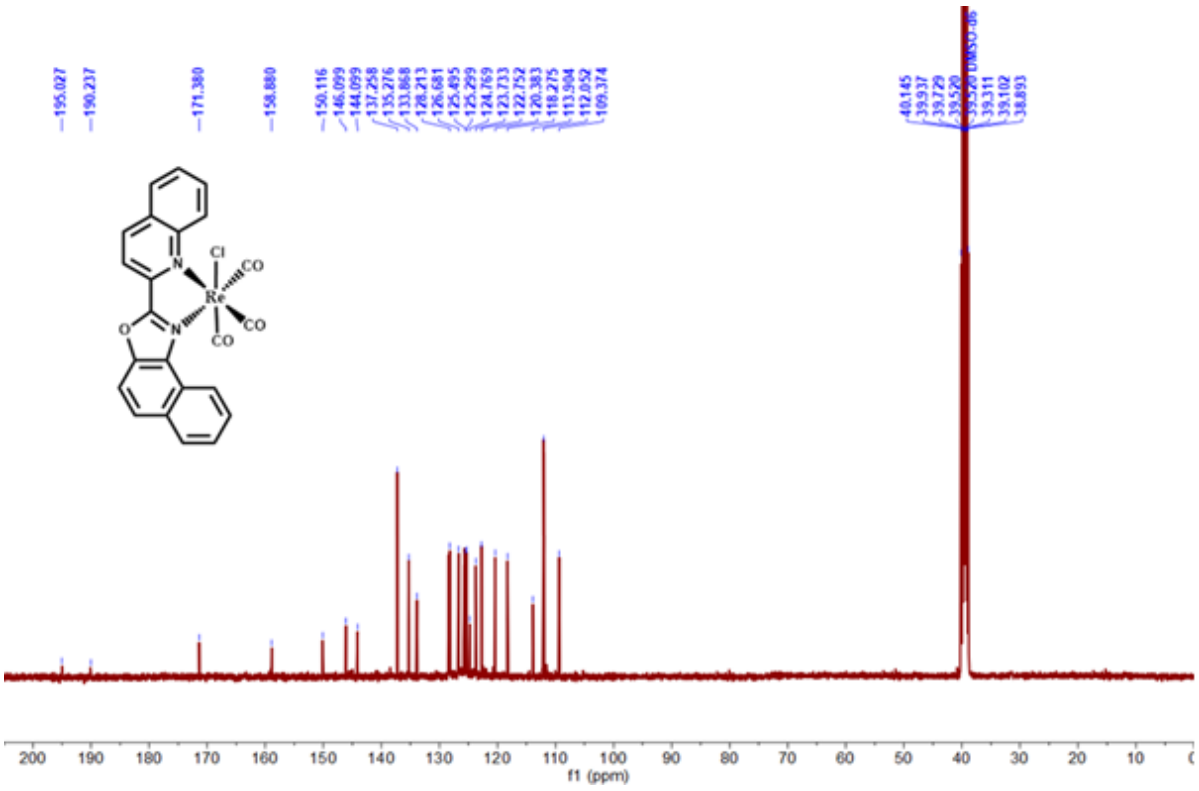

Figure III.23 ^{13}C NMR Spectrum of **Complex-2b** in DMSO-d_6.

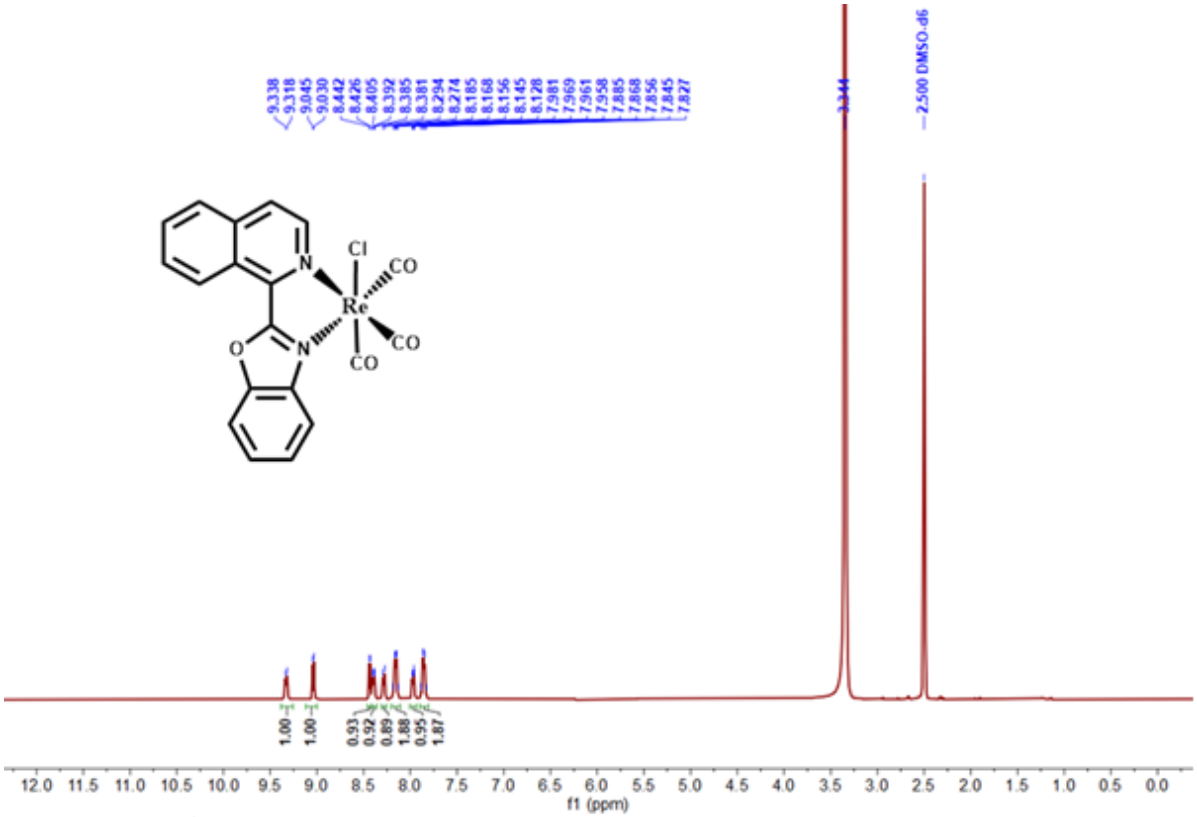

Figure III.24 ^{1}H NMR Spectrum of **Complex-3a** in DMSO-d_6

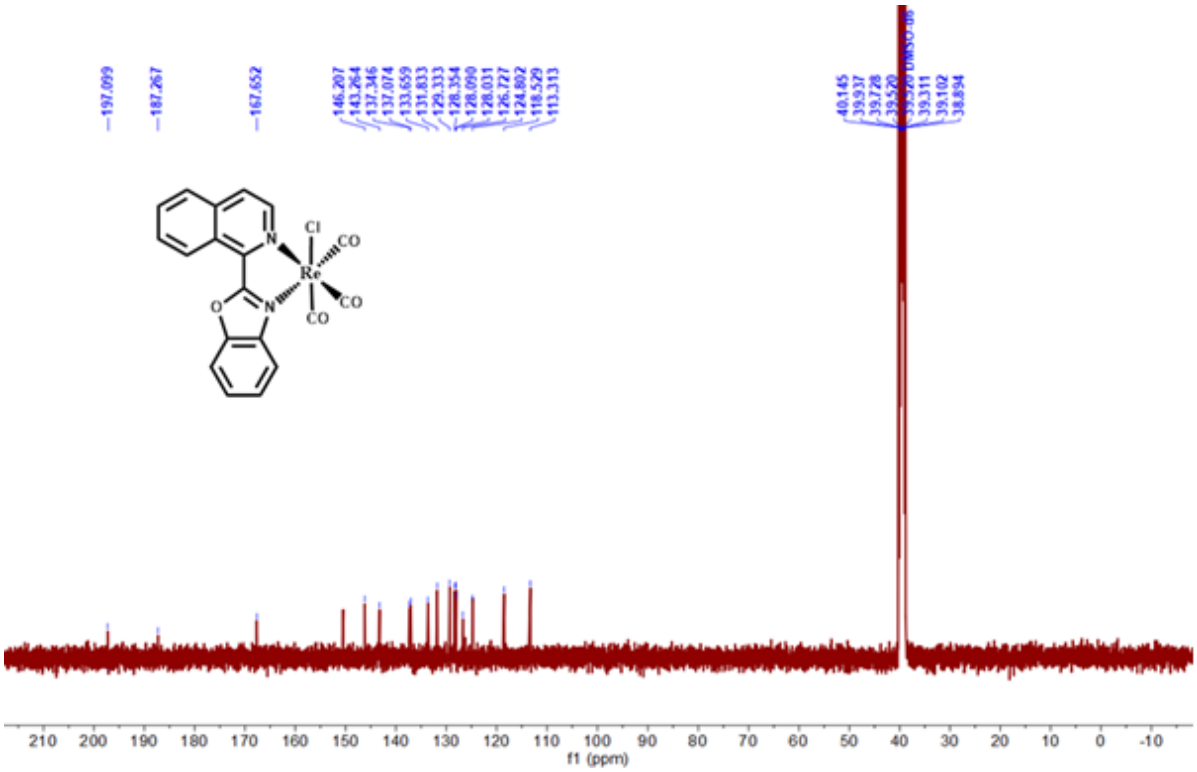

Figure III.25 ^{13}C NMR Spectrum of **Complex-3a** in DMSO-d_6.

III.2.4 Crystal Structures

A detailed comparison of the structures obtained through single-crystal X-ray diffraction offers valuable insights into the structural distinctions among the five complexes. All the crystals of complexes **1a**, **1b**, **1c**, **2b** and **3a** suitable for X-ray crystallography, were obtained by slow evaporation of a 1:1 (v/v) acetonitrile-toluene solution at room temperature. This structural analysis provides a clearer understanding of the coordination environments and geometrical differences within the complexes. Thermal ellipsoid representations of the five complexes are depicted in **Table III.1** to **Table III.5**. All the structures exhibit a distorted octahedral geometry, with three CO ligands coordinated in a facial configuration. The Re−$N_{diimine}$ bond lengths range from 2.158(4) to 2.254(6) Å, consistent with values observed in other rhenium−diimine complexes, including the recently reported rhenium complexes featuring pyridine−oxazoline ligands[56]. This similarity in bond distances further supports the structural consistency across these systems. The crystallographic data for complexes **1a**, **1b**, **1c**, **2b** and **3a** have been deposited in the Cambridge Crystallographic Data Centre (CCDC) as supplementary information under the CCDC numbers **2355624**, **2385160**, **2385164**, **2385178** and **2385175** respectively.

Table III.1. crystallographic data of the **complex 1a.**

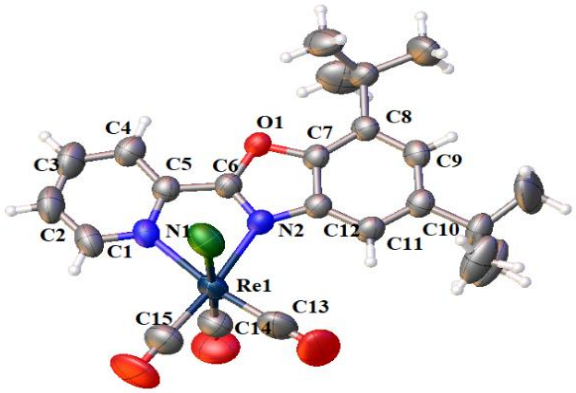

Complex-1a	
CCDC No. 2355624	
Formula	$C_{45.75}H_{48}Cl_2N_4O_8Re_2$
Molecular weight	1225.18
Crystal system	monoclinic
Space group	P 1 21/c 1
a/ Å	16.2390(11)
b/ Å	11.9393(8)
c/ Å	26.1931(17)
α/°	90
β/°	105.713(2)
γ/°	90
V/ $Å^3$	4888.6(6)
Z	4
Dcalcd /g cm^{-3}	1.665
Mu (mm-1)	5.110
T/K	273.15
R1 = 0.0316, wR2 = 0.0800	
GOF on F2	1.056

Bond length(Å)	
Re-N1	2.213(4)
Re-N2	2.170(4)
C6-O1	1.349(5)
O1-C7	1.395(5)
C6-N2	1.308(6)
N2-C12	1.399(6)

Table III.2. crystallographic data of the **complex 1b.**

<table>
<tr><td colspan="2" rowspan="14"> 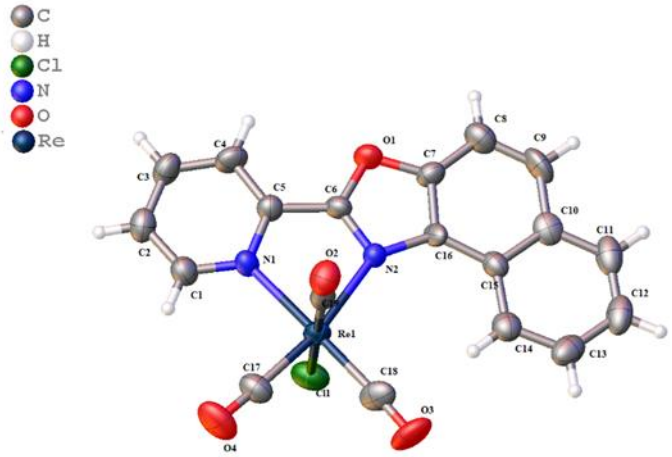
</td><td colspan="2">Complex-1b</td></tr>
<tr><td colspan="2">CCDC No. 2385160</td></tr>
<tr><td>Formula</td><td>C_{19} H_{10} Cl N_2 O_4 Re</td></tr>
<tr><td>Molecular weight</td><td>551.94</td></tr>
<tr><td>Crystal system</td><td>'triclinic'</td></tr>
<tr><td>Space group</td><td>P -1</td></tr>
<tr><td>a/ Å</td><td>6.977(5)</td></tr>
<tr><td>b/ Å</td><td>9.781(7)</td></tr>
<tr><td>c/ Å</td><td>13.71(1)</td></tr>
<tr><td>α/°</td><td>86.855(19)</td></tr>
<tr><td>β/°</td><td>75.528(18)</td></tr>
<tr><td>γ/°</td><td>76.140(18)</td></tr>
<tr><td>V/ $Å^3$</td><td>879.5(11)</td></tr>
<tr><td>Z</td><td>2</td></tr>
<tr><td>Dcalcd /g cm^{-3}</td><td>2.084</td></tr>
<tr><td colspan="2" rowspan="7">Bond length(Å)</td><td>Mu (mm-1)</td><td>7.088</td></tr>
<tr><td>T/K</td><td>273</td></tr>
<tr><td rowspan="2">R1 = 0.0488,
wR2 = 0.1139</td><td rowspan="2"></td></tr>
<tr><td></td></tr>
<tr><td>GOF on F2</td><td>1.074</td></tr>
<tr><td></td><td></td></tr>
<tr><td></td><td></td></tr>
<tr><td>Re-N1</td><td>2.211(6)</td><td colspan="2" rowspan="6"></td></tr>
<tr><td>Re-N2</td><td>2.254(6)</td></tr>
<tr><td>C6-O1</td><td>1.349(8)</td></tr>
<tr><td>O1-C7</td><td>1.377(9)</td></tr>
<tr><td>C6-N2</td><td>1.315(8)</td></tr>
<tr><td>N2-C16</td><td>1.411(9)</td></tr>
</table>

Table III.3. crystallographic data of the **complex 1c.**

<table>
<tr><td colspan="2" rowspan="14"> 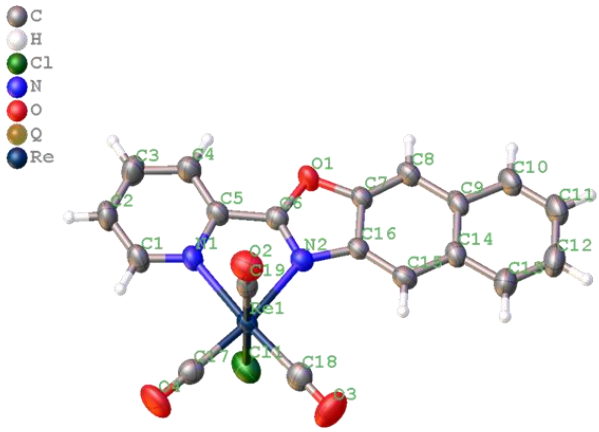
</td><td>Complex-1c</td></tr>
<tr><td>CCDC No. 2385164</td></tr>
<tr><td>Formula C_{19} H_{10} Cl N_2 O_4 Re, 1[CH_2Cl_2]</td></tr>
<tr><td>Molecular weight 636.87</td></tr>
<tr><td>Crystal system 'triclinic'</td></tr>
<tr><td>Space group P -1</td></tr>
<tr><td>a/ Å 9.4862(4)</td></tr>
<tr><td>b/ Å 9.5540(4)</td></tr>
<tr><td>c/ Å 13.1539(6)</td></tr>
<tr><td>α/° 96.340(1)</td></tr>
<tr><td>β/° 102.856(1)</td></tr>
<tr><td>γ/° 110.709(1)</td></tr>
<tr><td>V/ $Å^3$ 1063.54(8)</td></tr>
<tr><td>Z 2</td></tr>
<tr><td>Dcalcd /g cm^{-3} 1.989</td></tr>
<tr><td colspan="2">Bond length(Å)</td><td>Mu/mm^{-1} 6.119</td></tr>
<tr><td>Re-N1</td><td>2.205(3)</td><td>T/K 273</td></tr>
<tr><td>Re-N2</td><td>2.179(3)</td><td rowspan="2">R1 = 0.0252,
wR2 = 0.0550</td></tr>
<tr><td>C6-O1</td><td>1.352(5)</td></tr>
<tr><td>O1-C7</td><td>1.390(5)</td><td>GOF on F2 0.983</td></tr>
<tr><td>C6-N2</td><td>1.293(5)</td><td rowspan="2"></td></tr>
<tr><td>N2-C16</td><td>1.417(5)</td></tr>
</table>

Table III.4. crystallographic data of the **complex 2b.**

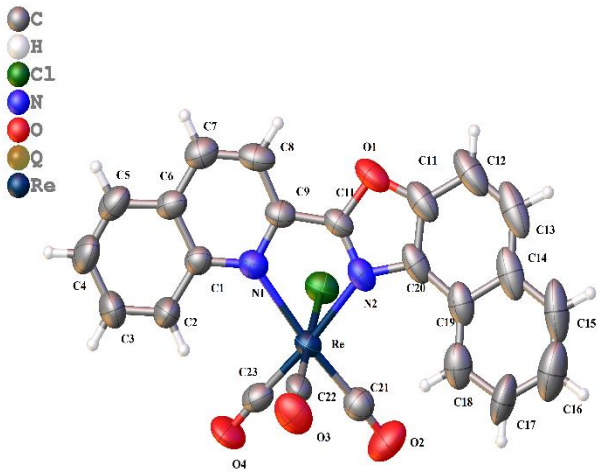

Complex-2b	
CCDC No. 2385178	
Formula	C23 H12 Cl N2 O4 Re
Molecular weight	602.00
Crystal system	'monoclinic'
Space group	P -1
a/ Å	7.2623(6)
b/ Å	9.6207(7)
c/ Å	14.8789(11)
α/°	99.464(2)
β/°	96.228(3)
γ/°	100.601(2)
V/ Å^3	997.54(13)
Z	2
Dcalcd /g cm^{-3}	2.004
Mu/mm^{-1}	6.259
T/K	273
R1 = 0.0400, wR2 = 0.1004	
GOF on F2	1.047

Bond length(Å)	
Re-N1	2.279(6)
Re-N2	2.209(6)
C10-O1	1.362(8)
O1-C11	1.376(12)
C10-N2	1.279(10)
N2-C20	1.396(10)

Table III.5. crystallographic data of the **complex 3a.**

<table>
<tr><td colspan="2" rowspan="13"> 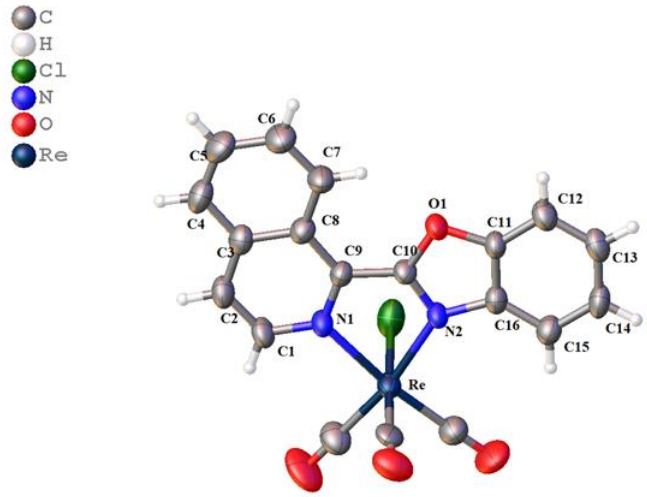
</td><td>Complex-3a</td></tr>
<tr><td>CCDC No. 2385175</td></tr>
<tr><td>Formula C19 H10 Cl N2 O4 Re</td></tr>
<tr><td>Molecular weight 551.94</td></tr>
<tr><td>Crystal system 'monoclinic'</td></tr>
<tr><td>Space group 'P 1 21/c 1'</td></tr>
<tr><td>a/ Å 8.3981(5)</td></tr>
<tr><td>b/ Å 16.0907(9)</td></tr>
<tr><td>c/ Å 13.2068(8)</td></tr>
<tr><td>α/° 90</td></tr>
<tr><td>β/° 93.733(2)</td></tr>
<tr><td>γ/° 90</td></tr>
<tr><td>V/ Å^3 1780.87(18)</td></tr>
<tr><td>Z 4</td></tr>
<tr><td colspan="2">Dcalcd /g cm^{-3} 2.059</td></tr>
<tr><td colspan="2">Bond length(Å)</td><td>Mu/mm^{-1} 7.002</td></tr>
<tr><td>Re-N1</td><td>2.210(5)</td><td>T/K 273</td></tr>
<tr><td>Re-N2</td><td>2.158(4)</td><td rowspan="2">R1 = 0.0346,
wR2 = 0.0976</td></tr>
<tr><td>C10-O1</td><td>1.350(6)</td></tr>
<tr><td>O1-C11</td><td>1.391(6)</td><td>GOF on F2 1.059</td></tr>
<tr><td>C10-N2</td><td>1.350(6)</td><td rowspan="2"></td></tr>
<tr><td>N2-C16</td><td>1.401(7)</td></tr>
</table>

III.2.5 IR spectra

The observed strong vibrations in the infrared spectrum, specifically those appearing around 1876 to 2021 cm^{-1}, are characteristic of the three carbonyl (CO) stretching vibrations found in a fac-$[Re(CO)_3]^+$ unit. This core structure exhibits pseudo-C_{3V} symmetry.

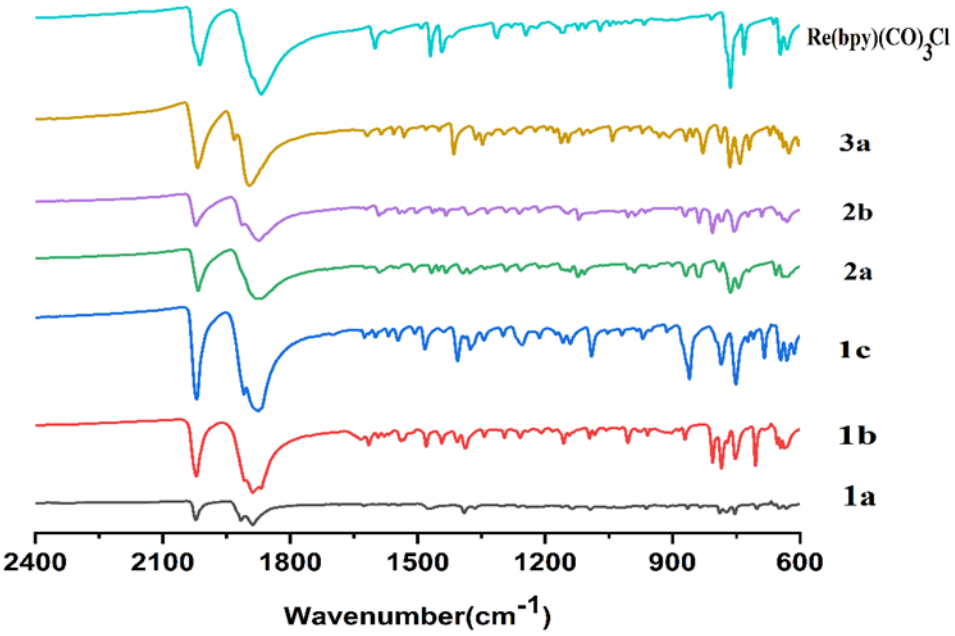

Figure III.26 FTIR Spectra of the complexes.

complex	**experimental ν_{CO} (cm^{-1})**
Complex-1a	2021, 1915, 1888
Complex-1b	2020, 1906, 1880
Complex-1c	2020, 1908, 1883
Complex-2a	2016, 1915, 1879
Complex-2b	2021, 1912, 1876
Complex-3a	2018, 1931, 1896

Table III.6 IR stretching frequencies of the complexes.

III.2.6 Absorption spectra and photophysical properties

The UV-vis absorption spectra of the studied $Re(CO)_3(N^N)Cl$ complexes in acetonitrile solution exhibit distinct features typical of such compounds. Broad, low-energy absorption bands appear with maxima between 380 and 450 nm, which are predominantly assigned to metal-to-ligand charge transfer (^{1}MLCT) transitions—from the Re dπ orbital to the π* orbital of the N^N ligand. In addition, strong absorption peaks observed between 320 and 380 nm, resembling those of the free ligands, correspond to ligand-centered π–π* transitions (spin-allowed $S_0 \rightarrow {}^1$IL transitions), as shown in **Figure III.27** and detailed in **Table III.7**.

The energy and intensity of the ^{1}MLCT and π–π* transitions are significantly influenced by the degree of π-conjugation in the ligand framework, especially when involving pyridine, quinoline, and isoquinoline moieties. Enhanced π-conjugation results in a red shift in the absorption spectrum, attributed to a reduced energy gap between the ground and excited states. Among the three moieties, the isoquinoline-based systems display the most prominent red shift. This trend is related to the higher basicity of isoquinoline (pKa = 5.46) compared to quinoline (pKa = 4.85), which increases the electron density on the nitrogen atom, thereby enhancing π-conjugation with the aromatic ring and extending the overall π-system.

Upon photoexcitation in the low-energy absorption region, the fac-$[Re(N^N)(CO)_3Cl]$ complexes exhibit characteristic photoluminescence (PL) emission arising from the lowest-lying triplet metal-to-ligand charge transfer (^{3}MLCT) excited state, consistent with typical Re(I) complex behavior. The emission spectra show a progressive bathochromic shift as the degree of conjugation in the N^N ligand increases. This shift is due to increased delocalization of electron density in the excited state, which lowers its energy.

Among all studied complexes, complex-1b shows the strongest photoluminescence. The normalized emission spectra are provided in **Figure III.28**, with **complex-1b** exhibiting the highest quantum yield (Φ_{em} = 0.51), as reported in **Table III.8**. To further understand the emissive properties and decay mechanisms of these coordination complexes, emission decay measurements were performed in CH_3CN at room temperature (**Figure III.29**).

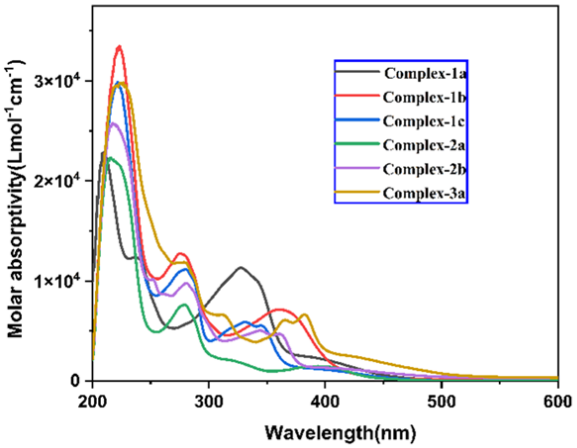

Figure III.27

Catalyst	λ_{max}(nm)(ε, M^{-1} cm^{-1})
Complex-1a	330(12880), 400(2580)
Complex-1b	277(14300), 360(7960), 400(1000)
Complex-1c	280(12480), 335(6600) 402(1600)
Complex-2a	280(8720), 320(2480), 400(1800)
Complex-2b	280(11200), 350(6000), 416(1600)
Complex-3a	280(13400), 380(7400), 430(2660).

Table III.7

Figure III.27 UV-Vis absorption spectra of **complex-1a**, **complex-1b**, **complex-1c, complex-2a**, **complex-2b** and **complex-3a**. in CH_3CN. **Table III.7** The absorption maxima wavelengths (λ_{max}) and molar extinction coefficients (ε) of *fac*-[Re(N^N)$(CO)_3$Cl] in CH_3CN.

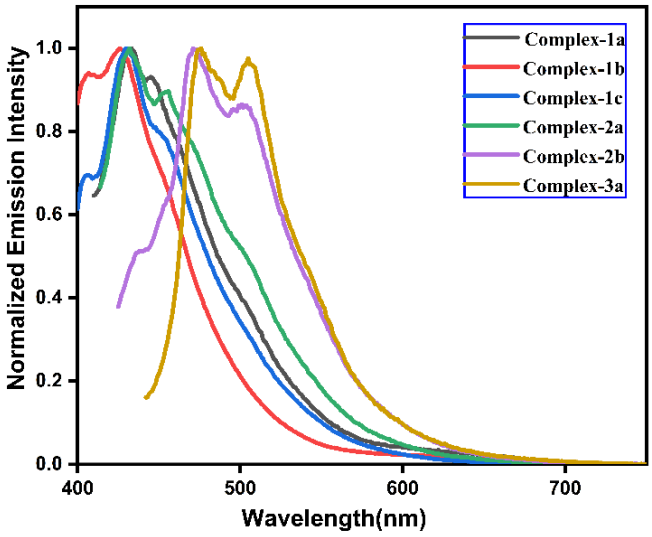

Figure III.28 Normalized Emission plots of the **complexes (1a, 1b, 1c, 2a, 2b, 3a)** recorded in CH_3CN at room temperature.

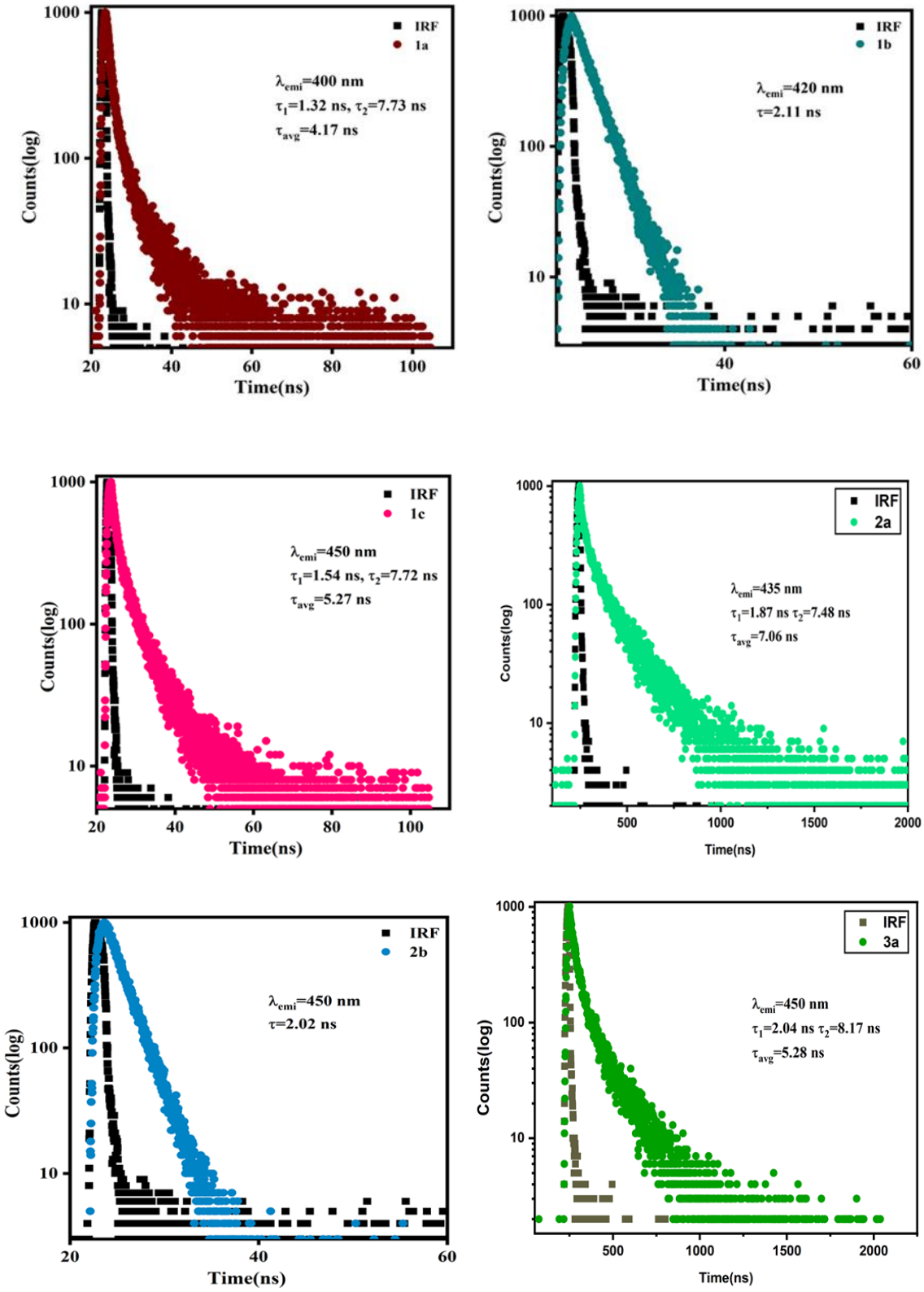

Figure III.29 Emission decay curves of **complex-1a, 1b, 1c, 2a, 2b** and **3a** in aerated CH_3CN.

Complex	λ_{exc}(nm)	λ_{emi}(nm)	Φ_{EM}	τ_1(ns)	τ_2(ns)	τ_{avg}(ns)	$k_r(s^{-1})\times10^7$	$k_{nr}(s^{-1})\times10^8$
1a	400	431,446	0.11	1.32	7.73	4.17	1.4	1.15
1b	400	405,424	0.51	2.11	-	2.11	24.1	2.32
1c	402	429	0.24	1.54	7.72	5.27	3.1	0.98
2a	400	431,455	0.13	1.87	7.48	7.06	1.7	1.26
2b	416	471,501	0.07	2.02	-	2.02	3.4	4.6
3c	430	474,504	0.05	2.04	8.17	5.28	0.6	1.16

Table III.8 Photophysical parameters of the complexes. All the complexes were excited at the maximum wavelength of absorption ($\lambda_{max}=\lambda_{exc}$).

III.2.7 Catalytic properties

A. Electrochemical Studies and CO_2 reduction

Electrochemical investigations were systematically conducted using cyclic voltammetry (CV) to explore the behaviour of all complexes under Ar atmospheres using 0.1 M tetrabutylammonium hexafluorophosphate ($[^nBu_4N]PF_6$) as a supporting electrolyte, glassy carbon as working electrode, platinum wire as counter electrode and scan rate was taken 100 mV/s in acetonitrile medium (**Figure III.30)**. A concentration of 0.1 mM was used for all the complexes. The electrochemical data are presented in **Table III.9.** A deeper examination of the electrochemical profiles revealed that, under Ar, all complexes exhibited one oxidation event and multiple reduction events within the experimental window. The oxidation potential ranging from 1.065 to 1.233 V *vs* Fc^+/Fc which was generally irreversible, is attributed to a metal-centered Re(I) to Re(II) oxidation. The first quasi-reversible reduction peaks, with $E_{1/2}$ values ranging from -1.1 to -1.6 V *vs* $Fc^{+/0}$ across all complexes, pointed to a ligand-based reduction, where the added electron likely resides on the pyridine, quinoline, or isoquinoline moieties to give $[Re^I(N\text{^}N)(CO)_3Cl]^{\bullet-}$ followed by Cl^- dissociation[59] . The second reduction event occurring within the -1.8 V to -2.1 *vs* $Fc^{+/0}$ range, resulting in the formation of a $[Re(N\text{^}N)(CO)_3]^-$.

The appearance of hump-like reduction peaks after the second reduction event was particularly noteworthy, as it indicated the reduction of the rhenium hydride complex formed after chloride dissociation. The varied reversibility of the first reduction peak, dependent on the ligand substituent, the first reduction potential of pyridine substituted complexes i.e for **complex 1a, 1b** and **1c** is ranging -1.355 V to -1.539, more than from the quinoline (-1.153 V *vs* $Fc^{+/0}$ for **complex 2a**) or isoquinoline (-1.189 V *vs* $Fc^{+/0}$ for

complex-3a) analogues. further underscored the nuanced electrochemical behaviour, with some complexes exhibiting quasi-reversibility while others displayed full reversibility (**Figure III.30)**.

In the final phase of our investigation, we focused on the voltammetric behaviour of all complexes under CO_2-saturated conditions. The results demonstrated a significant increase in current in the acetonitrile medium, while a comparatively lower current enhancement was observed in DMF. This notable difference highlighted the superior performance of the CH_3CN medium prompting its selection for all subsequent CV measurements under CO_2. Through this focused electrochemical study, we were able to affirm the capability of these complexes to electrochemically reduce CO_2.

To determine the most effective electrocatalyst, the maximum turnover frequency (TOF_{max}) can be calculated using the equation[64,65], $i_{cat}/i_p = 4.484(RT/F)^{1/2}(TOF_{max})^{1/2}\nu^{-1/2}$. TOF_{max} determined for the investigated complexes are as follows: 1.80 s^{-1} for **complex 1a**, 2.90 s^{-1} for **complex 1b**, 2.28 s^{-1} for **complex 1c**, 1.19 s^{-1} for **complex 2a**, 1.32 s^{-1} for **complex 2b**, and 0.62 s^{-1} for **complex 3a** (**Figure III.31 - Figure III.36, Table III.10)**. Among them, catalyst **complex 1b** exhibited the highest TOF_{max} of 2.90 s^{-1}, indicating its superior electrocatalytic activity. Since our primary focus is on the photocatalytic CO_2 reduction by the catalysts, we selected the most effective electrocatalyst, **complex 1b**, for further investigation. Accordingly, we performed controlled potential electrolysis (CPE) studies using catalyst **complex 1b**.

Controlled-potential electrolysis of complex **1b** was conducted in the presence of CO_2 with the addition of 0.1 M TFE. The electrolysis was performed using glassy carbon working electrode, a platinum wire counter electrode, and a 0.1 M $[^nBu_4N]PF_6$ as a supporting electrolyte, with a catalyst concentration of 1 mM and an applied potential of -2.5 V vs Ag/AgCl (**Figure III.37**). The primary product observed was carbon monoxide (CO), while a smaller amount of methane was also detected (**Figure III.38**). The faradaic efficiencies for CO and methane is 33 % and 6 % respectively (**Table III.11**).

TOF_{max} calculations from the cyclic voltammetry experiments:

The turnover frequency (TOF) is an inherent characteristic of catalysts, which represents the rate of conversion reactants into products per mole of active catalyst per unit time. The TOF value was derived using the following equation below from the catalytic cyclic voltammograms recorded CH_3CN solutions.

$$TOF = (Fvn_p^3/RT)(0.4463/n_{cat})(i_{cat}/i_p)^2$$

Where, i_p is peak current, i_{cat} is the catalytic current, F is Faraday's constant (F = 96500 C), R is the universal gas constant (R = 8.314 J K^{-1} mol^{-1}), T is temperature (T = 300 K) and ν is the scan rate. (where n_p is 1, the number of electrons transferred in the noncatalytic reduction, and n_{cat} is 2 for CO_2 reduction to CO, the number of electrons transferred in the catalytic reaction). The TOF was calculated from the slope of i_{cat}/i_p vs $\nu^{-1/2}$ plot.

$E_{1/2}$, V *vs* $Fc^{+/0}$				
	E_{ox1}	E_{red1}	E_{red2}	E_{red3}
Complex-1a	1.065	-1.539	-2.019	-2.348
Complex-1b	1.202	-1.460	-2.075	-2.463
Complex-1c	1.174	-1.355	-1.893	……
Complex-2a	1.171	-1.153	-1.912	-2.551
Complex-2b	1.233	-1.187	-1.849	-2.467
Complex-3a	1.117	-1.189	-1.908	-2.370

Table III.9 Peak Potentials of the complexes (**1a, 1b, 1c, 2a, 2b** and **3a**) in CH_3CN.

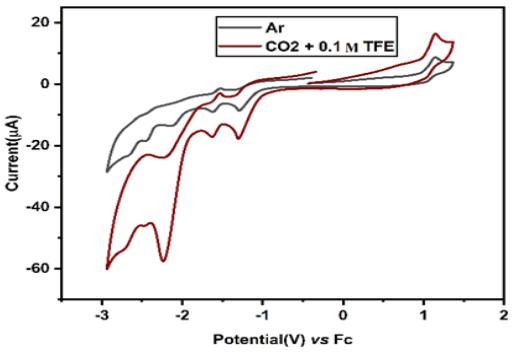

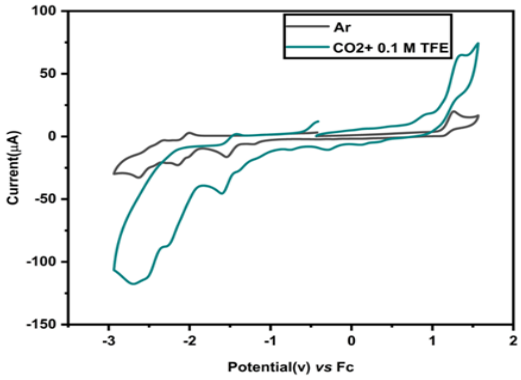

1a **1b**

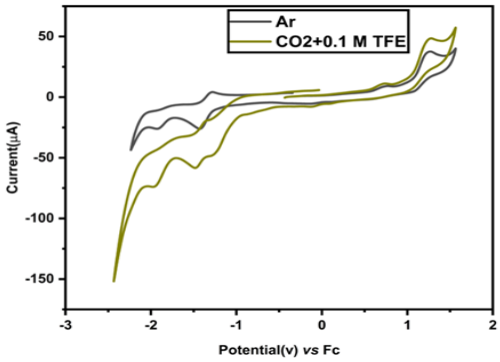

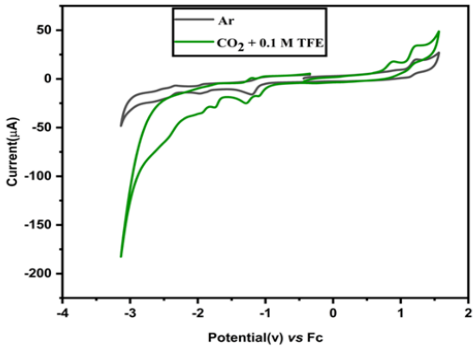

1c **2a**

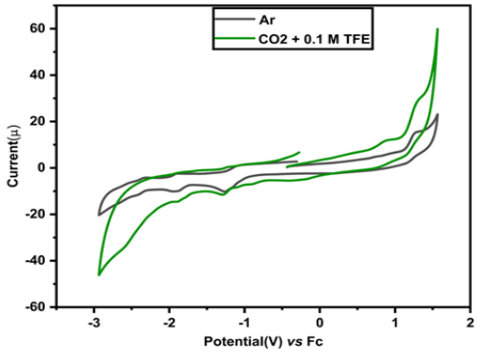

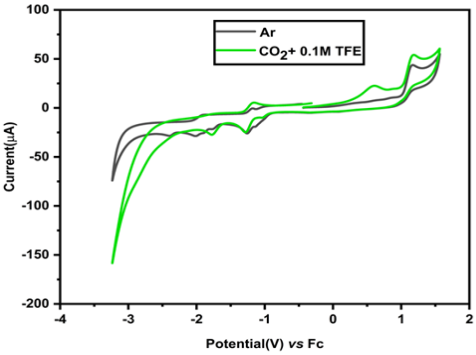

2b **3a**

Figure III.30 Cyclic voltammograms of 1 mM solution of **complexes 1a, 1b, 1c, 2a, 2b** and **3a** under Ar (black) and CO_2 atmosphere. Potential values are reported versus Fc^+/Fc.

Calculation of TOF_{max} for the Complexes:

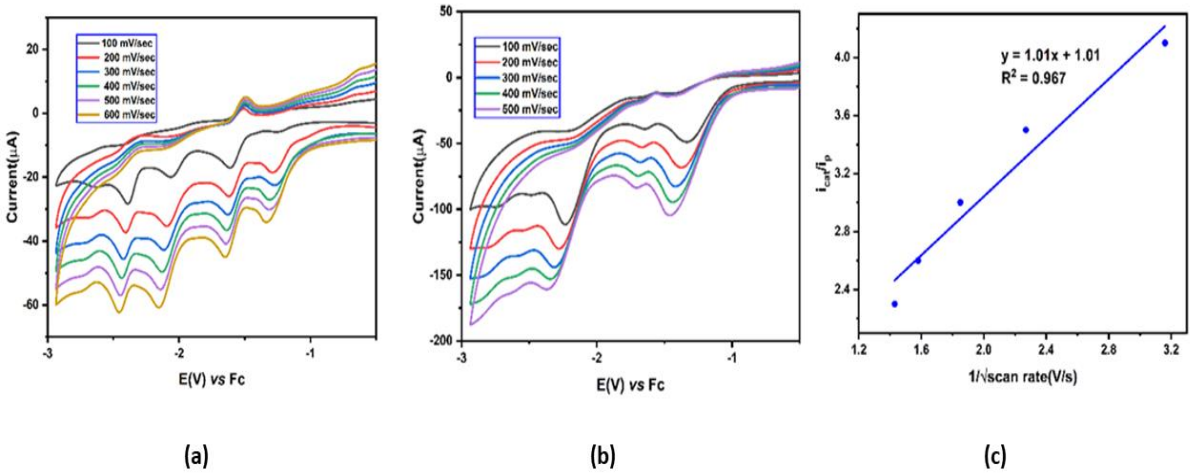

Figure III.31 Cyclic voltammogram scan rate dependence of 1 mM **complex-1a** under an atmosphere of argon **(a)** and under an atmosphere of CO_2 **(b)** in acetonitrile. **(c)** i_p/i_{cat} vs. 1/scan $rate^{1/2}$ plot of **complex-1a.** Electrochemical conditions were 0.1 M TBAH as supporting electrolyte, 3 mm diameter glassy carbon working electrode, Pt wire counter electrode, and Ag/AgCl reference electrode.

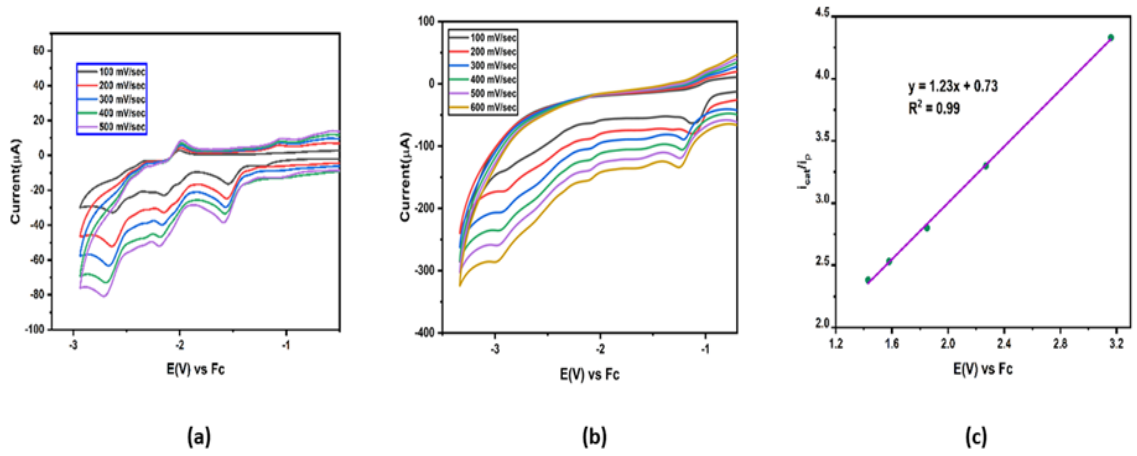

Figure III.32 Cyclic voltammogram scan rate dependence of 1 mM **complex-1b** under an atmosphere of argon **(a)** and under an atmosphere of CO_2 **(b)** in acetonitrile. **(c)** i_p/i_{cat} vs. 1/scan $rate^{1/2}$ plot of **complex-1b**. Electrochemical conditions were 0.1 M TBAH as supporting electrolyte, 3 mm diameter glassy carbon working electrode, Pt wire counter electrode, and Ag/AgCl reference electrode.

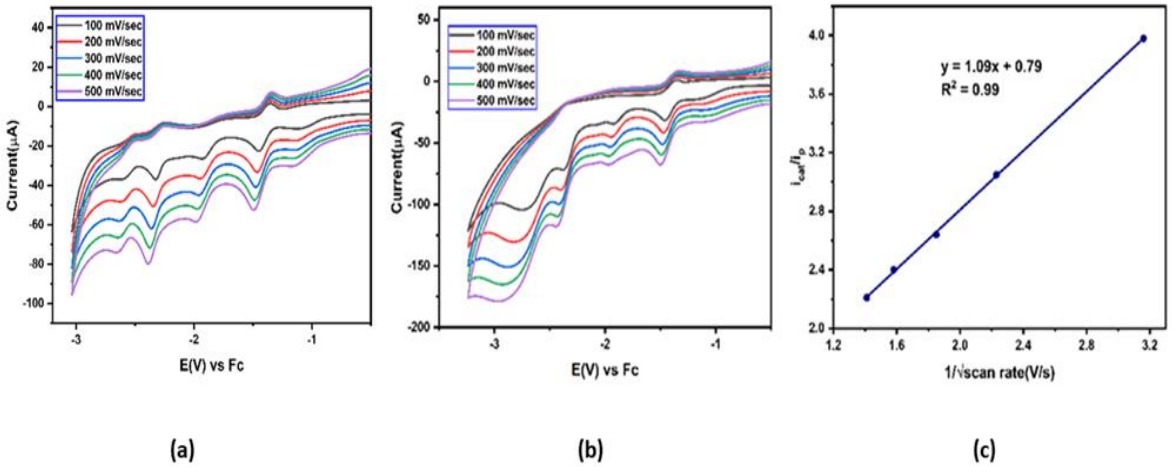

Figure III.33 Cyclic voltammogram scan rate dependence of 1 mM **complex-1c** under an atmosphere of argon **(a)** and under an atmosphere of CO_2 **(b)** in acetonitrile. **(c)** i_p/i_{cat} vs. 1/scan rate$^{1/2}$ plot of **complex-1c**. Electrochemical conditions were 0.1 M TBAH as supporting electrolyte, 3 mm diameter glassy carbon working electrode, Pt wire counter electrode, and Ag/AgCl reference electrode.

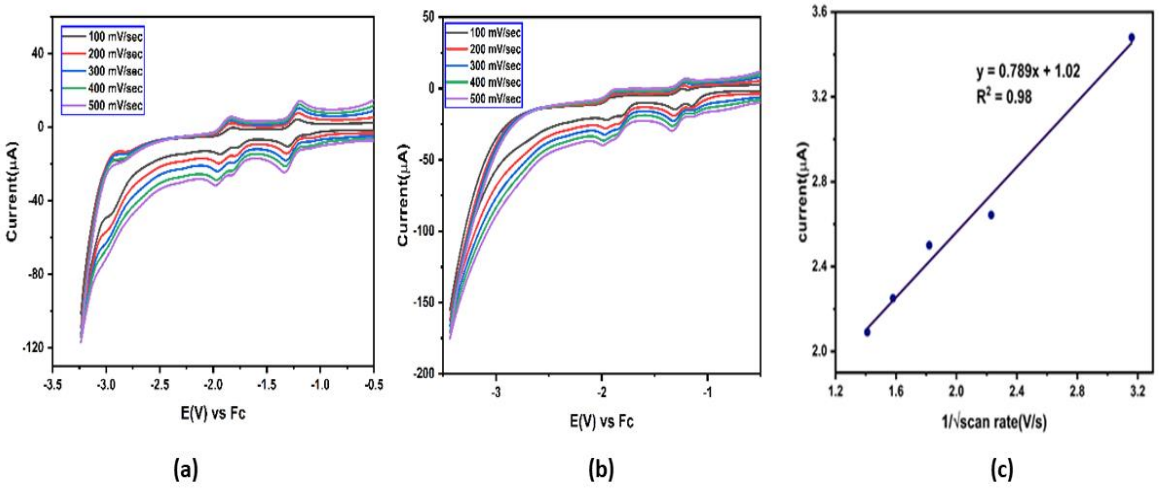

Figure III.34 Cyclic voltammogram scan rate dependence of 1 mM **complex-2a** under an atmosphere of argon **(a)** and under an atmosphere of CO_2 **(b)** in acetonitrile. **(c)** i_p/i_{cat} vs. 1/scan rate$^{1/2}$ plot of **complex-2a**. Electrochemical conditions were 0.1 M TBAH as supporting electrolyte, 3 mm diameter glassy carbon working electrode, Pt wire counter electrode, and Ag/AgCl reference electrode.

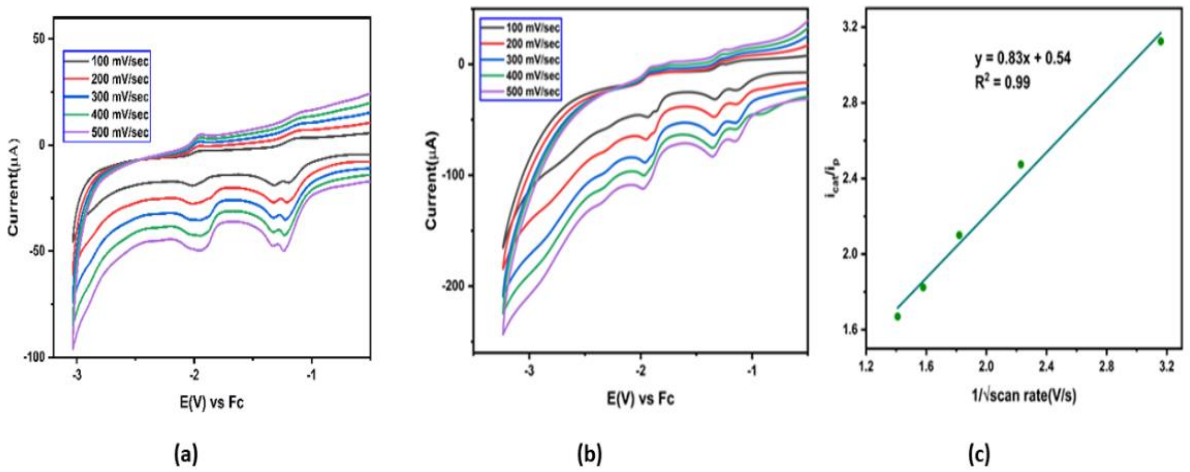

Figure III.35 Cyclic voltammogram scan rate dependence of 1 mM **complex-2b** under an atmosphere of argon **(a)** and under an atmosphere of CO_2 **(b)** in acetonitrile. **(c)** i_p/i_{cat} vs. 1/scan rate$^{1/2}$ plot of **complex-2b**. Electrochemical conditions were 0.1 M TBAH as supporting electrolyte, 3 mm diameter glassy carbon working electrode, Pt wire counter electrode, and Ag/AgCl reference electrode.

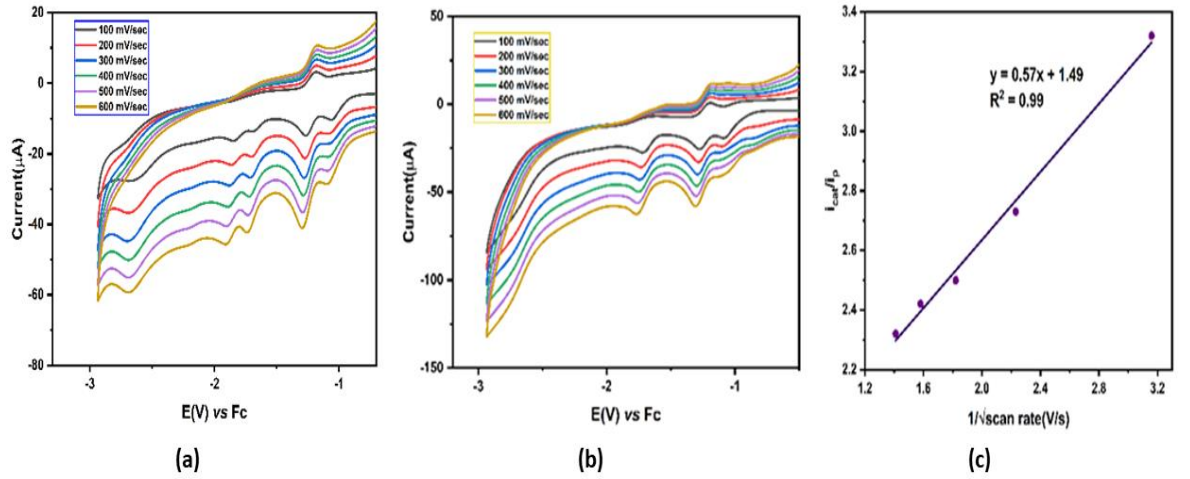

Figure III.36 Cyclic voltammogram scan rate dependence of 1 mM **complex-3a** under an atmosphere of argon **(a)** and under an atmosphere of CO_2 **(b)** in acetonitrile. **(c)** i_p/i_{cat} vs. 1/scan rate$^{1/2}$ plot of **complex-3a**. Electrochemical conditions were 0.1 M TBAH as supporting electrolyte, 3 mm diameter glassy carbon working electrode, Pt wire counter electrode, and Ag/AgCl reference electrode.

Catalyst	TOF_{max}
1a	1.80 s^{-1}
1b	2.90 s^{-1}
1c	2.28 s^{-1}
2a	1.19 s^{-1}
2b	1.32 s^{-1}
3a	0.62 s^{-1}

Table III.10 TOF_{max} of the complexes in CH_3CN.

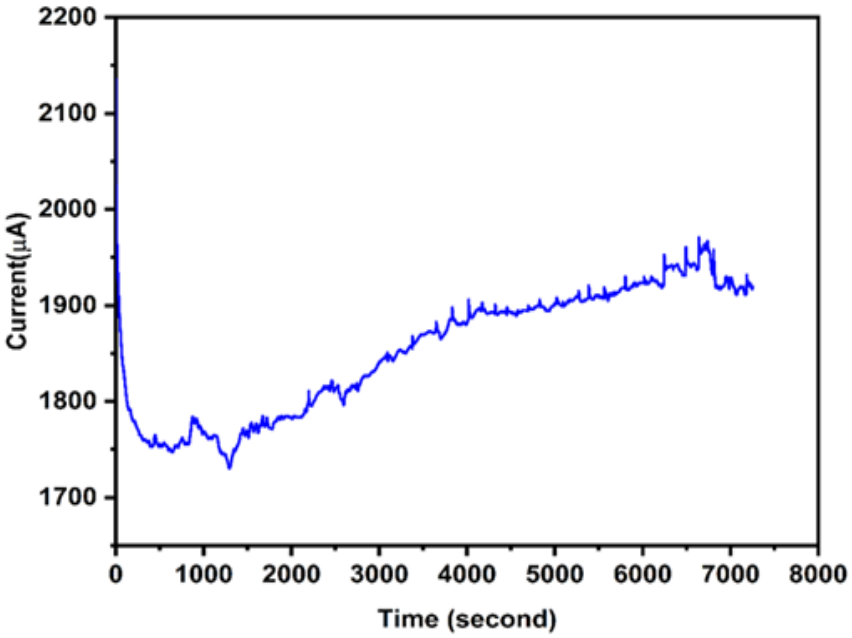

Figure III.37 Representative current versus time plots for controlled potential electrolyses of **Complex-1b**

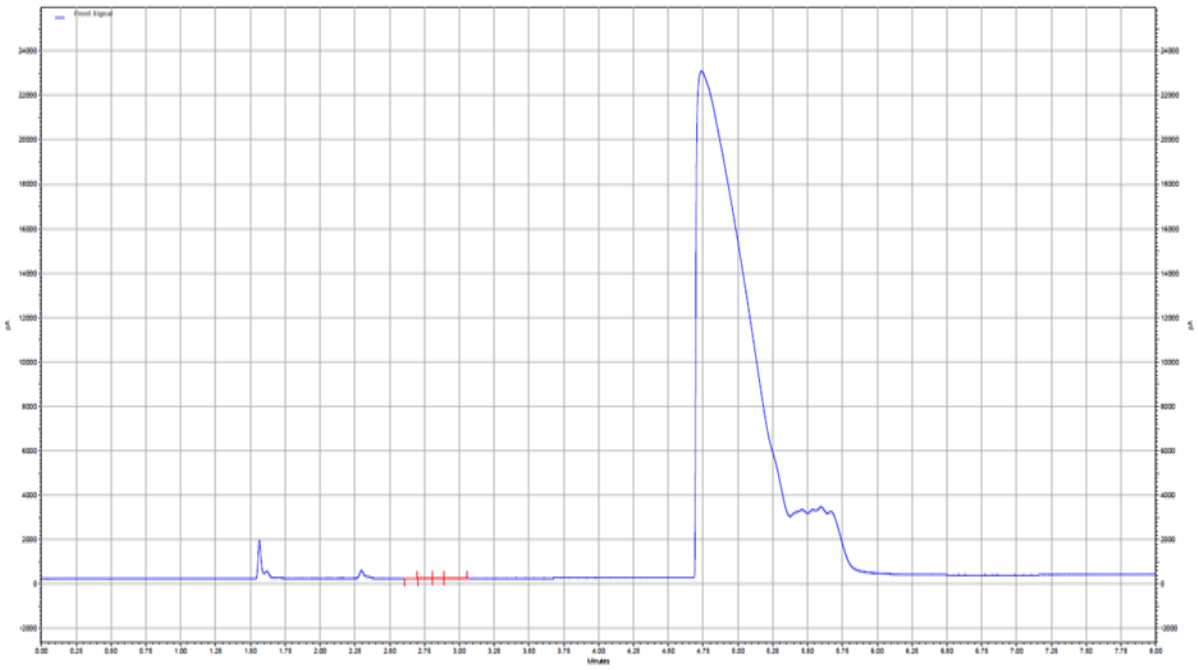

Figure III.38 GC-TCD data after controlled potential electrolyses.

Compound	Conc.(mM)	Faradaic efficiency (%)		
1b	1	H_2	CO	CH_4
		<1	33	6

Table III.11 Faradaic efficiencies, in CH_3CN and 0.1M TFE after CPE experiments with a carbon working electrode for the **complex 1b**, for 2 hours at -2.5 V vs Ag/AgCl.

B. Photocatalysis for CO_2 reduction

The photocatalytic reduction of CO_2 using **catalyst-1a** was studied in various solvents with different proton sources (**Table III.12)**. The system demonstrated the second-highest turnover number (TON) for CO production when employing acetonitrile (CH_3CN) as the solvent, triethanolamine (TEOA) as the proton source[10,63], and 1,3-dimethyl-2-phenyl-2,3-dihydro-1H-benzo[d]imidazole (BIH) as the sacrificial electron donor (SED). In contrast, when water was used as the proton source in dimethylformamide (DMF), CO production was maximized, accompanied by a reduced yield of hydrogen. However, the presence of water facilitated the hydrolysis of DMF, leading to the formation of formate[61]. This complication made the quantification of formate difficult, as it could not be reliably attributed to the catalytic reaction. Consequently, this condition was avoided in experiments with other complexes. Further experimentation with 2,2,2-trifluoroethanol (TFE) as the proton source in acetonitrile demonstrated improved selectivity. In this case, only trace amounts of hydrogen were detected. However, the TON values in this system were relatively low compared to the using of TEOA as the proton source. At higher concentrations of BIH (greater than 0.025 M), a decline in catalytic activity is observed (**Figure III.39**). This reduction in activity is attributed to the complex mechanisms that govern the photocatalytic CO_2 reduction system[62]. The system comprises two primary processes: electron relay cycle and catalytic cycle. In the electron relay cycle, electron transfer from BIH to the excited photosensitizer (PS*) occurs within an encounter complex, producing a reduced photosensitizer ($PS^{\cdot-}$). Simultaneously, protonation of BIH by $BIH^{\cdot+}$ inhibits back electron transfer, thereby improving electron transfer efficiency

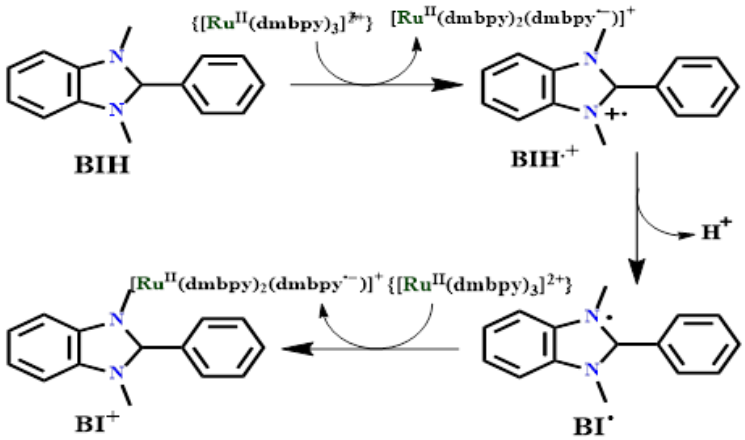

Scheme III.1 The electron relay cycle in the photochemical CO_2 reduction.

and boosting CO production (**Scheme III.1**). At high concentration of BIH progressive oxidation of BIH to BI^+ induces a decrease in solution basicity, impairing the reducing capacity of protonated BIH relative to BIH. This modification in electron transfer kinetics at higher $[BIH]_0$ adversely affects the efficiency of CO production.

All these observations highlight the importance of optimizing solvent choice, proton source and sacrificial electron donor (SED) as these factors play a crucial role in determining both the selectivity and efficiency of CO_2 reduction. To maximize selectivity, TON and TOF, CH_3CN was chosen as the solvent with TEOA as the proton source (4.0 mL, 10:1 v/v), 0.2 mM $Ru(dmbpy)_3^{2+}$ as phtosensitizer, 25 mM SED and 20 µM catalyst is used for all catalysts. Among all the complexes studied, $E_{1/2}$ of the 1st and 2nd reduction potential was more positive than that of $Ru(dmbpy)_3^{2+}$ (-1.74 V vs Ag/AgCl)[15]. This indicates that electron transfer from the OER species of the Ru center is thermodynamically favourable. Consequently, in all cases, the electron photochemically extracted from BIH to the Ru center undergoes rapid transfer to the Re center. Additionally, TEOA plays multiple roles beyond functioning as a proton source. It contributes to an alkaline environment that facilitates the deprotonation of oxidized BIH (by abstracting a proton from $BIH^{\bullet+}$), while also serving as a CO_2 absorber. The formation of a TEOA–CO_2 adduct is postulated to enhance photocatalytic performance by increasing the local CO_2 concentration within the reaction system[46].

For the **catalysts 1a**, **1b**, **1c**, **2a**, **3a** the photocatalytic reduction of CO_2 was also performed without $[Ru(dmbpy)_3]^{2+}$. Irradiation was carried out at $\lambda \geq 400$ nm using a 300 W Xenon lamp. The gaseous products in the headspace were analyzed and monitored using gas chromatography with a thermal conductivity detector (GC-TCD).

Additionally, NMR spectroscopy was utilized to examine the formation of formate during photoirradiation, both in the presence and absence of catalysts. In the catalyst-free experiments using the photosensitizer (PS), only small amounts of CO and H_2 (0.03 µmol CO) were detected, with no formate observed (**Figure III.42)**. To accurately quantify the CO and H_2 produced by the photocatalytic system, the background levels from the control experiment without the catalyst were subtracted. The TON value of Re-benzo[d]oxazole complexes exhibits significant disparities when compared to Re-bipyridine complexes. This pronounced difference in catalytic performance underscores the potential impact of ligand structure on the efficiency of rhenium-based photocatalysts for CO_2 reduction. The amount of H_2 and CO given in the **Table III.13.** The observed TON_{CO} values follow the trend: **complex-1b** > **complex-1c**

> **complex-1a** > **complex-2b** > **complex-2a > complex-3a** (**Figure III.40 (a))**. Under 5 hours of irradiation, **complex-1b** generated 66 μmol of CO, corresponding to a TON_{CO} of 660, while **complex-2a** and **complex 3a** produced 50.7 μmol 32.5 μmol of CO, achieving a TON_{CO} of 507 and 325 respectively under identical conditions.

The decrease in TON observed when transitioning from pyridine-benzo-oxazoline systems to quinoline- or isoquinoline-based systems can be attributed to the shift of metal-to-ligand charge transfer (MLCT) absorption into the visible region in the latter systems. This shift may result in competition between the photosensitizer and the catalyst for light absorption, thus diminishing overall catalytic efficiency or leading to the destabilization of the complexes. When the catalytic reaction was performed without an added photosensitizer under Xe light as well as in sunlight (**Figure III.40 (b)** and **Figure III.41**), **complex 1b** exhibited higher catalytic activity compared to other complexes. Additionally, after 2 hours, a more rapid fading of colour was observed for **complex 2b**, **3a** indicating greater instability. Under direct sunlight, the colour fades more rapidly. The TON value is significantly higher in the presence of a photosensitizer (PS) compared to when it is absent. This can be attributed to the very short lifetime of the excited state of the catalyst in the absence of a PS, leading to a rapid return of the catalyst to its ground state before it can effectively react with CO_2[39]. However, when comparing **complexes 1a**, **1b**, and **1c** or **2a** with **2b**, it is evident that an increase in aromatic conjugation correlates with an increase in the TON value. To verify that the CO generated originated solely from the photoreduction of CO_2 and not from the decomposition of other materials within the system, experiments were conducted under a $^{13}CO_2$ atmosphere. The resulting gaseous products were analyzed by GC-MS, which revealed a characteristic peak at m/z = 29, corresponding to ^{13}CO. This provides definitive evidence that the CO was produced through the reduction of $^{13}CO_2$ (**Figure III.43**)

No.	Solvent(4ml)	Electron donor	λ (nm)	Gas	Reduced products		TON_{CO}
					CO (μmol)	H_2 (μmol)	
1	DMF/H_2O(4:1)	BIH	$420 \leq \lambda \leq 750$	CO_2	42	0.012	420
2	DMF/TEOA(4:1)	BIH	$420 \leq \lambda \leq 750$	CO_2	26	3.03	260
3	DMA/H_2O(4:1)	BIH	$420 \leq \lambda \leq 750$	CO_2	33	0.01	330
4	DMF/TEA(4:1)	BIH	$420 \leq \lambda \leq 750$	CO_2	5	2.88	50
5	CH_3CN/H_2O(4:1)	BIH	$420 \leq \lambda \leq 750$	CO_2	9	<0.01	90
6	CH_3CN/TEOA(4:1)	BIH	$420 \leq \lambda \leq 750$	CO_2	37	0.01	370
7	CH_3CN/TFE(4:1)	BIH	$420 \leq \lambda \leq 750$	CO_2	22	<0.01	220
8	DMF/TFE(4:1)	BIH	$420 \leq \lambda \leq 750$	CO_2	27	1.32	270
9	CH_3CN/TEOA(4:1)	BIH	Dark	CO_2	0	0	0
10	CH_3CN/TEOA(4:1)	BIH	$420 \leq \lambda \leq 750$	N_2	0	0	0
11	CH_3CN/TEOA(4:1) + 0.1 ml TFE	BIH	$420 \leq \lambda \leq 750$	CO_2	33	0.2	330

Table III.12 Photocatalytic CO_2 reduction at different condition. For all catalysts, the photochemical conditions include 4 mL of solvent, 0.2 mM $Ru(dmbpy)_3^{2+}$ as the photosensitizer, 25 mM SED, and 20 µM **complex-1a**. The quantities of the reduced products generated by the catalysts were measured after 2 hours.

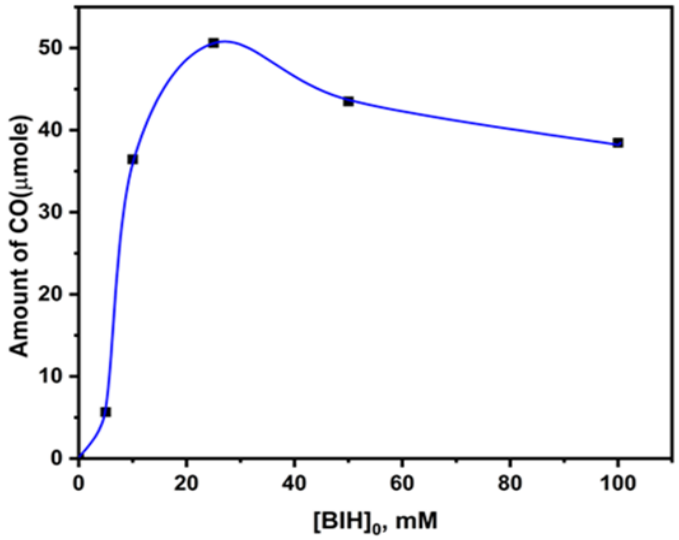

Figure III.39 The amount of CO produced after 4 hours of photocatalytic CO_2 reduction by **complex-1a** as a function of BIH concentration.

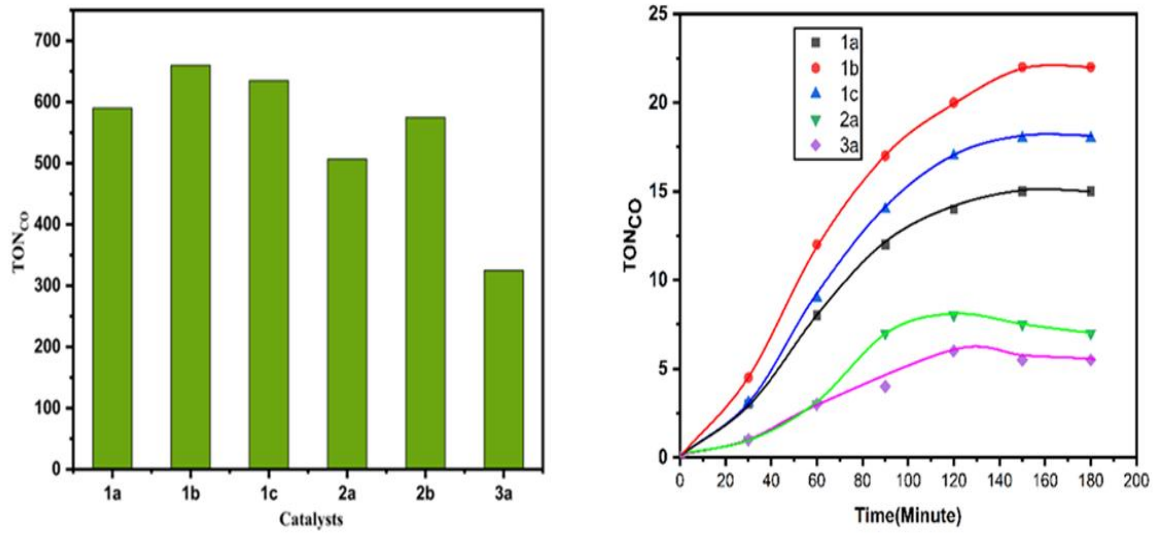

(a) (b)

Figure III.40 (a) TON_{CO} obtained by the catalysts after 5 h. CH_3CN was chosen as the solvent with TEOA as the proton source (4.0 mL, 10:1 v/v), 0.2 mM $Ru(dmbpy)_3^{2+}$ as phtosensitizer, 25 mM SED and 20 µM catalyst. **(b)** Turnover number versus time plots without added PS. Solvent CH_3CN with TEOA as the proton source (4.0 mL, 10:1 v/v), 25 mM SED and 0.1 mM catalyst is used.

With added photosensitizer					
Catalyst	CO (μmol)	H_2 (μmol)	TON_{CO}	TON_{H2}	TOF_{co} (min^{-1})
1a	59	0.023	590	0.23	1.96
1b	66	0.021	660	0.21	2.2
1c	63.5	0.027	635	0.27	2.1
2a	50.7	0.016	507	0.16	1.69
2b	57.5	0.024	575	0.24	1.91
3a	32.5	0.014	325	0.14	1.08
$Re(bpy)(CO)_3Cl$	12.6	0.01	126	0.1	0.42
Without added photosensitizer					
1a	6	0.005	15	0.012	0.125
1b	8.8	0.004	22	0.01	0.183
1c	7.2	0.005	18	0.012	0.15
2a	3.2	0.004	8	0.010	0.06
3a	2.4	0.002	6	0.005	0.05

Table III.13 The quantities of the reduced products generated by the catalysts were measured both with the addition of a photosensitizer (after 5 hours) and without the photosensitizer (after 2 hours). The corresponding turnover number (TON) values for each condition.

Figure III.41 Photocatalytic reduction of CO_2 in bare sunlight by **complex 1a, 2a** and **3a.**

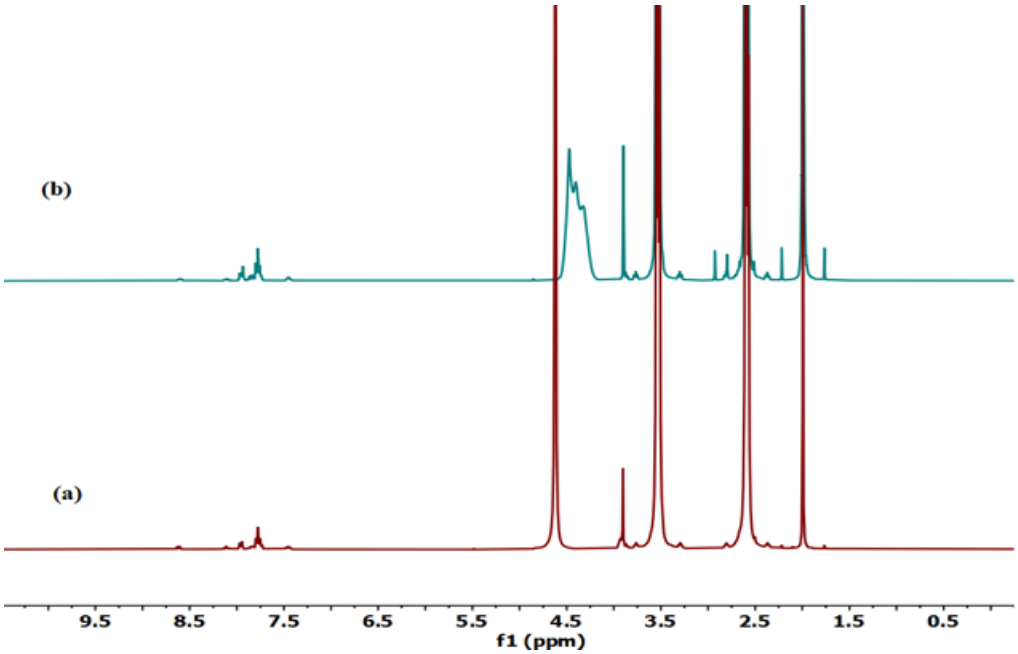

Figure III.42 ^1H NMR spectra in CD_3CN/TEOA in the presence of BIH, SP under CO_2 atmosphere and photo irradiation $\lambda \geq 400$ nm , irradiation time 5 hours **(a)** without catalyst **(b)** with catalyst.

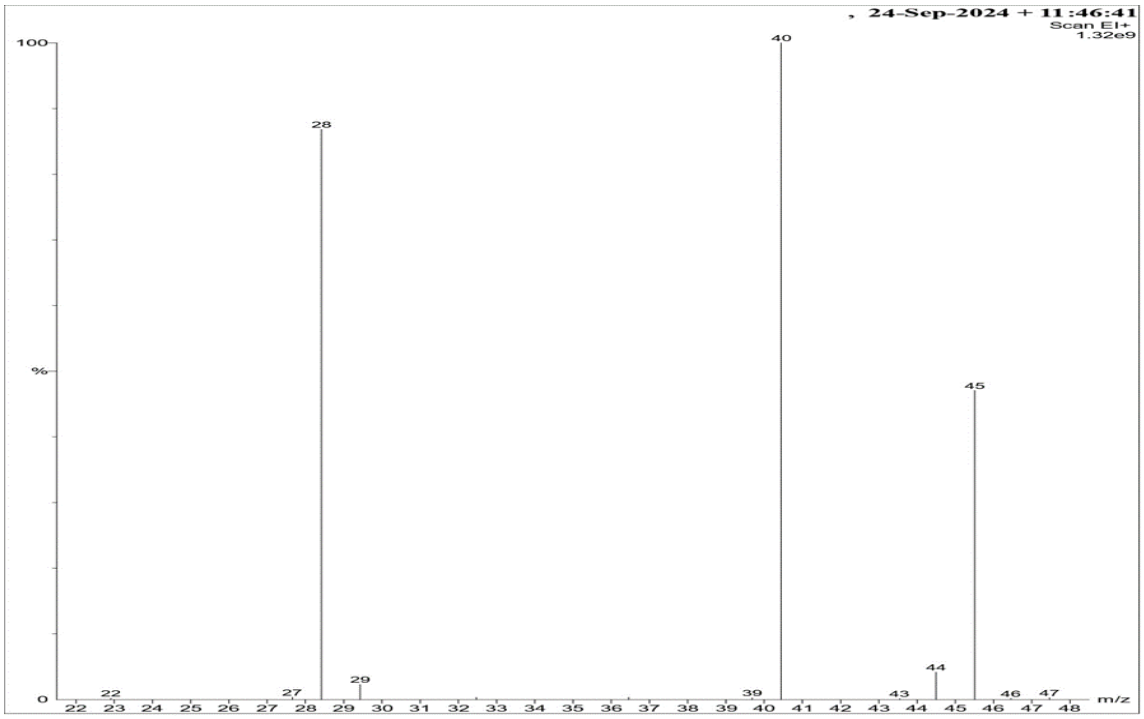

Figure III.43 Mass spectra obtained from GC-MS analysis using labelled $^{13}CO_2$.

III.3. Mechanistic Investigation:

To examine the active species involved in the photocatalytic reduction of CO_2, ^1H NMR spectroscopic studies were conducted in CD_3CN/TEOA (4:1), employing 5 mM BIH as a sacrificial reductant. Under photoirradiation in a CO_2 atmosphere, a gradual decrease in the ^1H NMR signal associated with BIH was observed (**Figure III.44**), concomitant with the emergence of a new peak attributed to the formation of BI^+. Notably, the consumption rate of BIH was significantly accelerated in the presence of the photosensitizer (PS) (**Figure III.45**). Additional mechanistic insights were gained through UV-vis spectroscopic analysis of the most efficient catalyst, **complex 1b**.

Upon irradiation, **complex-1b** exhibited a marked bleaching in the low-energy absorption band and the appearance of new, red-shifted maxima centered around 587 nm, indicative of the formation of the one-electron reduced species $[Re(N^N)(CO)_3Cl]^{\cdot-}$ **(Figure III.46)** . This assignment was corroborated by TD-DFT calculations on the one-electron reduced products (**Figure III.47**). TD-DFT calculations revealed that the UV peak observed for Complex-1b at 440 nm shifts to 500 nm upon one-electron reduction. This theoretical prediction closely aligns with experimental findings.

Interestingly, when the UV-vis spectrum was recorded in the presence of CO_2, the bathochromic shift of the low-energy peaks was absent, suggesting the formation of a new complex. Based on these experimental findings and computational mechanistic studies reported previously for rhenium-oxazoline[55,56] systems, a proposed mechanism is depicted in **Scheme III.2.**

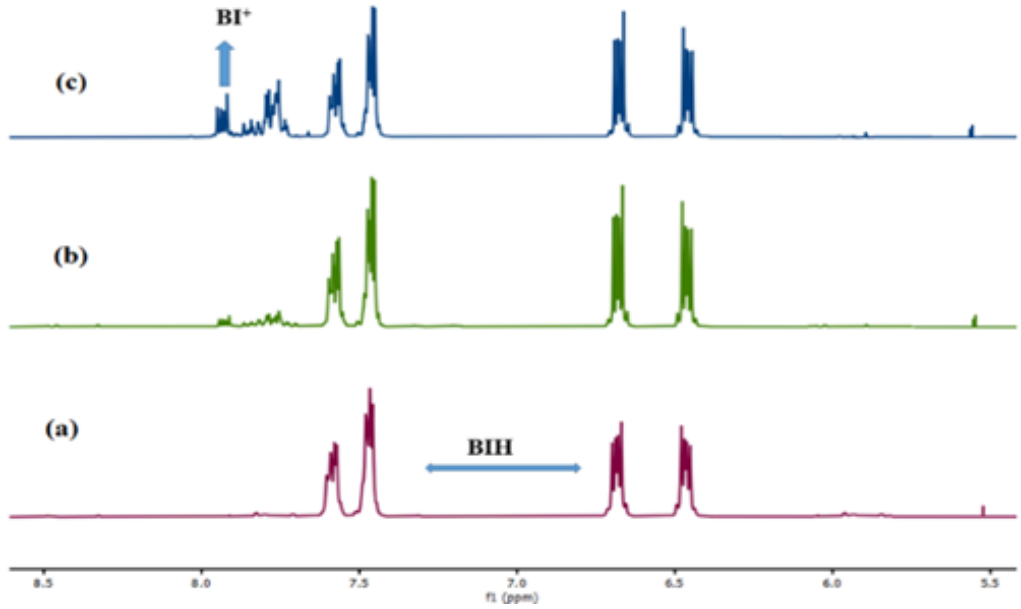

Figure III.44 ^{1}H NMR spectra of Complex 1b in CD_3CN/TEOA in the presence of BIH under CO_2 atmosphere and photo irradiation $\lambda \geq 400$ nm , irradiation time 0 min. (a), 60 min (b), 120 min(c).

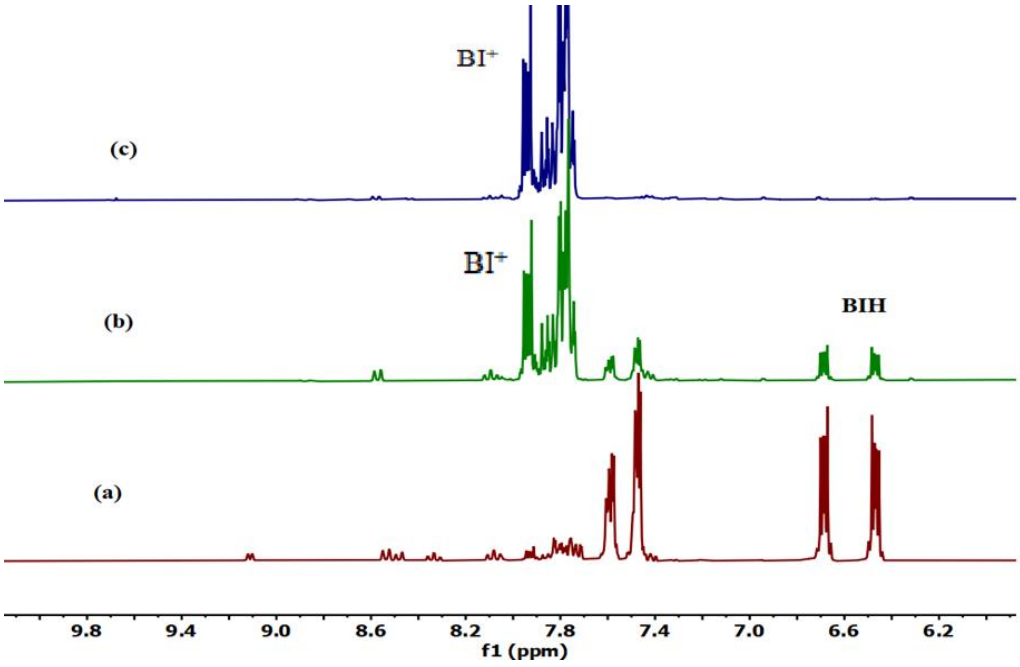

Figure III.45 ^{1}H NMR spectra of Complex-1b in CD_3CN/TEOA in the presence of BIH and PS under CO_2 atmosphere and photo irradiation $\lambda \geq 400$ nm , irradiation time 0 min. (a), 60 min (b), 120 min(c)

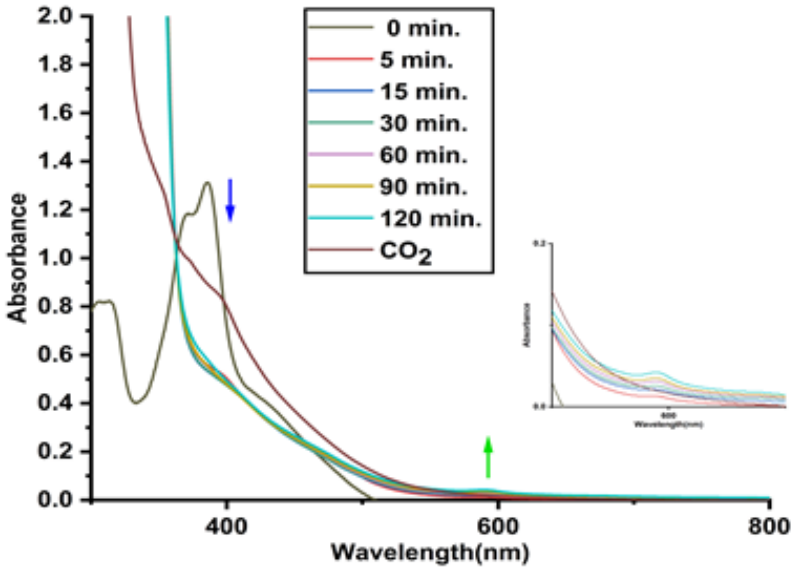

Figure III.46 UV−vis spectral changes measured during photocatalytic reactions using **complex-1b**. (λ_{irr} > 400 nm).

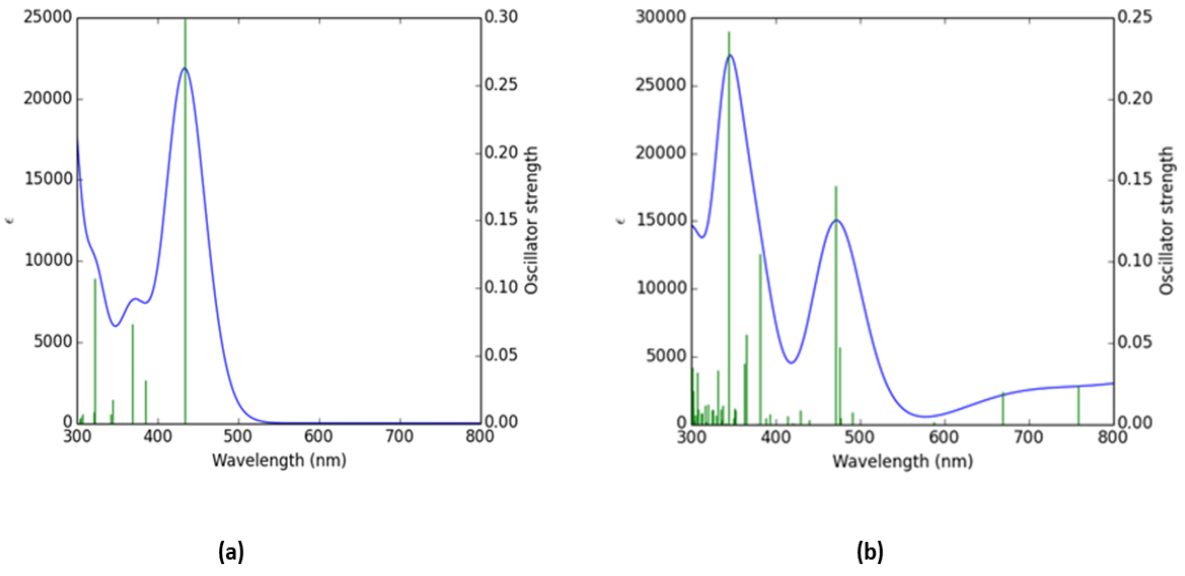

Figure III.47 TD-DFT calculation of **Complex-1b (a)** and its one electron reduced state **(b).**

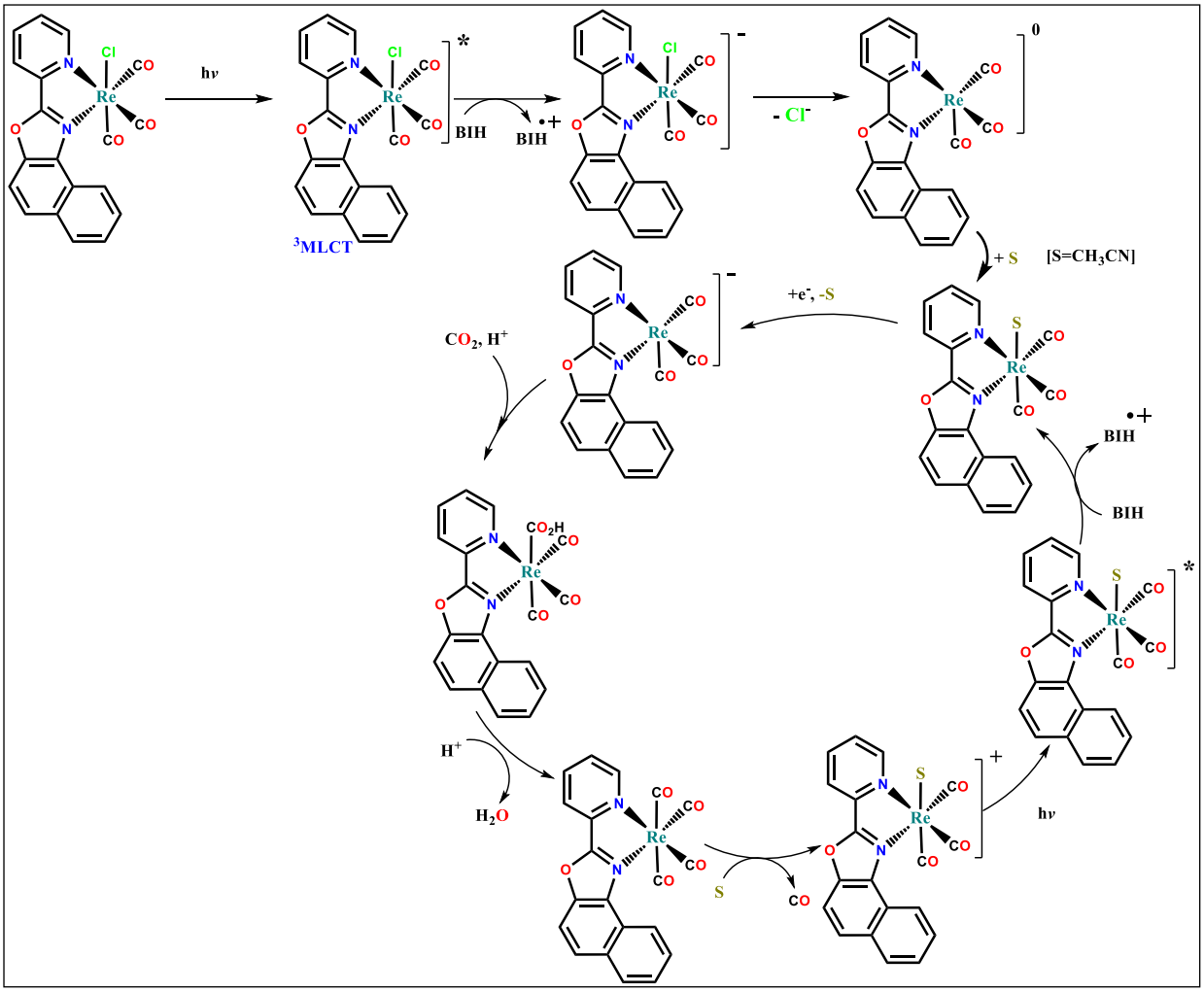

Scheme III.2 Proposed mechanism for the photochemical reduction of CO2 into CO catalyzed by rhenium benzo[d]oxazole Complexes. **Complex 1b** was employed to exemplify the mechanism

III.4. Conclusions:

In this study, a series of novel rhenium benzo[d]oxazole complexes were synthesized and evaluated for their catalytic activity in the photoreduction of CO_2 to CO. These complexes exhibited distinct phosphorescence properties, with emissions arising from both π-π* ligand-centered transitions and metal-to-ligand charge transfer (^{3}MLCT) transitions. Our findings demonstrate that all synthesized complexes achieve exceptional selectivity for CO_2 to CO conversion, exceeding 99% under photochemical conditions.

A key observation was that increasing the conjugation within the ligand framework induces a redshift in the ^{3}MLCT absorption band, extending its transition into the visible region. This enhancement enables more conjugated complexes to function as efficient photocatalysts under visible light irradiation without requiring an additional photosensitizer. Notably, these newly developed complexes exhibit approximately fivefold higher photocatalytic activity compared to conventional rhenium bipyridine systems. Furthermore, the tunability of the ligand structure allows for the development of self-sensitized photocatalysts, presenting a promising avenue for future research.

Additionally, the impact of ligand modifications on catalytic performance was systematically investigated. While an increase in Re–Cl bond length was anticipated to correlate with enhanced catalytic activity, following the ligand variation from pyridine to quinoline and isoquinoline the observed catalytic performance exhibited an inverse trend. This finding suggests that factors beyond Re–Cl bond length play a decisive role in governing overall catalytic efficiency. These insights contribute to the rational design of next-generation rhenium-based photocatalysts with improved performance and stability, advancing efforts toward sustainable CO_2 conversion technologies.

III.5. References

1. J. Bednar, M. Obersteiner, A. Baklanov, M. Thomson, F. Wagner, O. Geden, M. Allen, J. W. Hall, *Nature,* 2021, **596**, 377-383.
2. S. Berardi, S. Drouet, L. Francas, C. Gimbert-Surinach, M. Guttentag, C. Richmond, T. Stoll, A. Llobet, *Chem Soc Rev.*, 2014, **43**, 7501-7519.
3. D. G. Nocera, *Acc. Chem. Res.*, 2017, **50**, 616-619.
4. H. Rao, L. C. Schmidt, J. Bonin and M. Robert, *Nature*, 2017, **548**, 74-77.
5. T. Ouyang, H. H. Huang, J. W. Wang, D. C. Zhong and T. B. Lu, *Angew Chem Int Ed Engl*, 2017, **56**, 738-743.
6. D. Hong, Y. Tsukakoshi, H. Kotani, T. Ishizuka and T. Kojima, *J Am Chem Soc*, 2017, **139**, 6538-6541.
7. H. Takeda, H. Kamiyama, K. Okamoto, M. Irimajiri, T. Mizutani, K. Koike, A. Sekine and O. Ishitani, *J Am Chem Soc*, 2018, **140**, 17241-17254.
8. N. Elgrishi, M. B. Chambers, X. Wang and M. Fontecave, *Chem Soc Rev*, 2017, **46**, 761-796.
9. S. Zhang, Q. Fan, R. Xia and T. J. Meyer, *Acc Chem Res*, 2020, **53**, 255-264.
10. S. Sato, T. Morikawa, T. Kajino and O. Ishitani, *Angew Chem Int Ed Engl*, 2013, **52**, 988-992.
11. S. Sato and T. Morikawa, *ChemPhotoChem*, 2017, **2**, 207-212.
12. K. Kamada, J. Jung, T. Wakabayashi, K. Sekizawa, S. Sato, T. Morikawa, S. Fukuzumi and S. Saito, *J Am Chem Soc*, 2020, **142**, 10261-10266.
13. L. Y. Peng, G. N. Pan, W. K. Chen, X. Y. Liu, W. H. Fang and G. Cui, *Angew Chem Int Ed Engl*, 2024, **63**, e202315300.
14. S. Das, R. R. Rodrigues, R. W. Lamb, F. Qu, E. Reinheimer, C. M. Boudreaux, C. E. Webster, J. H. Delcamp and E. T. Papish, *Inorg Chem*, 2019, **58**, 8012-8020.
15. Y. Arikawa, I. Tabata, Y. Miura, H. Tajiri, Y. Seto, S. Horiuchi, E. Sakuda and K. Umakoshi, *Chemistry*, 2020, **26**, 5603-5606.

16. D. J. Boston, C. Xu, D. W. Armstrong and F. M. MacDonnell, *J Am Chem Soc*, 2013, **135**, 16252-16255.

17. R. N. Sampaio, D. C. Grills, D. E. Polyansky, D. J. Szalda and E. Fujita, *J Am Chem Soc*, 2020, **142**, 2413-2428.

18. S. Gonell, M. D. Massey, I. P. Moseley, C. K. Schauer, J. T. Muckerman and A. J. M. Miller, *J Am Chem Soc*, 2019, **141**, 6658-6671.

19. J. Palion-Gazda, K. Choroba, M. Penkala, P. Rawicka and B. Machura, *Inorg Chem*, 2024, **63**, 1356-1366.

20. R. Giereth, P. Lang, E. McQueen, X. Meißner, B. Braun-Cula, C. Marchfelder, M. Obermeier, M. Schwalbe and S. Tschierlei, *ACS Catalysis*, 2020, **11**, 390-403.

21. C. J. Stanton, C. W. Machan, J. E. Vandezande, T. Jin, G. F. Majetich, H. F. Schaefer, C. P. Kubiak, G. Li and J. Agarwal, *Inorg Chem*, 2016, **55**, 3136-3144.

22. A. J. Huckaba, E. A. Sharpe and J. H. Delcamp, *Inorg Chem*, 2016, **55**, 682-690.

23. H. Takeda, K. Koike, H. Inoue, O. Ishitani, *J. AM. CHEM. SOC*. 2008, **130**, 2023-2031.

24. S. Fernandez, F. Franco, C. Casadevall, V. Martin-Diaconescu, J. M. Luis and J. Lloret-Fillol, *J Am Chem Soc*, 2020, **142**, 120-133.

25. Z. Guo, S. Cheng, C. Cometto, E. Anxolabehere-Mallart, S. M. Ng, C. C. Ko, G. Liu, L. Chen, M. Robert and T. C. Lau, *J Am Chem Soc*, 2016, **138**, 9413-9416.

26. T. Jin, C. Liu and G. Li, *Chem Commun*, 2014, **50**, 6221-6224.

27. F. Wang, B. Cao, W.-P. To, C.-W. Tse, K. Li, X.-Y. Chang, C. Zang, S. L.-F. Chan and C.-M. Che, *Catalysis Science & Technology*, 2016, **6**, 7408-7420.

28. Y. Wei, L. Chen, H. Chen, L. Cai, G. Tan, Y. Qiu, Q. Xiang, G. Chen, T. C. Lau and M. Robert, *Angew Chem Int Ed Engl*, 2022, **61**, e202116832.

29. J. Bonin, M. Robert and M. Routier, *J Am Chem Soc*, 2014, **136**, 16768-16771.

30. J. Bonin, M. Chaussemier, M. Robert and M. Routier, *ChemCatChem*, 2014, **6**, 3200-3207.

31. Y. K. Zhang, L. Zhao, W. J. Xie, H. R. Li and L. N. He, *ChemSusChem*, 2024, **17**, e202400090.

32. T. Wakabayashi, K. Kamada, K. Sekizawa, S. Sato, T. Morikawa, J. Jung and S. Saito, *Organometallics*, 2022, **41**, 1865-1871.

33. Y. Wang, T. Liu, L. Chen and D. Chao, *Inorg Chem*, 2021, **60**, 5590-5597.

34. D. Hong, Y. Tsukakoshi, H. Kotani, T. Ishizuka and T. Kojima, *J Am Chem Soc*, 2017, **139**, 6538-6541.

35. S. E. Lee, A. Nasirian, Y. E

36. . Kim, P. T. Fard, Y. Kim, B. Jeong, S. J. Kim, J. O. Baeg and J. Kim, *J Am Chem Soc*, 2020, **142**, 19142-19149.

37. S. Y. Manafe, N. Le, E. C. Lambert, C. Curiac, D. Nugegoda, S. Das, L. A. Hunt, F. Qu, L. M. Whitt, I. Fedin, N. I. Hammer, C. E. Webster, J. H. Delcamp and E. T. Papish, *ACS Catalysis*, 2024, **14**, 6589-6602.

38. J.-W. Wang, H.-H. Huang, J.-K. Sun, D.-C. Zhong and T.-B. Lu, *ACS Catalysis*, 2018, **8**, 7612-7620.

39. H. Yuan, A. Krishna, Z. Wei, Y. Su, J. Chen, W. Hua, Z. Zheng, D. Song, Q. Mu, W. Pan, L. Xiao, J. Yan, G. Li, W. Yang, Z. Deng and Y. Peng, *J Am Chem Soc*, 2024, **146**, 10550-10558.

40. L. A. Hunt, S. Das, R. W. Lamb, D. Nugegoda, C. Curiac, M. T. Figgins, E. C. Lambert, F. Qu, N. I. Hammer, J. H. Delcamp, C. E. Webster and E. T. Papish, *ACS Catalysis*, 2023, **13**, 5986-5999.

41. A. M. Cancelliere, F. Puntoriero, S. Serroni, S. Campagna, Y. Tamaki, D. Saito and O. Ishitani, *Chem Sci*, 2020, **11**, 1556-1563.

42. S. K. Lee, M. Kondo, M. Okamura, T. Enomoto, G. Nakamura and S. Masaoka, *J Am Chem Soc*, 2018, **140**, 16899-16903.

43. N. P. Liyanage, W. Yang, S. Guertin, S. Sinha Roy, C. A. Carpenter, R. E. Adams, R. H. Schmehl, J. H. Delcamp and J. W. Jurss, *Chem Commun*, 2019, **55**, 993-996.

44. A. V. Müller, L. A. Faustino, K. T. de Oliveira, A. O. T. Patrocinio and A. S. Polo, *ACS Catalysis*, 2022, **13**, 633-646.

45. S. Sinha, A. Sonea, W. Shen, S. S. Hanson and J. J. Warren, *Inorg Chem*, 2019, **58**, 10454-10461.

46. K. Kamogawa, A. Santoro, A. M. Cancelliere, Y. Shimoda, K. Miyata, K. Onda, F. Puntoriero, S. Campagna, Y. Tamaki and O. Ishitani, *ACS Catalysis*, 2023, **13**, 9025-9032.

47. L. Q. Qiu, Z. W. Yang, X. Yao, X. Y. Li and L. N. He, *ChemSusChem*, 2022, **15**, e202200337.

48. S. Sato, T. Morikawa, T. Kajino and O. Ishitani, *Angew Chem Int Ed Engl*, 2013, **52**, 988-992.

49. L.-Q. Qiu, K.-H. Chen, Z.-W. Yang and L.-N. He, *Green Chemistry*, 2020, **22**, 8614-8622.

50. Q. Feng, C. Huang, Z. Chen, Z. Huang, H. H. Huang, H. Hu, F. Liang and D. Liu, *Inorg Chem*, 2023, **62**, 21416-21423.

51. J. Hawecker, J. M. Lehn, R. Ziessel, *J. Chem. Soc., Chem. Commun*, 1983, 536-538.

52. J. Hawecker, J.-M. Lehn, R. Ziessel, *Helv. Chim. Acta*, 1986, **69**, 1990−2012.

53. A. Chapovetsky, T. H. Do, R. Haiges, M. K. Takase and S. C. Marinescu, *J Am Chem Soc*, 2016, **138**, 5765-5768.

54. C. Riplinger, M. D. Sampson, A. M. Ritzmann, C. P. Kubiak and E. A. Carter, *J Am Chem Soc*, 2014, **136**, 16285-16298.

55. S. Sung, X. Li, L. M. Wolf, J. R. Meeder, N. S. Bhuvanesh, K. A. Grice, J. A. Panetier and M. Nippe, *J Am Chem Soc*, 2019, **141**, 6569-6582.

56. J. K. Nganga, L. M. Wolf, K. Mullick, E. Reinheimer, C. Saucedo, M. E. Wilson, K. A. Grice, M. Z. Ertem and A. M. Angeles-Boza, *Inorg Chem*, 2021, **60**, 3572-3584.

57. J. K. Nganga, C. R. Samanamu, J. M. Tanski, C. Pacheco, C. Saucedo, V. S. Batista, K. A. Grice, M. Z. Ertem and A. M. Angeles-Boza, *Inorg Chem*, 2017, **56**, 3214-3226.

58. R. Czerwieniec, A. Kapturkiewicz, J. Lipkowski and J. Nowacki, *Inorganica Chimica Acta*, 2005, **358**, 2701-2710.

59. A. Albertino, C. Garino, S. Ghiani, R. Gobetto, C. Nervi, L. Salassa, E. Rosenberg, A. Sharmin, G. Viscardi, R. Buscaino, G. Croce and M. Milanesio, *Journal of Organometallic Chemistry*, 2007, **692**, 1377-1391.

60. C. J. Stanton, 3rd, C. W. Machan, J. E. Vandezande, T. Jin, G. F. Majetich, H. F. Schaefer, 3rd, C. P. Kubiak, G. Li and J. Agarwal, *Inorg Chem*, 2016, **55**, 3136-3144.

61. J. Agarwal, T. W. Shaw, C. J. Stanton, 3rd, G. F. Majetich, A. B. Bocarsly and H. F. Schaefer, 3rd, *Angew Chem Int Ed Engl*, 2014, **53**, 5152-5155

62. Y. Kuramochi, J. Itabashi, K. Fukaya, A. Enomoto, M. Yoshida and H. Ishida, *Chem Sci*, 2015, **6**, 3063-3074.

63. Z. C. Fu, C. Mi, Y. Sun, Z. Yang, Q. Q. Xu and W. F. Fu, *Molecules*, 2019, **24**.

64. A. C. Tsipis and A. A. Sarantou, Dalton Trans, 2021, 50, 14797-14809.

65. S. Roy, B. Sharma, J. Pécaut, P. Simon, M. Fontecave, P. D. Tran, E. Derat, V. Artero, *J Am Chem Soc*, 2017, **139**, 3685−3696.

66. U. Shee, D. Sinha, S. Mondal, K. K. Rajak, *Dalton Trans.*, 2024, **53**, 8254-8263

Chapter IV

Design Evolution of Ruthenium Polypyridyl Complexes: Achieving Self-Sensitized CO_2 Photoreduction via BODIPY Incorporation

IV. 1. INTRODUCTION

The escalating atmospheric concentration of carbon dioxide (CO_2), a primary driver of climate change[1], necessitates the development of sustainable technologies for its conversion into valuable chemical feedstocks. Fossil fuels, the dominant energy source, contribute significantly to anthropogenic CO_2 emissions, prompting research into renewable alternatives[2]. Sunlight, an abundant and clean energy source, offers a promising pathway for photocatalytic CO_2 reduction, enabling the synthesis of fuels and commodity chemicals such as carbon monoxide (CO), methane (CH_4), formic acid (HCOOH) etc[3].

Photochemical CO_2 reduction has witnessed substantial progress, with catalysts based on various transition metals, including Ir[4], Ru[5], Re[6] etc. demonstrating catalytic activity. However, a significant challenge lies in achieving efficient and selective CO_2 reduction in aqueous environments due to the competitive proton reduction reaction.

Photocatalytic CO_2 reduction systems typically consist of three fundamental components: a photosensitizer for light absorption and energy capture, an electron donor to supply reducing equivalents, and a catalyst to drive CO_2 reduction. While conventional molecular systems often employ a two-component approach, where the photosensitizer and catalyst function separately, the development of self-photosensitizing mononuclear complexes has introduced a more efficient strategy by integrating light absorption and catalytic activity within a single molecular entity. Building upon this concept, homogeneous catalytic systems utilizing molecular dyads, in which a photosensitizer and a carbon dioxide reduction catalyst are covalently linked, have garnered significant attention for their potential in achieving efficient CO_2 conversion[7]. These systems operate through an elegant mechanism involving intramolecular electron transfer. Upon photoexcitation of the photosensitizer and subsequent reductive quenching by an external electron donor, the resulting reduced photosensitizer moiety facilitates electron transfer to the proximally bound CO_2 reduction catalyst, thereby initiating the catalytic cycle. This approach offers the advantage of minimizing diffusional limitations and promoting faster reaction kinetics by keeping the active components in close proximity.

Building upon the quest for efficient light-harvesting components in artificial photosynthesis, recent advancements have explored the incorporation of Boron-dipyrromethene (BODIPY) derivatives into catalyst frameworks[8]. Characterized by their sharp absorption in the visible light region and high molar extinction coefficients, BODIPY dyes present themselves as excellent candidates for light-harvesting applications relevant to CO_2 reduction[9]. While

BODIPYs have found widespread use as triplet photosensitizers in photoredox catalysis, solar energy conversion, and photodynamic therapy, their superior fluorescent properties also make them highly attractive as functional organic fluorescent dyes with main absorption bands typically around 500 nm. Modifications to the BODIPY core structure by incorporating electron-donating substituents and π-conjugation systems allow for tuning of their photophysical properties, potentially leading to enhanced performance in photocatalytic CO_2 reduction systems[10].

Motivated by the potential of molecular dyads and self-photosensitizing systems for efficient CO_2 reduction, and inspired by the favorable photophysical properties of BODIPY derivatives, this study investigates a series of novel ruthenium complexes strategically designed to incorporate both substituted bis(2-picolyl)amine and bipyridine ligands alongside a BF_2-chelated dipyrromethane moiety. Furthermore, the BODIPY moieties within these complexes are modified by incorporating different electron-donating substituents. The primary aim of this research is to enhance light harvesting capabilities and catalytic activity within a single molecular framework to achieve efficient CO_2 reduction. Consequently, this work specifically focuses on the photocatalytic reduction of CO_2 to carbon monoxide using these novel ruthenium complexes under visible light irradiation. To gain a comprehensive understanding of the catalytic process, the study explores the influence of various reaction parameters, including solvent effects, the temporal evolution of the product, and the selectivity of the reaction. Complementary electrochemical studies are also conducted to thoroughly assess the redox properties of the synthesized complexes in relation to their ability to facilitate CO_2 reduction.

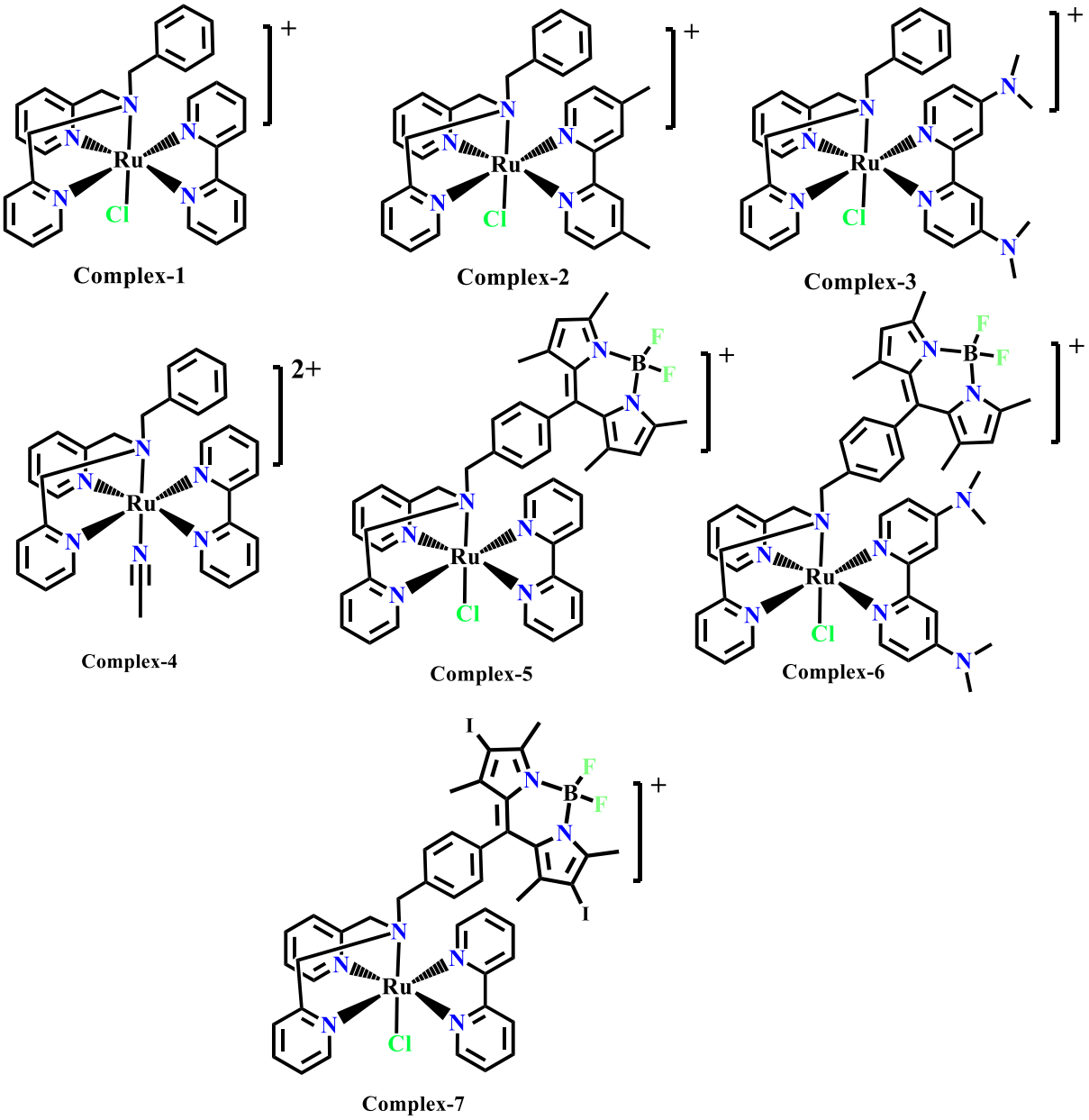

Figure IV.1 Structure of the catalysts.

IV.2. Result and Discussion

IV.2.1 Materials:

Acetonitrile, toluene, hexane, ethyl acetate, methanol, ethanol, dichloromethane, N,N-dimethylformamide, and triethylamine were procured from Merck and dried before use. The compounds bis(pyridin-2-ylmethyl)amine, benzaldehyde, 2,4-dimethyl-1H-pyrrole, 4-(chloromethyl)benzoyl chloride, 2,2'-bipyridine, 4,4'-dimethyl-2,2'-bipyridine, 4,4'-bis(N,N-dimethylamino)-2,2'-bipyridine, 2,3-dihydro-1,3-dimethyl-2-phenylbenzimidazole (BIH), Boron Trifluoride Diethyl Etherate, N-Iodosuccinimide (NIS) and ruthenium trichloride were purchased from Sigma-Aldrich. Tetrabutylammonium hexafluorophosphate ($[nBu_4N]PF_6$) of electrochemical grade and ≥99.0% purity was also obtained from Sigma-Aldrich.

IV.2.2 Synthesis:

Synthesis of ligand N,N-bis-(2-pyridylmethyl)benzylamine (dpba):

The ligand **dpba** was synthesized following a modified procedure based on reported methods. Benzaldehyde (1 mmol) was dissolved in methanol (10 mL), and N,N-bis-(2-pyridylmethyl)amine (1 mmol) was added to the solution. Subsequently, two drops of acetic acid were introduced, and the mixture was stirred. Sodium cyanoborohydride (1 mmol) was then added under an argon atmosphere, and the reaction mixture was stirred at room temperature for 72 hours. After completion, the reaction mixture was acidified with dilute hydrochloric acid to neutralize any excess sodium cyanoborohydride and then dried. The mixture was washed with water (3 × 10 mL) and extracted with dichloromethane. The organic layer was concentrated under reduced pressure. The crude product was purified by column chromatography on silica gel using a dichloromethane/ethanol gradient (from 100:0 to 90:10 v/v) to afford the pure ligand as an orange oil. ^{1}H NMR (400 MHz, $CDCl_3$) δ 8.42 (q, *J* = 6.3, 5.5 Hz, 2H), 7.53 (h, *J* = 6.9 Hz, 4H), 7.34 (q, *J* = 7.0, 6.4 Hz, 2H), 7.28 – 7.19 (m, 2H), 7.18 – 7.10 (m, 1H), 7.03 (dq, *J* = 10.5, 5.6, 4.6 Hz, 2H), 3.88 – 3.49 (m, 6H). ^{13}C NMR (101 MHz, $CDCl_3$) δ 159.63, 159.61, 157.73, 149.24, 148.91, 148.80, 148.78, 138.85, 138.83, 136.72, 136.50, 128.80, 128.28, 127.80, 127.78, 127.05, 126.79, 126.77, 123.10, 123.07, 122.80, 122.50, 121.98, 121.69, 77.73, 77.41, 77.10, 64.30, 60.14, 59.86, 59.84, 58.50, 58.48, 58.16, 57.00.

Synthesis of the ligand dpba-bdp:

The step-by-step procedure is illustrated in **Scheme IV.1**. The compound was synthesized according to a modified version of a previously reported method. First, dichloromethane was

deoxygenated by bubbling nitrogen gas through it. To the deoxygenated solvent, 1 equivalent of 4-(chloromethyl)benzoyl chloride and 2 equivalents of 2,4-dimethyl-1H-pyrrole were added. The reaction mixture was then heated at 50 °C for approximately 2 hours under an argon atmosphere. After cooling to room temperature, triethylamine was added, and the mixture was stirred for an additional 15 minutes. Subsequently, boron trifluoride diethyl etherate was added, and the reaction was heated again at 50 °C for about 2 hours. The reaction mixture was then dried, washed with water, extracted with DCM, and the crude product was purified by column chromatography on silica gel using a hexane/DCM (50:50 v/v) eluent. This yielded an orange solid, designated as intermediate **(i).** Next, the obtained orange solid was transferred to a round-bottom flask, and acetonitrile was added. Potassium iodide (KI), bis(pyridin-2-ylmethyl)amine, triethylamine, and two drops of water were then added to the solution. The mixture was stirred overnight at room temperature under an argon atmosphere. After completion, the reaction mixture was dried, washed with water, extracted with DCM, and the product was purified by column chromatography on silica gel using a DCM/methanol (10:1 v/v) eluent. The final product, **dpba-bdp**, was obtained as a deep orange-red oily material. ^{1}H NMR (300 MHz, $CDCl_3$) δ 8.56 (ddd, *J* = 4.9, 1.9, 0.9 Hz, 2H), 7.71 (td, *J* = 7.6, 1.8 Hz, 2H), 7.60 – 7.52 (m, 4H), 7.26 (d, *J* = 8.0 Hz, 3H), 7.19 (ddd, *J* = 7.4, 4.9, 1.3 Hz, 2H), 5.97 (s, 2H), 3.81 (d, *J* = 15.9 Hz, 6H), 2.57 (s, 6H), 1.66 (s, 6H). ^{13}C NMR (75 MHz, $CDCl_3$) δ 159.53, 155.85, 155.39, 149.38, 149.14, 149.04, 148.30, 143.06, 141.70, 139.89, 136.99, 136.56, 133.82, 131.47, 129.89, 127.95, 123.38, 122.85, 122.71, 122.36, 122.23, 122.13, 121.19, 63.34, 59.78, 58.11, 53.07, 44.76, 42.52, 14.58, 14.34.

Synthesis of the ligand dpba-bdp-I_2:

The ligand **dpba-bdp** was placed in a round-bottom flask and dissolved in dichloromethane (DCM). The solution was deoxygenated by bubbling argon through it. Subsequently, 2 equivalents of N-iodosuccinimide (NIS) were added gradually, and the reaction mixture was stirred at room temperature for approximately 2 hours under an argon atmosphere. After completion, the reaction mixture was dried, washed with water, and extracted with DCM. The crude product was purified by column chromatography on silica gel using a DCM/methanol (10:1 v/v) eluent, affording the ligand **dpba-bdp-I_2** as a solid deep pink-red product. ^{1}H NMR (400 MHz, $CDCl_3$) δ 8.58 (dd, *J* = 4.9, 1.6 Hz, 2H), 7.72 (td, *J* = 7.7, 1.8 Hz, 2H), 7.58 (t, *J* = 8.2 Hz, 4H), 7.21 (dd, *J* = 10.4, 6.7 Hz, 4H), 3.84 (d, *J* = 14.6 Hz, 6H), 2.66 (s, 6H), 1.36 (s, 6H). ^{13}C NMR (101 MHz, $CDCl_3$) δ 159.32, 156.74, 149.10, 145.28, 140.56, 136.61, 133.54, 131.35, 130.16, 127.80, 122.91, 122.20, 59.77, 58.01, 30.94, 29.71, 16.95, 16.02.

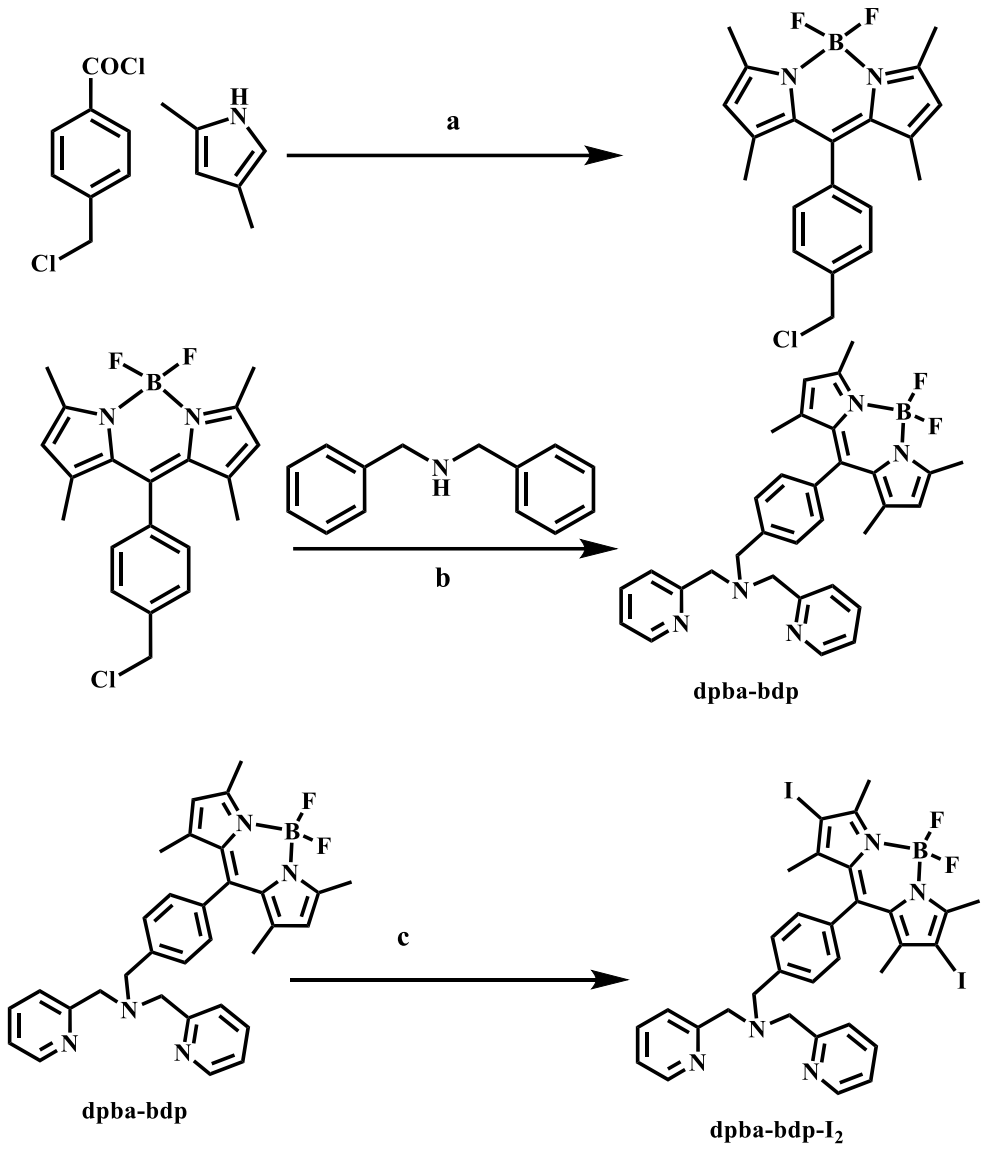

Scheme IV.1 Preparation of the ligands. **a) (i)** DCM, 50 °C, 80 min; **ii)** triethylamine, $BF_3.Et_2O$, CH_2Cl_2, 50 °C, 1 h; **(b)** Triethylamine, KI, Acetonitrile, 5 h R. T. **(c)** N-Iodosuccinimide (NIS), DCM, 2 h R.T.

Synthesis of the complex 1; [Ru(dpba)(bpy)Cl]Cl

$RuCl_3 \cdot 3H_2O$ (132.5 mg, 0.5 mmol) was refluxed in a degassed mixture of water and ethanol (1:4 v/v, 10 mL total) under a nitrogen atmosphere for about 5 hours, until the solution turned blue. Next, 1 mL of concentrated HCl was added, followed by the dropwise addition of 5 mL of an ethanolic solution of ligand **dpba**. The reaction mixture was then heated for an additional 5 hours and subsequently cooled to room temperature. The volume was adjusted to 5 mL, and the solution was refrigerated overnight, yielding a yellow precipitate, which was collected by filtration and washed with cold water. The resulting solid (100 mg, 0.2 mmol), lithium chloride (25 mg, 0.3 mmol), and **2,2′-bipyridine** (**bpy**) (0.2 mmol) were then placed in a round-bottom flask under nitrogen. To this, 10 mL of nitrogen-degassed ethanol containing trimethylamine (42 μL, 0.3 mmol) was added, and the mixture was refluxed overnight. After cooling to room temperature, the mixture was filtered, and the filtrate was concentrated under reduced pressure. The crude product was purified by column chromatography on neutral alumina using an acetonitrile/methanol mixture (20:1 v/v) as the eluent, affording the desired dark red solid. ^{1}H NMR (400 MHz, CD_3CN) δ 9.51 (d, *J* = 5.7 Hz, 2H), 8.55 – 8.48 (m, 4H), 8.01 – 7.94 (m, 2H), 7.71 (dd, *J* = 8.5, 7.0 Hz, 3H), 7.51 – 7.45 (m, 2H), 7.40 – 7.36 (m, 2H), 7.34 – 7.25 (m, 4H), 7.23 – 7.16 (m, 2H), 4.39 (d, *J* = 16.2 Hz, 2H), 3.77 (d, *J* = 16.4 Hz, 2H), 3.06 (d, *J* = 7.3 Hz, 2H). ^{13}C NMR (101 MHz, CD_3CN) δ 161.19, 158.61, 155.08, 154.78, 154.55, 152.54, 152.43, 151.96, 136.62, 136.37, 135.75, 135.44, 135.35, 135.27, 132.23, 132.10, 131.53, 130.64, 129.05, 128.84, 128.54, 126.12, 125.80, 125.68, 124.25, 123.92, 123.86, 123.33, 123.25, 122.91, 121.93, 121.37, 121.26, 67.78, 67.25, 65.85, 65.75, 65.11, 45.57.

Synthesis of the complex 2; [Ru(dpba)(bpy-Me)Cl]Cl

The complex was synthesized using the same procedure as for complex 1, except that bipyridine was replaced with 4,4'-dimethyl-2,2'-bipyridine. ^{1}H NMR (400 MHz, CD_3CN) δ 9.52 – 9.46 (m, 2H), 8.38 (s, 2H), 8.31 (d, *J* = 6.1 Hz, 2H), 7.71 – 7.68 (m, 2H), 7.40 – 7.24 (m, 9H), 7.18 (d, *J* = 7.4 Hz, 2H), 4.33 (d, *J* = 16.1 Hz, 2H), 3.74 (d, *J* = 16.4 Hz, 2H), 3.11 (s, 2H), 2.60 (s, 6H). ^{13}C NMR (101 MHz, CD_3CN) δ 163.68, 161.67, 161.31, 159.47, 158.77, 158.12, 154.87, 154.18, 153.83, 152.50, 152.10, 151.82, 148.72, 147.65, 147.51, 136.38, 135.46, 135.19, 132.20, 132.08, 131.50, 130.67, 129.04, 128.83, 128.55, 127.00, 126.75, 126.65, 124.16, 124.06, 124.01, 123.82, 123.71, 121.76, 121.25, 121.21, 67.62, 67.26, 65.76, 65.43, 65.04, 45.58, 29.36, 20.20, 20.11, 20.01.

Synthesis of the complex 3; [Ru(dpba)(bpy-NMe_2)Cl]Cl

The complex was synthesized using the same procedure as for complex 1, except that bipyridine was replaced with 4,4'-bis(N,N-dimethylamino)-2,2'-bipyridine. ^{1}H NMR (400 MHz, CD_3CN) δ 9.49 (d, *J* = 5.6 Hz, 2H), 7.87 (d, *J* = 6.6 Hz, 2H), 7.65 – 7.57 (m, 4H), 7.40 (dt, *J* = 14.4, 7.0 Hz, 3H), 7.21 (q, *J* = 8.4, 7.4 Hz, 6H), 6.69 (dd, *J* = 6.3, 3.0 Hz, 2H), 4.21 (d, *J* = 16.0 Hz, 2H), 3.71 (d, *J* = 16.0 Hz, 2H), 3.21 (d, *J* = 7.0 Hz, 14H). ^{13}C NMR (101 MHz, CD_3CN) δ 162.01, 158.05, 154.12, 152.86, 150.84, 134.32, 131.43, 130.96, 128.94, 128.56, 123.46, 120.81, 108.93, 105.86, 67.70, 67.61, 38.97.

Synthesis of the complex 4; [Ru(dpba)(bpy)CH_3CN][PF_6]$_2$

Complex 1 was dissolved in 10 mL of CH_3CN, and 2 equivalents of $AgBF_4$ were added. The reaction mixture was then heated at 50 °C for approximately 3 days. The product was purified by column chromatography using a CH_3CN:MeOH (10:1) eluent with adding NH_4PF_6. ^{1}H NMR (400 MHz, DMSO) δ 8.95 (d, *J* = 5.4 Hz, 2H), 8.82 (d, *J* = 8.5 Hz, 2H), 8.40 (d, *J* = 5.7 Hz, 2H), 8.23 (t, *J* = 8.0 Hz, 2H), 7.84 (t, *J* = 7.9 Hz, 2H), 7.72 – 7.63 (m, 2H), 7.47 – 7.35 (m, 7H), 7.30 (d, *J* = 7.8 Hz, 2H), 4.70 (d, *J* = 16.6 Hz, 2H), 3.97 (d, *J* = 16.6 Hz, 2H), 3.07 (s, 2H), 2.06 (t, *J* = 2.1 Hz, 3H). ^{13}C NMR (101 MHz, DMSO) δ 161.21, 157.56, 153.23, 152.03, 138.22, 137.77, 132.27, 130.59, 129.62, 128.96, 127.93, 126.49, 125.07, 124.59, 122.59, 79.37, 79.04, 67.12, 66.02, 4.56.

Synthesis of the complex 5; [Ru(dpba-bdp)(bpy)Cl]Cl

A solution of **dpba-bdp** (1.5 equivalent) in 4 mL of chloroform was added dropwise to a magnetically stirred solution of $RuCl_3 \cdot 3H_2O$ (1 equivalent) in 30 mL of dry ethanol under a nitrogen atmosphere. The mixture was heated at 75 °C for 4 h. The reaction volume was then reduced to approximately 10 mL, and the resulting precipitate was collected by filtration, washed thoroughly with methanol (100 mL) and diethyl ether, and dried under vacuum. The obtained orange solid was placed in a Schlenk flask together with lithium chloride and **bpy** ligand under nitrogen. Nitrogen-degassed ethanol (10 mL) containing triethylamine was added, and the reaction mixture was stirred at 75 °C in the dark for 16 h. After cooling, the mixture was filtered through a Celite pad, and the solvent was removed under reduced pressure. The crude product was purified by column chromatography on neutral alumina using an acetonitrile/methanol (9:1, v/v) mixture as eluent, affording the desired complex as a dark brown solid (51 mg, ~54% yield). ^{1}H NMR (400 MHz, DMSO) δ 9.37 (s, 2H), 8.74 (d, *J* = 8.7 Hz, 2H), 8.42 (d, *J* = 4.8 Hz, 2H), 8.04 (t, *J* = 8.0 Hz, 2H), 7.75 (t, *J* = 8.0 Hz, 3H), 7.58 – 7.13

(m, 9H), 6.21 – 6.03 (m, 2H), 4.61 (d, *J* = 16.1 Hz, 2H), 3.88 (d, *J* = 3.0 Hz, 2H), 3.15 (s, 2H), 2.50 (s, 6H), 1.30 – 1.17 (m, 6H).

Synthesis of the complex 6; [Ru(dpba-bdp)(bpy-NMe$_2$)Cl]Cl: The procedure for complex 5 was followed, except that 4,4′-bis(N,N-dimethylamino)-2,2′-bipyridine was used in place of bipyridine.^{1}H NMR (400 MHz, $CDCl_3$) δ 8.54 (s, 2H), 7.96 (d, *J* = 72.5 Hz, 8H), 7.54 (d, *J* = 73.9 Hz, 8H), 6.14 (s, 2H), 3.98 (s, 2H), 3.50 (d, *J* = 5.5 Hz, 2H), 3.33 (s, 2H), 2.65 (s, 6H), 1.68 (s, 18H).

Synthesis of the complex 7; [Ru(dpba-bdp-I$_2$)(bpy)Cl]Cl : The synthesis was carried out following the procedure for complex 5, except that dpba-bdp-I$_2$ was used in place of dpba-bdp. ^{1}H NMR (400 MHz, DMSO) δ 9.37 (s, 2H), 8.74 (d, *J* = 8.7 Hz, 2H), 8.42 (d, *J* = 4.8 Hz, 2H), 8.04 (t, *J* = 8.0 Hz, 2H), 7.75 (t, *J* = 8.0 Hz, 3H), 7.60 – 7.13 (m, 9H), 4.61 (d, *J* = 16.1 Hz, 2H), 3.93 – 3.81 (m, 2H), 3.15 (s, 2H), 2.50 (s, 6H), 1.31 – 1.17 (m, 6H).

IV.2.3. NMR spectra

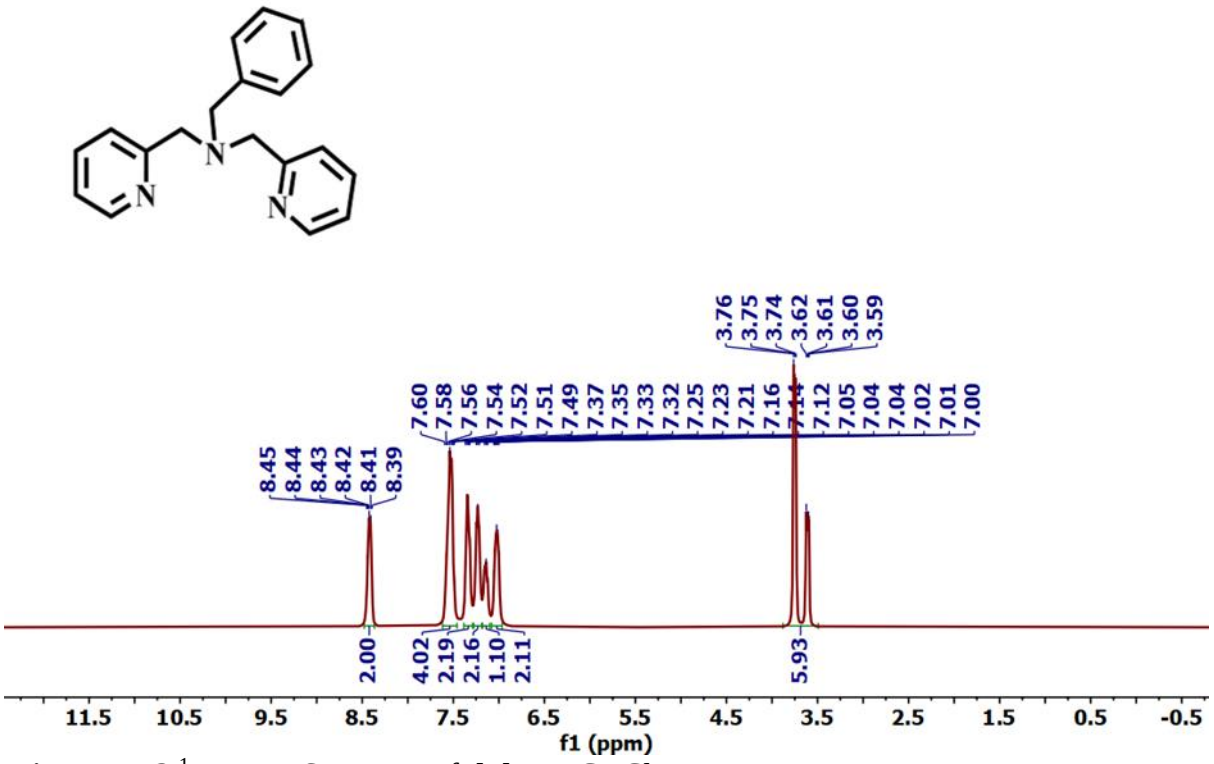

Figure IV.2 ^{1}H NMR Spectrum of **dpba** in $CDCl_3$.

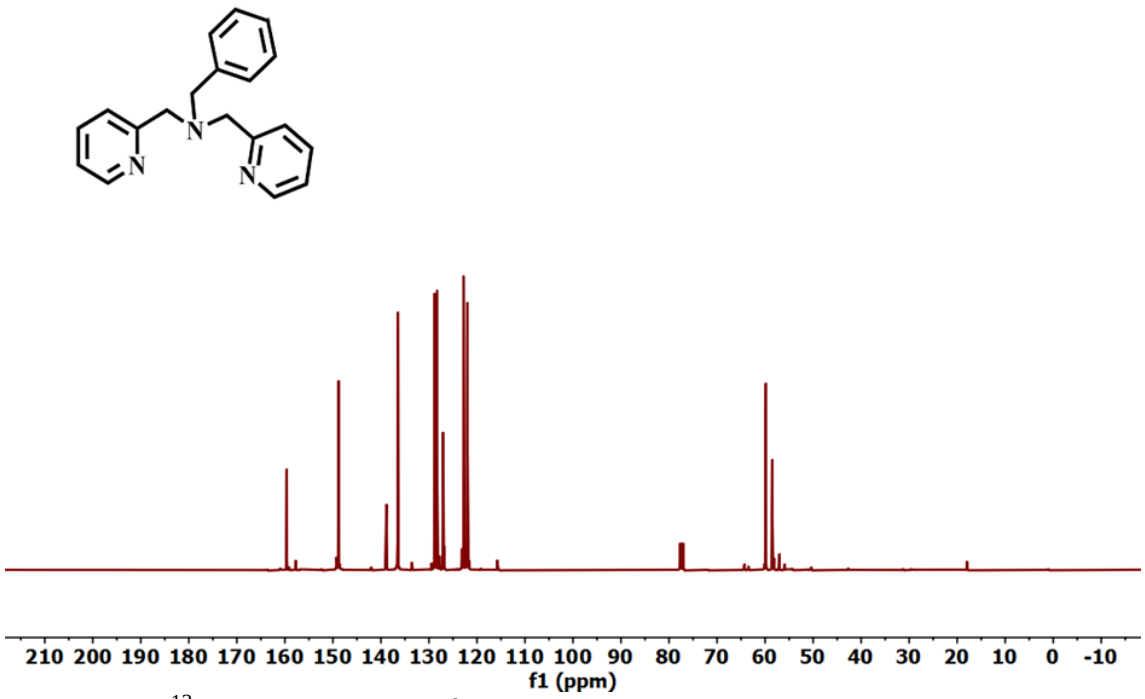

Figure IV.3 ^{13}C NMR Spectrum of **dpba** in $CDCl_3$.

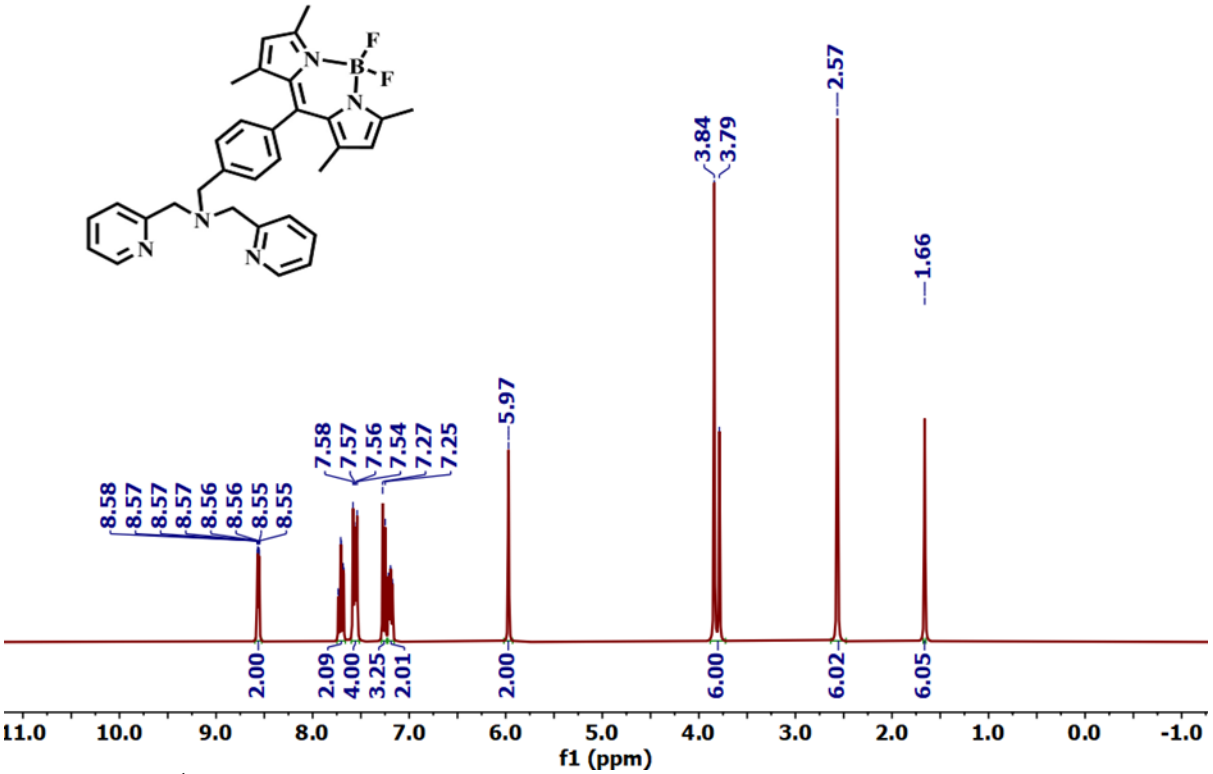

Figure IV.4 ^{1}H NMR Spectrum of **dpba-bdp** in $CDCl_3$.

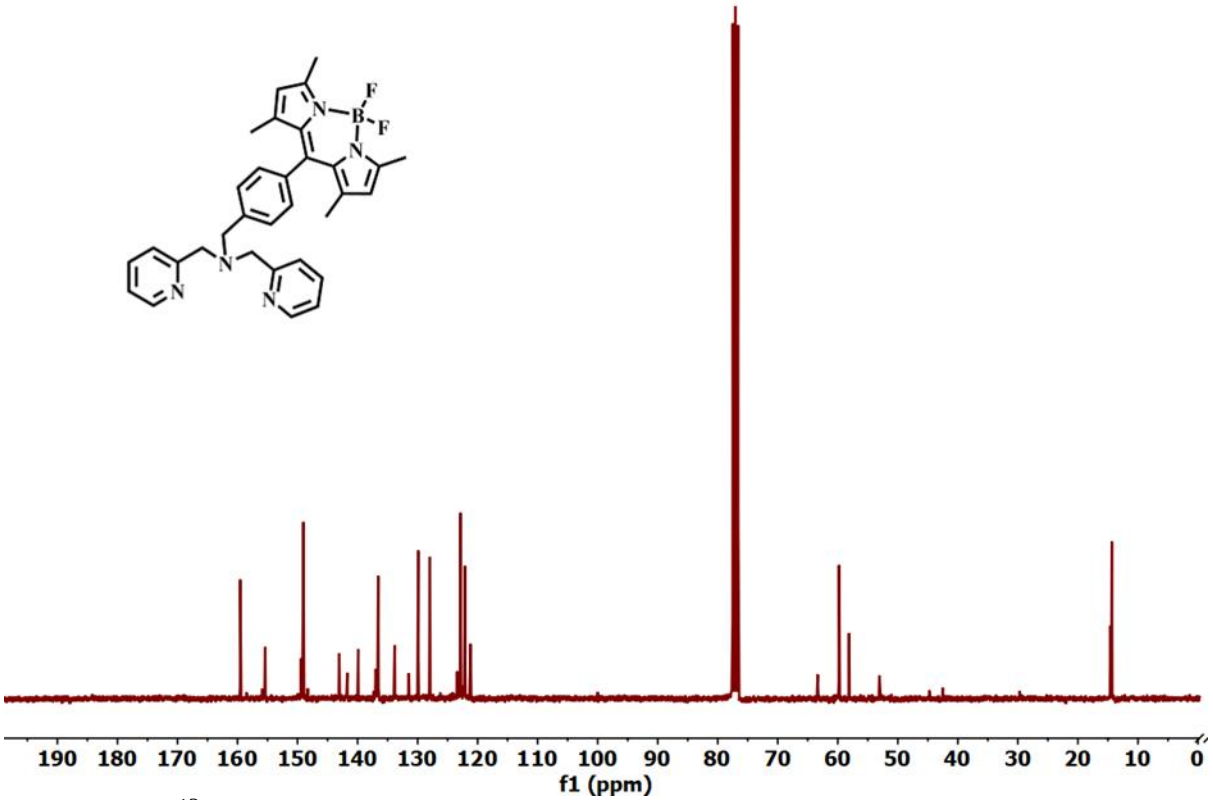

Figure IV.5 ^{13}C NMR Spectrum of **dpba-bdp** in $CDCl_3$.

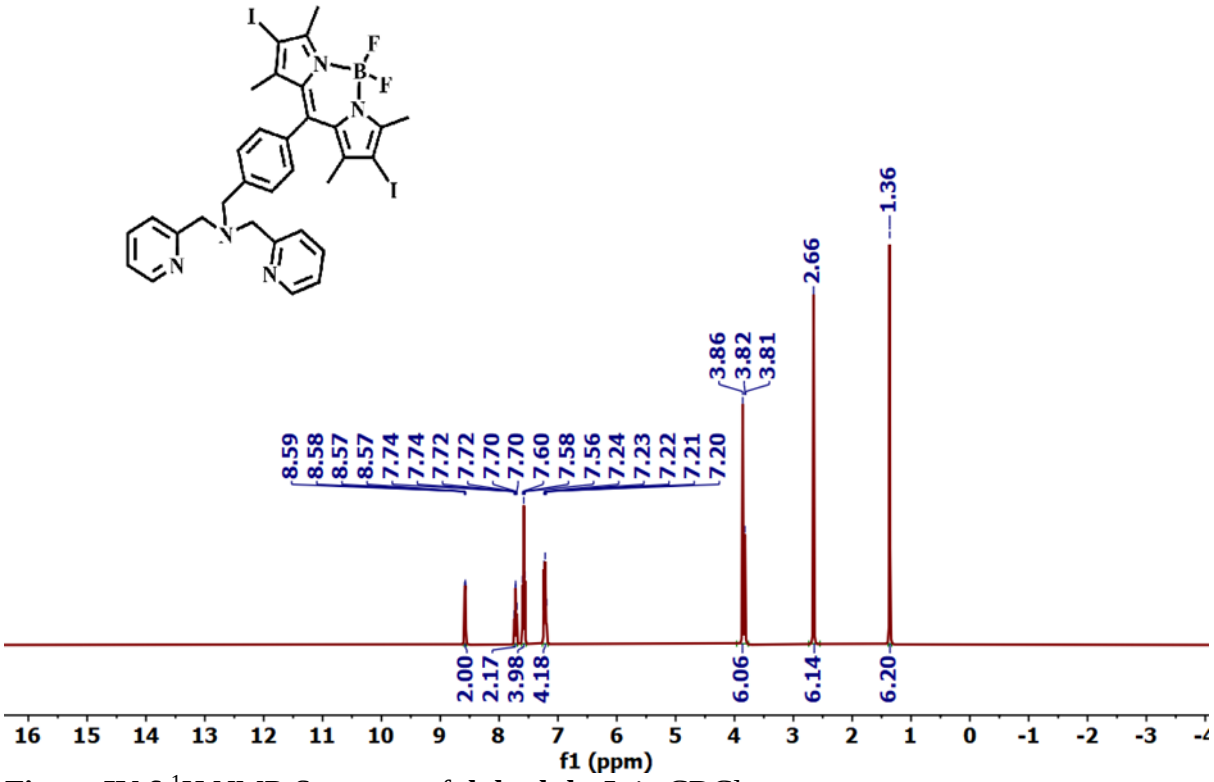

Figure IV.6 ^{1}H NMR Spectrum of **dpba-bdp-I$_2$** in $CDCl_3$

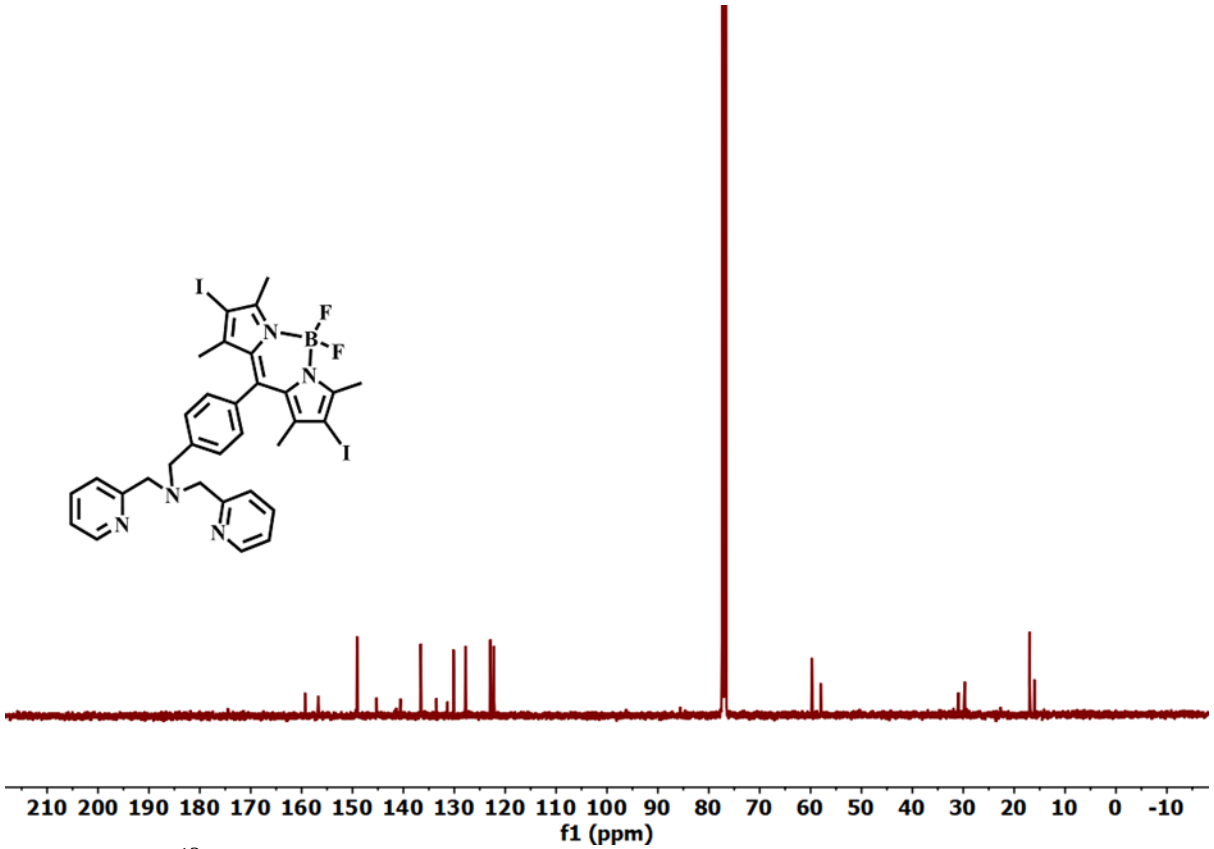

Figure IV.7 ^{13}C NMR Spectrum of **dpba-bdp-I$_2$** in $CDCl_3$

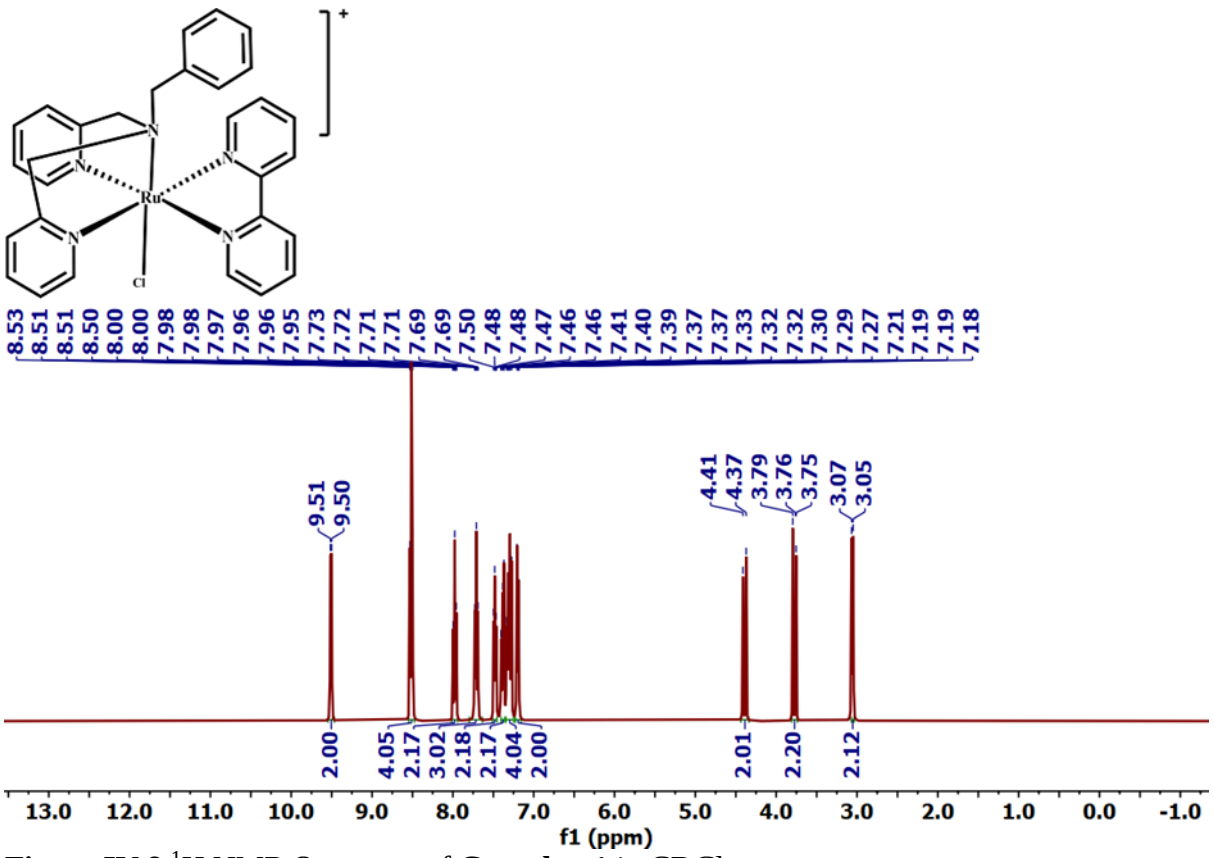

Figure IV.8 ^{1}H NMR Spectrum of **Complex-1** in $CDCl_3$

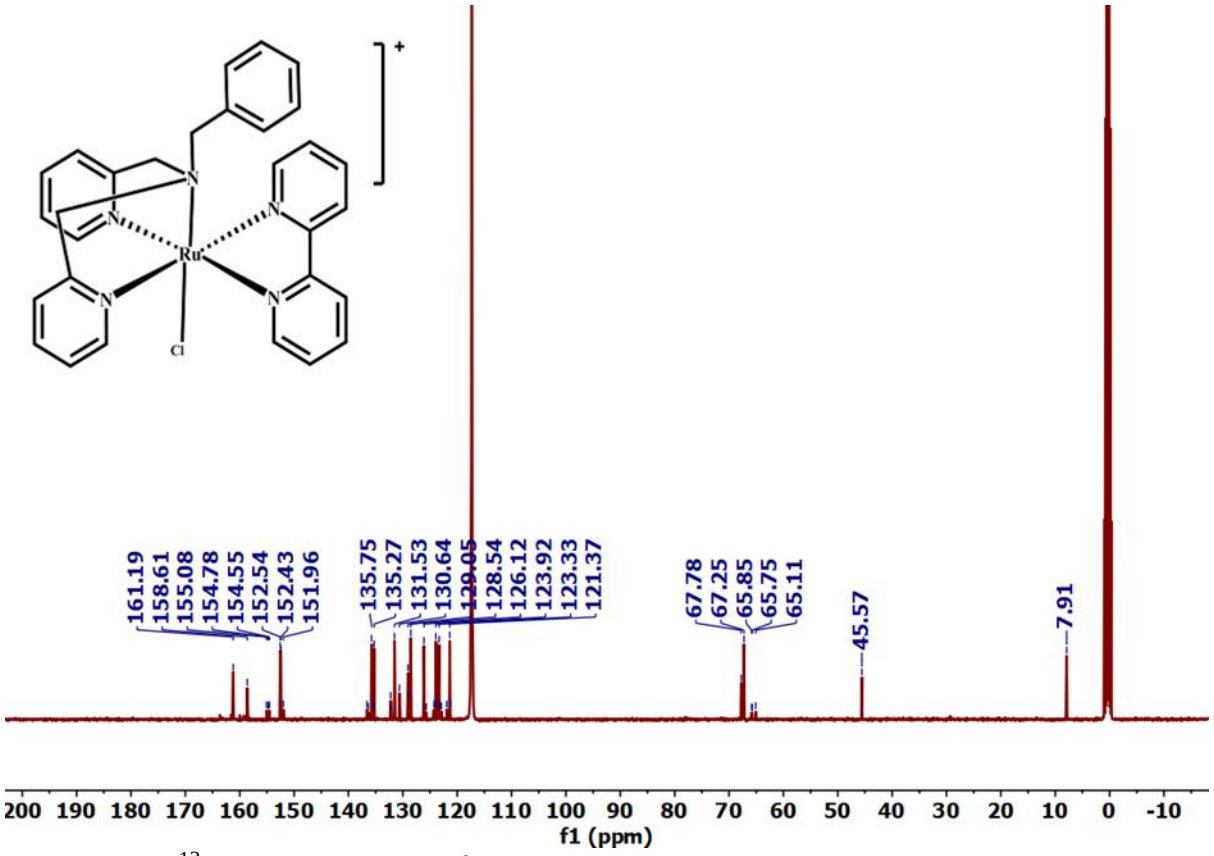

Figure IV.9 ^{13}C NMR Spectrum of **Complex-1** in $CDCl_3$

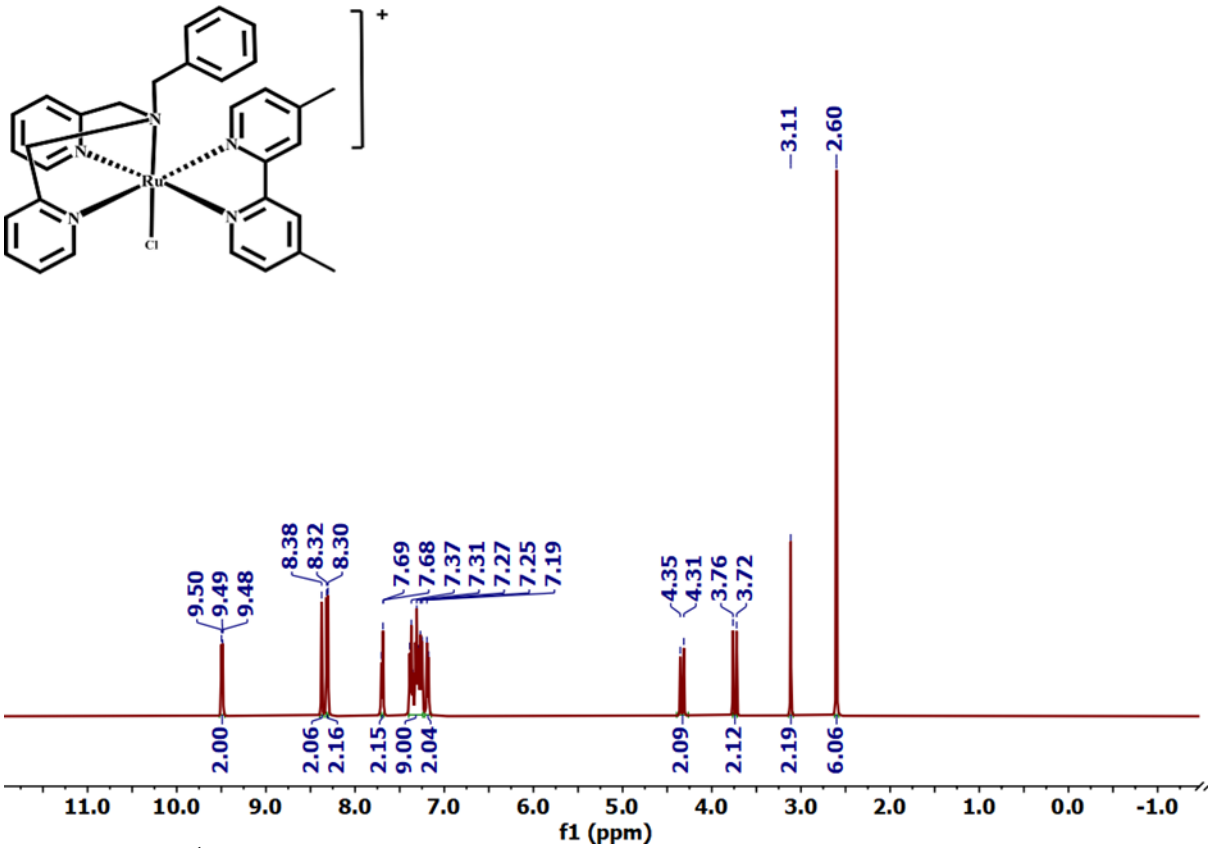

Figure IV.10 ^{1}H NMR Spectrum of **Complex-2** in $CDCl_3$

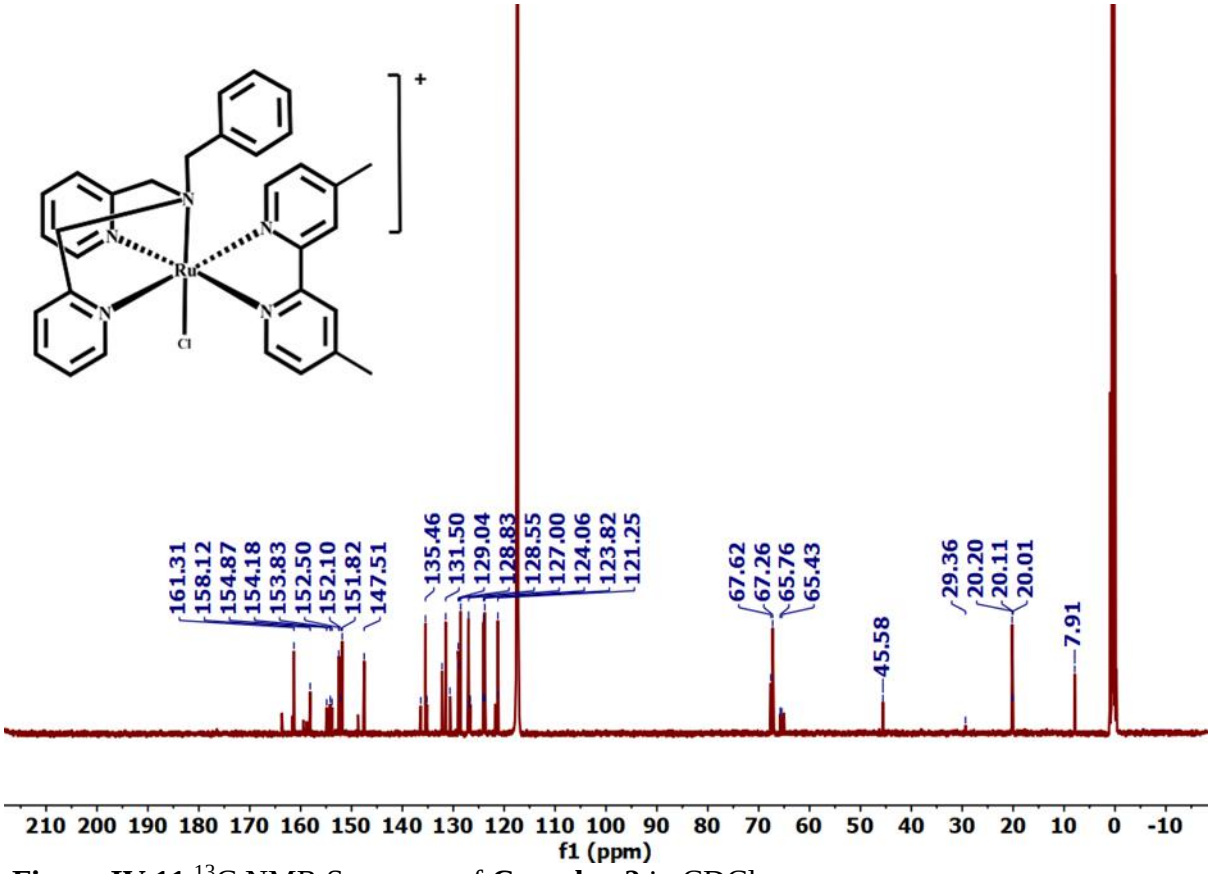

Figure IV.11 ^{13}C NMR Spectrum of **Complex-2** in $CDCl_3$

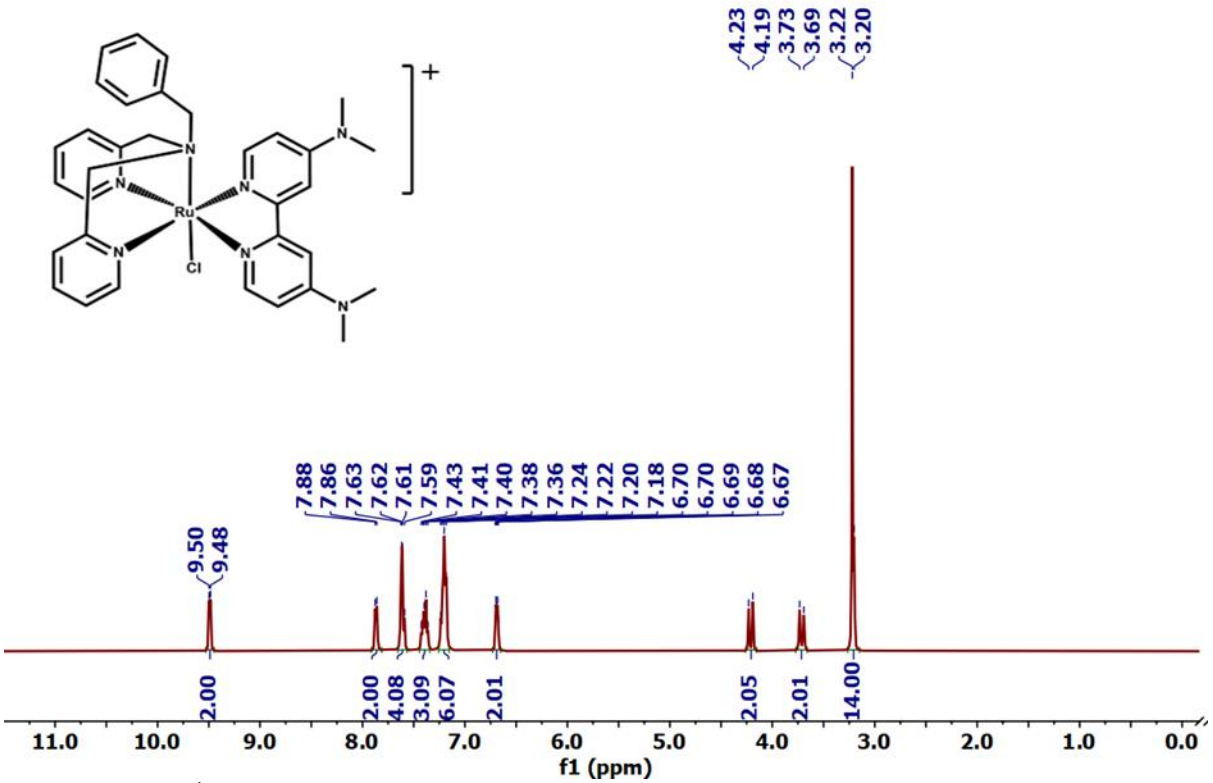

Figure IV.12 ^{1}H NMR Spectrum of **Complex-3** in $CDCl_3$

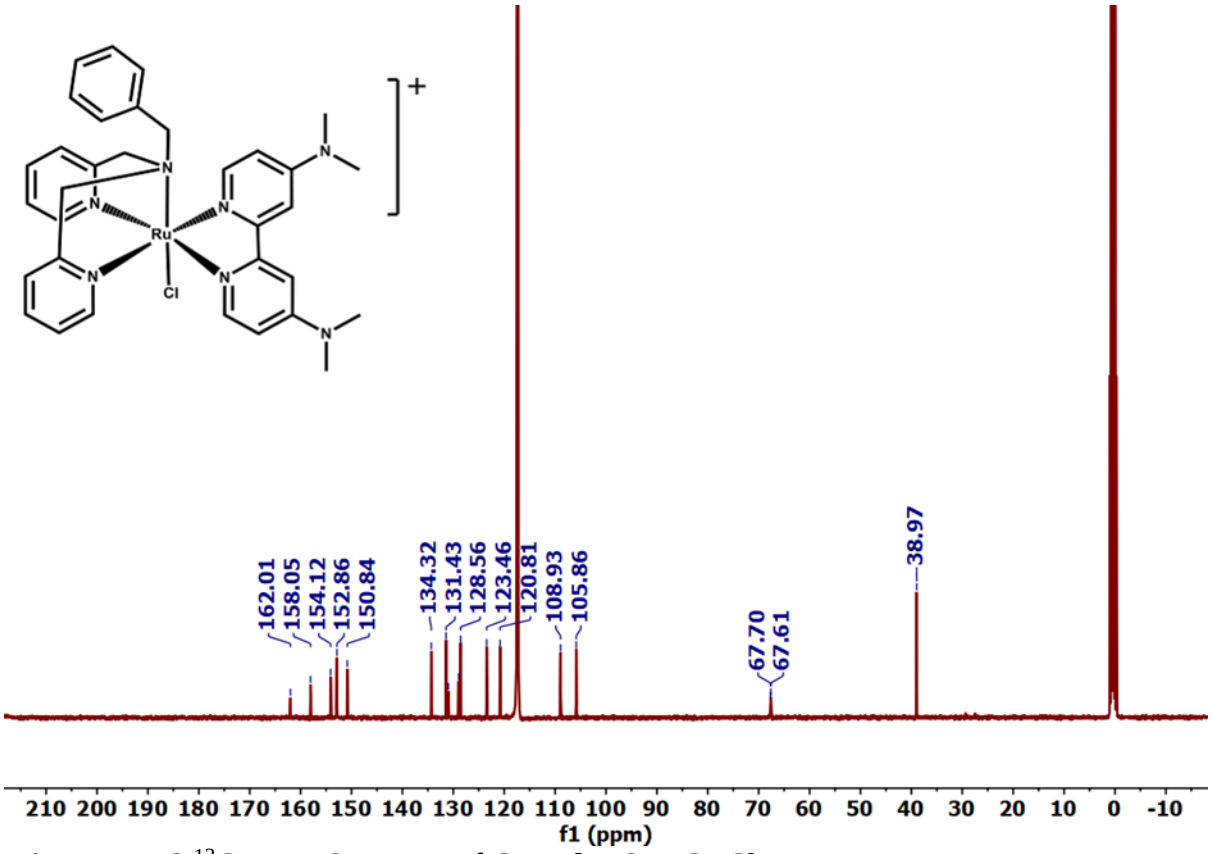

Figure IV.13 ^{13}C NMR Spectrum of **Complex-3** in $CDCl_3$

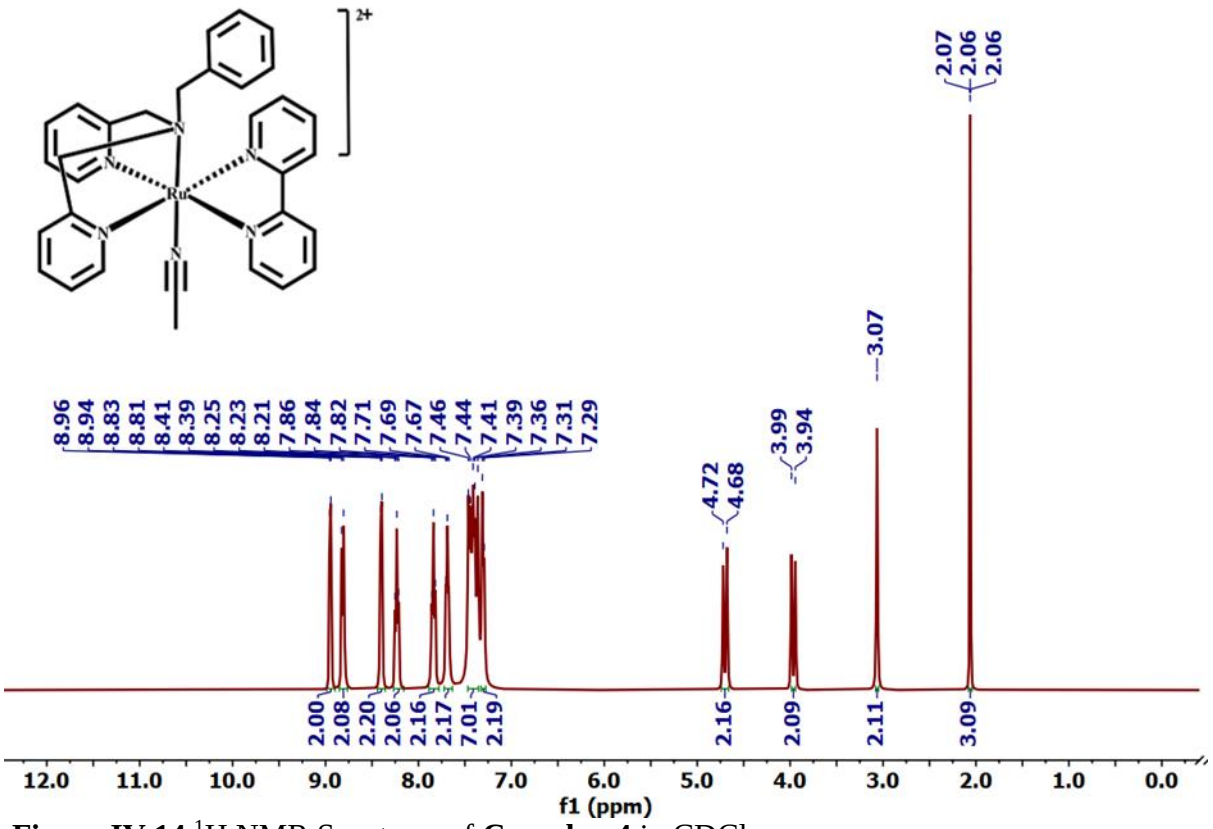

Figure IV.14 ^{1}H NMR Spectrum of **Complex-4** in $CDCl_3$

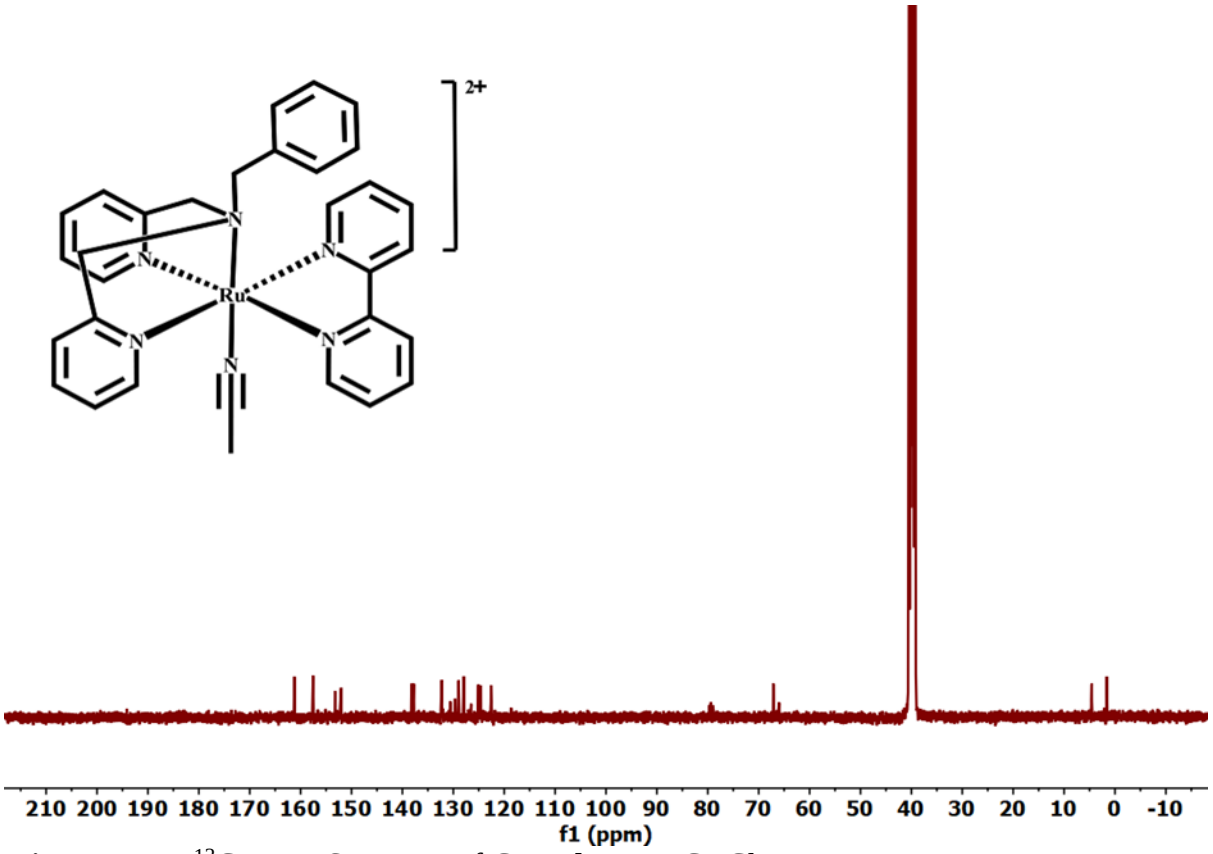

Figure IV.15 ^{13}C NMR Spectrum of **Complex-4** in $CDCl_3$

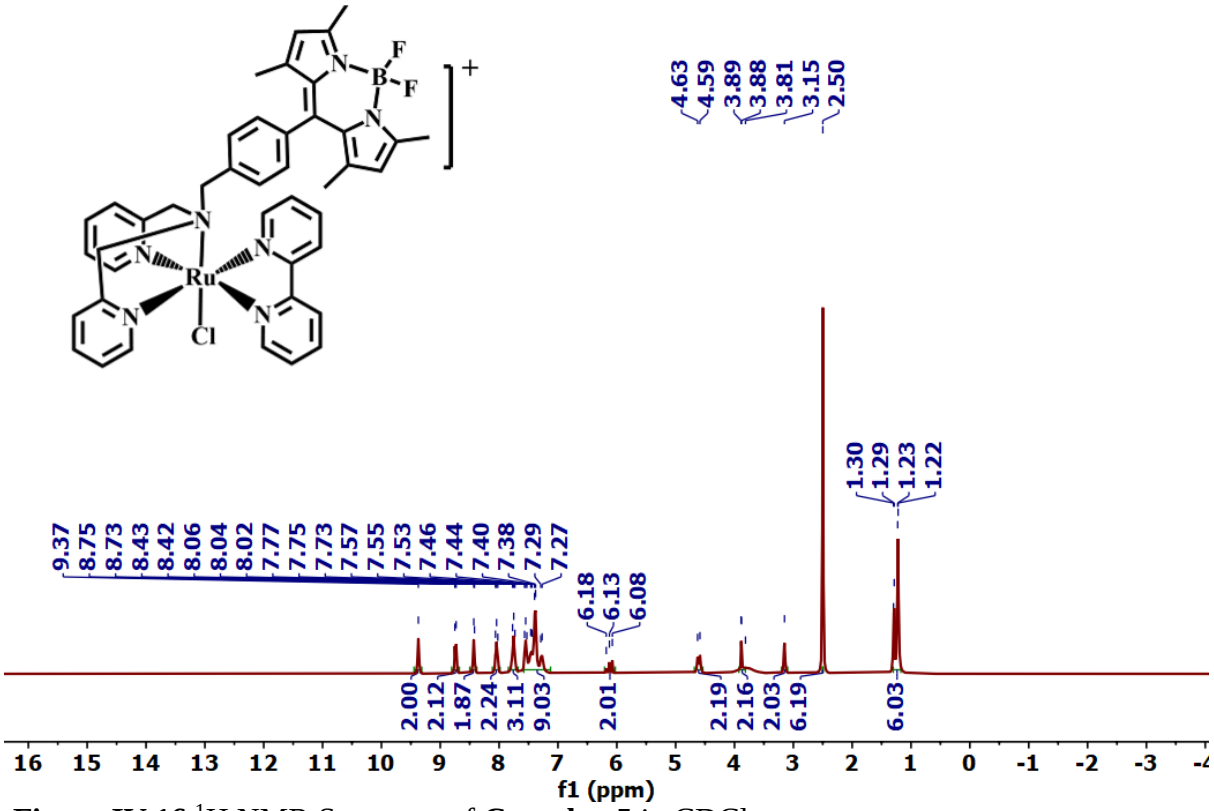

Figure IV.16 ^{1}H NMR Spectrum of **Complex-5** in $CDCl_3$

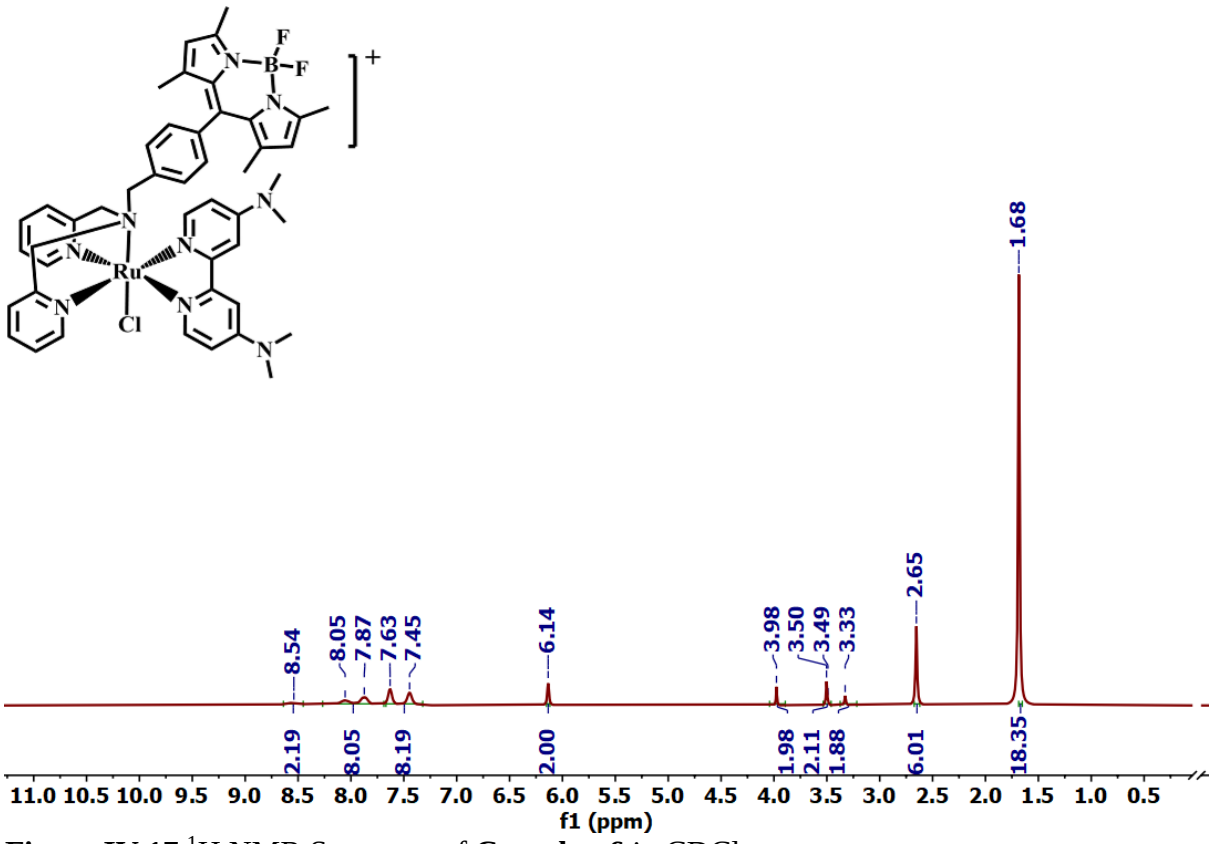

Figure IV.17 ^{1}H NMR Spectrum of **Complex-6** in $CDCl_3$

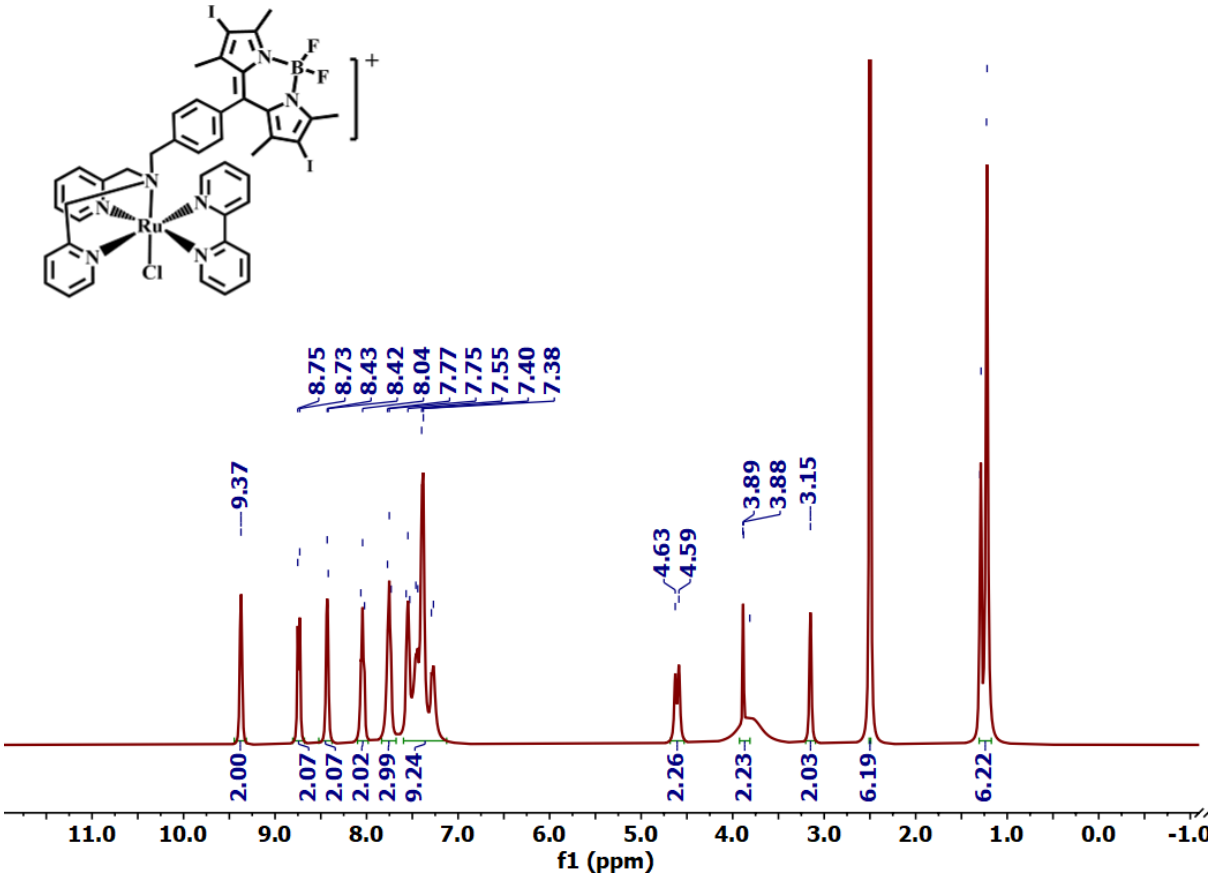

Figure IV.18 ^{1}H NMR Spectrum of **Complex-7** in $CDCl_3$

IV.2.4 Crystal Structures

Single-crystal X-ray diffraction analysis of complexes **1**, **2**, **3**, **4**, and **6** provides detailed insights into their structural features and comparative geometries. High-quality crystals suitable for X-ray studies were obtained by layering methanolic solutions of the respective complexes with diethyl ether. This comparative structural investigation reveals the coordination environments and geometric variations among the complexes. Thermal ellipsoid plots for each structure are presented in Tables **IV.1–IV.5**. All five complexes adopt a distorted octahedral coordination geometry, with closely comparable bond distances, indicating a high degree of structural consistency within this series. The crystallographic data have been deposited with the Cambridge Crystallographic Data Centre (CCDC) under deposition numbers **2333295**, **2471746**, **2335459**, **2471751**, and **2479497** respectively.

Table IV.1. crystallographic data of the **Complex 1.**

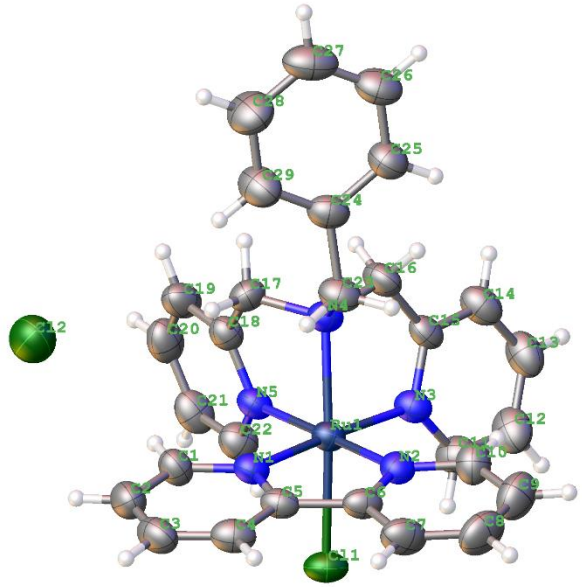

Complex-1	
CCDC No. 2333295	
Formula moiety	'C$_{29}$H$_{27}$ClN$_5$Ru,Cl'
Molecular weight	617.52
Crystal system	monoclinic
Space group	P 1 21/c 1
a/ Å	7.8797(9)
b/ Å	18.0830(17)
c/ Å	20.4461(18)
α/°	90
β/°	100.577(3)
γ/°	90
V/ Å^3	2863.8(5)
Z	4
Dcalcd /g cm^{-3}	1.432
Mu (mm-1)	0.770
T/K	296 K
R1 = 0.0566(3881)	
wR2 = 0.1562(6287)	
GOF on F2	0.983

Bond length(Å)	
Ru-N1	2.047(4)
Ru-N2	2.048(4)
Ru-N3	2.055(4)
Ru-N4	2.144(4)
Ru-N5	2.066(4)
Ru-Cl	2.4079(12)

Table IV.2. crystallographic data of the **Complex 2.**

<table>
<tr><td colspan="2" rowspan="13"> 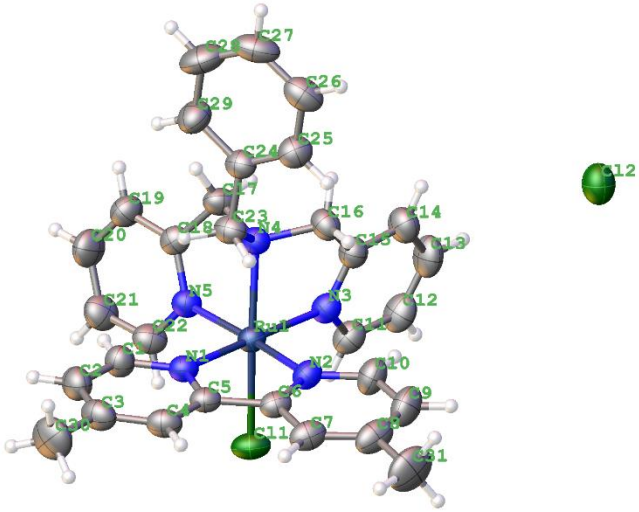 </td><td>Complex-2</td></tr>
<tr><td>CCDC No. 2471746</td></tr>
<tr><td>Formula moiety
$C_{30.968}H_{30.968}ClN_5$ Ru,Cl</td></tr>
<tr><td>Molecular weight 645.16</td></tr>
<tr><td>Crystal system monoclinic</td></tr>
<tr><td>Space group P 1 21/c 1</td></tr>
<tr><td>a/ Å 7.8383(12)</td></tr>
<tr><td>b/ Å 16.843(3)</td></tr>
<tr><td>c/ Å 23.938(4)</td></tr>
<tr><td>α/° 90</td></tr>
<tr><td>β/° 93.302(5)</td></tr>
<tr><td>γ/° 90</td></tr>
<tr><td>V/ $Å^3$ 3155.1(9)</td></tr>
<tr><td>Z 4</td></tr>
<tr><td>Dcalcd /g cm^{-3} 1.358</td></tr>
<tr><td colspan="2">Bond length(Å)</td><td>Mu (mm-1) 0.693</td></tr>
<tr><td>Ru-N1</td><td>2.050(2)</td><td>T/K 273 K</td></tr>
<tr><td>Ru-N2</td><td>2.052(2)</td><td rowspan="2">R1 = 0.0381(6307)
wR2 = 0.1248(6959)</td></tr>
<tr><td>Ru-N3</td><td>2.062(2)</td></tr>
<tr><td>Ru-N4</td><td>2.136(2)</td><td>GOF on F2 1.070</td></tr>
<tr><td>Ru-N5</td><td>2.069(2)</td><td rowspan="2"></td></tr>
<tr><td>Ru-Cl</td><td>2.4036(8)</td></tr>
</table>

Table IV.3. crystallographic data of the **Complex 3.**

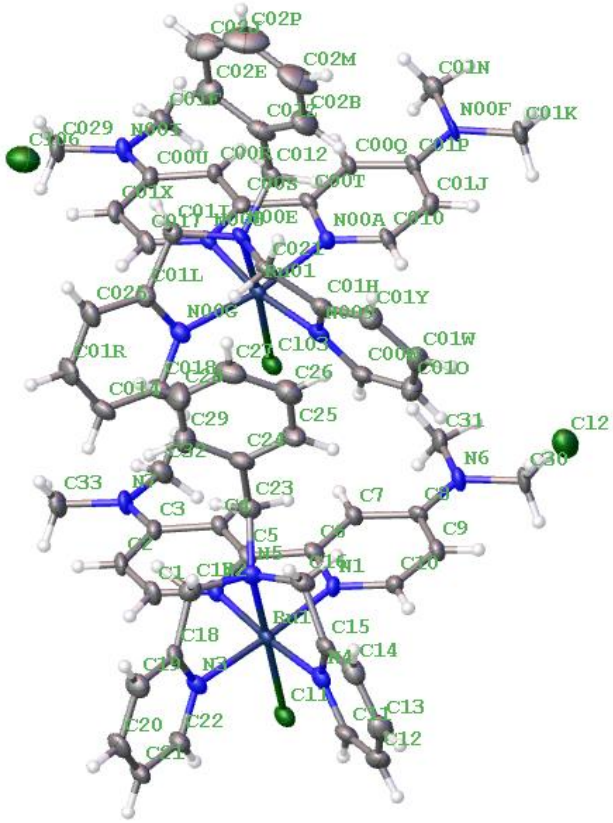

Complex-3	
CCDC No. 2335459	
Formula moiety $C_{33}H_{37}ClN_7Ru,Cl$	
Molecular weight	703.67
Crystal system	triclinic
Space group	P -1
a/ Å	13.4792(15)
b/ Å	16.1532(19)
c/ Å	18.861(2)
α/°	76.205(3)
β/°	85.140(3)
γ/° 88.807(3)	
V/ $Å^3$	3973.9(8)
Z	2
Dcalcd /g cm^{-3}	1.407
Mu (mm-1)	0.575
T/K	296 K
R1 = 0.0647(9541) wR2 = 0.1875(15297)	
GOF on F2	1.042

Bond length(Å)	
Ru-N1	2.050(4)
Ru-N2	2.053(5)
Ru-N3	2.071(4)
Ru-N4	2.032(5)
Ru-N5	2.117(5)
Ru-Cl	2.4346(15)

Table IV.4. crystallographic data of the **Complex 4.**

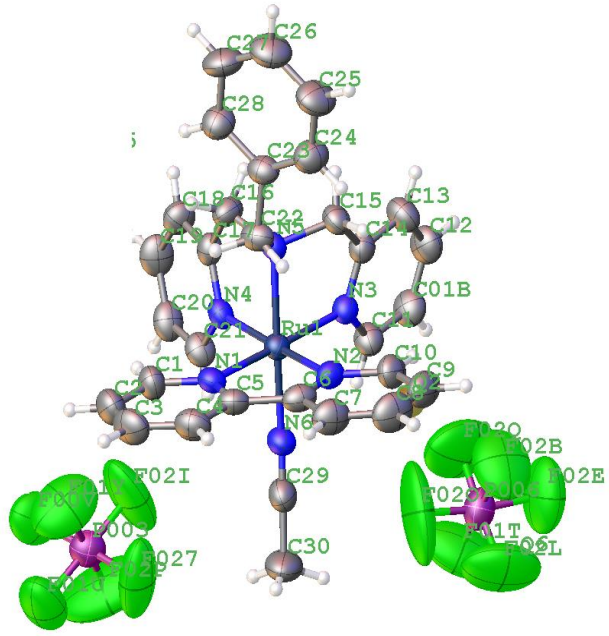

Bond length(Å)	
Ru-N1	2.062(4)
Ru-N2	2.056(4)
Ru-N3	2.063(4)
Ru-N4	2.064(4)
Ru-N5	2.137(4)
Ru-N6	2.040(4)
C29-N6	1.124(6)

Complex-4	
CCDC No. 2471751	
Formula moiety	$C_{31}H_{30}N_6Ru,2(F_6$ P), 0.45[CH_3CN], 0.5[CH_3CN]
Molecular weight	916.62
Crystal system	triclinic
Space group	P -1
a/ Å	8.9477(10)
b/ Å	19.133(2)
c/ Å	22.471(3)
α/°	90.593(3)
β/°	99.792(3)
γ/° 94.589(3)	
V/ $Å^3$	3777.8(7)
Z	4
Dcalcd /g cm^{-3}	1.612
Mu (mm^{-1})	0.594
T/K	273 K
R1 = 0.0638(11074)	
wR2 = 0.1921(16776)	
GOF on F2	1.031

Table IV.5. crystallographic data of the **Complex 6.**

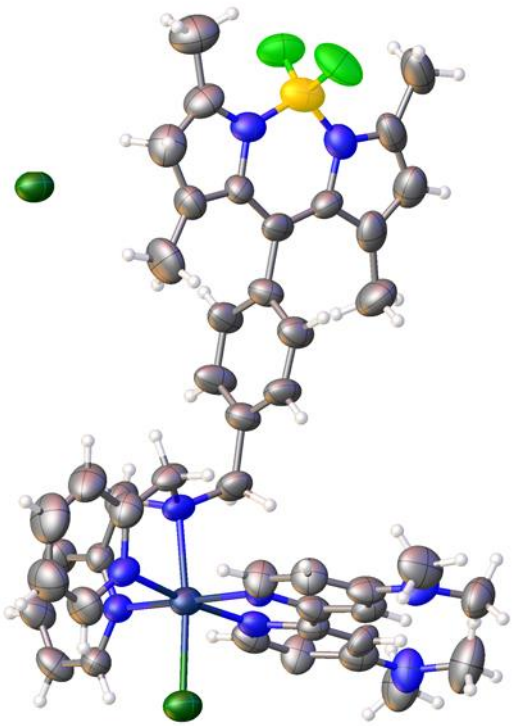	**Complex-6**
	CCDC No. 2479497
	Formula moiety $C_{46}H_{51}BF_2ClN_9$ Ru, Cl, 4[CH_3CH_2OH]
	Molecular weight 1135.01
	Crystal system triclinic
	Space group P -1
	a/ Å 13.3750(18)
	b/ Å 13.6199(15)
	c/ Å 16.609(2)
	α/° 94.970(3)
	β/° 103.278(3)
	γ/° 115.130(3)
	V/ $Å^3$ 2607.1(6)
	Z 2
	Dcalcd /g cm^{-3} 1.446
Mu (mm^{-1}) 0.466	
T/K 273 K	
R1 = 0.0858(3845)	
wR2 = 0.2829(8136)	
GOF on F2 0.974	

IV.2.5 Absorption spectra and photophysical properties:

The UV–Vis absorption spectra of the ruthenium complexes were recorded in acetonitrile at room temperature. Complexes 1–4 display broad, low-energy absorption bands around ~500 nm, which are primarily assigned to singlet metal-to-ligand charge transfer (^{1}MLCT) transitions from the Ru dπ orbitals to the π* orbitals of the coordinated ligands. Additional absorption features near 380 nm are also attributed to ^{1}MLCT transitions. In the higher-energy region (257–295 nm), all complexes exhibit intense absorption peaks, which are assigned to singlet ligand-to-ligand charge transfer (^{1}LLCT) transitions, corresponding to electronic excitation between π-systems within the ligands. For complex 4, a noticeable blue shift of the MLCT band is observed. This shift arises from the coordination of an acetonitrile in place of -Cl to the ruthenium center. The electron-withdrawing nature of CH_3CN lowers the energy of the Ru dπ orbitals, which in turn shifts the MLCT absorption to shorter wavelengths (**Figure IV.19, Table IV.6.**).

Complexes 5 and 7, both incorporating a green-light-absorbing BODIPY ligand, display intense absorption peaks at 500 nm and 530 nm respectively, corresponding to BODIPY-centered π–π* transitions. Complex 7 features an iodinated BODIPY unit, whereas complex 5 contains the non-iodinated analogue. The iodination of the BODIPY core in complex 7 also leads to more fluorescence quenching compared to complex 5, consistent with the heavy-atom effect. This effect promotes intersystem crossing to the triplet state, thereby reducing fluorescence quantum yield, as reported for other halogenated BODIPY derivatives (**Figure IV.19**).

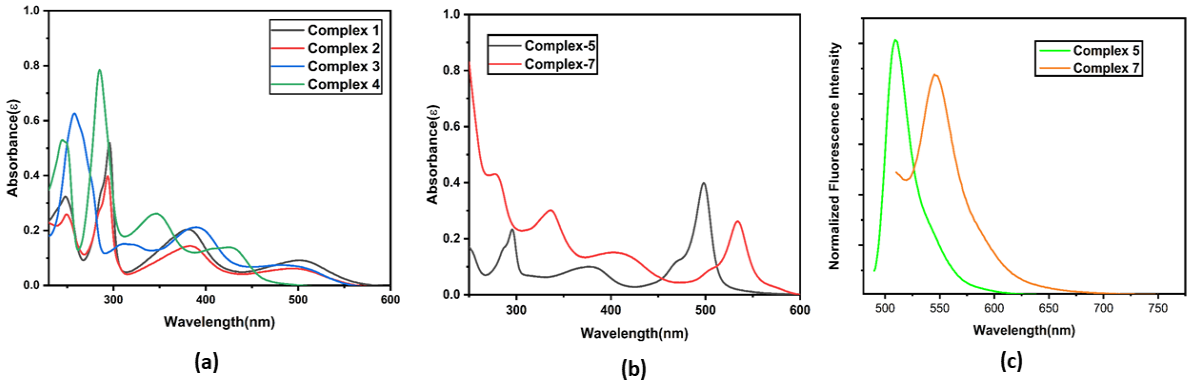

Figure IV.19 UV-Vis absorption spectra of **(a) complex 1-4** (b) **complex 5,7** in CH_3CN. **(c)** Normalized Emission plots of the **complex 5,7** recorded in CH_3CN at room temperature.

Table IV.6. Main calculated optical transition for the complex **1-4** with composition in terms of molecular orbital contribution of the transition, vertical excitation energies (λ/nm), and oscillator strength in acetonitrile.

Compound	Electronic transition	Composition	Excitation energy(eV)	Oscillator strength (f)	C.I.	Assign	λ_{exp} in nm (ε in $M^{-1}cm^{-1}$)
1	$S_0 \rightarrow S_3$	H-2→L	2.6659 (465 nm)	0.1146	0.5526	^{1}MLCT	500 (4500)
	$S_0 \rightarrow S_{13}$	H-2→L+2	3.4577 (358 nm)	0.0633	0.5255	^{1}MLCT	378 (10000)
	$S_0 \rightarrow S_{32}$	H-4→L	4.4279 (280 nm)	0.4831	0.53012	^{1}LLCT	295 (26100)
2	$S_0 \rightarrow S_4$	H-2→L	2.6710 (464 nm)	0.1301	0.5406	^{1}MLCT	493 (3250)
	$S_0 \rightarrow S_{13}$	H-1→L+3	3.4482 (359 nm)	0.0903	0.5818	^{1}MLCT	382 (7450)
	$S_0 \rightarrow S_{31}$	H-3→L	4.4365 (279 nm)	0.5480	0.5377	^{1}LLCT	293 (20000)
3	$S_0 \rightarrow S_3$	H-1→L	2.6326 (470 nm)	0.0999	0.6039	^{1}MLCT	491 (3500)
	$S_0 \rightarrow S_{14}$	H-3→L+9	3.4053 (364 nm)	0.1356	0.4019	^{1}MLCT	389 (10750)
	$S_0 \rightarrow S_{26}$	H-1→L+7	3.9425 (314 nm)	0.0810	0.4579	^{1}MLCT	310 (7850)
	$S_0 \rightarrow S_{49}$	H-3→L+4	4.7820 (259 nm)	0.6571	0.4779	^{1}LLCT	257 (31500)
4	$S_0 \rightarrow S_3$	H-2→L	2.9797 (416 nm)	0.1259	0.6776	^{1}MLCT	426 (7000)
	$S_0 \rightarrow S_9$	H→L+2	3.6065 (343 nm)	0.0766	0.4444	^{1}MLCT	345 (13000)
	$S_0 \rightarrow S_{27}$	H-5→L	4.4372 (279 nm)	0.5991	0.6374	^{1}LLCT	285 (39000)

IV.2.6 Electronic Spectra:

Electrochemical Studies

Cyclic voltammetry (CV) was employed to examine the electrochemical behaviour of the synthesized ruthenium complexes (**1-4**) under both argon and carbon dioxide atmospheres, with the dual objective of elucidating their redox properties and evaluating their thermodynamic suitability for CO_2 reduction catalysis in conjunction with photosensitizers.

Electrochemical measurements were systematically performed using 0.1 M tetrabutylammonium hexafluorophosphate ($[nBu_4N]PF_6$) as the supporting electrolyte in acetonitrile. A glassy carbon working electrode, a platinum wire counter electrode, and a scan rate of 100 mV s^{-1} were employed in all experiments. Under an argon atmosphere, all complexes exhibited two distinct oxidation processes along with multiple reduction events within the accessible potential window. The first oxidation wave, generally reversible and occurring in the range +0.03 to +0.38 V vs Fc, is attributed to the metal-centred Ru(II)/Ru(III) redox couple. The second oxidation process, observed between +0.70 and +1.02 V, corresponds to the Ru(III)/Ru(IV) transformation.

The influence of ligand electronics was evident in the case of the complex bearing the electron-rich 4,4′-bis(N,N-dimethylamino)-2,2′-bipyridine ligand, which displayed a significantly lower oxidation potential, consistent with enhanced electron-donating effects that stabilize higher oxidation states.

All complexes exhibited multiple cathodic features. The first reduction wave, typically quasi-reversible and appearing between −1.79 and −2.34 V, is assigned to a ligand-centred reduction involving the bipyridine moiety ($bpy^{\bullet-}$/bpy). This process is followed by chloride dissociation, which subsequently generates species capable of undergoing further reduction at more negative potentials (**Figure IV.20** and **Table IV.7**).

Under a CO_2 atmosphere, a pronounced increase in cathodic current was observed beginning from the second reduction event, consistent with electrocatalytic CO_2 reduction following chloride dissociation. Notably, the magnitude of current enhancement diminished upon incorporation of electron-donating substituents (methyl or N,N-dimethyl) at the 4,4′-positions of the bipyridine ligands, indicating a decrease in CO_2 reduction activity. This trend suggests that excessive electron density at the metal centre may disfavour the binding or activation of CO_2 (**Figure IV.20**).

Furthermore, complexes bearing labile acetonitrile (**Complex-4**) ligands exhibited substantially greater catalytic current enhancement compared to their halide-containing analogues, underscoring the beneficial influence of ligand lability on catalytic performance. These results collectively highlight the interplay between ligand electronics, coordination environment, and catalytic activity in the electrochemical CO_2 reduction process.

$E_{1/2,}$ (V) *vs* $Fc^{+/0}$				
	E_{ox1}	E_{ox2}	E_{red1}	E_{red2}
Complex-1	0.37	0.73	-2.02	-2.52
Complex-2	0.32	0.70	-2.08	-2.60
Complex-3	0.03	0.73	-2.34	-2.80
Complex-4	0.38	1.02	-1.79	-2.40

Table IV.7 Peak Potentials of the complexes **1-4** in CH_3CN.

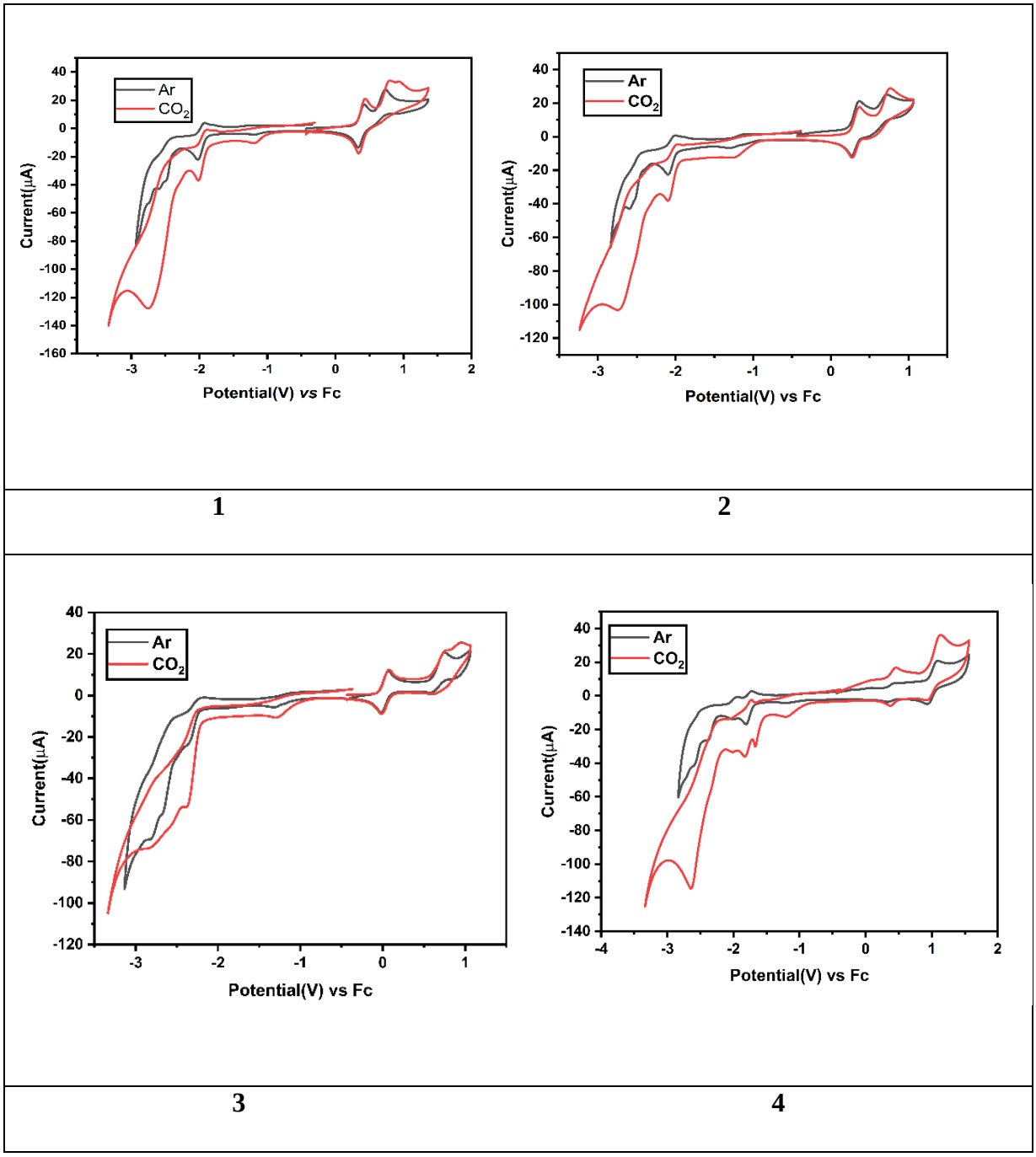

Figure IV.20 Cyclic voltammograms of 1 mM solution of **complexes 1-4** under Ar (black) and CO_2 atmosphere. Potential values are reported versus Fc^+/Fc.

TOF_{max} calculations from the cyclic voltammetry experiments:

The turnover frequency (TOF) is an inherent characteristic of catalysts, which represents the rate of conversion reactants into products per mole of active catalyst per unit time. The TOF value was derived using the following equation below from the catalytic cyclic voltammograms recorded CH_3CN solutions.

$$TOF = (Fvn_p^3/RT)(0.4463/n_{cat})(i_{cat}/i_p)^2$$

Where, i_p is peak current, i_{cat} is the catalytic current, F is Faraday's constant (F = 96500 C), R is the universal gas constant (R = 8.314 J K^{-1} mol^{-1}), T is temperature (T = 300 K) and ν is the scan rate. (where n_p is 1, the number of electrons transferred in the noncatalytic reduction, and n_{cat} is 2 for CO_2 reduction to CO, the number of electrons transferred in the catalytic reaction). The TOF was calculated from the slope of i_{cat}/i_p vs $\nu^{-1/2}$ plot. TOF_{max} determined for the investigated complexes are as follows: 0.3 s^{-1} for **complex 1**, 0.15 s^{-1} for **complex 2**, 0.07 s^{-1} for **complex 3** and 4.5 s^{-1} for **complex 4**, (**Figure IV.21-Figure IV.24, Table IV.8)**. Among them, catalyst **complex 4** exhibited the highest TOF_{max} of 4.5 s^{-1}, indicating its superior electrocatalytic activity Since our primary focus was on the photocatalytic CO_2 reduction activity of the catalysts, no further investigations were carried out.

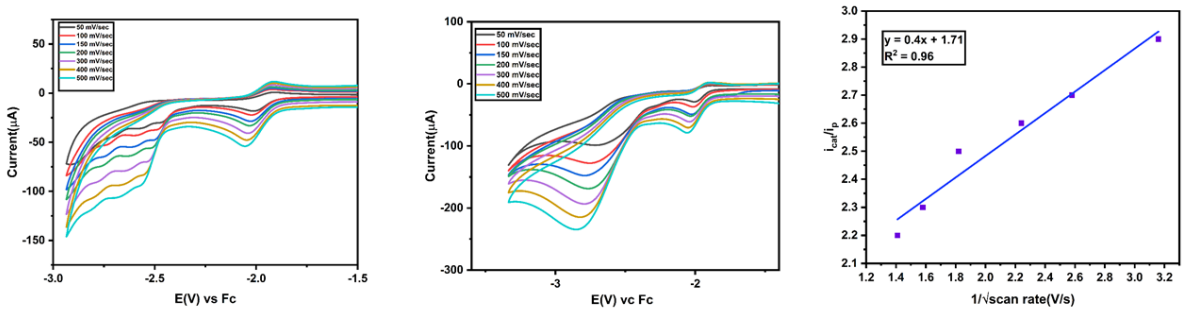

Figure IV.21 Cyclic voltammogram scan rate dependence of 1 mM **complex-1** under an atmosphere of argon **(a)** and under an atmosphere of CO_2 **(b)** in acetonitrile. **(c)** i_p/i_{cat} vs. 1/scan $rate^{1/2}$ plot of **complex-1.** Electrochemical conditions were 0.1 M TBAH as supporting electrolyte, 3 mm diameter glassy carbon working electrode, Pt wire counter electrode.

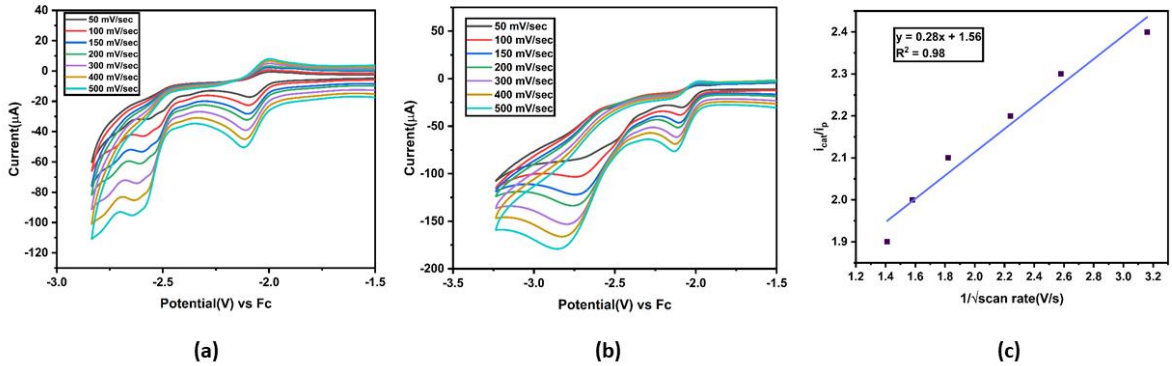

Figure IV.22 Cyclic voltammogram scan rate dependence of 1 mM **complex-2** under an atmosphere of argon **(a)** and under an atmosphere of CO_2 **(b)** in acetonitrile. **(c)** i_p/i_{cat} vs. 1/scan rate$^{1/2}$ plot of **complex-2.** Electrochemical conditions were 0.1 M TBAH as supporting electrolyte, 3 mm diameter glassy carbon working electrode, Pt wire counter electrode.

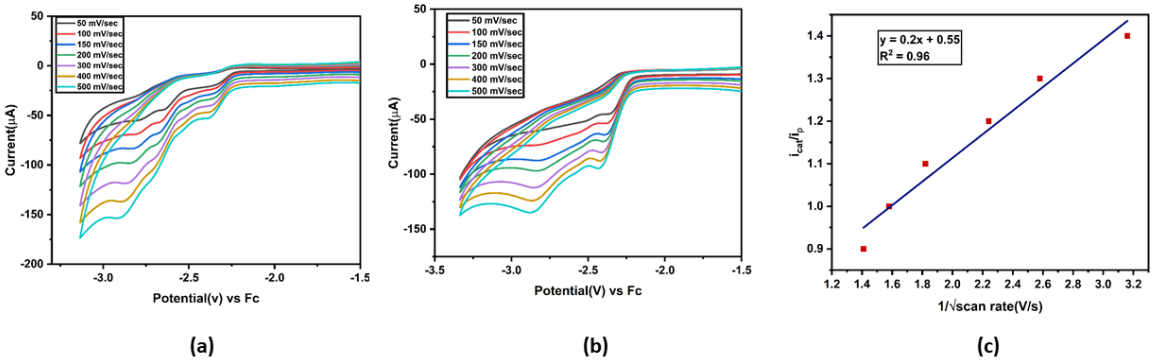

Figure IV.23 Cyclic voltammogram scan rate dependence of 1 mM **complex-3** under an atmosphere of argon **(a)** and under an atmosphere of CO_2 **(b)** in acetonitrile. **(c)** i_p/i_{cat} vs. 1/scan rate$^{1/2}$ plot of **complex-3.** Electrochemical conditions were 0.1 M TBAH as supporting electrolyte, 3 mm diameter glassy carbon working electrode, Pt wire counter electrode.

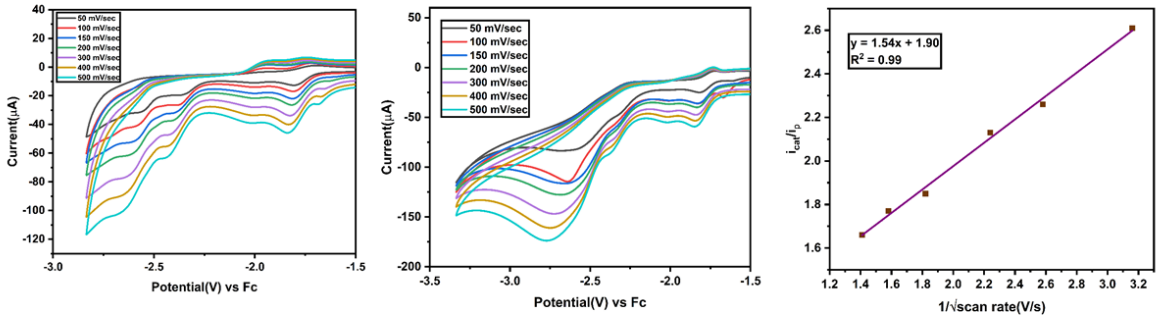

Figure IV.24 Cyclic voltammogram scan rate dependence of 1 mM **complex-4** under an atmosphere of argon **(a)** and under an atmosphere of CO_2 **(b)** in acetonitrile. **(c)** i_p/i_{cat} vs. 1/scan rate$^{1/2}$ plot of **complex-4.** Electrochemical conditions were 0.1 M TBAH as supporting electrolyte, 3 mm diameter glassy carbon working electrode, Pt wire counter electrode.

Catalyst	**TOF_{max}**
1	0.31 s^{-1}
2	0.15 s^{-1}
3	0.07 s^{-1}
4	4.5 s^{-1}

Table IV.8 TOF_{max} of the complexes in CH_3CN.

IV.2.7 Photocatalysis:

Photocatalytic CO_2 reduction experiments were conducted in a glass reactor containing a CO_2-saturated DMA/H_2O mixture (4.0 mL, 3:1 v/v) at room temperature. For complexes **1–4**, an external photosensitizer (PS) was employed: $[Ru(bpy)_3]^{2+}$ (0.5 mM), with BIH (0.25 mM) as the sacrificial electron donor and catalyst loading of 20 μM. The suspension was irradiated with $\lambda \geq 420$ nm using a 275 W Xe source, and gaseous products accumulating in the headspace were periodically quantified by GC-TCD.

Within the externally sensitized series (**1–4**), the influence of ligand electronics on activity was probed by varying substituents on the bipyridine framework. Electron-donating groups on the 4,4′-positions decreased CO production relative to the unsubstituted analogue, for complex **4**, TON_{CO} was 440, indicating that modest perturbations to the bipyridine π-system can alter excited-state energetics and redox matching with the PS/BIH pair, thereby impacting productive electron transfer versus deactivation pathways. Under these conditions, complex **4** delivered the highest turnover number 1700 among **1–4** (see **Figure IV.25 (a)**).

To eliminate reliance on an external PS and streamline the system, we next designed self-sensitized catalysts by appending a BODIPY light-harvesting unit (complexes **5** and **7**). Complex **5** bears the non-iodinated BODIPY, whereas complex **7** incorporates an iodinated BODIPY unit. Both complexes absorb strongly in the visible region, enabling direct photoactivation under $\lambda \geq 420$ nm without $[Ru(bpy)_3]^{2+}$. Notably, complex **7** achieved a higher TON, 55 than complex 5 (TON 17) (see **Figure IV.25 (b)**). under otherwise identical conditions. We ascribe this enhancement to the heavy-atom effect of iodine within the BODIPY chromophore, which promotes intersystem crossing and lengthens the triplet-state lifetime. The resulting increase in triplet population and lifetime improves intramolecular charge separation and accelerates electron transfer from the photoexcited BODIPY to the catalytic center, while suppressing back-electron transfer—collectively yielding superior CO_2-to-CO performance.

In summary: complex 4 is the top performer within the externally sensitized set (**1–4**); transitioning to self-sensitized designs obviates the external PS; and within that family, the iodinated BODIPY complex **7** outperforms complex **5**, consistent with heavy-atom-enabled triplet harvesting and more efficient photoredox coupling.

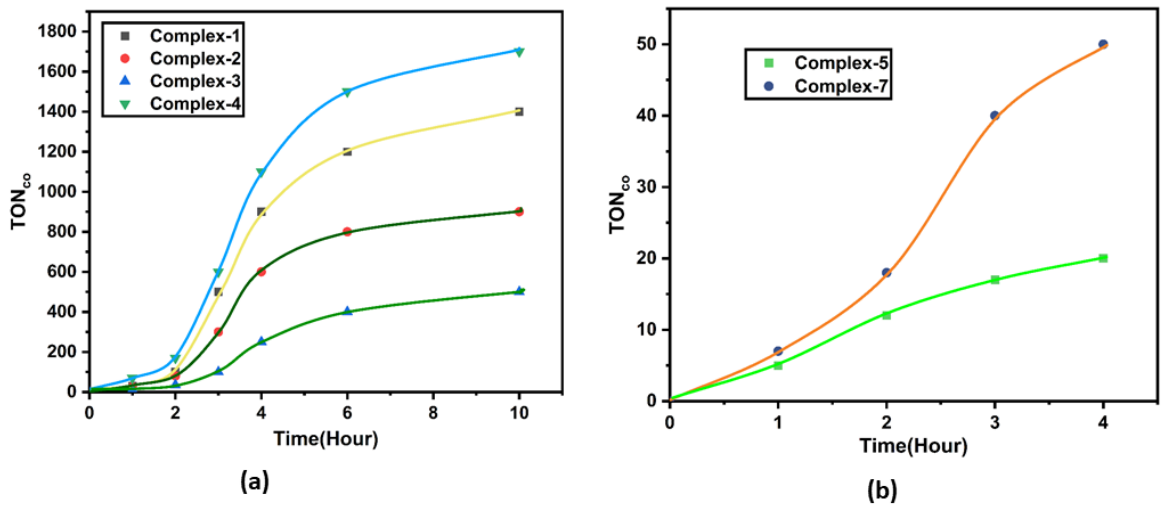

Figure IV.25 (a) TON_{CO} obtained by the catalysts after 10 h. DMA was chosen as the solvent with water as the proton source (4.0 mL, 10:1 v/v), 0.2 mM $Ru(dmbpy)_3^{2+}$ as phtosensitizer, 25 mM SED and 20 µM catalyst. **(b)** Turnover number versus time plots after 4 h without added PS. Solvent DMA with water as the proton source (4.0 mL, 10:1 v/v), 25 mM SED and 0.1 mM catalyst is used.

IV.3. Mechanistic Discussion:

For complexes **1-4**, photocatalytic CO_2 reduction proceeds via an external photosensitizer pathway in which $[Ru(bpy)_3]^{2+}$ absorbs visible light ($\lambda \geq 420$ nm) and is excited to its singlet state, followed by intersystem crossing to the triplet state. This triplet photosensitizer is reductively quenched by BIH, generating the reduced $[Ru(bpy)_3]^{+}$ species, which subsequently transfers an electron to the Ru catalyst, producing the active Ru(I) species. Ru(I) binds CO_2 to form a Ru–CO_2 adduct, which undergoes stepwise proton-coupled electron transfer to release CO and regenerate Ru(II). In the self-sensitized systems (complexes **5** and **7**), the BODIPY chromophore is covalently attached to the Ru catalytic site, eliminating the need for an external photosensitizer. Upon light absorption, BODIPY is excited to the singlet state, and in complex **7**, iodination promotes efficient intersystem crossing to the triplet state via the heavy-atom effect, producing a longer-lived excited state than in complex **5**. The excited BODIPY is reductively quenched by BIH to form a BODIPY radical anion, which transfers an electron intramolecularly to the Ru center to generate the Ru(I) active species, followed by CO_2 activation and reduction to CO as in the external PS pathway. The enhanced triplet yield and

prolonged lifetime in complex **7** facilitate more efficient electron transfer, accounting for its superior turnover number compared to complex **5.** (See **Scheme IV.2)**

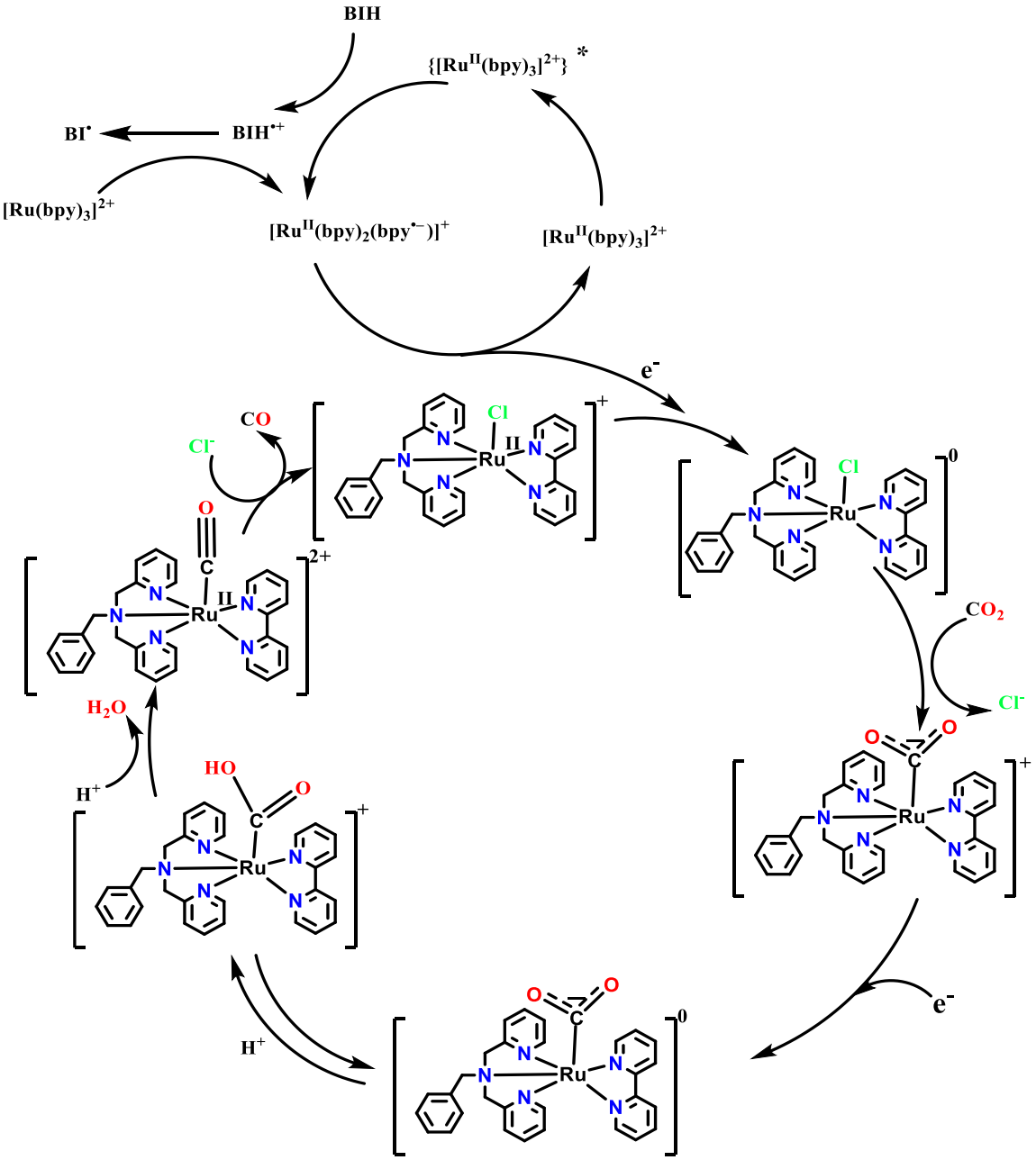

Scheme IV.2 Proposed mechanism for the photochemical reduction of CO_2 into CO catalyzed by the Complexes. **Complex 1** was employed to exemplify the mechanism.

IV.4. DISCUSSION AND CONCLUSIONS:

The photocatalytic CO_2 reduction studies reveal that the catalytic performance is highly sensitive to both the ligand framework and the mode of photosensitization. Complexes 1–4, evaluated in the presence of an external photosensitizer ($[Ru(bpy)_3]^{2+}$), show clear trends correlating ligand electronic properties with activity. Substitution at the 4,4′-positions of the bipyridine moiety with electron-donating methyl groups (complex **2**) results in a decrease in CO yield compared to the unsubstituted analogue (complex **1**), suggesting that increased electron density on the ligand may destabilize the key metal–carbon intermediates. More pronounced electron donation, as in 4,4′-bis(N,N-dimethylamino) substitution (complex **3**), leads to a substantial loss of activity, likely due to suppression of efficient photoinduced electron transfer from the photosensitizer to the catalyst. In contrast, complex **4**, bearing a coordinated acetonitrile ligand, exhibits the highest turnover number among the external-PS systems. The electron-withdrawing nature of the CH_3CN ligand likely lowers the reduction potential, facilitating CO_2 activation. To circumvent the need for an external photosensitizer, BODIPY-based complexes **5** and **7** were designed as self-sensitized catalysts. The incorporation of a BODIPY chromophore allows direct harvesting of visible light, with intramolecular electron transfer from the photoexcited BODIPY to the Ru catalytic center driving CO_2 reduction. Notably, complex **7**, containing an iodinated BODIPY unit, demonstrates superior TON relative to complex **5**. This enhancement can be attributed to the heavy-atom effect of iodine, which promotes intersystem crossing to the triplet excited state, increasing the lifetime of the charge-separated species and thus improving photocatalytic efficiency. The combined results confirm that both the photophysical and electronic properties of the ligands play decisive roles in dictating catalytic activity.

This study establishes a clear structure–activity relationship in Ru-based CO_2 reduction catalysts, highlighting the delicate balance between ligand electronics and photophysical properties. Complex **4** achieves the highest performance among the external-photosensitizer systems, while the self-sensitized iodinated BODIPY complex **7** surpasses TON from the complex **5**, eliminating the need for an auxiliary photosensitizer. These findings demonstrate that strategic ligand design particularly through integration of strong light-absorbing units and judicious modulation of their electronic character—offers an effective route to enhance photocatalytic CO_2 reduction. The insights gained here provide a valuable framework for the future development of efficient, self-sensitized photocatalysts for sustainable fuel generation.

IV.5. References:

1. Nunes, L.J.R. The Rising Threat of Atmospheric CO_2: A Review on the Causes, Impacts, and Mitigation Strategies. *Environments.* 2023, **10**, 66.
2. J. Bednar, M. Obersteiner, A. Baklanov, M. Thomson, F. Wagner, O. Geden, M. Allen, J. W. Hall, *Nature*, 2021, **596**, 377-383.
3. (a) Pan, H.; Heagy, M.D. Photons to Formate: A Review on Photocatalytic Reduction of CO_2 to Formic Acid. *Nanomaterials.* 2020, **10**, 2422. (b) N. Elgrishi, M. B. Chambers, X. Wang and M. Fontecave, *Chem Soc Rev*, 2017, **46**, 761-796.
4. (a) K. Kamada, J. Jung, T. Wakabayashi, K. Sekizawa, S. Sato, T. Morikawa, S. Fukuzumi and S. Saito, *J Am Chem Soc*, 2020, **142**, 10261-10266. (b) L. Y. Peng, G. N. Pan, W. K. Chen, X. Y. Liu, W. H. Fang and G. Cui, *Angew Chem Int Ed Engl*, 2024, **63**, e202315300.
5. (a) R. N. Sampaio, D. C. Grills, D. E. Polyansky, D. J. Szalda and E. Fujita, *J Am Chem Soc*, 2020, **142**, 2413-2428. (b) S. Gonell, M. D. Massey, I. P. Moseley, C. K. Schauer, J. T. Muckerman and A. J. M. Miller, *J Am Chem Soc*, 2019, **141**, 6658-6671.
6. (a) J. Palion-Gazda, K. Choroba, M. Penkala, P. Rawicka and B. Machura, *Inorg Chem*, 2024, **63**, 1356-1366. (b) R. Giereth, P. Lang, E. McQueen, X. Meißner, B. Braun-Cula, C. Marchfelder, M. Obermeier, M. Schwalbe and S. Tschierlei, *ACS Catalysis*, 2020, **11**, 390-403.
7. (a) H. Yuan, A. Krishna, Z. Wei, Y. Su, J. Chen, W. Hua, Z. Zheng, D. Song, Q. Mu, W. Pan, L. Xiao, J. Yan, G. Li, W. Yang, Z. Deng and Y. Peng, *J Am Chem Soc*, 2024, **146**, 10550-10558. (b) L. A. Hunt, S. Das, R. W. Lamb, D. Nugegoda, C. Curiac, M. T. Figgins, E. C. Lambert, F. Qu, N. I. Hammer, J. H. Delcamp, C. E. Webster and E. T. Papish, *ACS Catalysis*, 2023, **13**, 5986-5999. (c) A. M. Cancelliere, F. Puntoriero, S. Serroni, S. Campagna, Y. Tamaki, D. Saito and O. Ishitani, *Chem Sci*, 2020, **11**, 1556-1563.
8. (a) S. Paul, P. Kundu, U. Bhattacharyya, A. Garai, R. C. Maji, P. Kondaiah and A. R. Chakravarty, *Inorg. Chem.*, 2020, **59**, 913–924. (b) N. E. Aksakal, E. T. Eçik, H. H. Kazan, G. Y. Çiftçi and F. Yuksel, *Photochem. Photobiol. Sci.*, 2019, **18**, 2012-2022. (c) A. Aguiar, J. Farinhas, W. da Silva, M. E. Ghica, C. M. A. Brett, J. Morgado and A. J. F. N. Sobral, *Dyes Pigm.*, 2019, **168**, 103–110.

9. (a) J. J. Teesdale, A. J. Pistner, G. P. A. Yap, Y.-Z. Ma, D. A. Lutterman and J. Rosenthal, *Catal. Today*, 2014, **225**, 149–157. (b) G. A. Andrade, A. J. Pistner, G. P. A. Yap, D. A. Lutterman and J. Rosenthal, *ACS Catal.*, 2013, **3**, 1685–1692.

10. (a) J. Bartelmess, A. J. Francis, K. A. El Roz, F. N. Castellano, W. W. Weare and R. D. Sommer, *Inorg. Chem.*, 2014, **53**, 4527–4534. (b) L.-Q. Qiu, Z.-W. Yang, X. Yao, X.-Y. Li and L.-N. He, *ChemSusChem*, 2022, **15**, e202200337.

Chapter V

Highly Efficient Homogeneous Friedländer Quinoline Formation Mediated by a Stable Pincer-Ruthenium(III) Catalyst

V.1. Introduction

Quinolines constitute a significant class of nitrogen-containing heterocycles, widely recognized for their broad range of applications in pharmaceutical development, agrochemical formulations, and functional materials[1-3]. Numerous synthetic strategies have been developed to construct the quinoline core, including classical methods such as the Combes, Doebner–von Miller, Conrad–Limpach, Gould–Jacobs, Skraup, and Povarov reactions[4-5]. However, these traditional approaches are often constrained by harsh reaction conditions, prolonged reaction times, suboptimal stereoselectivity, and a narrow substrate scope.

To address these drawbacks, acceptorless dehydrogenative coupling (ADC) reactions have emerged as a green and atom-economical alternative, allowing direct access to quinolines from primary amino alcohols *via* a tandem alcohol dehydrogenation and cyclization process[6-8]. Such transformations are typically facilitated by transition metal catalysts, with ruthenium complexes demonstrating particular promise due to their versatile redox chemistry, thermal stability, and compatibility with a broad range of functional groups[9-10]. Ruthenium-catalyzed indirect Friedländer-type annulations have been effectively utilized by several groups including Shim, Yus, Milstein, and Liu. Nevertheless, the continued exploration of well-defined Ru-based catalysts that operate under milder, more selective, and operationally simple conditions remains highly desirable[11-14].

Considerable advances have been achieved in the synthesis of N-heterocycles through direct dehydrogenative functionalization of alcohols, where precious heavy metal catalysts such as Ru[15-16], Rh[17-18], and Ir[19-20] have played a central role. Among these, ruthenium-based systems have demonstrated remarkable efficiency and versatility, making them one of the most widely employed catalysts for such transformations. Nevertheless, the dependence on noble metals raises concerns regarding cost, toxicity, and long-term sustainability. In contrast, first-row transition-metal alternatives (e.g., Mn, Fe, Co, Cu, Ni) are more earth-abundant and environmentally benign, yet they often face challenges including poor product selectivity, generation of hazardous byproducts, low turnover numbers (TONs), the need for high catalyst loadings, and difficulties in recovery and reuse. Homogeneous catalysts, in particular, suffer from limited recyclability, which restricts their industrial applicability. For example, in the case of copper, in-situ generated species derived from simple salts frequently require stoichiometric or excess loadings, resulting in low TONs and reduced sustainability[21]. Therefore, while non-precious metals remain attractive for developing greener catalytic strategies, ruthenium

continues to be a catalyst of choice due to its superior activity and robustness in enabling efficient Friedländer quinoline synthesis under homogeneous conditions. Cooperative catalysis, involving the synergistic participation of metal centers and ligand frameworks, further enhances the potential of Ru systems to accomplish demanding transformations under relatively mild conditions.

Herein, we report organocatalytic dehydrogenative transformations catalyzed by structurally well-defined Ru(III) polypyridyl complexes. The reaction involves the synthesis of substituted quinolines *via* dehydrogenative annulation of 2-aminobenzyl alcohols with secondary alcohols and ketones. This reactivity showcases the efficiency and versatility of Ru(III)-polypyridyl systems in mediating challenging oxidative couplings. The redox-active nature of the polypyridyl ligand framework is proposed to play a cooperative role with the metal center, promoting efficient hydrogen removal and facilitating key bond-forming steps. These findings highlight the underexplored potential of Ru(III) polypyridyl catalysts in dehydrogenative transformations and contribute to the advancement of atom-economical synthetic methodologies.

V.2. Result and Discussion

V.2.1 Materials:

Acetonitrile, toluene, hexane, ethyl acetate, methanol, ethanol, dichloromethane, and N,N-dimethylformamide were obtained from Merck and purified by standard drying procedures prior to use. Bis(pyridin-2-ylmethyl)amine, salicylaldehyde, 5-methoxysalicylaldehyde, 5-methylsalicylaldehyde, 5-bromosalicylaldehyde, and dichloro(p-cymene)ruthenium(II) dimer were purchased from Sigma-Aldrich.

V.2.2 Synthesis of ligands and complexes:

Synthesis of 2-((bis(pyridin-2-ylmethyl)amino)methyl)phenol (Lig-1):

The ligand-1 was synthesized following a modified procedure based on reported methods. Salicylaldehyde (1 mmol) was dissolved in methanol (10 mL), and N,N-bis-(2-pyridylmethyl)amine (1 mmol) was added to the solution. Subsequently, two drops of acetic acid were introduced, and the mixture was stirred. Sodium cyanoborohydride (1 mmol) was then added under an argon atmosphere, and the reaction mixture was stirred at room temperature for 72 hours. After completion, the reaction mixture was acidified with dilute hydrochloric acid to neutralize any excess sodium cyanoborohydride and then dried. The mixture was washed with water (3 × 10 mL) and extracted with dichloromethane. The organic

layer was concentrated under reduced pressure. The crude product was purified by column chromatography on silica gel using a dichloromethane/ethanol gradient (90:10 v/v) to afford the pure ligand-1. ^{1}H NMR (300 MHz, $CDCl_3$) δ 8.59 – 8.49 (m, 2H), 7.60 (tt, *J* = 7.7, 1.8 Hz, 2H), 7.33 (dd, *J* = 8.1, 1.5 Hz, 2H), 7.22 – 7.10 (m, 3H), 7.05 (dd, *J* = 7.4, 1.7 Hz, 1H), 6.91 (dd, *J* = 8.1, 1.2 Hz, 1H), 6.76 (td, *J* = 7.3, 1.3 Hz, 1H), 3.82 (d, *J* = 27.1 Hz, 6H). ^{13}C NMR (75 MHz, $CDCl_3$) δ 158.19, 157.54, 148.80, 136.89, 130.20, 129.08, 123.27, 122.81, 122.29, 118.90, 116.53, 58.98, 56.92, 29.69.

Synthesis of 2-((bis(pyridin-2-ylmethyl)amino)methyl)-4-methylphenol (Lig-2): The synthesis of the ligand was carried out following the same procedure as described for ligand 1, except that 5-methylsalicylaldehyde was used in place of salicylaldehyde.^{1}H NMR (300 MHz, CDCl3) δ 8.56 (ddd, *J* = 5.1, 1.8, 0.9 Hz, 2H), 7.61 (td, *J* = 7.7, 1.8 Hz, 2H), 7.35 (dt, *J* = 7.8, 1.1 Hz, 2H), 7.15 (ddd, *J* = 7.5, 4.9, 1.2 Hz, 2H), 6.98 (dd, *J* = 8.3, 2.2 Hz, 1H), 6.89 – 6.79 (m, 2H), 3.87 (s, 4H), 3.75 (s, 2H), 2.24 (s, 3H). ^{13}C NMR (75 MHz, $CDCl_3$) δ 158.29, 155.15, 149.03, 148.84, 136.84, 130.72, 129.49, 129.12, 127.87, 123.26, 122.50, 122.25, 116.27, 116.02, 63.71, 59.08, 57.03, 20.48, 20.42.

Synthesis of 2-((bis(pyridin-2-ylmethyl)amino)methyl)-4-methoxyphenol (Lig-3): The synthesis of the ligand was carried out following the same procedure as described for ligand 1, except that 5-methoxy salicylaldehyde was used in place of salicylaldehyde. ^{1}H NMR (300 MHz, CDCl3) δ 8.54 (dd, *J* = 5.0, 1.7 Hz, 2H), 7.60 (dt, *J* = 7.7, 1.4 Hz, 2H), 7.33 (d, *J* = 7.8 Hz, 2H), 7.17 – 7.09 (m, 2H), 6.84 (d, *J* = 8.8 Hz, 1H), 6.73 (dd, *J* = 8.7, 3.0 Hz, 1H), 6.64 (d, *J* = 3.0 Hz, 1H), 3.86 (s, 3H), 3.83 – 3.54 (m, 6H). ^{13}C NMR (75 MHz, $CDCl_3$) δ 160.13, 158.13, 152.30, 151.34, 148.84, 148.68, 136.87, 136.59, 126.98, 123.43, 123.31, 122.73, 122.30, 121.93, 116.90, 116.75, 115.85, 114.00, 113.73, 113.32, 63.49, 59.05, 57.03, 55.78, 50.96, 17.94.

Synthesis of 2-((bis(pyridin-2-ylmethyl)amino)methyl)-4-bromophenol (Lig-4): The synthesis of the ligand was carried out following the same procedure as described for ligand 1, except that 5 bromo salicylaldehyde was used in place of salicylaldehyde. ^{1}H NMR (300 MHz, $CDCl_3$) δ 8.50 (dt, *J* = 5.4, 2.5 Hz, 2H), 7.55 (ddt, *J* = 7.8, 4.9, 2.6 Hz, 2H), 7.42 – 7.16 (m, 3H), 7.15 – 6.91 (m, 3H), 6.75 (dt, *J* = 8.7, 1.9 Hz, 1H), 3.81 (t, *J* = 2.3 Hz, 4H), 3.68 (d, *J* = 2.4 Hz, 2H).^{13}C NMR (75 MHz, $CDCl_3$) δ 158.57, 157.93, 156.83, 149.17, 148.95, 148.72, 136.92, 136.66, 136.57, 136.55, 132.63, 131.70, 130.98, 130.34, 125.17, 123.15, 122.48,

122.33, 122.20, 122.09, 118.48, 117.69, 110.34, 63.46, 62.05, 60.14, 58.79, 56.28, 54.17, 29.65.

Synthesis of complex-1: Initially, 2 equivalents of the ligand were dissolved in dichloromethane in a round-bottom flask, followed by the addition of 1 equivalent of dichloro(p-cymene)ruthenium(II) dimer. The reaction mixture was stirred overnight at room temperature. Upon completion, the mixture was subjected to column chromatography, affording the desired product as a blue solid using CH_3CN:MeOH (9:1) as the eluent.

Synthesis of complex-2: The synthesis was carried out following the same procedure as described for complex 1.

Synthesis of complex-3: The synthesis was carried out following the same procedure as described for complex 1.

Synthesis of complex-4: The synthesis was carried out following the same procedure as described for complex 1.

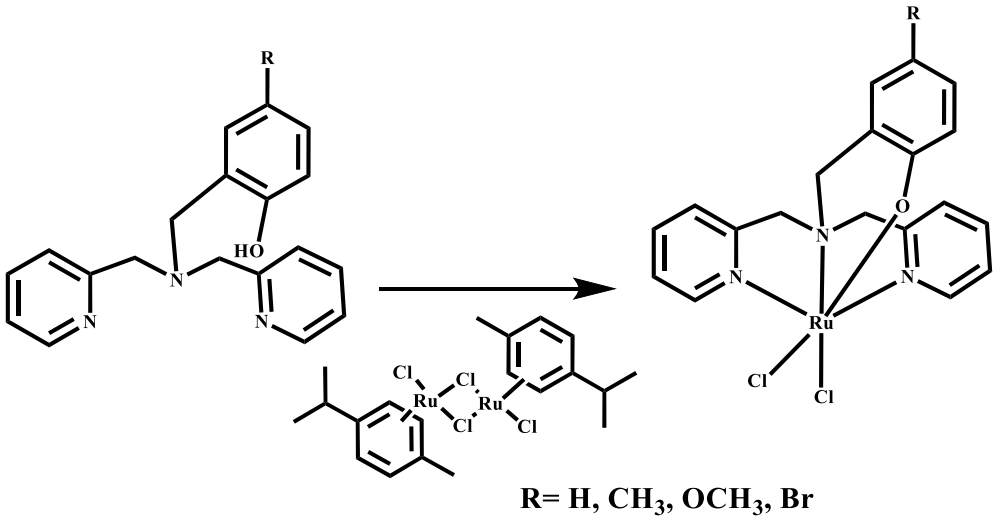

Scheme V.1. Synthetic Procedure for the Complexes.

V.2.3. NMR spectra

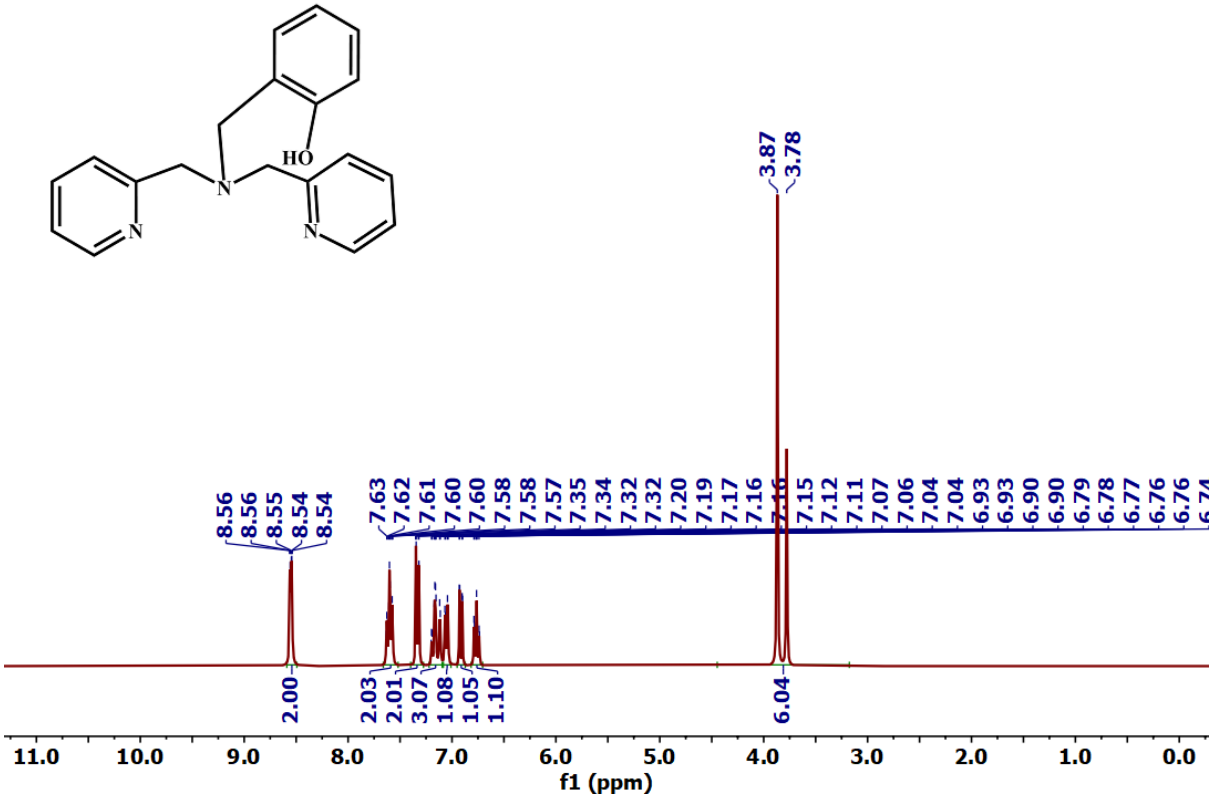

Figure V.1 ^{1}H NMR Spectrum of **Lig-1** in $CDCl_3$.

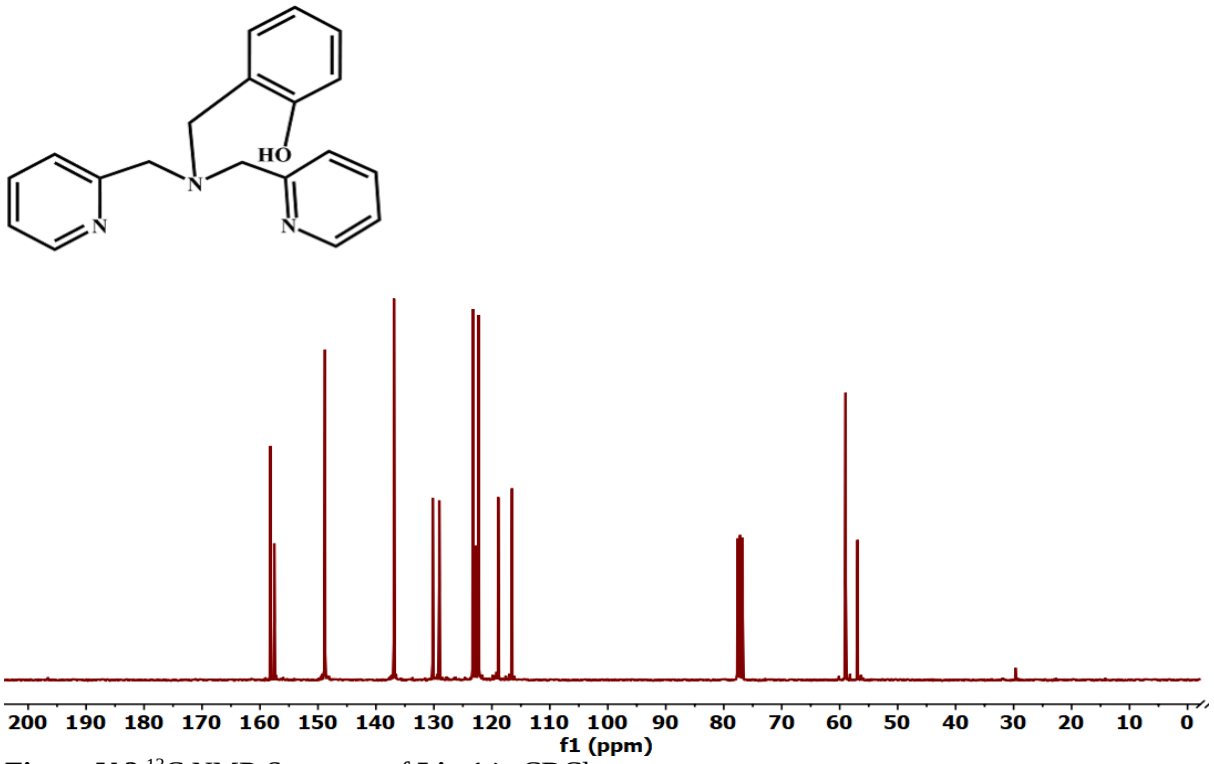

Figure V.2 ^{13}C NMR Spectrum of **Lig-1** in $CDCl_3$.

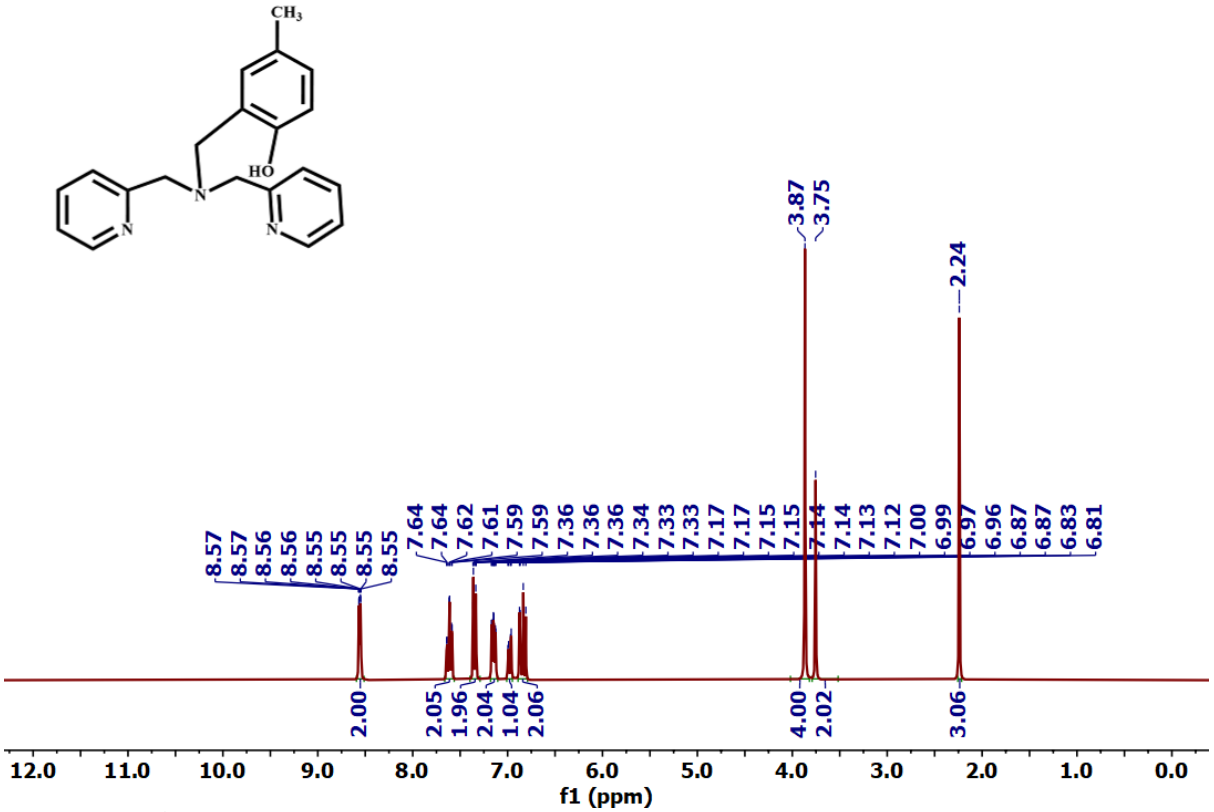

Figure V.3 ^{1}H NMR Spectrum of **Lig-2** in $CDCl_3$

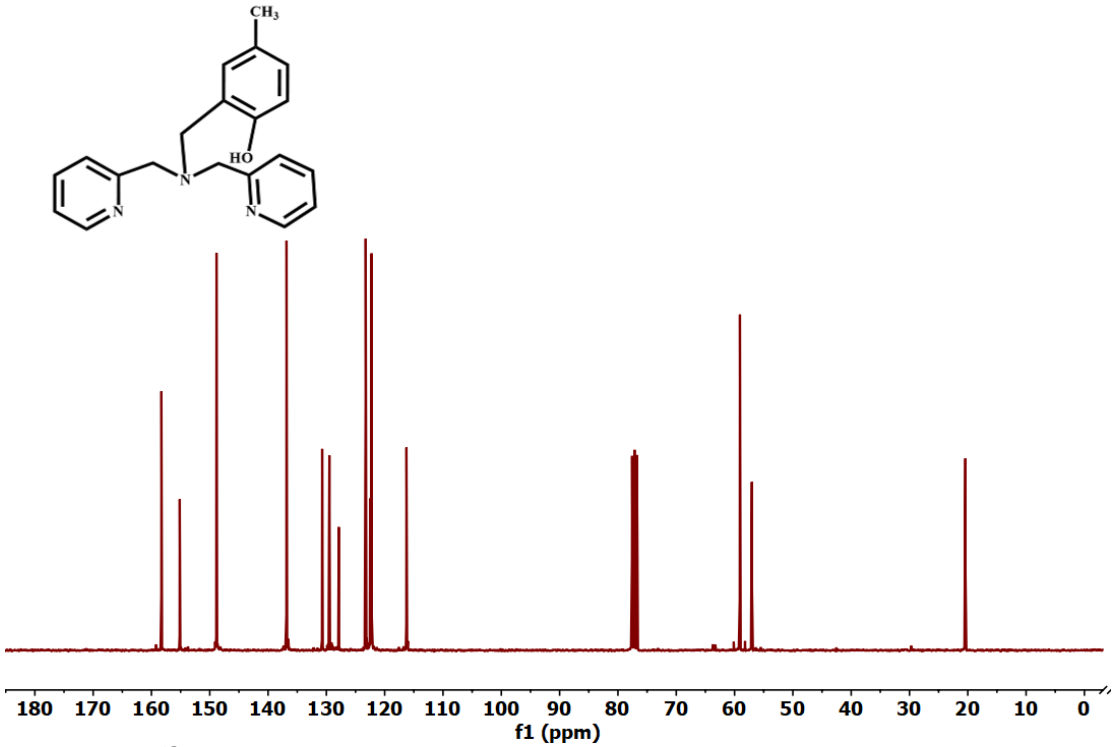

Figure V.4 ^{13}C NMR Spectrum of **Lig-2** in $CDCl_3$.

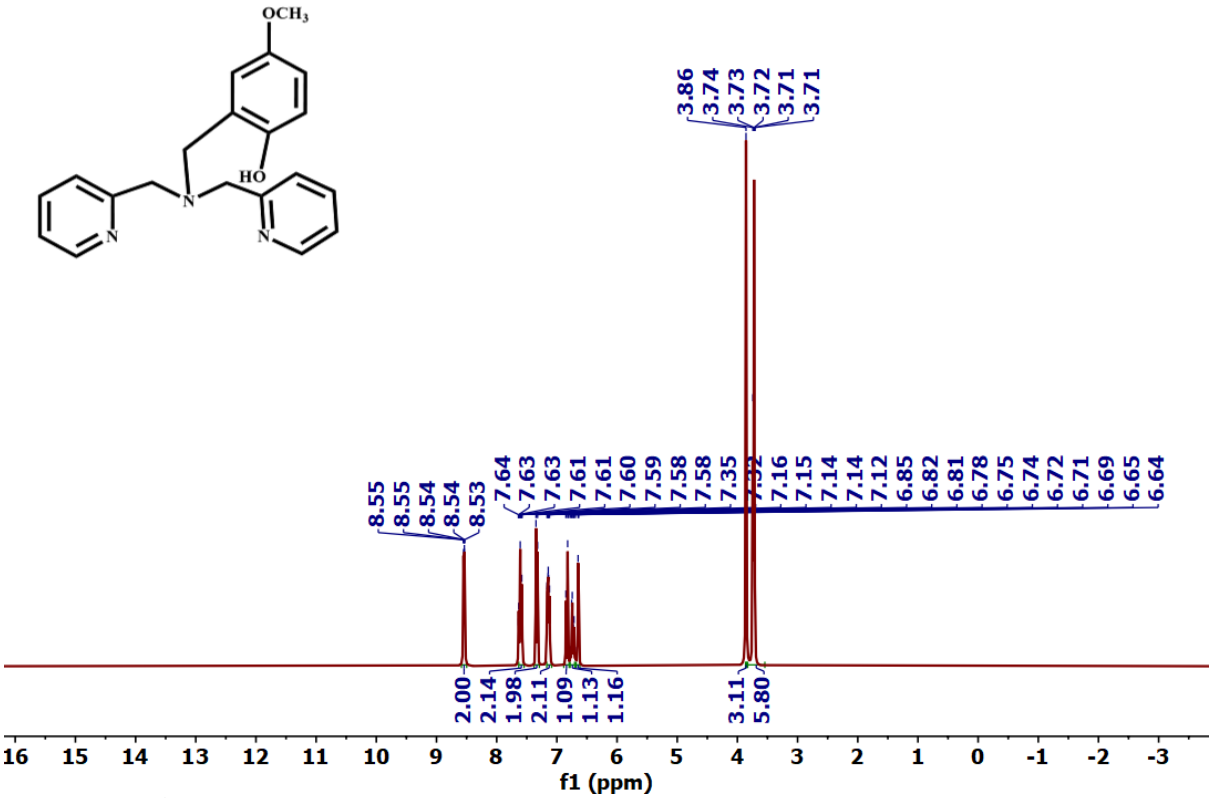

Figure V.5 ^{1}H NMR Spectrum of **Lig-3** in $CDCl_3$

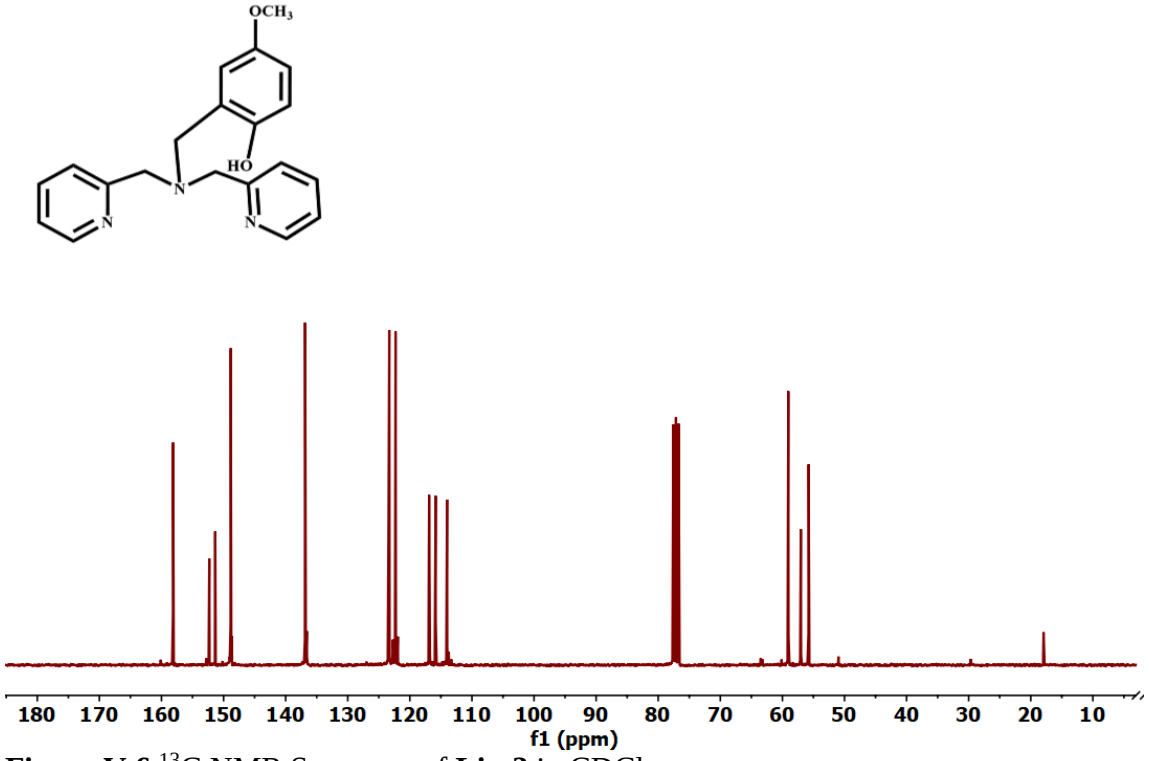

Figure V.6 ^{13}C NMR Spectrum of **Lig-3** in $CDCl_3$.

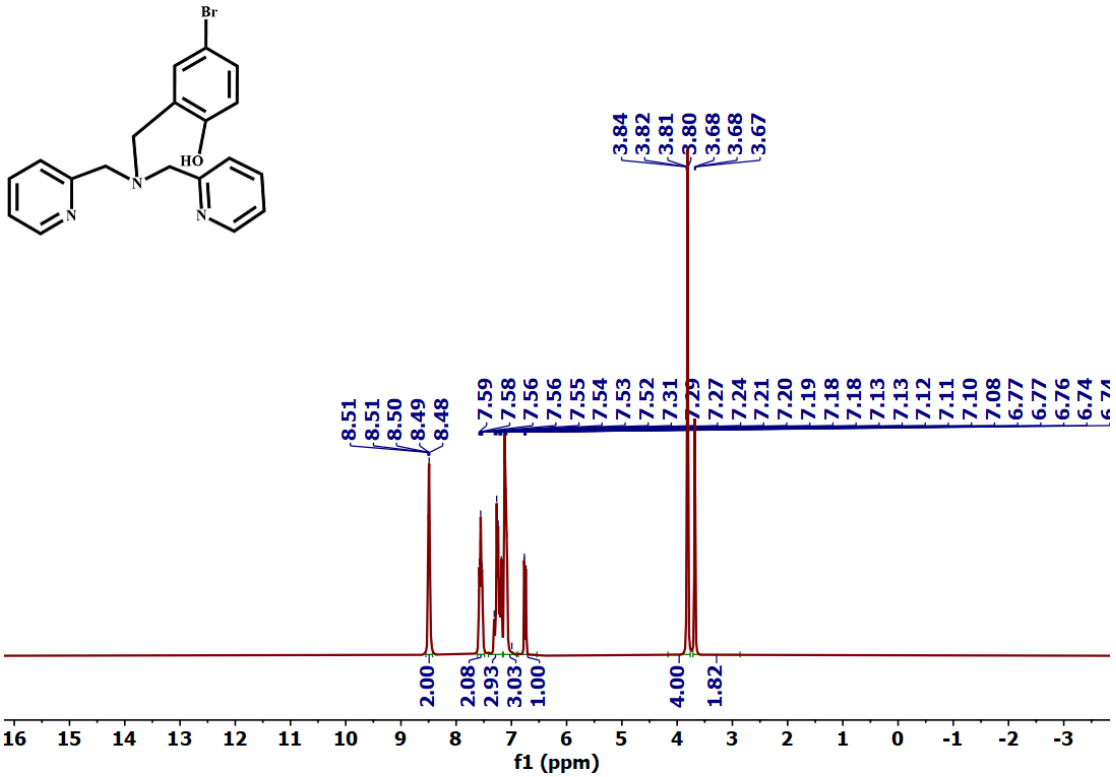

Figure V.7 ^{1}H NMR Spectrum of **Lig-4** in $CDCl_3$

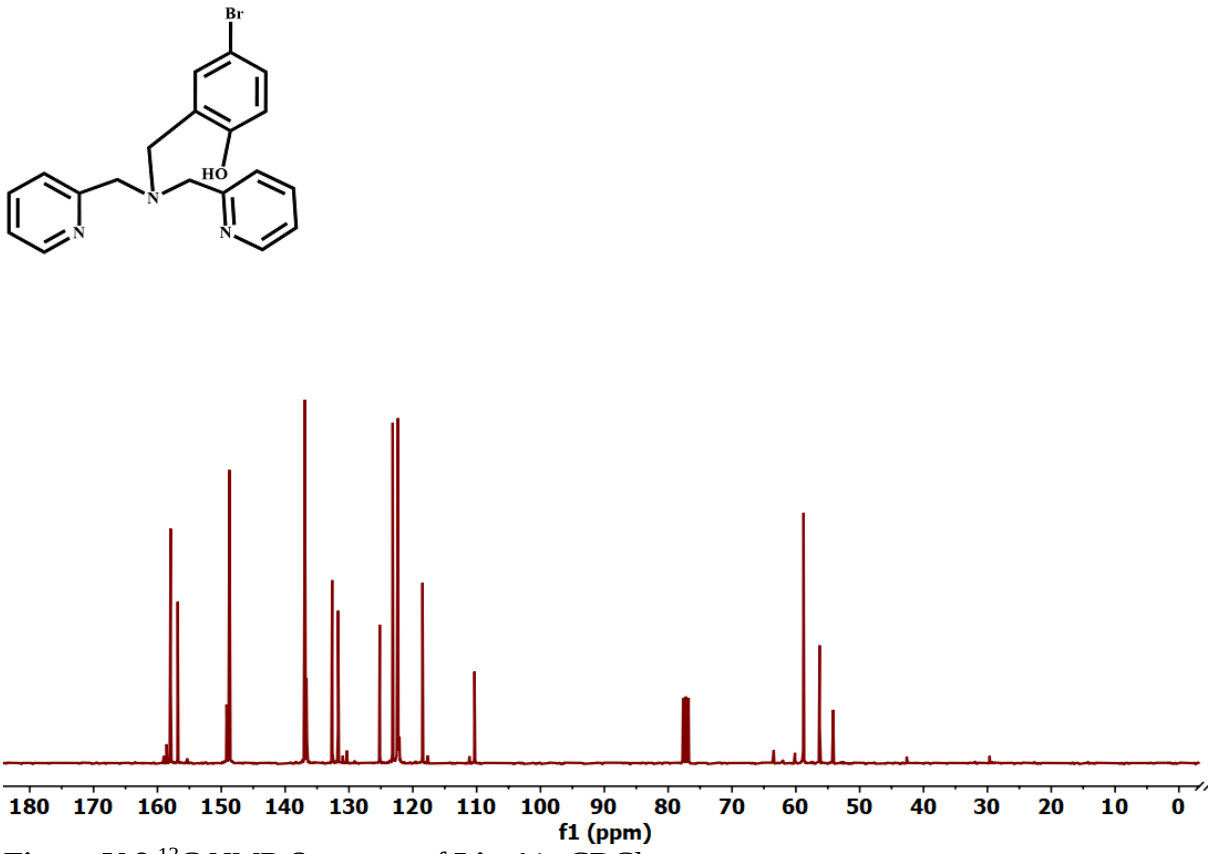

Figure V.8 ^{13}C NMR Spectrum of **Lig-4** in $CDCl_3$.

V.2.4 Crystal Structures:

Single-crystal X-ray diffraction studies of complexes 1–4 provided detailed information on their structural characteristics and comparative geometries. Suitable single crystals for X-ray analysis were obtained by layering methanolic solutions of the respective complexes with diethyl ether. The comparative structural examination highlights the coordination environments and geometric variations across the series. Thermal ellipsoid representations of the complexes are shown in Tables **V.1–V.4.** All four complexes exhibit a distorted octahedral coordination geometry with closely comparable bond parameters, reflecting a high degree of structural uniformity within the series. The crystallographic data have been deposited in the Cambridge Crystallographic Data Centre (CCDC) under deposition numbers 2333903, 2334355, 2480982 and 2480992.

Table V.1. crystallographic data of the **Complex 1.**

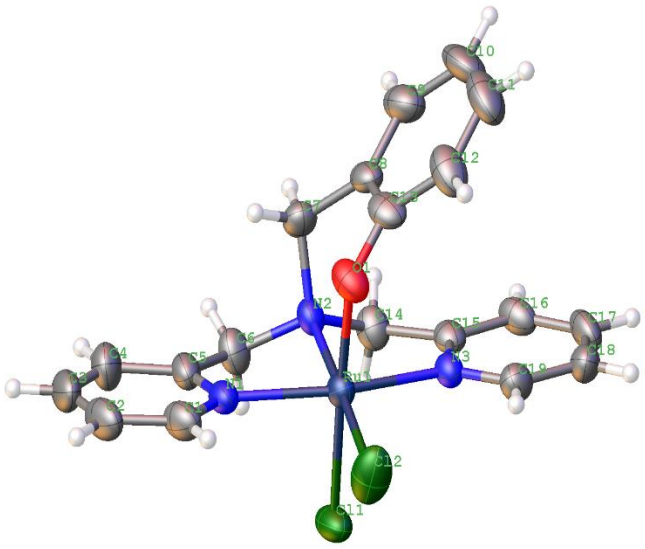

Complex-1	
CCDC No. 2333903	
Formula moiety	$C_{19}H_{18}Cl_2N_3ORu$
Molecular weight	496.50
Crystal system	monoclinic
Space group	P 1 21/c 1
a/ Å	10.1531(6)
b/ Å	13.3819(8)
c/ Å	14.9665(9)
α/°	90
β/°	100.656(2)
γ/°	90
V/ Å^3	1998.4(2)
Z	4
Dcalcd /g cm^{-3}	1.650
Mu (mm-1)	1.067
T/K	273 K
R1 = 0.0546(2786)	
wR2 = 0.1327(3470)	
GOF on F2	1.074

Bond length(Å)	
Ru-N1	2.065(5)
Ru-N2	2.061(5)
Ru-N3	2.051(5)
Ru-O1	1.976(4)
Ru-Cl1	2.3716(17)
Ru-Cl2	2.3966(19)
O1-C13	1.336(8)

Table V.2. crystallographic data of the **Complex 2.**

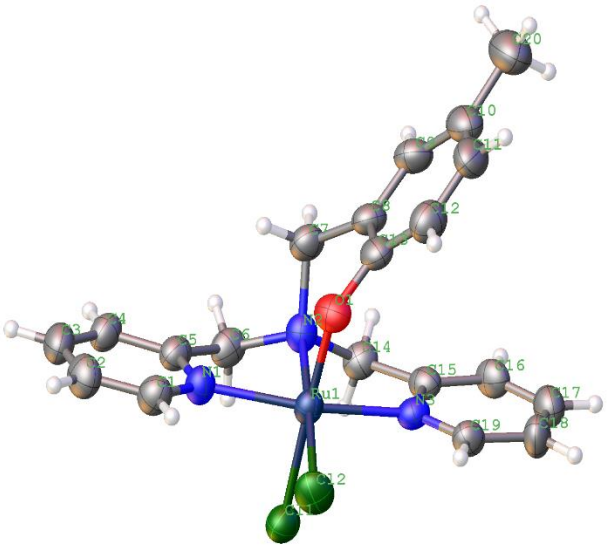

Complex-2	
CCDC No. 2334355	
Formula moiety	$C_{20}H_{20}Cl_2N_3ORu$
Molecular weight	536.44
Crystal system	'orthorhombic'
Space group	P212121
a/ Å	11.8251(7)
b/ Å	13.3394(8)
c/ Å	14.5582(8)
α/°	90
β/°	90
γ/°	90
V/ $Å^3$	2296.4(2)
Z	4
Dcalcd /g cm^{-3}	1.552
Mu (mm-1)	0.939
T/K	273 K
R1 = 0.0277(3783)	
wR2 = 0.0563(4062)	
GOF on F2	1.051

Bond length(Å)	
Ru-N1	2.073(3)
Ru-N2	2.070(3)
Ru-N3	2.053(3)
Ru-O1	1.970(2)
Ru-Cl1	2.3789(9)
Ru-Cl2	2.4001(9)
O1-C13	1.351(4)

Table V.3. crystallographic data of the **Complex 3.**

<table>
<tr><td colspan="2" rowspan="14"> 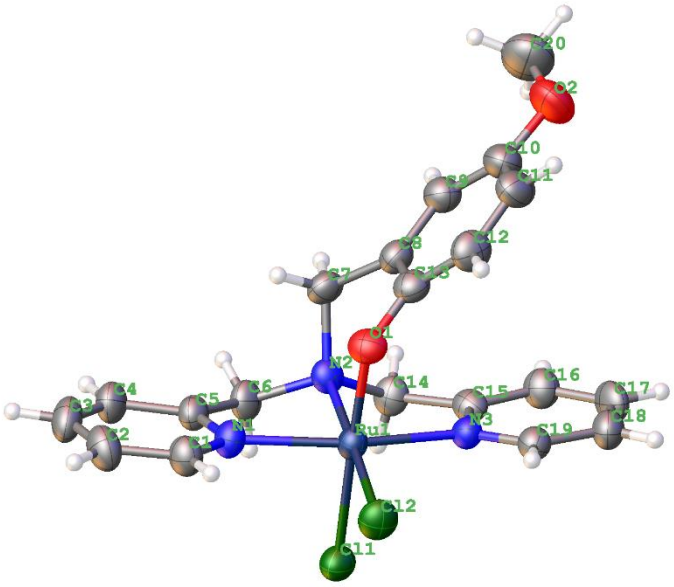 </td><td colspan="2">Complex-3</td></tr>
<tr><td colspan="2">CCDC No. 2480982</td></tr>
<tr><td>Formula moiety</td><td>$C_{20}H_{20}Cl_2N_3O_2Ru$</td></tr>
<tr><td>Molecular weight</td><td>644.58</td></tr>
<tr><td>Crystal system</td><td>'orthorhombic'</td></tr>
<tr><td>Space group</td><td>P212121</td></tr>
<tr><td>a/ Å</td><td>11.7242(6)</td></tr>
<tr><td>b/ Å</td><td>13.2328(7)</td></tr>
<tr><td>c/ Å</td><td>15.0351(8)</td></tr>
<tr><td>α/°</td><td>90</td></tr>
<tr><td>β/°</td><td>90</td></tr>
<tr><td>γ/°</td><td>90</td></tr>
<tr><td>V/ Å^3</td><td>2332.6(2)</td></tr>
<tr><td>Z</td><td>4</td></tr>
<tr><td>Dcalcd /g cm^{-3}</td><td>1.835</td></tr>
<tr><td colspan="2">Bond length(Å)</td><td>Mu (mm-1)</td><td>0.939</td></tr>
<tr><td>Ru-N1</td><td>2.076(3)</td><td>T/K</td><td>273 K</td></tr>
<tr><td>Ru-N2</td><td>2.071(3)</td><td colspan="2" rowspan="2">R1 = 0.0321(4906)
wR2 = 0.0994(5132)</td></tr>
<tr><td>Ru-N3</td><td>2.055(3)</td></tr>
<tr><td>Ru-O1</td><td>1.971(2)</td><td>GOF on F2</td><td>1.054</td></tr>
<tr><td>Ru-Cl1</td><td>2.3815(9)</td><td colspan="2"></td></tr>
<tr><td>Ru-Cl2</td><td>2.3998(10)</td><td colspan="2"></td></tr>
<tr><td>O1-C13</td><td>1.350(4)</td><td colspan="2"></td></tr>
</table>

Table V.4. crystallographic data of the **Complex 4.**

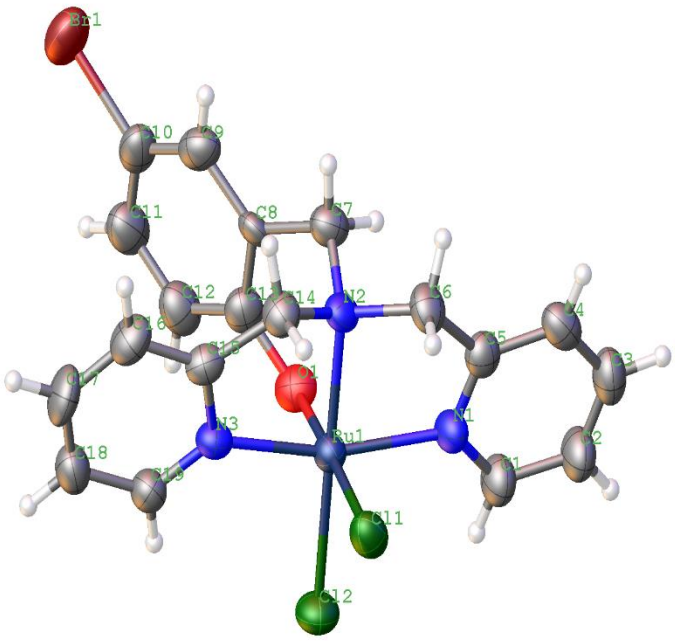

Complex-4	
CCDC No. 2480992	
Formula moiety Ru,1.5[CH_3CH_2OH]	$C_{19}H_{17}BrCl_2N_3O$
Molecular weight	624.34
Crystal system	'orthorhombic'
Space group	P212121
a/ Å	11.764(2)
b/ Å	13.181(2)
c/ Å	15.012(3)
α/°	90
β/°	90
γ/°	90
V/ $Å^3$	2327.8(7)
Z	4
Dcalcd /g cm^{-3}	1.782
Mu (mm-1)	2.652
T/K	273 K
R1 = 0.0436(4366)	
wR2 = 0.1223(4844)	
GOF on F2	1.050

Bond length(Å)	
Ru-N1	2.077(5)
Ru-N2	2.085(4)
Ru-N3	2.051(5)
Ru-O1	1.995(4)
Ru-Cl1	2.3782(14)
Ru-Cl2	2.3971(16)
O1-C13	1.353(7)

V.2.5. Catalytic Activity:

In this study, we report the dehydrogenative coupling of secondary alcohols or ketones with 2-amino primary alcohol derivatives, catalyzed by the synthesized stable octahedral Ru(III) polypyridyl complexes. These complexes exhibited excellent catalytic efficiency in the one-pot cascade synthesis of quinoline derivatives, using 2-aminobenzyl alcohol as the coupling partner. Conventionally, Friedländer annulation reactions employ the condensation of 2-aminobenzaldehydes with ketones under either basic or acidic conditions[22]. However, such methods are often limited by the instability of 2-aminobenzaldehydes, which are prone to self-condensation and undesired side reactions. To overcome these drawbacks, we developed a more sustainable approach based on acceptorless dehydrogenative coupling (ADC), utilizing catalytic amounts of base and the more stable 2-aminobenzyl alcohol and its derivatives.

The reaction of 2-aminobenzyl alcohol with acetophenone was selected as a model system to optimize conditions for mono-dehydrogenative cyclization, affording quinoline derivatives (Condition-A). Building on these results, the feasibility of double-dehydrogenative cyclization involving secondary alcohols and 2-aminobenzyl alcohol was subsequently examined (Condition-B). Remarkably, the benchmark reaction of 1-phenylethanol with 2-aminobenzyl alcohol proceeded smoothly, delivering the desired quinoline derivatives in good yields, as summarized in Table V.5.

Preliminary experiments were conducted using 1.00 mol% of catalyst Complex-1 and 100 mol% of KO*t*Bu under open-air conditions at 85 ºC, yielding 95% and 92% of 1 under condition A and condition B, respectively (Table V.5, entry 1).

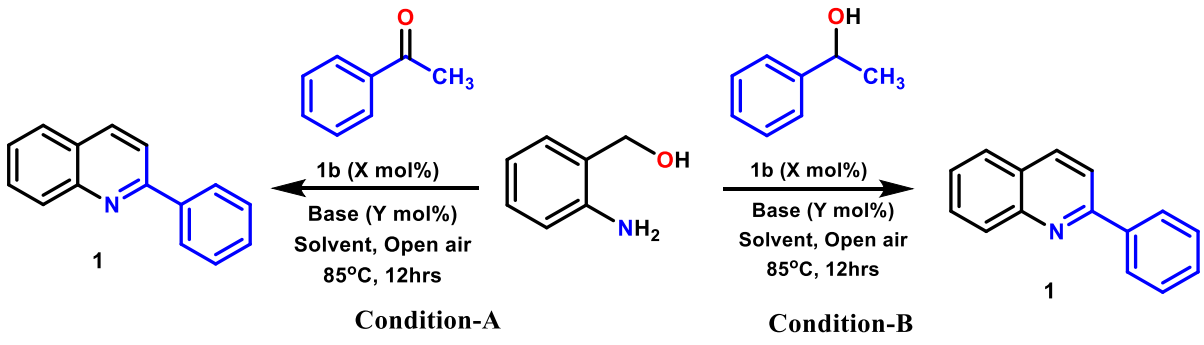

Scheme V.1. The reaction of 2-aminobenzyl alcohol with acetophenone and 1-phenylethanol at different condition.

Table V.5. Optimization of the reaction conditions for the Ru(III) catalyzed acceptorless mono- and double-dehydrogenative coupling of 2-aminobenzylalcohol with acetophenone and 1-phenylethanol.

Entry	Catalyst (X mol%)	Solvent	Base (Y mol%)	Temp (ºC)	Yield[b,f] (%)	Yield[b,g] (%)
1	Complex-1(1.00mol%)	Toluene	KO^{t}Bu (100)	85	95	92
2	Complex-1(1.00mol%)	Toluene	KO^{t}Bu (50)	85	93	90
3	Complex-1(1.00mol%)	Toluene	KO^{t}Bu (20)	85	87	70
4	Complex-1(1.00mol%)	Toluene	KO^{t}Bu (40)	85	90	87
5	Complex-1(1.00mol%)	Toluene	NaO^{t}Bu (40)	85	87	60
6	Complex-1(1.00mol%)	Toluene	NaOH (40)	85	90	60
7	Complex-1(1.00mol%)	Toluene	KOH (40)	85	87	62
8	Complex-1(1.00mol%)	Toluene	K_2CO_3 (40)	85	50	20
9	Complex-1(1.00mol%)	Xylene	KO^{t}Bu (40)	85	80	55
10	Complex-1(1.00mol%)	THF	KO^{t}Bu (40)	85	50	25
11	Complex-1(1.00mol%)	EtOH	KO^{t}Bu (40)	85	ND	ND
12[c]	Complex-1(1.00mol%)	Toluene	KO^{t}Bu (40)	RT	NR	ND
13	Complex-1(1.00mol%)	Toluene	KO^{t}Bu (40)	100	92	90
14		Toluene	KO^{t}Bu (40)	85	ND	ND
15[d]	Complex-1(1.00mol%)	Toluene	KO^{t}Bu (40)	85	trace	trace
16[e]	Complex-1(1.00mol%)	Toluene	KO^{t}Bu (40)	85	78	35
17	Complex-2(1.00mol%)	Toluene	KO^{t}Bu (40)	85	85	82
18	Complex-3(1.00mol%)	Toluene	KO^{t}Bu (40)	85	95	93
19	Complex-4(1.00mol%)	Toluene	KO^{t}Bu (40)	85	83	80

[a]Reaction Conditions: mono-dehydrogenation: condition **A**: 2-Amino benzyl alcohol **6a** (1.00 mmol), acetophenone **3a** (1.00 mmol). Double-dehydrogenation: condition **B**: 2-Amino benzyl alcohol **6a** (1.00 mmol), 1-phenylethanol **4a** (1.00 mmol), Base, 5.0 ml toluene, Reaction time 18 hrs, open air.
[b]Isolated yield after coloumn chromatography.
[c]RT = Room Temperature.
[d]Under an argon atmosphere.
[e]Reaction time 6 hrs, ND = Not Detected.
[f]represents the yield of the mono-dehydrogenative coupling reaction.
[g]represents the yield of the double-dehydrogenative coupling reaction.

Upon reducing the base loading to 40 mol%, the yield of the desired products remained largely unaffected (Table **V.5**, entries **4**). However, a further reduction to 20 mol% severely diminished the product yield (Table **V.5**, entries **3**). Among the various trial bases, including NaO*t*Bu, KOH, NaOH, K_2CO_3 and KO*t*Bu, the highest yield of the desired 1 was achieved using 40 mol% of KO*t*Bu with 1 mol% catalyst. Notably, KO*t*Bu proved to be the most efficient base for this reaction, affording 1 in excellent yields. The reaction efficiency was maximized in aprotic solvents such as xylene, toluene, and THF, whereas the yield decreased drastically in protic solvents like ethanol (Table **V.5**, entries **11**). Additionally, the yield of 1 dropped significantly when the temperature was reduced from 85 ºC to room temperature. However, increasing the temperature beyond 85 ºC did not lead to a significant improvement in yield.

The ligand framework plays a pivotal role in determining the catalytic behaviour of the complexes. The catalytic activity is strongly influenced by the substituent positioned opposite to the phenolic –OH group. Incorporation of electron-withdrawing groups at this site enhances the catalytic performance, as the increased electron deficiency strengthens the polarity of the Ru–O bond, thereby facilitating its easier dissociation from the metal centre. Thus, complex-3 displayed the highest catalytic activity, which can be attributed to the presence of the –OMe group positioned opposite to the phenolic –OH functionality. Accordingly, the catalytic efficiency of the complexes follows the order: **complex-3** > **complex-1** > **complex-2** > **complex-4**.

Table V.6 Screening of various secondary alcohols and ketones for dehydrogenative coupling reaction.

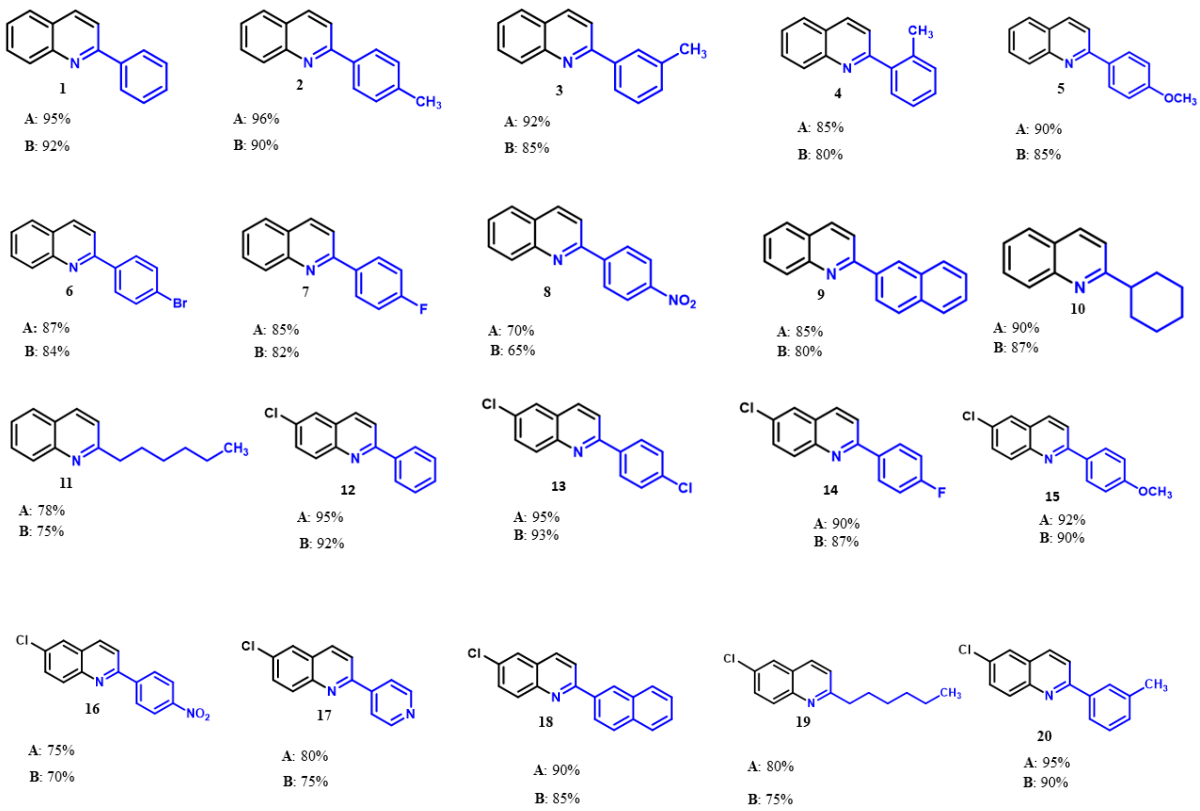

V.3. Mechanism:

Based on previous reports[15,16,23,24], a plausible mechanism for the Ru(II)-catalyzed ADC reaction is proposed, as illustrated in Scheme 4. Under the reaction conditions, the Ru(III) precatalyst is first reduced in situ to generate the active Ru(II) species. In the presence of KOtBu and alcohol, this species undergoes transformation to form the Ru(II)-alkoxy intermediate. Subsequent transfer of the α-hydrogen from the alkoxy moiety to the metal center furnishes the hydrido species along with the corresponding ketone. The hydrido intermediate then releases H_2, regenerating the active Ru(II) species (Scheme **V.2**).

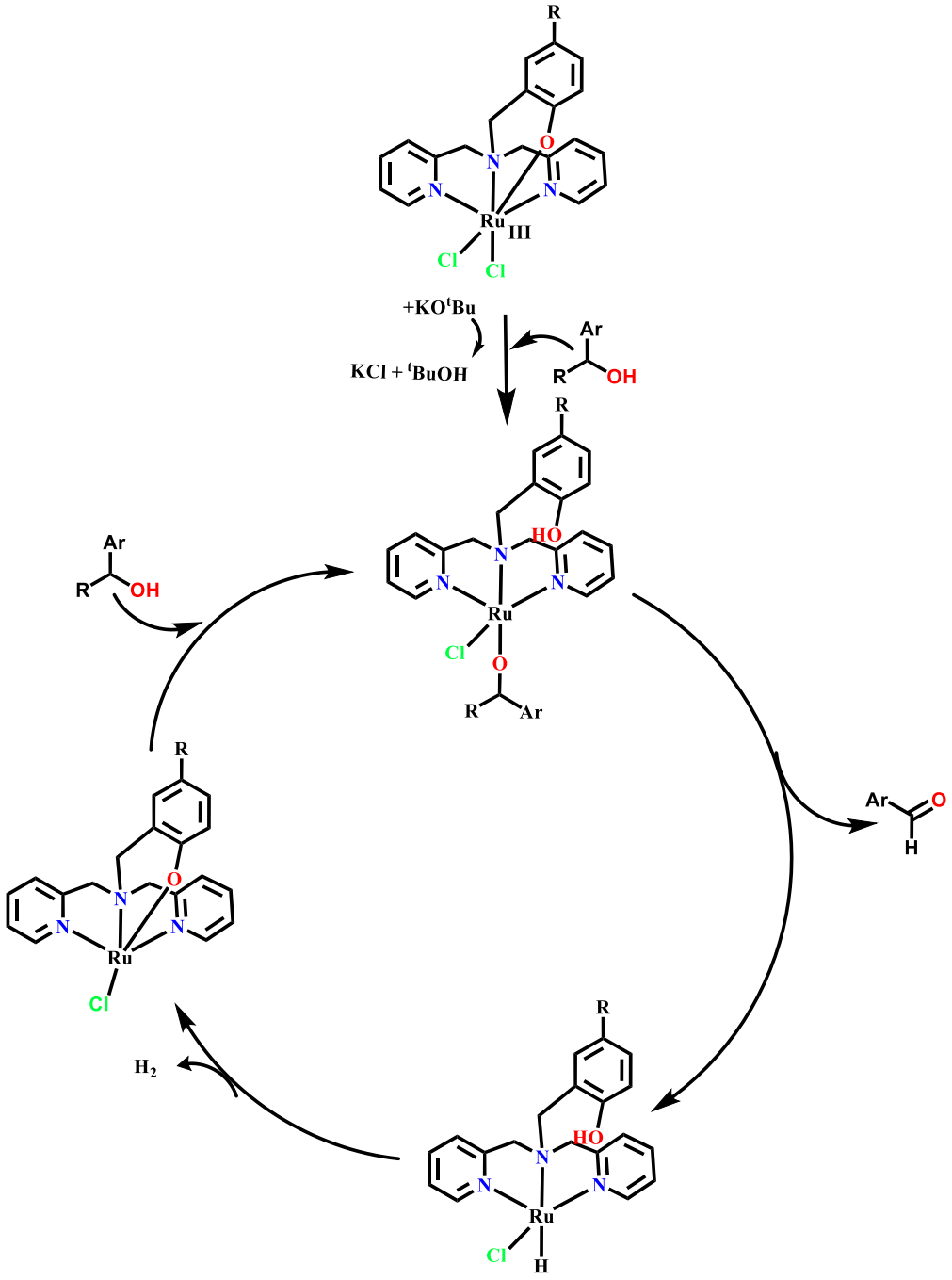

Scheme V.2. Proposed reaction mechanism for Ru(III)-mediated catalytic reaction.

V.4. Conclusion

This study demonstrates that Ru(III) polypyridyl complexes serve as highly effective catalysts for acceptorless dehydrogenative coupling, providing a sustainable route to substituted quinoline derivatives. The method offers clear advantages over traditional Friedländer annulation by utilizing stable 2-aminobenzyl alcohols and avoiding the limitations associated with unstable 2-aminobenzaldehydes. Reaction optimization established KOtBu as the most suitable base, with 40 mol% loading and 1 mol% catalyst affording excellent yields under open-air conditions. Solvent and temperature screening further revealed that aprotic solvents and elevated temperatures are essential for achieving maximum efficiency.

The catalytic performance was found to be strongly dependent on the ligand environment, particularly the substituent positioned opposite to the phenolic –OH group. The –OMe group in complex-3 significantly enhanced Ru–O bond polarity, leading to the highest catalytic activity. Accordingly, the activity trend among the complexes was identified as complex-3 > complex-1 > complex-2 > complex-4. These findings highlight the potential of Ru(III) polypyridyl systems in promoting challenging oxidative couplings and open new avenues for designing redox-active ligand frameworks in atom-economical catalysis.

V.5 Characterization data of Ru(III) catalyzed compounds:

All the reactions were carried out in 1.0 mmol scale of reactant and according to the general procedure for synthesis of quinoline derivatives.

2-phenyl quinoline (**1**): Eluent: Hexane/Ethyl acetate (20:1). white solid (yield = 95%). ^{1}H

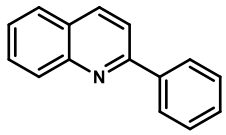

NMR (400 MHz, $CDCl_3$) δ 8.20 – 8.09 (m, 3H), 8.04 (d, *J* = 8.6 Hz, 1H), 7.83 (d, *J* = 8.6 Hz, 1H), 7.75 (d, *J* = 2.4 Hz, 1H), 7.66 (dd, *J* = 9.0, 2.4 Hz, 1H), 7.55 (dd, *J* = 8.3, 6.2 Hz, 2H), 7.53 – 7.48 (m, 1H). ^{13}C NMR (101 MHz, $CDCl_3$) δ 157.46, 146.63, 139.16, 131.91, 131.33, 130.56, 127.54, 126.16, 119.71.

2-(p-tolyl)quinoline (2): Eluent: Hexane/Ethyl acetate (20:1). white solid (yield = 96%). ^{1}H

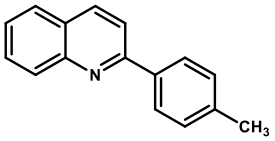

NMR (300 MHz, CDCl3) δ 8.21 (d, *J* = 8.6 Hz, 2H), 8.17 – 8.06 (m, 2H), 7.92 – 7.80 (m, 2H), 7.75 (ddd, *J* = 8.4, 6.9, 1.5 Hz, 1H), 7.54 (ddd, *J* = 8.0, 6.8, 1.2 Hz, 1H), 7.41 – 7.32 (m, 2H), 2.47 (s, 3H). ^{13}C NMR (75 MHz, CDCl3) δ 157.35, 148.32, 139.43, 136.90, 136.69, 129.68, 129.61, 127.48, 127.13, 126.11, 118.89, 21.38.

2-(m-tolyl)quinoline (**3**): Eluent: Hexane/Ethyl acetate (20:1). Yellowish Liquid (yield =

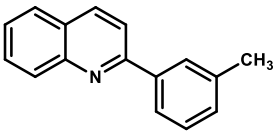

92%). 1H NMR (300 MHz, $CDCl_3$): δ (ppm) 8.25-8.20 (m, 2H), 7.95 (d, *J* = 7.7 Hz, 1H), 7.85 (d, *J* = 6.6 Hz, 1H), 7.80-7.73 (m, 2H), 7.55 (t, *J* = 6.9 Hz, 1H), 7.47-7.37(m, 2H), 7.31 (d, *J* = 6.7 Hz, 1H), 2.51 (s, 3H). ^{13}C NMR (75 MHz, $CDCl_3$): δ (ppm) 157.6, 148.3, 138.5, 136.7, 133.8, 130.1, 129.7, 129.6, 128.7, 128.4, 128.3, 127.4, 126.2, 124.7, 119.1, 21.6.

2-(o-tolyl)quinoline (4): Eluent: Hexane/Ethyl acetate (20:1). white solid (yield = 85%). ^{1}H

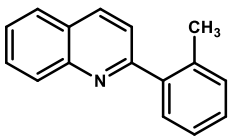

NMR (400 MHz, $CDCl_3$) δ 8.22 (dd, *J* = 18.0, 8.5 Hz, 2H), 7.89 (dd, *J* = 8.1, 1.5 Hz, 1H), 7.77 (ddd, *J* = 8.5, 6.8, 1.5 Hz, 1H), 7.62 – 7.51 (m, 3H), 7.35 (h, *J* = 3.2, 2.5 Hz, 3H), 2.44 (s, 3H). ^{13}C NMR (101 MHz, $CDCl_3$) δ 160.28, 147.85, 140.68, 136.14, 136.01, 130.88, 129.71, 129.66, 129.57, 129.05, 128.54, 127.52, 126.76, 126.44, 126.02, 122.40, 20.35.

2-(4-methoxyphenyl)quinoline (5): Eluent: Hexane/Ethyl acetate (20:1). pastel orange solid

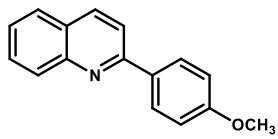

(yield = 90%). ^{1}H NMR (300 MHz, $CDCl_3$): δ (ppm) 8.22-8.15 (m, 4H), 7.88-7.82 (m, 2H), 7.73 (t, *J* = 6.9 Hz, 1H), 7.52 (t, *J* = 7.5 Hz, 1H),7.08 (d, *J* = 8.9 Hz, 2H), 3.92 (s, 3H). ^{13}C NMR (75 MHz, $CDCl_3$): δ (ppm) 160.8, 157.0, 148.3, 136.7, 132.3, 129.6, 129.5, 128.9, 127.4, 126.9, 125.9, 118.6, 114.2, 55.4.

2-(4-bromophenyl)quinoline (6): Eluent: Hexane/Ethyl acetate (20:1). fawn solid (yield = 87%). 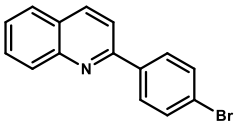 ^{1}H NMR (300 MHz, $CDCl_3$): δ (ppm) 8.26 (d, *J* = 7.8 Hz, 1H), 8.18 (dd, *J* = 8.5, 1.0 Hz, 1H), 8.08 (d, *J* = 8.6 Hz,2H), 7.87 (d, *J* = 8.6 Hz,2H), 7.79-7.74(m, 1H), 7.68(d, *J* = 8.6 Hz, 2H), 7.57 (t, *J* = 6.9 Hz,1H). ^{13}C NMR (75 MHz, $CDCl_3$): δ (ppm) 156.1, 148.3, 138.5, 137.0, 132.0, 131.4, 129.9, 129.7, 129.1, 127.5, 127.3, 126.6, 123.9, 118.5.

2-(4-fluorophenyl)quinoline (7): Eluent: Hexane/Ethyl acetate (20:1). white solid (yield = 85%). 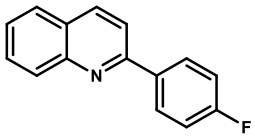 ^{1}H NMR (400 MHz, CDCl3) δ 8.32 – 8.11 (m, 4H), 7.85 (d, *J* = 8.4 Hz, 2H), 7.80 – 7.71 (m, 1H), 7.59 – 7.51 (m, 1H), 7.23 (t, *J* = 8.6 Hz, 2H). ^{13}C NMR (101 MHz, CDCl3) δ 165.06, 162.58, 156.26, 148.24, 136.93, 135.85, 135.82, 129.81, 129.65, 129.47, 129.39, 127.50, 127.10, 126.37, 118.65, 115.90, 115.68.

2-(4-nitrophenyl)quinoline (8): Eluent: Hexane/Ethyl acetate (20:1). beige solid (yield = 70%). 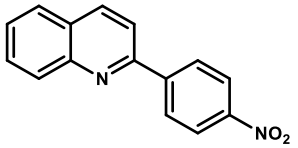 ^{1}H NMR (300 MHz, $CDCl_3$): δ (ppm) 8.43-8.36 (m, 4H), 8.35-8.32 (m, 1H), 8.24-8.20 (m, 1H), 7.96 (d, *J* = 8.6 Hz, 1H), 7.92-7.89 (m, 1H), 7.84-7.78 (m, 1H), 7.65-7.60 (m, 1H). ^{13}C NMR (75 MHz, $CDCl_3$): δ (ppm) 157.6, 148.4, 148.3, 145.5, 137.4, 130.3, 130.0, 128.4, 128.2, 127.6, 127.3, 124.1, 118.8.

2-(naphthalen-2-yl)quinoline (9): Eluent: Hexane/Ethyl acetate (20:1). white solid (yield = 85%). 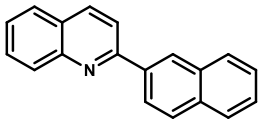 ^{1}H NMR (300 MHz, $CDCl_3$) δ 8.65 (d, *J* = 1.8 Hz, 1H), 8.41 (dd, *J* = 8.6, 1.8 Hz, 1H), 8.36 – 8.22 (m, 2H), 8.18 – 7.95 (m, 3H), 7.95 – 7.73 (m, 3H), 7.71 – 7.43 (m, 3H). ^{13}C NMR (75 MHz, $CDCl_3$) δ 157.18, 148.39, 136.97, 136.86, 133.91, 133.54, 129.78, 129.76, 128.88, 128.62, 127.69, 127.54, 127.21, 126.76, 126.38, 126.14, 125.79, 125.11, 119.19.

2-cyclohexylquinoline (10): Eluent: Hexane/Ethyl acetate (20:1). yellowish oil (yield = 90%). 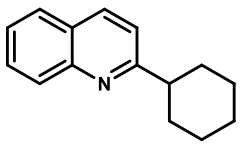 ^{1}H NMR (300 MHz, $CDCl_3$): δ (ppm) 8.11 (d, *J* = 3.0 Hz, 1H), 8.08 (d, *J* = 3.4 Hz, 1H), 7.79 (dd, *J* = 8.1, 1.5 Hz, 1H), 7.70 (ddd, *J* = 8.5, 6.9, 1.5 Hz, 1H), 7.50 (ddd, *J* = 8.1, 6.9, 1.2 Hz, 1H), 7.36 (d, *J* = 8.6 Hz, 1H), 2.99-2.93 (m, 1H), 2.09-2.03 (m, 3H), 1.95-1.90 (m, 2H), 1.69-1.48 (m, 5H). ^{13}C NMR (75 MHz, $CDCl_3$): δ (ppm) 166.8, 147.9, 136.2, 129.2, 129.0, 128.2, 127.4, 125.6, 119.6, 47.62, 32.8, 28.5, 26.6, 26.2, 25.7.

2-hexylquinoline (11): Eluent: Hexane/Ethyl acetate (20:1). colorless oil (yield = 78%). ^{1}H NMR (400 MHz, $CDCl_3$) δ 8.00 (d, *J* = 8.7 Hz, 2H), 7.75 (dd, *J* = 18.4, 2.3 Hz, 1H), 7.60 (ddd, *J* = 24.5, 9.0, 2.4 Hz, 1H), 7.34 (d, *J* = 8.4 Hz, 1H), 3.02 – 2.93 (m, 2H), 1.87 – 1.77 (m, 2H), 1.47 – 1.33 (m, 6H), 0.90 (td, *J* = 5.8, 4.7, 2.4 Hz, 3H). ^{13}C NMR (101 MHz, $CDCl_3$) δ 163.49, 146.23, 135.29, 130.42, 130.27, 127.30, 126.16, 125.61, 122.27, 39.27, 31.71, 29.89, 29.21, 22.57, 14.07.

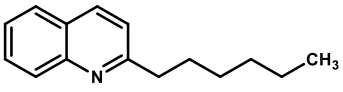

6-chloro-2-phenylquinoline (12): Eluent: Hexane/Ethyl acetate (20:1). white solid (yield = 95%). ^{1}H NMR (300 MHz, $CDCl_3$): δ (ppm) 8.19-8.12(m, 4H), 7.92 (d, *J* = 8.7 Hz, 1H), 7.83 (d, *J* = 2.3 Hz, 1H), 7.68 (dd, *J* = 9.0, 2.3 Hz, 1H), 7.59-7.47 (m, 3H). ^{13}C NMR (75 MHz, $CDCl_3$): δ (ppm) 157.6, 146.7, 139.2, 135.9, 131.9, 131.3, 130.6, 129.6, 128.9, 127.7, 127.5, 126.2, 119.8.

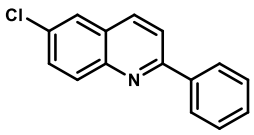

6-chloro-2-(4-chlorophenyl)quinoline (13): Eluent: Hexane/Ethyl acetate (20:1). white solid (yield = 95%). ^{1}H NMR (300 MHz, $CDCl_3$) δ 8.18 – 8.07 (m, 4H), 7.91 – 7.82 (m, 2H), 7.69 (dd, *J* = 9.0, 2.3 Hz, 1H), 7.55 – 7.48 (m, 2H). ^{13}C NMR (75 MHz, $CDCl_3$) δ 156.23, 146.62, 137.59, 136.04, 135.85, 132.18, 131.30, 130.79, 129.11, 128.77, 127.77, 126.18, 119.38.

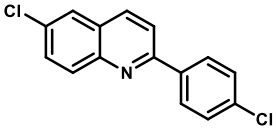

6-chloro-2-(4-fluorophenyl)quinoline (14): Eluent: Hexane/Ethyl acetate (20:1). white solid (yield = 92%). ^{1}H NMR (300 MHz, CDCl3) δ 8.24 – 8.14 (m, 3H), 8.10 (dt, *J* = 9.0, 0.7 Hz, 1H), 7.92 – 7.80 (m, 2H), 7.68 (dd, *J* = 9.0, 2.4 Hz, 1H), 7.28 – 7.19 (m, 2H). ^{13}C NMR (75 MHz, $CDCl_3$) δ 165.60, 162.29, 156.46, 146.62, 136.00, 132.00, 131.25, 130.73, 129.45, 129.34, 127.63, 126.17, 119.44, 116.02, 115.74.

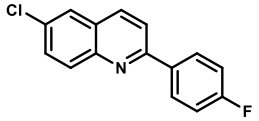

6-chloro-2-(4-methoxyphenyl)quinoline (15): Eluent: Hexane/Ethyl acetate (20:1). white solid (yield = 92%). ^{1}H NMR (300 MHz, $CDCl_3$) δ 8.20 – 8.04 (m, 4H), 7.85 (d, *J* = 8.7 Hz, 1H), 7.79 (d, *J* = 2.4 Hz, 1H), 7.65 (dd, *J* = 9.0, 2.4 Hz, 1H), 7.12 – 7.01 (m, 2H), 3.91 (s, 3H). ^{13}C NMR (75 MHz, $CDCl_3$) δ 161.02, 157.11, 146.68, 135.69, 131.77, 131.46, 131.11, 130.46, 128.87, 127.45, 126.13, 119.33, 114.30, 55.42.

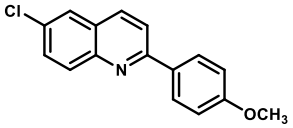

6-chloro-2-(4-nitrophenyl)quinoline (16): Eluent: Hexane/Ethyl acetate (20:1). white solid (yield = 75%). ^{1}H NMR (300 MHz, $CDCl_3$): δ (ppm) 8.23 (d, *J* = 8.7 Hz, 2H), 7.96 (d, *J* = 8.6 Hz, 2H), 7.86 (d, *J* = 2.3 Hz, 2H), 7.74 (d, *J* = 2.3 Hz, 1H), 7.45 (d, *J* = 2.5 Hz, 1H), 6.63 (d, *J* = 8.8 Hz, 1H). ^{13}C NMR (75 MHz, $CDCl_3$): δ (ppm) 154.7, 148.5, 146.4, 144.7, 136.6, 133.2, 131.4, 129.3, 128.4, 128.1, 126.3, 124.1, 119.7.

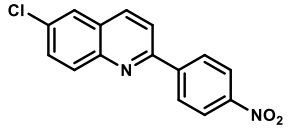

6-chloro-2-(pyridin-4-yl)quinoline (17): Eluent: Hexane/Ethyl acetate (20:1). white solid (yield = 80%). 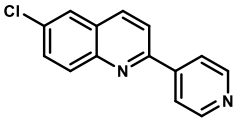 ^{1}H NMR (300 MHz, $CDCl_3$) δ 8.84 – 8.71 (m, 2H), 8.23 – 8.09 (m, 2H), 8.05 (d, *J* = 5.3 Hz, 2H), 7.95 – 7.87 (m, 1H), 7.86 – 7.75 (m, 1H), 7.73 – 7.56 (m, 1H). ^{13}C NMR (75 MHz, $CDCl_3$) δ 154.63, 150.49, 146.62, 136.37, 133.02, 131.11, 130.03, 128.35, 127.25, 126.24, 121.67, 119.26.

6-chloro-2-(naphthalen-2-yl)quinoline (18): Eluent: Hexane/Ethyl acetate (20:1). white solid (yield = 90%). 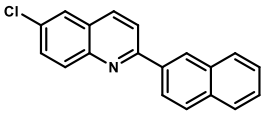 ^{1}H NMR (300 MHz, $CDCl_3$) δ 8.62 (d, *J* = 1.8 Hz, 1H), 8.37 (dd, *J* = 8.6, 1.9 Hz, 1H), 8.17 (dd, *J* = 8.8, 4.5 Hz, 2H), 8.06 – 7.89 (m, 4H), 7.70 (dd, *J* = 9.0, 2.4 Hz, 1H), 7.57 (qd, *J* = 6.4, 2.5 Hz, 3H). ^{13}C NMR (75 MHz, $CDCl_3$) δ 157.39, 146.75, 143.23, 136.49, 135.89, 133.49, 131.33, 130.66, 128.87, 128.32, 127.96, 127.77, 126.91, 126.46, 126.20, 124.89, 123.85, 123.82, 119.97.

6-chloro-2-hexylquinoline (19): Eluent: Hexane/Ethyl acetate (20:1). colorless oil (yield = 78%, 193mg). 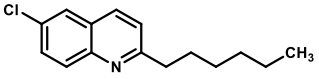 ^{1}H NMR (300 MHz, $CDCl_3$): δ (ppm) 8.00-7.92 (m, 2H), 7.77-7.71 (m, 1H), 7.64-7.53 (m, 1H), 7.34-7.28 (m, 1H), 2.97 (dd, *J* = 8.6, 7.2 Hz, 2H), 1.86-1.76 (m, 2H), 1.46-1.40 (m, 5H), 0.97-0.87 (m, 4H). ^{13}C NMR (75 MHz, $CDCl_3$): δ (ppm) 163.5, 146.2, 135.3, 131.2, 130.4, 130.2, 127.3, 126.1, 122.3, 39.3, 31.7, 29.9, 29.2, 22.6, 14.1.

6-chloro-2-(m-tolyl)quinoline (20): Eluent: Hexane/Ethyl acetate (20:1). white solid (yield = 95%). 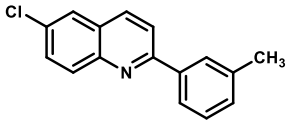 ^{1}H NMR (400 MHz, $CDCl_3$) δ 8.14 (dd, *J* = 8.8, 4.9 Hz, 2H), 8.01 (s, 1H), 7.92 (t, *J* = 8.9 Hz, 2H), 7.83 (d, *J* = 2.3 Hz, 1H), 7.68 (dd, *J* = 9.1, 2.4 Hz, 1H), 7.44 (t, *J* = 7.6 Hz, 1H), 7.32 (d, *J* = 7.6 Hz, 1H), 2.51 (s, 3H). ^{13}C NMR (101 MHz, $CDCl_3$) δ 157.81, 146.66, 139.20, 138.63, 135.79, 131.85, 131.31, 130.55, 130.39, 128.81, 128.21, 127.73, 126.15, 124.67, 119.98, 21.60.

V.6. NMR spectra of selected compounds

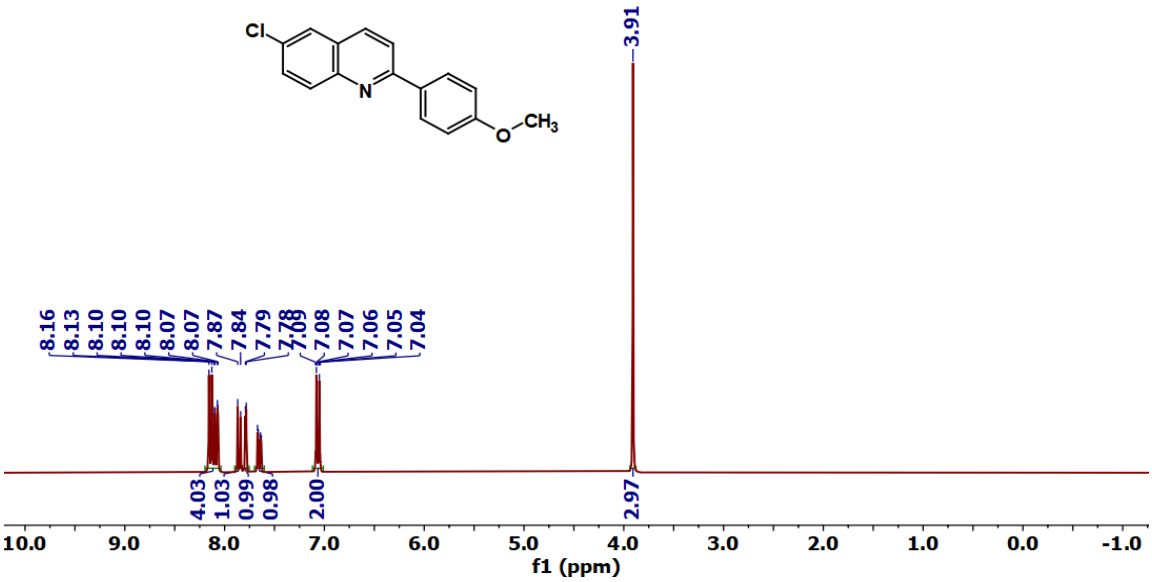

Figure V.9. ^{1}H NMR spectrum of compound **15** in $CDCl_3$

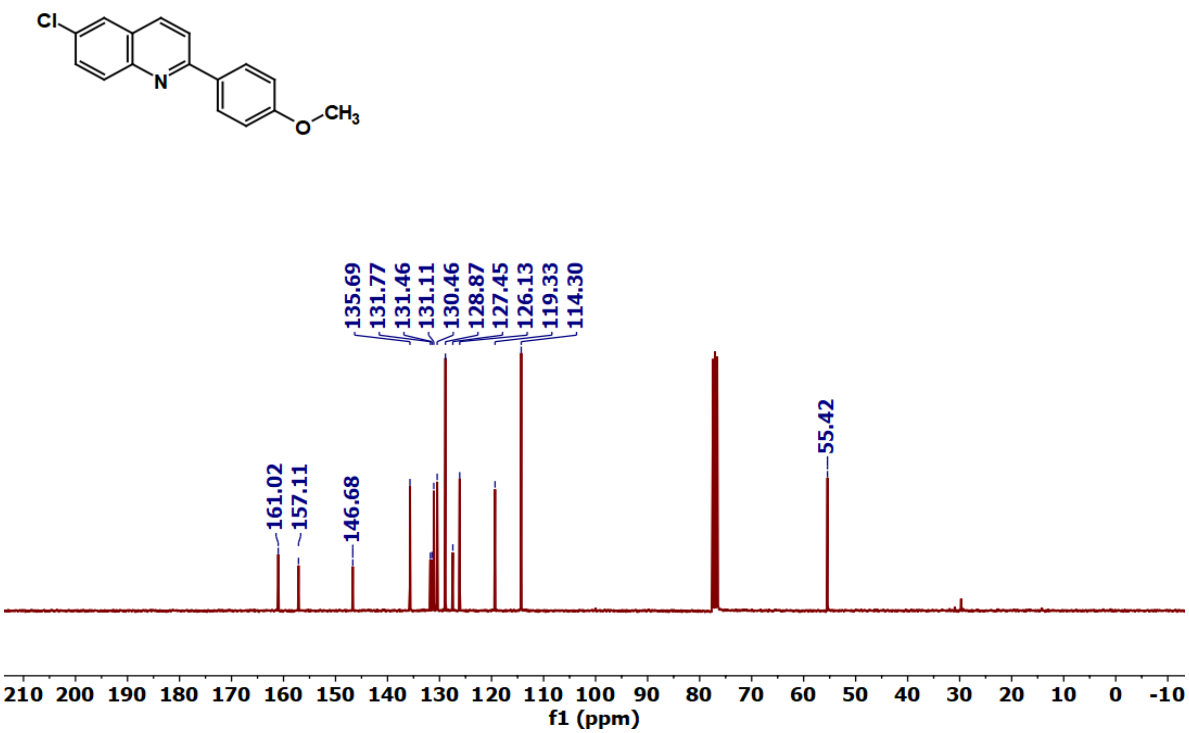

Figure V.10. ^{13}C NMR spectrum of compound **15** in $CDCl_3$.

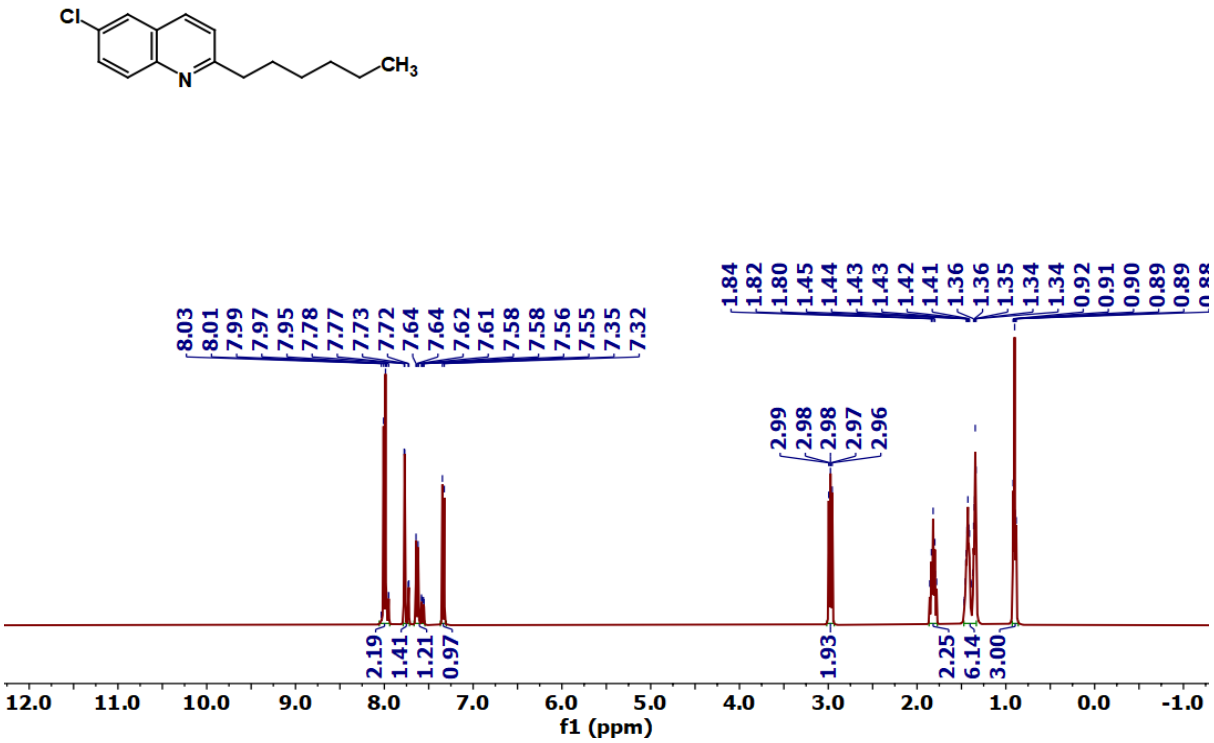

Figure V.11. ^{1}H NMR spectrum of compound **19** in $CDCl_3$.

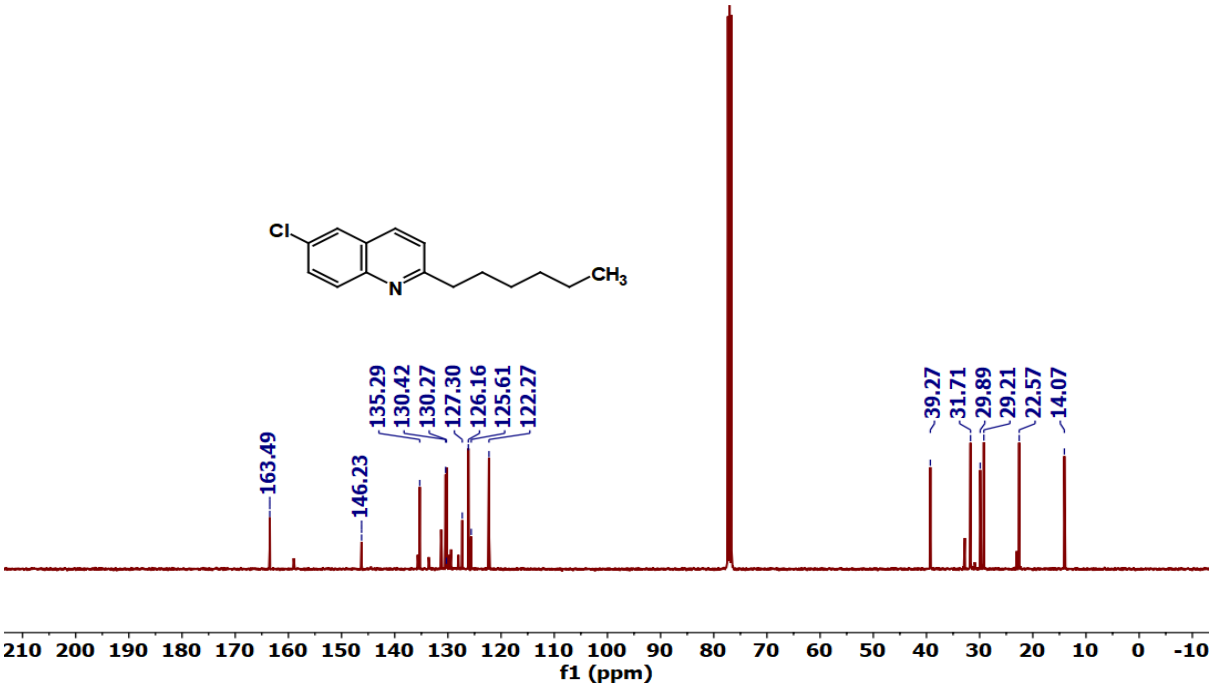

Figure V.12. ^{13}C NMR spectrum of compound **19** in $CDCl_3$.

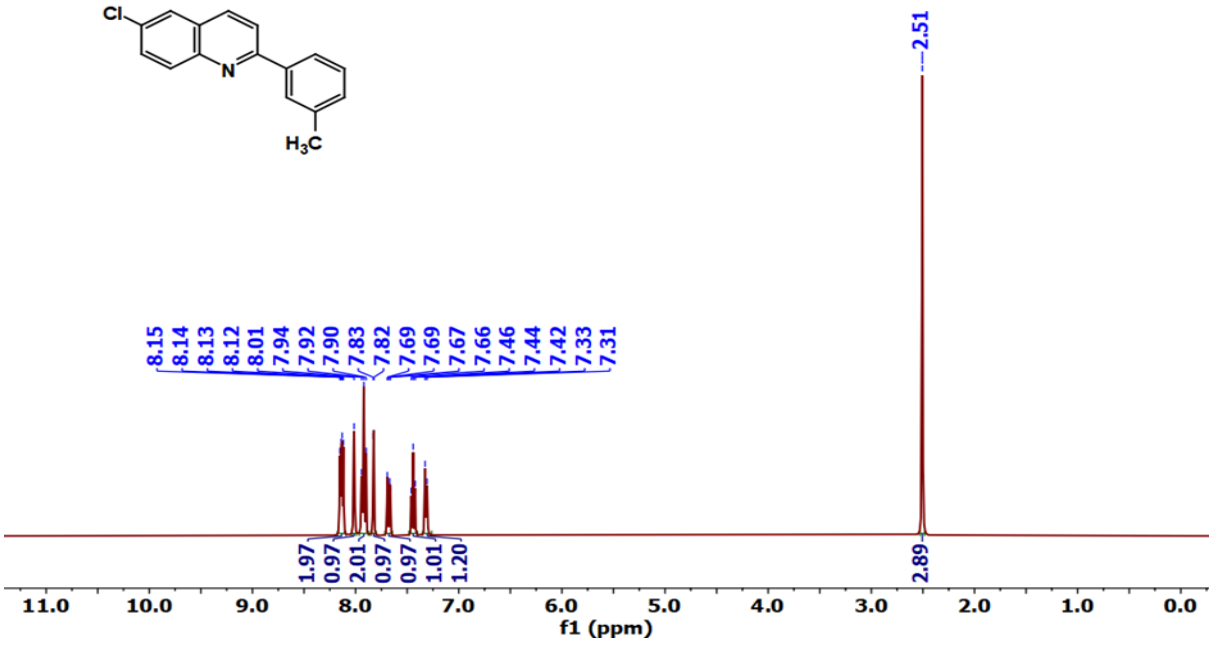

Figure V.13. ^{1}H NMR spectrum of compound **20** in $CDCl_3$.

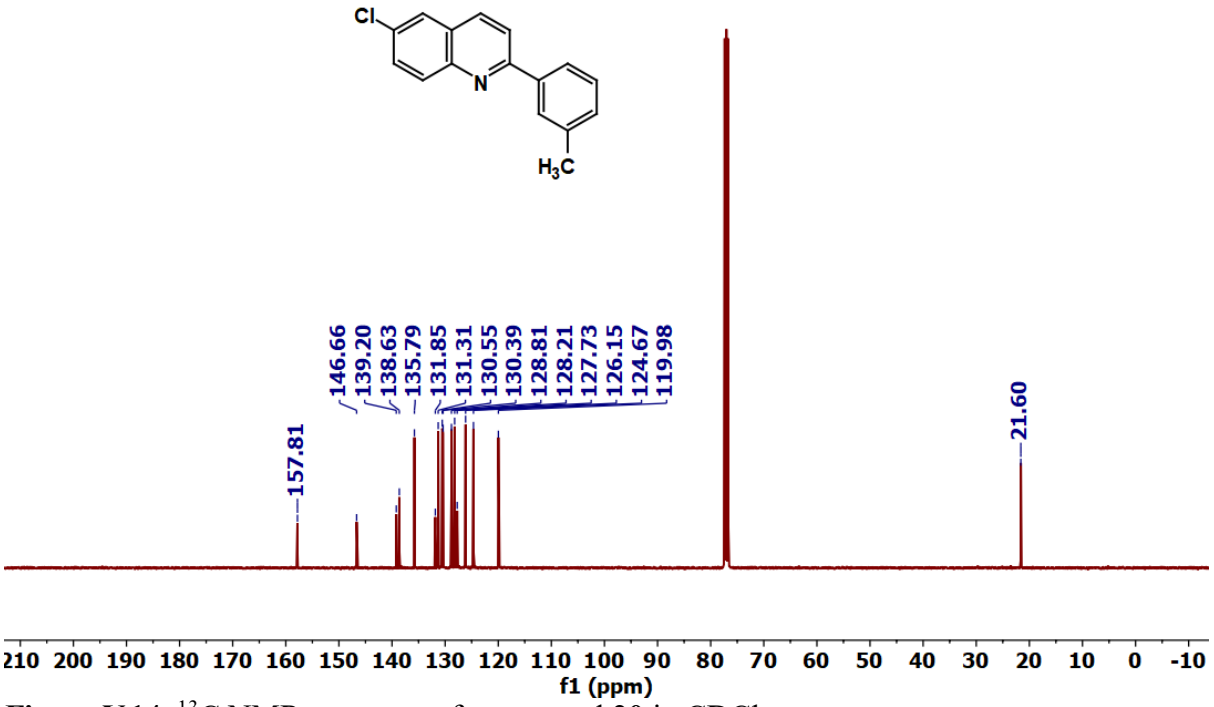

Figure V.14. ^{13}C NMR spectrum of compound **20** in $CDCl_3$.

V.7. References

1. Y. Zhou, W. Li, L. Yu, Y. Liu, X. Wang, M. Zhou, *Dalton Trans.* 2015, **44**, 1858–1865.
2. R. Musiol, *Expert Opin. Drug Discovery.* 2017, **12**, 583–597.
3. Gopaul, Kaalin; A. Shintre, Suhas; A. Koorbanally, Neil; *Anti-Cancer Agents Med. Chem.* 2015, **15**, 631–646.
4. R. Sharma, P. Kour, A. Kumar, *J. Chem. Sci*. 2018, **130**, 73–98.
5. G. Chelucci, A. Porcheddu, *Chem. Rec.* 2017, **17**, 200–216.
6. F. Huang, Z. Q. Liu, Z. K. Yu, *Angew*. *Chem*. *Int*. Ed. 2016, **55**, 862–875.
7. N. Anand, S. Koley, B. J. Ramulu, M. S. Singh, *Org*. *Biomol*. *Chem*. 2015, **13**, 9570–9574.
8. S. Yao, K. J. Zhou, J. B. Wang, H. E. Cao, L. Yu, J. Z. Wu, P. H. Qiu, Q. Xu, *Green Chem*. 2017, **19**, 2945–2951.
9. M.-J. Zhang; H.-X. Li; D. J. Young; H.-Y. Li; J.-P. Lang. *Org. Biomol. Chem.* 2019, **17**, 3567−3574.
10. K. Singh; M. Vellakkaran; D. Banerjee. *Green Chem.* 2018, **20**, 2250−2256.
11. R. Martínez; D. J. Ramon; M. Yus; *Eur*. *J. Org. Chem*. 2007, **2007**, 1599−1605.
12. H. V. Vander; Mierde, N. Ledoux; B. Allaert; P. V. D.Voort; R. Drozdzak; D. D. Vos; F. Verpoort; *New J. Chem.* 2007, **31**, 1572−1574.
13. D. Srimani; Y. Ben-David; D. Milstein; *Chem. Commun*. 2013, **49**, 6632−6634.
14. B. Pan; B. Liu; E. Yue; Q. Liu; X. Yang; Z. Wang; W.-H. A. Sun; *ACS Catal*. 2016, **6**, 1247−1253.
15. D. Bhattacharyya, P. Adhikari, K. Deoria and A. Das, *Catal. Sci. Technol*., 2022, **12**, 5695.
16. B. Guo, T.-Q. Yu, H.-X. Li, S.-Q. Zhang, P. Braunstein, D. J. Young, H.-Y. Li and J.-P. Lang, *ChemCatChem*, 2019, **11**, 3623–3631.
17. X. Wang, C. Wang, Y. Liu and J. Xiao, *Green Chem*., 2016, **18**, 4605–4610.
18. I. Dutta, A. Sarbajna, P. Pandey, S. M. W. Rahaman, K. Singh and J. K. Bera, *Organometallics*, 2016, **35**, 1505–1513.
19. F. Li; L. Lu; J. Ma; *Org. Chem. Front*. 2015, **2**, 1589−1597.
20. J. Zhou and J. Fang, *J. Org. Chem.*, 2011, **76**, 7730–7736.
21. D.-W. Tan, H.-X. Li, M.-J. Zhang, J.-L. Yao and J.-P. Lang, *ChemCatChem*, 2017, **9**, 1113-1118.
22. J. Marco-Contelles, E. Pérez-Mayoral, A. Samadi, M. C. Carreiras and E. Soriano, *Chem. Rev*., 2009, **109**, 2652–2671.
23. D. Srimani, Y. Ben-David, D. Milstein, *Chem. Commun.* 2013, **49**, 6632-6634.
24. B. Pan, B. Liu, E. L. Yue, Q. B. Liu, X. Z. Yang, Z. Wang, W. H. Sun, *ACS Catal*. 2016, **6**, 1247-1253.

LIST OF PUBLICATIONS

1. **U. Shee**, D. Sinha, S. Mondal, K. K. Rajak., Electrochemical water oxidation reaction by dinuclear Re(v) oxo complexes with a 1,4-benzoquinone core *via* the redox induced electron transfer (RIET) process, *Dalton Trans.*, 2024,***53***, 8254-8263. **doi.org/10.1039/D4DT00057A**.

2. **U. Shee**, B. Khutia, S. Ray, S. Ghosh, K. K. Rajak., Highly efficient photocatalytic reduction of CO_2 to CO under visible light using rhenium benzo[*d*]oxazole complexes, Dalton Trans., 2025,**54**, 7294-7305. **doi.org/10.1039/D4DT03400G**.

Uday Shee
26/08/2025

Dalton Transactions

ROYAL SOCIETY OF CHEMISTRY

PAPER

View Article Online
View Journal

Cite this: DOI: 10.1039/d4dt00057a

Electrochemical water oxidation reaction by dinuclear Re(v) oxo complexes with a 1,4-benzoquinone core *via* the redox induced electron transfer (RIET) process†

Uday Shee,[a] Debopam Sinha,[a,b] Sandip Mondal*[c] and Kajal Krishna Rajak *[a]

We report two dinuclear rhenium(v) oxo complexes **1** and **2** types, $[Re^{V}(O)(Cl)_3(L^{2-})Re^{V}(O)(Cl)_3][NBu_4]_2$ (**1**, L^{2-} = dianionic 2,5-dihydroxy 1,4-benzoquinone (DBQ^{2-})) and (**2**, L^{2-} = dianionic chloranilic acid ($\mathbf{CA^{2-}}$) ligands), as a homogeneous electrocatalyst for water oxidation reactions in the acetonitrile–water mixture. The evolution of dioxygen gas at the anode was confirmed by a GC-TCD study. In controlled potential electrolysis (CPE), oxidation at 1.30 V (*vs.* Ag/AgCl) at neutral pH, **1** and **2** afforded $\mathbf{1^+}$ $[Re^{VI}(O)(Cl)_3(DBQ^{\bullet 3-})Re^{VI}(O)(Cl)_3]^-$ and $\mathbf{2^+}$ $[Re^{VI}(O)(Cl)_3(CA^{\bullet 3-})Re^{VI}(O)(Cl)_3]^-$ ions, respectively, *via* the redox induced electron transfer (RIET) process. Electrochemically generated species of $\mathbf{1^+}$ and $\mathbf{2^+}$ could be isolated in dry acetonitrile. $\mathbf{1^+}$ and $\mathbf{2^+}$ ions give strong EPR signals in fluid solution as well as under frozen glass conditions due to the $[Re^{VI}(O)(Cl)_3(L^{\bullet 3-})Re^{VI}(O)(Cl)_3]^- \leftrightarrow [Re^{VI}(O)(Cl)_3(L^{2-})Re^{V}(O)(Cl)_3]^-$ (where L^{2-} = DBQ^{2-} and CA^{2-}) equilibrium. However, the continuation of the CPE study (1.30 V *vs.* Ag/AgCl) in the presence of acetonitrile–water mixture oxidised the *in situ* generated species of $\mathbf{1^+}$ and $\mathbf{2^+}$ to higher valent $Re^{VI}{=}O$ species. These species ($\mathbf{1^+}$ and $\mathbf{2^+}$) bound water through the water nucleophilic attack (WNA) to produce peroxide intermediate species of $[Re^{V}(OOH)(Cl)_3(DBQ^{2-})Re^{V}(OOH)(Cl)_3]$ (**A1**) and $[Re^{V}(OOH)(Cl)_3(CA^{2-})Re^{V}(OOH)(Cl)_3]$ (**A2**) for catalysts **1** and **2**, respectively. Interestingly, **A1** and **A2** were authenticated and analysed by ESI mass spectrometry and infrared spectroscopy and were the active precursors of this water oxidation process. The extent of current generation under similar conditions suggested that complex **1** is superior to complex **2** for the water oxidation reaction. Notably, the maximum turnover frequency (TOF_{max}) of catalysts **1** and **2** were 2.1 and 1.6 s^{-1} at 0.27 V and 0.24 V over potential, respectively, which is very significant in WOR.

Received 8th January 2024,
Accepted 4th April 2024

DOI: 10.1039/d4dt00057a

rsc.li/dalton

Introduction

Shortage of energy is one of the biggest problems that humanity is now facing. Another is global warming. The creation of novel technologies and energy storage systems is necessary to meet the increasing demand for energy worldwide. There is a pressing need to switch from fossil fuels to renewable energy sources to limit fossil resources and reduce CO_2 emissions that cause global warming.[1] One of the most promising methods to develop our society with sustainable energy systems is artificial photosynthesis.[2,3] Artificial photosynthesis systems have attracted considerable attention as promising solutions to these problems. The energy from sunlight is transformed into chemical energy in the form of carbohydrates during natural photosynthesis. The artificial photosynthesis reaction imitates natural photosynthesis and can generate valuable chemical fuels from environmentally favourable sources such as CO_2 and H_2O. The majority of artificial photosynthesis consists of two half-processes: the oxidation and reduction reactions and the water oxidation process occurs *via* either $2H_2O \rightarrow H_2O_2 + 2H^+ + 2e^-$ (E^0 = 1.76 V *vs.* NHE) or by $2H_2O \rightarrow O_2 + 4H^+ + 4e^-$, ($E^0$ = 1.23 V *vs.* NHE). Hence, in the case of the former 2e oxidation reaction, H_2O_2 as a product of water oxidation[4–6] has not attracted any issues; however, the 4e oxidation process using easily affordable catalysts such as transition-metal-basedmaterials[7] and complexes[8] are the focus of water oxidation field to produce a high yield of O_2. The described catalysts could be divided into heterogeneous and homogeneous catalysts. The former primarily comprises metal

[a]Inorganic Chemistry Section, Department of Chemistry, Jadavpur University, Kolkata, 700032, India. E-mail: kajalrajak@gmail.com
[b]Department of Chemistry, Vijaygarh Jyotish Ray College, Kolkata, 700032, India
[c]Department of Chemistry, Darjeeling Govt. College, Darjeeling, 734101, India. E-mail: sandipmondal30@gmail.com

†Electronic supplementary information (ESI) available. CCDC 2181451. For ESI and crystallographic data in CIF or other electronic format see DOI: https://doi.org/10.1039/d4dt00057a

Dalton Transactions

ROYAL SOCIETY OF CHEMISTRY

PAPER

View Article Online
View Journal

Cite this: DOI: 10.1039/d4dt03400g

Highly efficient photocatalytic reduction of CO_2 to CO under visible light using rhenium benzo[*d*]oxazole complexes†

Uday Shee, Biswajit Khutia, Sneha Ray, Sumona Ghosh and Kajal Krishna Rajak *

A series of six isomeric rhenium(I) tricarbonyl complexes featuring asymmetric diimine ligands 5,7-di-*tert*-butyl-2-(pyridin-2-yl)benzo[*d*]oxazole, 2-(pyridin-2-yl)naphtho[1,2-*d*]oxazole, 2-(pyridin-2-yl)naphtho[2,3-*d*]oxazole, 2-(quinolin-2-yl)benzo[*d*]oxazole, 2-(quinolin-2-yl)naphtho[1,2-*d*]oxazole, and 2-(isoquinolin-1-yl)benzo[*d*]oxazole, was synthesized and comprehensively characterized through analytical techniques, spectroscopy, and single-crystal X-ray diffraction. These complexes were assessed as catalysts for visible-light-driven CO_2 reduction, both with and without an external photosensitizer (PS), and also exhibited catalytic activity in electrochemical CO_2 reduction, effectively functioning in both regimes. In the presence of a proton donor, trifluoroethanol (TFE), the complexes produced methane and carbon monoxide (CO) electrochemically. Under photochemical conditions, high selectivity for CO production was achieved in acetonitrile with triethanolamine (TEOA) as the proton source. This work highlights the tunability of metal complex photocatalysts for solar-to-fuel conversion through ligand design. Among the complexes studied, the rhenium complex featuring the 2-(pyridin-2-yl)naphtho[1,2-*d*]oxazole ligand demonstrated the highest catalytic efficiency, achieving a turnover number of 660 for CO_2 reduction to CO after 5 hours. Mechanistic studies employing NMR, UV-vis spectroscopy, and time-dependent density functional theory (TD-DFT) calculations provided insights into the catalytic process. These rhenium(I) complexes demonstrate promising potential for photocatalytic CO_2 reduction to CO, offering valuable insights into the design and development of efficient catalysts for artificial photosynthesis and solar-to-fuel conversion.

Received 6th December 2024,
Accepted 25th March 2025

DOI: 10.1039/d4dt03400g

rsc.li/dalton

Introduction

The escalating global climate crisis, primarily attributed to anthropogenic greenhouse gases, mainly carbon dioxide (CO_2) emissions, necessitates innovative strategies for CO_2 mitigation. Fossil fuel combustion contributes significantly to atmospheric CO_2 levels, surpassing 400 parts per million (ppm), and exacerbating climate change impacts.[1] Consequently, the conversion of CO_2 into valuable liquid fuels using renewable energy sources has emerged as a critical research frontier.[2,3] Solar energy offers a promising avenue for the photocatalytic reduction of CO_2 to products such as CO, CH_4, HCOOH, *etc.*[4–8]

To achieve this goal, both homogeneous and heterogeneous systems have been explored. However, homogeneous catalysis offers more flexibility in catalyst design and optimization due to its potential for gradual improvement in catalytic efficiency, sustainability, and atom economy.[9] A diverse range of metal complexes, including those based on Ir,[10–13] Ru,[14–18] Re,[19–23] Co,[24–27] Fe,[28–33] and Ni,[34–38] have been investigated as catalysts for CO_2 reduction. The general mechanism for the photocatalytic reduction of CO_2 involves light absorption by a photosensitizer (PS) for harvesting the energy of light and a sacrificial electron donor (SED) that provides electrons for the reduction, followed by a catalyst that accepts these electrons and reacts with CO_2 to produce the reduced products. Most molecular systems developed for the photocatalytic reduction of CO_2 typically comprise two distinct components, each serving a specific function: one molecule acts as the catalyst, while the other operates as a photosensitizer.

Recently, the development of self-photosensitizing mononuclear complexes that act as both photosensitizers and CO_2 reduction catalysts has been reported, marking a significant advancement in this field.[39–49] The pioneering work by Lehn *et al.* on the photo- and electrocatalytic reduction of CO_2 to CO using $Re(bpy)(CO)_3X$ complexes (where bpy = 2,2′-bipyridine and X represents a monodentate apical ligand) laid the foundation for subsequent research in this field.[50,51] The photoche-

Inorganic Chemistry Section, Department of Chemistry, Jadavpur University, Kolkata-700032, India. E-mail: kajalk.rajak@jadavpuruniversity.in, kajalrajak@rediffmail.com

† Electronic supplementary information (ESI) available. CCDC 2355624, 2385160, 2385164, 2385178 and 2385175. For ESI and crystallographic data in CIF or other electronic format see DOI: https://doi.org/10.1039/d4dt03400g